



DESIGN AND OPTIMIZATION OF LATTICE STRUCTURES FOR AEROSPACE APPLICATIONS

Enrico Stragiotti

François-Xavier Irisarri¹, Cédric Julien¹ and Joseph Morlier²

1: ONERA - The French Aerospace Lab
DMAS - Département matériaux et structures
92320 Châtillon, France
{francois-xavier.irisarri, cedric.julien}@onera.fr

2: ICA - Institut Clément Ader
ISAE - SUPAERO
31400 Toulouse, France
joseph.morlier@isae-supraero.fr
January 15, 2024

PhD manuscript

ONERA – ISAE Supaero

Colophon

This document was typeset with the help of KOMA-Script and L^AT_EX using the kaobook class.

ONERA – ISAE Supaero

CONTENTS

Contents	iii
List of Figures	v
List of Tables	x
List of Abbreviations	xii
1. Literature review	1
1.1. An introduction to structural optimization	1
1.1.1. Optimizers	3
1.2. Ultra-lightweight structures optimization approaches	5
1.2.1. Density-based topology optimization	6
1.2.2. Feature-Mapping topology optimization	10
1.2.3. Truss topology optimization (TTO)	10
1.3. Modular structures and lattice materials	14
1.3.1. Modular structures and lattice materials optimization	17
1.3.2. Multi-scale structures optimization	18
1.3.3. Full-scale structures optimization	20
2. Evaluating discretization approaches for ultralight structure optimization	23
2.1. The formulation of a shared problem: volume minimization with stress constraints	23
2.1.1. Density-based topology optimization minimum volume formulation	23
2.1.2. Truss Topology Optimization (TTO) minimum volume formulation	30
2.2. Comparison between density-based topology optimization and TTO	32
2.2.1. Definition of a test case for the comparison	32
2.2.2. Numerical application	33
2.2.3. Discussion	40
2.3. Conclusion	43
3. Enriching the classic TTO formulation with advanced mechanical constraints	45
3.1. Advanced mechanical constraints	45
3.1.1. Minimum slenderness constraints	46
3.1.2. Local and topological buckling constraints	47
3.1.3. Kinematic compatibility constraints	49
3.2. Optimization formulation and solving strategy	50
3.2.1. Optimization strategy	51
3.2.2. First step: SLP optimization	51
3.2.3. Handling local minima: reinitialization strategy	53
3.2.4. Second step: NLP optimization	55
3.3. Numerical application	56
3.3.1. L-shaped beam	58
3.3.2. Ten-bar truss	59

3.3.3. 2D cantilever beam	62
3.3.4. Simply supported 3D beam	65
3.3.5. Ten-bar truss with multiple load cases	67
3.4. Conclusion	70
4. Optimizing modular structures	71
4.1. Formulation of a modular structure optimization algorithm	71
4.1.1. Variable linking	71
4.1.2. Topological buckling of modular structures	73
4.1.3. Optimization formulation	73
4.1.4. Sensitivity analysis	75
4.2. Numerical application	76
4.2.1. On the equivalence of multi-load cases and modular structures	76
4.2.2. Parametric study on the number of subdomains and the complexity of the module	78
4.2.3. Comparison with the optimized octet-truss	86
4.2.4. Using multiple module topologies	91
4.3. Conclusion	94
5. Optimizing the layout of the modules in space	97
5.1. Optimize the modules' layout using a modified DMO algorithm	97
5.1.1. Definition of the subdomains cross-sectional areas	97
5.1.2. Variables penalization schemes	98
5.1.3. The optimization formulation and resolution algorithm	100
5.1.4. Optimization initialization: a clustering algorithm to identify similarly behaving subdomains	102
5.2. Numerical application	104
5.2.1. Layout optimization of fixed topology modules	105
5.2.2. Modules and layout optimization	107
5.2.3. A benchmark case study: a simply supported modular bridge	110
5.2.4. Simply supported 3D beam	115
5.3. Conclusion	116
Bibliography	119
Appendix	143
A. Sensitivity analysis of the modular structure optimization algorithm	145
A.1. Optimization formulation, objective function and constraints	145
A.2. Common derivatives	146
A.3. Gradient	147
A.4. Jacobian matrix	147
A.5. Hessian matrix	149

LIST OF FIGURES

1.1.	Visual representation of (a) size, (b) shape, and (c) topology optimization [1].	1
1.2.	The domain Ω is discretized using $N_e = N_x N_y$ continuous 4-nodes elements.	7
1.3.	Comparison between SIMP model with the Hashin-Strikman upper bound, considering an isotropic material with a Poisson ratio of 1/3 mixed with void. The Hashin-Strikman upper bound is illustrated with microstructures approaching the specified bounds. [51].	8
1.4.	Kernel of the 2D convolution operator.	8
1.5.	Component (a) and density (b) plot of a short cantilever beam optimized using the component-based topology optimization method Generalized Geometry Projection (GGP) [72].	10
1.6.	The TTO algorithm can be divided into 4 steps: (a) specification of the design space, loads, and boundary conditions; (b) discretization of the design space; (c) the ground structure is generated depending on the desired connectivity level; (d) resolution of the optimization problem and plot of the solution [77].	11
1.7.	The domain Ω is discretized using a set of straight members connecting a set of nodes. This framework is known as the ground structure.	12
1.8.	The optimal structures found by layout optimization tend at Michell-like structures, made up of a very large number of infinitesimal struts [85].	13
1.9.	The natural evolution process frequently generates lattice materials and modular structures; (a) The spore-bearing gills of a Hypholoma fasciculare [97] (b) SEM image of a leaf microstructure [98] (c) cellular stucture of the wing of a dragonfly [99] (d) internal structure of a human bone [100].	14
1.10.	Density versus yield strength Ashby chart. Exploiting the architecture of the material as a variable to design new metamaterials, empty spaces of the graph can be filled (see dots) [93].	15
1.11.	The different length scales present in a modular structure [107]. The size of the Representative Volume Element (RVE) is comparable with the dimensions of the wing, especially in the thickness. We therefore talk about modular structure and not lattice material.	15
1.12.	Vickers Wellingtons, bombers utilized during World War II, remained operational despite sustaining extensive damage, thanks to their lattice fuselage. When one of the ribs was damaged, the load was redistributed to the others, allowing the structure to remain functional [117].	16
1.13.	A stretch-dominated and a bending-dominated RVE. Bending-dominated structures act as a mechanism if the joints cannot withstand moments. The scaling laws are different for the two structure families [93].	17
1.14.	Graphical representation of the asymptotic homogenization method used to retrieve the equivalent mechanical properties of a periodic cell [134].	18
1.15.	In the study of Zhang <i>et al.</i> [106] the same test case is optimized using a different number of microstructures. Here we show the multi-scale optimized structures using 3 and 19 different microstructures.	19

1.16. Three structures with the same volume are optimized for compliance minimization using three different methods: on the left, a classic mono-scale topology optimization algorithm. Middle: the variable linking method is used to enforce the pattern repetition on the structure. On the right an optimized structure with local volume constraints. The algorithms used to optimize the last two structures belong to the family of <i>full-scale</i> methods. [122].	20
2.1. A four-node quadrilateral element. GP is the Gaussian integration point for which the equivalent stress is evaluated.	25
2.2. On the left, plot of the L-shape beam test case, on the right the graphical representations of the two discretizations used, the continuous (above) composed of 600×600 quadrilateral elements, and the truss-like (below) discretized using 33×33 nodes and a fully connected ground structure. The images represent a coarser discretization for visual clarity.	33
2.3. (a-d) Topology of the optimized structures for different values of the material allowable $\sigma_L = 10.00, 2.00, 0.40$, and 0.25 , showing a volume fraction of $V_f = 1.60\%, 4.04\%, 18.03\%$ and 34.71% , respectively. (e-h) Von Mises stress distribution for the optimized structures.	34
2.4. The intermediate resulting structure for $\sigma_L = 0.2$ with $V_f = 48.08\%$ after 7500 optimization iterations.	36
2.6. Linear (a) and logarithmic (b) plot of the volume fraction V_f and the compliance C with respect to the maximum material allowable σ_L for the continuous mesh structures. Areas in red represent the zones outside the domains of applicability of the applied method.	37
2.5. The optimized structure for $\sigma_L = 10.0$ with $V_f = 1.60\%$. Some of the structure's features present not even a fully-dense element in their thickness.	37
2.7. Topology (a) and stress distribution (b) plot for the Truss Topology Optimization (TTO) optimized structure of the L-shape beam test case with varying values of the material allowable σ_L on a 33×33 nodes ground structure. The structure topology is invariant with respect to the value of σ_L	38
2.8. Optimized structure obtained using a fully connected ground structure with 13×13 nodes and 7705 candidates.	38
2.9. Linear (a) and logarithmic (b) plot of the volume fraction V_f and the compliance C with respect to the value of the maximum material allowable σ_L for the TTO optimized structures. Areas in red represent the zones outside the domains of applicability of the truss discretization.	39
2.10. Compliance C versus maximum material allowable σ_L plot for the density-based topology optimization and the TTO algorithms.	40
2.11. Maximum material allowable σ_L versus volume fraction V_f plot for the density-based topology optimization and the TTO algorithms.	41
2.12. Compliance C versus volume fraction V_f plot for the density-based topology optimization and the TTO algorithms.	41
2.13. Computational time t versus volume fraction V_f plot for the density-based topology optimization and the TTO algorithms.	42
3.1. The three ground structures loaded in compression are used to highlight the topological buckling problem in TTO. (a) Two-bar ground structure loaded in compression; (b) single bar ground structure; (c) overlap of the a and b ground structures.	48

3.2.	Flowchart of the two-step optimization strategy used to solve Problem \mathbb{P}_1	52
3.3.	Linearization of the local buckling constraints for a single bar.	53
3.4.	The linearized buckling constraints (blue dashed line) limit the design space of successive iterations when evaluated on compressive bars with very small areas. Additionally, the gradient of the linearized buckling constraint tends to 0.	53
3.5.	The reinitialization strategy modifies the linearization point of the members with a small area to promote their reintroduction in the optimization problem.	54
3.6.	Flowchart of the Sequential Linear Programming (SLP) strategy with reinitialization used to solve Problem \mathbb{P}_2	55
3.7.	Boundary conditions of the L-shaped beam test case.	58
3.8.	Topology of the optimized truss structures for different material admissibles $\sigma_L = 1.0, 0.8, 0.3$ and 0.2 with a minimum slenderness limit $\lambda < 15$	58
3.9.	The ten-bar truss ground structure and load case.	59
3.10.	Scatter plot of the four benchmarked optimization algorithms on the ten-bar truss. The 2S-5R shows a 100 % convergence rate to the lightest structure found. The dashed lines represent the mean of the distributions.	60
3.11.	Volume convergence history for the proposed two-step resolution strategy with one step of reinitialization (2S-1R) for the initialization point a_s^0 . The reinitialization strategy permits to jump from the local minimum (b), with $V = 87857$, to the lighter structure (d), with $V = 85534$. Only the SLP step is plotted because the solution is statically determinate and kinematic compatibility constraints are already satisfied. In red the members loaded in tension, in blue the members loaded in compression.	61
3.12.	The 2D cantilever beam load case with a first-order connectivity ground structure. The total number of candidate members is $N_{el} = 90$	62
3.13.	(a) Non-Linear Programming (NLP) optimized design of the 2D cantilever beam with a volume of $V = 80.67$ and high number of active and crossing bars $N_{el} = 66$; (b) 2S-5R solution $V = 77.78$ with $N_{el} = 31$. In red the members loaded in tension, in blue the members loaded in compression.	63
3.14.	Left: scatter plot of three of the four benchmarked optimization algorithms on the 2D cantilever beam compared to the solution by Achtziger [180]. The dashed lines represent the mean of distributions. Right: histogram of the distribution of the results of the optimization algorithms.	64
3.15.	The simply supported 3D beam example with the load case and boundary conditions. In blue we plot the symmetry planes.	65
3.16.	Ground structure composed of $N_{el} = 496$ elements of the symmetric portion used to optimize the simply supported 3D beam.	65
3.17.	Orthographic views of the topology of the optimized simply supported 3D beam. (a) XZ plane (b) YZ plane (c) XY plane (d) auxiliary perspective view.	66
3.18.	Maximum stress constraint value (a) and buckling constraint value (b) plotted on the optimized topology of the simply supported 3D beam.	66
3.19.	Ground structure of the ten-bar truss with two applied load cases P_1 and P_2	68
3.20.	Maximum stress constraint value (left) and buckling constraint value (right) plotted on the optimized design of the multiple load cases ten-bar truss.	68

3.21. Iteration history of the ten-bar truss with multiple load cases example solved with the 2S-5R algorithm; (a) objective function history for the SLP and NLP step (b) constraint violation for the NLP step.	70
4.1. Notations used for the definition of the variable linking approach used to apply the modularity constraints.	72
4.2. Notations used for the evaluation of the sensitivities for the modular structure optimization based on the variable linking scheme.	76
4.3. Boundary conditions of the multi-subdomains (a) and the multi-load cases (b) test cases.	77
4.4. Optimized structures of the multi-subdomains (a) and the multi-load cases (b) test cases. The resulting module topology is equal for the two cases. In red the bars are in a tensile state, and in blue the bars are in a compressive state.	78
4.5. Symmetric boundary conditions of the simply supported 3D beam. In gray are the symmetry planes of the test case.	78
4.6. Perspective view of the monolithic simply supported 3D beam optimized structure with $V = 9.907 \text{ cm}^3$	78
4.7. Influence of the number of subdomains on the volume of the optimized modular structure.	79
4.8. Influence of the number of subdomains on the computational time of the optimization.	79
4.9. Rendering of the optimized structures with $6 \times 2 \times 3$ (a-e), $12 \times 4 \times 6$ (b-f), $18 \times 6 \times 9$ (c-g), and $30 \times 10 \times 15$ (d-h) subdomains. The module presents a $2 \times 2 \times 2$ complexity.	81
4.10. Influence of the number of subdomains on the loading metrics φ and ψ of the optimized structures.	81
4.11. Stress (a-c) and local buckling (b-d) failure criteria plotted on the monolithic and the $12 \times 4 \times 6$ - $3 \times 3 \times 3$ cases.	82
4.12. Rendering of the optimized structures with $2 \times 2 \times 2$ (a-e), $3 \times 3 \times 3$ (b-f), $4 \times 4 \times 4$ (c-g), and $5 \times 5 \times 5$ (d-h) module complexity. The number of subdomains is $6 \times 2 \times 3$	83
4.13. Influence of the module complexity on the volume of the optimized modular structure.	84
4.14. Influence of the module complexity on the computational time of the optimization.	84
4.15. Influence of the module complexity on the loading metrics φ and ψ of the optimized structures.	84
4.16. Design of experiments (DOE) response curves and isolines plot for the volume (a-b) and computational time (c-d).	87
4.17. Main effects plot of volume (a) and computational time (b).	88
4.18. Rendering of a single octet-truss module.	89
4.19. Comparison of the octet-truss structures (a-c-e-g) and the TTO structures (b-d-f-h) for two different numbers of submodules, $6 \times 2 \times 3$ and $12 \times 4 \times 6$	90
4.20. Graphical representation of the given module layout for the simply supported 3D beam.	91
4.21. Orthographic views of the topology of the optimized modular simply supported 3D beam. (a) XZ plane (b) YZ plane (c) XY plane (d) auxiliary perspective view.	92
4.22. Comparison of the volume and computational time of the structure with multiple modules with the monolithic and the fully modular structures.	92
4.23. Stress (a-c) and local buckling (b-d) failure criteria plotted on the multiple and single module modular structures.	93

5.1.	A modular cantilever beam with $N_{\text{sub}} = 8$. The subdomains' topology is defined as the weighted sum of two modules' topologies.	98
5.2.	A dual-phase RAMP interpolation scheme is used to penalize the intermediate weights and promote 0-1 designs.	99
5.3.	The stress values of the initial ground structure evaluated using a Finite Element Method (FEM) analysis are used to identify similar behaving subdomains. The sets are calculated using the k-means clustering technique with N_T number of clusters.	103
5.4.	The proposed starting point for the first-step of the optimization: a fully-connected ground structure with uniform cross-sectional areas and a biased α_{init} distribution, as suggested by the k-means clustering.	104
5.5.	Boundary conditions of the 2D cantilever beam divided in 24x12 subdomains. In the upper part of the image the ground structure of the module composed of $\bar{n} = 6$ elements.	105
5.6.	Monolithic optimized structure for the cantilever beam 2D test case with a maximum cross-sectional area $a_{\max} = 0.6$. This solution represents the lower bound solution for this test case with a volume $V = 832.848$	106
5.7.	Fully-modular structure in which every subdomain is populated with the given module. The structural volume is $V = 9832.935$	106
5.8.	Optimization of the fixed module topology 2D cantilever beam. (a-d) shows the solution without penalizing intermediate weights with a final volume $V = 8808.671$; (e-h) shows the solution in which the RAMP interpolation helps reducing intermediate weights. The final structural volume is $V = 3414.214$	107
5.9.	Two different examples of the optimization of a modular 2D cantilever beam using $N_T = 2$ fixed topology modules. (a-b) show the topology and the module layout of the structure obtained using two modules with identical topology, but different cross-sectional areas, while the solution showed in (c-d) is obtained using two modules with identical cross-sectional areas, but different topology. In (a) and (c) red bars are loaded in tension, while blue bars are loaded in compression.	108
5.10.	Optimized topology of the modular structure (a) and the module (b) for the 2D cantilever beam optimized using a single module ($N_T = 1$). Red bars are loaded in tension, while blue bars are loaded in compression.	108
5.11.	Similarly stressed submodules are identified using the k-means clustering algorithm to suggest a starting point for the first step of the proposed optimization algorithm. In the figure we show the resulting distribution for $N_T = 2$ and $N_T = 5$ obtained from the Finite Element Analysis (FEA) stress.	108
5.12.	Influence of the number of modules N_T on the volume V and the loading metric ψ of the optimized 2D cantilever beam.	109
5.13.	Visual representation of the optimized modular 2D cantilever beam together with the corresponding module topologies for (a) $N_T = 2$ and (b) $N_T = 5$	110
5.14.	Optimized 2D cantilever beam obtained using the variable linking formulation with fixed modules' layout and $N_T = 5$. The modules' layout is obtained using the k-means clustering technique. The final volume is $V = 1727.314$	110
5.15.	Bailey bridge placed on construction site road over Orava river (Slovakia) [208].	110
5.16.	Graphical representation of the 2D Bailey bridge test case. The structure is divided into $N_{\text{sub}} = 10$. The bridge is symmetric, and we are here optimizing only the right part of it.	111

5.17. Visual comparison of the 2D Bailey bridge test case without local buckling constraints proposed by Tugilimana <i>et al.</i> [151] obtained for different number of modules N_T . The images (a-j) represent the Tugilimana optimized structures, while the images (k-t) show the structures obtained with the proposed optimization method.	112
5.18. Normalized volume values plotted against the number of modules N_T . The buckling constraints do not change the trend of the beneficial effect of using multiple modules N_T on the structure.	113
5.19. Visual representation of the optimized structures obtained for different values of N_T for the 2D Bailey bridge test case with local buckling constraints.	114
5.20. Study of the influence of the parameters N_{sub} and N_T on the volume and the topology of the 2D Bailey bridge test case.	114
5.21. Normalized volume values plotted against the number of subdomains N_{sub} for different values of N_T	115
5.22. Symmetric boundary conditions of the simply supported 3D beam. In gray are the symmetry planes of the test case.	115
5.23. Rendering of the optimized structures with $N_T = 1$ (a,d), $N_T = 2$ (b,e), and $N_T = 3$ (c,f).	116
5.24. Perspective view of the monolithic simply supported 3D beam optimized structure with $V = 9.907 \text{ cm}^3$	116

LIST OF TABLES

2.1. Material data used for the optimizations. The value of the maximum material allowable σ_L is used as the parameter to generate multiple optimized topologies. The Poisson module is used only in density-based topology optimization.	33
2.2. Numerical results of the topology optimization method of the L-shape beam load case with varying material allowable σ_L on a 600×600 elements mesh. Numbers in red highlight the results that have not converged.	36
2.3. Numerical results of the TTO method of the L-shape beam test case with varying values of the material allowable σ_L on a 33×33 nodes ground structure. Numbers in red highlight the results that lie outside the domains of applicability of the optimization method.	38
3.1. Non-exhaustive list of the existing research in Truss Topology Optimization (TTO) with their corresponding scientific contributions.	46
3.2. Values and description of the parameters used for the SLP and NLP optimizations. . .	57
3.3. Material data used for the optimizations.	58
3.4. Numerical comparison of the effect of the minimum slenderness constraint on the optimization of the 2D L-shaped beam.	59
3.5. Material data used for the ten-bar truss optimization.	59
3.6. Numerical comparison of the four optimization algorithms on the ten-bar truss for 50 different initial points. The 2S-5R algorithm shows a 100 % convergence rate to the lightest structure found. The iteration count and time are from the first initialization point a_s^0	60

3.7. Material data used for the 2D cantilever beam optimization.	62
3.8. Numerical comparison of the 2D cantilever beam of the four algorithms for 100 random initial points. The 2S-5R algorithm shows a good balance between the volume, complexity, and dispersion of the solutions.	63
3.9. Optimal values of the member forces, areas, and volumes of the 2D cantilever beam. .	63
3.10. Material data used for the simply supported 3D beam optimization.	65
3.11. Numerical results of the optimization of the simply supported 3D beam.	66
3.12. Material data used for the ten-bar truss optimization.	67
3.13. Numerical comparison of the four optimization algorithms on the ten-bar truss for 50 different initial points.	67
3.14. Comparison of the results of the SLP step and NLP step for the multiple load cases ten-bar truss.	69
3.15. Optimal values of the member forces, areas, and volumes of the members of the ten-bar truss with multiple load cases.	69
 4.1. Reminder of the parameters used to set the reinitialization parameters for the modular optimization. The full list of values and tolerances used for the setup of the optimization algorithm can be found in Table 3.2.	76
4.3.	77
4.2. Material data used for the modular bridge section 2D structure.	77
4.4. Material data used for the simply supported 3D beam optimization.	78
4.5. Numeric results of the parametric study on the influence of the number of subdomains on the optimized structures.	80
4.6. Numeric results of the parametric study on the influence of the module complexity on the optimized structures.	83
4.7. Coefficients of the quadratic function used to model how the volume V varies with the number of subdomains N_{sub} and the module complexity \bar{n}	85
4.8. Coefficients of the quadratic function used to model how the computational time t varies with the number of subdomains N_{sub} and the module complexity \bar{n}	85
4.9. Numerical results of the comparison between octet-truss and TTO structures.	89
4.10. Numerical results of the comparison between the structure with multiple modules with the monolithic and the fully-modular structures.	94
 5.1. Material data used for the 2D cantilever beam.	105
5.2. Numeric results of the parametric study on the influence of the number of modules on the optimized 2D cantilever beam.	109
5.3. Material data used for the 2D Bailey bridge without local buckling constraints test case to compare with the work of Tugilimana <i>et al.</i> [151].	111
5.4. Material data used for the 2D Bailey bridge with local buckling constraints test case. .	113
5.5. Material data used for the simply supported 3D beam optimization.	115
5.6. Numeric results of the parametric study on the influence of the number of modules N_T on the simply supported 3D beam.	116

A.1. Reminder of the indexes used for the sensitivity analysis of the layout and topology optimization of modular structures.	145
---------------------------------------------------------------------------------------------------------------------------------------	-----

LIST OF ABBREVIATIONS

AD	Alternate Directions
AI	Artificial Intelligence
BESO	Bi-directional ESO
CONLIN	CONvex LINearization
DMO	Discrete Material Optimization
DOE	Design of experiments
DOFs	Degrees Of Freedom
DSI	Degree of Static Indeterminacy
ESO	Evolutionary Structural Optimization
FEA	Finite Element Analysis
FEM	Finite Element Method
GA	Genetic Algorithm
GBMMA	Gradient Based MMA
GCMMA	Globally Convergent MMA
GGP	Generalized Geometry Projection
GP	Geometry Projection
HS	Hashin-Shtrikman
KS	Kreisselmeier-Steinhausen
LP	Linear Programming
MILP	Mixed-Integer Linear Programming
MIP	Mixed-Integer Programming
MMA	Method of Moving Asymptotes
MMC	Moving Morphable Components
MPVCs	Mathematical Programs with Vanishing Constraints
NAND	Nested Analysis and Design
NLP	Non-Linear Programming
OC	Optimality Criteria
RAMP	Rational Approximation of Material Properties
RVE	Representative Volume Element
SA	Simulated Annealing
SAND	Simultaneous Analysis and Design
SIMP	Solid Isotropic Material with Penalization Method
SLA	Stereolithography
SLP	Sequential Linear Programming
SLSQP	Sequential Least Square Quadratic Programming
SQP	Sequential Quadratic Programming

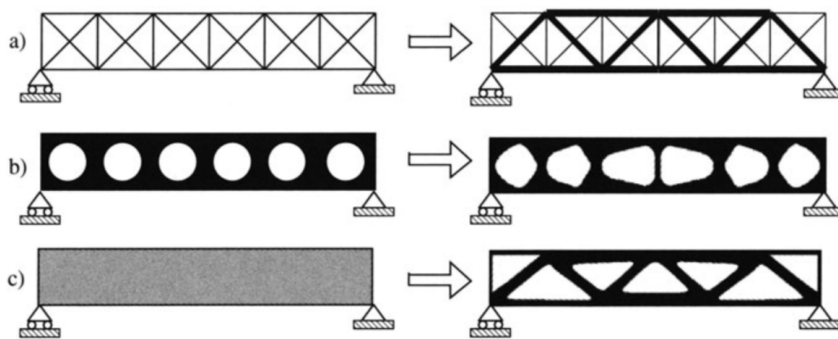
TTO Truss Topology Optimization

LITERATURE REVIEW

This thesis focuses on numerical optimization in the structural engineering domain. As such, one needs familiarity with existing optimization methods and contemporary engineering practices. The purpose of this chapter is to provide the reader with a non-exhaustive historical overview of structural optimization, particularly in the context of ultralight and modular structures. Additionally, we introduce crucial concepts and terminology that will be employed consistently throughout the document.

1.1. AN INTRODUCTION TO STRUCTURAL OPTIMIZATION

Structural optimization is a multidisciplinary field within engineering that aims to systematically improve structural performance—considering factors like mass, stiffness, and dynamic response—by optimizing their shape, material distribution, and overall design. Historically, structural optimization algorithms are categorized into three families: sizing, shape, and topology optimization. Sizing optimization concentrates on determining the optimal distribution of variables, where both the design and state variable domains are known *a priori* and remain constant during optimization. In contrast, shape optimization aims to discover the optimal shape of a predefined domain, treating the domain itself as a design variable allowing for flexibility in shaping the structure. Topology optimization goes further, involving the determination of features like the number, location, and shape of holes, as well as the connectivity of the structural domain. This approach offers a more comprehensive exploration of possibilities in structural design. A visual representation of the three families is provided in Fig. 1.1.



1.1 AN INTRODUCTION TO STRUCTURAL OPTIMIZATION	1
1.2 ULTRA-LIGHTWEIGHT STRUCTURES OPTIMIZATION APPROACHES	5
1.3 MODULAR STRUCTURES AND LATTICE MATERIALS	14

Figure 1.1: Visual representation of (a) size, (b) shape, and (c) topology optimization [1].

Structural optimization involves using mathematical algorithms, computational models, and iterative analyses to explore and refine design solutions. For that reason, we introduce the basic concepts and terminology behind numerical optimization. In numerical optimization, algorithms are employed to minimize or maximize a specific function by adjusting various design variables. The problem may or may not be subject to constraints. Formulating an optimization problem is a crucial step to prevent common conceptual errors, such as confusing constraints with objective functions. An incorrect problem formulation can lead to a failed solution or yield a mathematical optimum that lacks feasibility from an engineering perspective.

The most general formulation of an optimization problem is written as:

$$\begin{aligned} \min_x \quad & f(x) \\ \text{by varying} \quad & x \in [l^-, l^+] \\ \text{s.t.} \quad & g_e(x) = 0 \\ & g_i(x) > 0, \end{aligned} \tag{1.1}$$

where $f(x)$ is the objective function to minimize, x is the vector of design variables bounded between l^- and l^+ , and g_e and g_i represent the equality and inequality constraints, respectively.

OBJECTIVE FUNCTION In numerical optimization, the objective function $f(x)$ represents the scalar that we aim to minimize. Should the goal be to maximize a function, one can achieve this by minimizing the opposite of that function, maintaining adherence to the convention. Common objective functions in structural design include the minimization of volume or structural compliance. The objective function can take the form of an explicit function or result from a highly complex computational procedure. The selection of the objective function is crucial to propose a design that is feasible from an engineering perspective, regardless of the precision of the optimization scheme employed.

Optimization problems are categorized in the literature based on how the objective function is with respect to design variables, whether linear, quadratic, or generally non-linear. It is possible to concurrently optimize multiple objective functions, but this usually results in a family of optimum designs with differing emphases on the various objectives called the Pareto front. When possible, it is more straightforward to convert these diverse objectives into constraints [2].

². Martins et al. (2021), 'Engineering Design Optimization'

DESIGN VARIABLES The design variables x are the parameters that the optimizer algorithm changes to minimize the objective function. Design variables could be continuous or discrete if only some distinct values are allowed (for example, only a certain size for a hole in a

structural analysis). The optimization problem formulation allows for the lower and upper boundary for each design variable known in the literature as variable bounds.

CONSTRAINTS The constraints are functions used to restrict the design variables in some way. They serve the purpose of preventing the algorithm from converging to a numerical minimum that is not feasible due to physical and engineering constraints. Similar to the objective function, constraint functions can take on linear, quadratic, or generally non-linear forms, and different algorithms must be applied accordingly.

Constraint functions can be further classified into two types: equality constraints (g_e), which arise when the design variables are restricted to be equal to a fixed quantity, and inequality constraints (g_i), which come into play when the design variables are required to be greater than or equal to a certain quantity.

1.1.1. OPTIMIZERS

The field of numerical optimizers is extensive. For that reason, our focus here will be specifically on algorithms employed in structural optimization. Various algorithm types have been applied to address structural optimization problems, predominantly categorized into three main families: optimality criteria, metaheuristic algorithms, and gradient-based strategies.

Optimality Criteria (OC) refer to mathematical conditions or rules used to assess and guide the modification of a design or structure to achieve the desired performance [3, 4]. In the context of topology optimization, OC are primarily applied in compliance minimization problems, as each element contributes independently to the overall compliance. Bendsøe used OC to seek the stiffest plate i.e. compliance minimization—that can be made of a given amount of material and, together with Kikuchi [5], they used OC to obtain optimal shape design of structural elements based on boundary variations without the use of remeshing. Later, Bendsøe and Sigmund [6, 7] introduced a heuristic update scheme for isotropic materials, while Allaire *et al.* [8] demonstrated the convergence proof for both isotropic and anisotropic materials using the Alternate Directions (AD) approach. In both methods mechanical analysis provides essential information for solving closed-form conditions, allowing iterative updates of variables until convergence is achieved. Recently, OC methods gained interest again thanks to the reduced calculation time [9, 10] thanks to a modified Anderson acceleration strategy [11].

Metaheuristic (or gradient-free) algorithms offer a broader range of options compared to their gradient-based counterparts. While gradient-based algorithms typically conduct local searches, possess

3. Prager et al. (1968), 'Problems of Optimal Structural Design'
4. Prager (1968), 'Optimality Criteria in Structural Design'
5. Bendsøe et al. (1988), 'Generating optimal topologies in structural design using a homogenization method'
6. Bendsøe (1995), 'Optimization of Structural Topology, Shape, and Material'
7. Sigmund (2001), 'A 99 line topology optimization code written in Matlab'
8. Allaire et al. (1996), 'The homogenization method for topology and shape optimization. Single and multiple loads case'
9. Li et al. (2020), 'Accelerated fixed-point formulation of topology optimization'
10. Ferrari et al. (2020), 'A new generation 99 line Matlab code for compliance topology optimization and its extension to 3D'
11. Anderson (1965), 'Iterative Procedures for Nonlinear Integral Equations'

- 12. Conn et al. (2009), 'Introduction to Derivative-Free Optimization'
- 13. Audet et al. (2017), 'Derivative-Free and Blackbox Optimization'
- 14. Simon (2013), 'Evolutionary optimization algorithms'
- 15. Balamurugan et al. (2011), 'A two phase approach based on skeleton convergence and geometric variables for topology optimization using genetic algorithm'
- 16. Sigmund (2011), 'On the usefulness of non-gradient approaches in topology optimization'
- 17. Luh et al. (2009), 'Structural topology optimization using ant colony optimization algorithm'
- 18. Luh et al. (2011), 'A binary particle swarm optimization for continuum structural topology optimization'
- 19. Stolpe (2004), 'Global optimization of minimum weight truss topology problems with stress, displacement, and local buckling constraints using branch-and-bound'
- 20. Mattheck et al. (1990), 'A new method of structural shape optimization based on biological growth'
- 21. Xie et al. (1993), 'A simple evolutionary procedure for structural optimization'
- 22. Manickarajah et al. (1998), 'An evolutionary method for optimization of plate buckling resistance'
- 23. Young et al. (1999), '3D and multiple load case bi-directional evolutionary structural optimization (BESO)'

mathematical justification, and operate deterministically, metaheuristic algorithms are simpler and usually take much less developer time to use, and are perfect candidates for smaller problems. They find very diverse application cases and are useful when the design space is discrete, with multiple objective functions, or highly non-linear with many local minima (multimodal). The works authored by Conn *et al.* [12] and Audet and Hare [13] offer a comprehensive exploration of gradient-free optimization algorithms. Evolutionary algorithms, a prominent category, simulate natural selection by retaining the fittest solutions in each generation while introducing mutations or cross-overs for improvement. A review of these optimization methods is given in the following reference [14]. These algorithms, also called Genetic Algorithm (GA), are employed for example by Balamurugan *et al.* [15] for compliance minimization, showcase versatility but face challenges with combinatorial considerations as the number of design variables increases [16]. Particle swarm and ant colony algorithms, inspired by nature, provide alternative strategies with randomness and new search directions. However, these non-gradient methods require regularization schemes for topology optimization, as outlined by Luh, Lin, and others [17, 18]. Targeting the resolution of Mixed-Integer Programming (MIP) problems, branch-and-bound algorithms divide the feasible set of the original problem into subsets through a process known as branching. These subsets are then further segmented to refine the partition of the feasible set. For each subset, lower bounds and optionally upper bounds on the objective function value are determined, a process referred to as bounding. Typically, the lower bounding problems are convex problems that can be efficiently solved to global optimality. Stolpe [19] addresses a volume minimization problem on a truss using a continuous branch-and-bound method, ensuring convergence to a globally optimal solution. The Evolutionary Structural Optimization (ESO) framework, initially a metaheuristic, removes less solicited elements iteratively [20, 21]. These methods offer freedom in optimization and improved convergence to local minima, especially in handling various optimization problems like buckling [22]. The ESO algorithm has been enhanced by the Bi-directional ESO (BESO) framework [23], which allows both removal and addition of elements.

Gradient-based algorithms in optimization leverage local information at a trial point to comprehend the shape of the local objective function in the neighborhood. This insight is crucial for determining the optimal direction to minimize the objective function. Typically, only the Jacobian (first derivative) is utilized, though more advanced algorithms incorporate the Hessian (second derivative). The computational demand for gradient calculation often constitutes the most resource-intensive aspect of the optimization loop. When constraints are present, solving the problem directly on the analytic response surface of the objective function becomes impractical. Consequently,

the approach involves creating local approximations of the problem at the current design point using gradient information. These approximations are designed so that specialized algorithms can efficiently solve them. The categorization of gradient-based algorithms is often based on how this local approximation is constructed.

The most used approximations in structural optimization includes among others Sequential Linear Programming (SLP), Sequential Quadratic Programming (SQP) and Sequential Least Square Quadratic Programming (SLSQP) [24], Method of Moving Asymptotes (MMA) [25] and its amelioration Globally Convergent MMA (GCMMA) [26] and Gradient Based MMA (GBMMA) [27], and CONvex LINearization (CONLIN) [28]. Specialized algorithms for solving the approximated problems are, among others, the primal-dual method and interior-point method.

An interior-point method is a numerical optimization algorithm used to solve constrained optimization problems. The key idea behind interior-point methods is to transform the constrained optimization problem into a sequence of unconstrained problems, allowing for efficient iterative solutions. The method introduces a barrier function that penalizes points outside the feasible region, effectively creating a "barrier" against leaving that region. This barrier function is incorporated into the objective function, and as the optimization progresses, it guides the search towards the interior of the feasible region. The term "interior point" originated from early methods that relied on interior penalty techniques, assuming the initial point was feasible. Nevertheless, contemporary interior-point methods such as the open source IPOPT [29] are more versatile and can start from infeasible points. Rojas Labanda and Stolpe conducted a benchmark of various optimization algorithms and structural optimization formulations using a compliance minimization problem. Their findings highlight the efficacy of employing interior-point algorithms such as IPOPT in topology optimization problems [30].

1.2. ULTRA-LIGHTWEIGHT STRUCTURES OPTIMIZATION APPROACHES

Two of the most frequently employed formulations for structural optimization are the minimization of volume while adhering to stress constraints and the minimization of compliance under volume constraints. Historically, the volume minimization formulation has been used in the first works of structural optimization of truss structures [31–33]. The problem was initially formulated in terms of member forces, ignoring the kinematic compatibility to obtain a Linear Programming (LP) problem. The formulation was modeled using the Simultaneous Analysis and Design (SAND) approach, in which the equations of nodal equilibrium are treated as equality constraints, and

24. Kraft (1988), 'A software package for sequential quadratic programming'

25. Svanberg (1987), 'The method of moving asymptotes—a new method for structural optimization'

26. Svanberg (2002), 'A Class of Globally Convergent Optimization Methods Based on Conservative Convex Separable Approximations'

27. Bruyneel et al. (2002), 'A family of MMA approximations for structural optimization'

28. Fleury et al. (1986), 'Structural optimization'

29. Wächter et al. (2006), 'On the implementation of an interior-point filter line-search algorithm for large-scale nonlinear programming'

30. Rojas Labanda et al. (2015), 'Benchmarking optimization solvers for structural topology optimization'

31. Dorn et al. (1964), 'Automatic design of optimal structures'

32. Chan (1964), 'Optimum structural design and linear programming'

33. Hemp (1973), 'Optimum Structures'

- 34.** Sankaranarayanan et al. (1994), 'Truss topology optimization with simultaneous analysis and design'
- 5.** Bendsøe et al. (1988), 'Generating optimal topologies in structural design using a homogenization method'
- 35.** Bendsøe (1989), 'Optimal shape design as a material distribution problem'
- 36.** Sigmund (1994), 'Materials with prescribed constitutive parameters'
- 37.** Zhang et al. (2006), 'Scale-related topology optimization of cellular materials and structures'
- 38.** Collet et al. (2018), 'Topology optimization for microstructural design under stress constraints'
- 39.** Borrvall et al. (2003), 'Topology optimization of fluids in Stokes flow'
- 40.** Bruyneel et al. (2005), 'Note on topology optimization of continuum structures including self-weight'
- 41.** Sigmund (2009), 'Manufacturing tolerant topology optimization'
- 42.** Brackett et al. (2011), 'Topology Optimization for Additive Manufacturing'
- 43.** Sigmund (1997), 'On the Design of Compliant Mechanisms Using Topology Optimization*
- 44.** Bruns et al. (2001), 'Topology optimization of non-linear elastic structures and compliant mechanisms'
- 45.** Wang et al. (2020), 'Space-time topology optimization for additive manufacturing'
- 46.** Allaire et al. (2002), 'A level-set method for shape optimization'
- 47.** Wang et al. (2003), 'A level set method for structural topology optimization'
- 48.** Allaire et al. (2004), 'Structural optimization using sensitivity analysis and a level-set method'
- 1: This proposition holds when referring to the end of the 1980s when computational power was scarce compared to what we have today.
- 2.** Martins et al. (2021), 'Engineering Design Optimization'
- 49.** Tortorelli et al. (1994), 'Design sensitivity analysis'
- 1.** Bendsøe et al. (2004), 'Topology Optimization'

where both nodal displacements and the cross-sectional areas of truss members serve as design variables [34]. These methods are known in the literature as layout optimization or Truss Topology Optimization (TTO).

However, to attain greater design freedom, the structure optimization field later transitioned from truss structures to continuous discretization (also called density methods). While truss structures offered simplicity and ease of analysis, they imposed limitations on the design due to their discrete member configurations and their inability to transmit moments, handle torsional effects, and represent complex structural elements such as plates or volumes. The continuum mesh offered instead more versatility [5, 35], and has since been used for multiple different applications, e.g. the design of optimized repetitive metamaterials [36–38], fluids optimization [39], modelization of self-weight of the structure [40], the simulation of advanced manufacturing constraints [41, 42], the design of compliant mechanism [43, 44], or the optimization for additive manufacturing [45]. Other than the density methods, other ways to deal with topology optimization exist, like level-set methods [46–48]. The SAND approach is, however, incompatible with continuum meshes due to its excessive number of variables¹. Given this limitation, a new approach was required to better handle the complexity of continuum meshes.

In the density-based Nested Analysis and Design (NAND) approach, the nodal displacement (state) variables are eliminated from the optimization problem through a process where the structural equilibrium equation is solved every iteration instead of being used as a constraint of the optimization. This results in an independent nested phase where the state equation of structural equilibrium is solved separately from the optimization algorithm. This creates a dense coupling between displacement and material density variables, necessitating a computationally expensive sensitivity analysis within the nested algorithm, typically employing the adjoint method (more information about the adjoint method on the following resources [2, 49]). Nevertheless, if the problem is reformulated as a compliance minimization with volume constraints, the problem is self-adjoint and the adjoint algorithm is no longer necessary to evaluate the gradient sensitivities [1], and this reduces considerably the computational times.

Both the TTO methods based on the ground structure and the density-based topology optimization approaches are good candidates for the optimization of ultra-light structures. We review here their main characteristics and numerical properties, starting from density-based approaches.

1.2.1. DENSITY-BASED TOPOLOGY OPTIMIZATION

Let $\Omega \in \mathbb{R}^2$ be a rectangular domain of dimensions X and Y , containing respectively N_x and N_y linear 4-nodes elements, for a total

of $N_e = N_x N_y$ elements and M nodes (see Fig. 1.2). The objective of the optimization is the minimization of the compliance C of the structure, equivalent to finding the structure with the least possible nodal displacement with respect to a defined set of boundary conditions.

COMPLIANCE MINIMIZATION FORMULATION The Problem \mathbb{T}_0 is stated in terms of the design variables ρ as follows:

$$\begin{aligned} \min_{\rho} \quad & C = \sum_i \mathbf{u}_{e,i}^T \mathbf{K}_{e,i} \mathbf{u}_{e,i} = \mathbf{f}^T \mathbf{u} \quad \forall i \in [0, \dots, N_e] \\ \text{s.t.} \quad & \frac{1}{V_p} \frac{\sum_i (\bar{\rho}_i v_i)}{V_0} - 1 \leq 0 \quad \forall i \in [0, \dots, N_e] \quad (\mathbb{T}_0) \\ & \mathbf{K}\mathbf{u} = \mathbf{f} \\ & 0 \leq \rho_i \leq 1. \quad \forall i \in [0, \dots, N_e] \end{aligned}$$

The design variables ρ are defined for every element of the structure as $\rho = [\rho_1, \rho_2, \dots, \rho_{N_e}]^T$, with $\rho_i \in [0, 1]$, $\forall i \in [0, \dots, N_e]$. The physical densities $\bar{\rho}$ are related to the design variable ρ through density filtering and threshold projection [50], as explained later in the document. V_p is the prescribed volume fraction that acts as the constraint of the minimization problem, while v_i represents the area of the i -th element and V_0 is the total area of the domain Ω . $\mathbf{K}\mathbf{u} = \mathbf{f}$ is the state equation of the problem and defines the elastic response of the structure to an external nodal load $\mathbf{f} = [f_1, f_2, \dots, f_{2M}]^T$. The global stiffness matrix \mathbf{K} is assembled from the element stiffness matrix $\mathbf{K}_{e,i}$ and $\mathbf{K}_{e,i} = E_i \mathbf{K}_{e,0}$ where $\mathbf{K}_{e,0}$ represents the element stiffness matrix relative to the chosen type of element (linear or quadratic) and $E_i(\bar{\rho}_i)$ the Young's modulus of the i -th element.

The material scheme used to interpolate between void and full material is the well-known Solid Isotropic Material with Penalization Method (SIMP) [35, 51] approach. It is governed by the equation:

$$E_i(\bar{\rho}_i) = E_{\min} + \bar{\rho}_i^p (E_0 - E_{\min}), \quad (1.2)$$

where the parameter p penalizes the intermediate densities and pushes the result to a black-and-white result. E_0 is the Young's modulus of the dense material and E_{\min} is a small value used to avoid the global stiffness matrix \mathbf{K} from being singular when $\bar{\rho}_i = 0$.

The SIMP exponent p is constrained to be greater than or equal to 1. From a physical perspective, the extreme case of $p = 1$ makes sense only in a two-dimensional optimization context, where it becomes equivalent to optimizing membrane thickness. When $p > 1$, the interpolation results in an equivalent homogenized stiffness tensor for intermediate densities, determined by the material-to-void ratio ρ . This mirrors microstructures conforming to the Hashin-Shtrikman

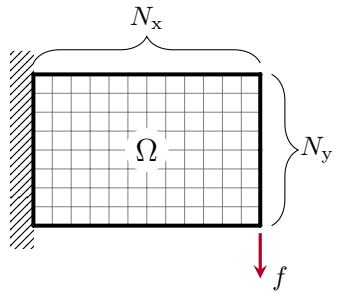


Figure 1.2.: The domain Ω is discretized using $N_e = N_x N_y$ continuous 4-nodes elements.

50. Wang et al. (2011), 'On projection methods, convergence and robust formulations in topology optimization'

35. Bendsøe (1989), 'Optimal shape design as a material distribution problem'

51. Bendsøe et al. (1999), 'Material interpolation schemes in topology optimization'

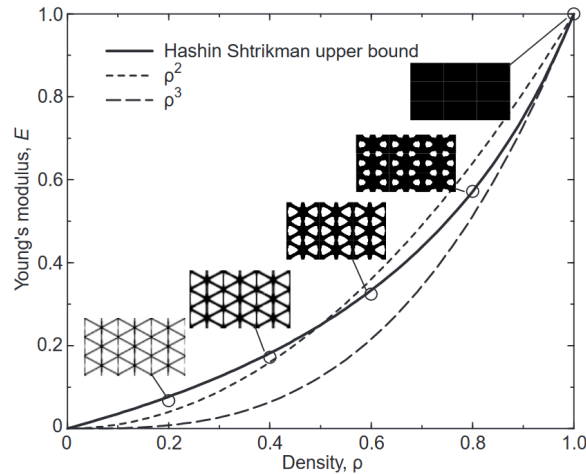


Figure 1.3.: Comparison between SIMP model with the Hashin-Shtrikman upper bound, considering an isotropic material with a Poisson ratio of 1/3 mixed with void. The Hashin-Shtrikman upper bound is illustrated with microstructures approaching the specified bounds. [51].

52. Hashin et al. (1963), 'A variational approach to the theory of the elastic behaviour of multiphase materials'

51. Bendsøe et al. (1999), 'Material interpolation schemes in topology optimization'

(HS) conditions, which estimate the theoretical lower and upper bounds for the elastic modulus of a homogeneous, isotropic mixture of different materials based on their elastic modulus and volume fractions [52]. If the exponent p exceeds 3, Bendsøe [51] mathematically proves that the equivalent homogenized stiffness tensor adheres to the upper bound of the HS conditions (refer to Fig. 1.2). It is important to note that in the mono-scale topology optimization context, deviating from the HS bounds for intermediate densities is allowed. The objective is to drive the density distribution towards a black-and-white result with minimal intermediate densities, without concerning whether the equivalent homogenized stiffness tensor can be replicated by a real microstructure.

53. Díaz et al. (1995), 'Checkerboard patterns in layout optimization'

43. Sigmund (1997), 'On the Design of Compliant Mechanisms Using Topology Optimization*

54. Sigmund (1994), 'Design of Material Structures using Topology Optimization'

55. Sigmund (2007), 'Morphology-based black and white filters for topology optimization'

SPATIAL FILTERING AND PROJECTION Multiple approaches have been developed to solve the problems linked to mesh discretization, such as mesh dependency or the checkerboard problem [53]. Filtering the sensitivity information of the optimization problem proved to be an effective approach to guarantee independence from mesh resolution [43, 54]. Another possibility is instead to directly filter the density field ρ using the 2D convolution operator [55]. The weight function w (or kernel) of the convolution is defined as:

$$w(d_j) = R - d_j, \quad j \in \mathbb{N}_{i,R} \quad (1.3)$$

where $\mathbb{N}_{i,R}$ represent the set of elements lying within a circle of radius R centered on the i -th element and d_j is the distance of the j -th element to the center of the filter (see Fig. 1.4).

The filtered values $\tilde{\rho}$ of the design variable ρ are calculated as:

$$\tilde{\rho}_i = \frac{\sum_{j \in \mathbb{N}_{i,R}} w(d_j) v_j \rho_j}{\sum_{j \in \mathbb{N}_{i,R}} w(d_j) v_j}. \quad (1.4)$$

As the filtering phase produces a large number of gray elements,

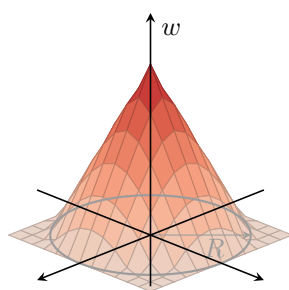


Figure 1.4.: Kernel of the 2D convolution operator.

a smooth projection technique based on the *tanh* function is implemented [50] to evaluate the value of the physical density $\tilde{\rho}$ of the structure:

$$\tilde{\rho}_j = \frac{\tanh(\beta\eta) + \tanh(\beta(\tilde{\rho}_j - \eta))}{\tanh(\beta\eta) + \tanh(\beta(1 - \eta))}, \quad (1.5)$$

where β is a parameter that defines the slope of this approximation function: the larger the value of β , the fewer elements with intermediate density are present in the structure topology. η is the threshold value of the projection.

In the domain of structural topology optimization, it is a widely adopted strategy to employ continuation methods. Introduced in the 90s [56, 57], they are used to converge towards more optimized structures. These methods solve a sequence of problems with increasing values of the SIMP material penalization parameter p . Many researchers such as Bendsøe and Sigmund [1] and Rozvany [58] consider, among others, continuation methods as a standard procedure in topology optimization. However, this approach comes at the expense of an increased number of iterations and, consequently, augmented computational time [59]. In an effort to mitigate this drawback, Rojas Labanda and Stolpe [60] have derived an automatic penalization scheme. This innovative scheme aims to reduce both the objective function value and the number of iterations, providing an improvement over the classical formulation with a fixed penalty parameter. While the literature is predominantly focused on the continuation scheme on the SIMP material penalization parameter p , it is worth noting that similar techniques could be employed for other optimization parameters e.g. the filter radius R or the projection parameter β .

While density-based topology optimization offers tremendous benefits in terms of weight reduction and structural efficiency, it is important to acknowledge the challenges associated with manufacturing such designs. The intricate and complex geometries generated through the optimization can pose difficulties in the fabrication process, often requiring advanced manufacturing techniques, specialized equipment, and specific constraints in the optimization [42, 61, 62]. Additionally, the computational time required for generating such optimized designs, particularly for low-volume fractions typical of the aerospace domain, can be significant [63], impacting the overall efficiency of the design process. This remains true even with the use of adaptive meshes [64, 65]. Even if the freedom of the design space offered by continuum meshes is high, it is known that at very low volume fractions (e.g. ultralight structures), and, especially if buckling constraints and manufacturing considerations (e.g. minimum length scale), are taken into account, the optimal topology resembles a truss-like structure [66]. As a result, a distinct branch of continuous topology optimization has emerged specifically tailored for optimizing truss-like structures,

50. Wang et al. (2011), 'On projection methods, convergence and robust formulations in topology optimization'

56. Allaire et al. (1993), 'A Numerical Algorithm for Topology and Shape Optimization'

57. Allaire et al. (1993), 'Topology Optimization and Optimal Shape Design Using Homogenization'

1. Bendsøe et al. (2004), 'Topology Optimization'

58. Rozvany (2009), 'A critical review of established methods of structural topology optimization'

59. Petersson et al. (1998), 'Slope constrained topology optimization'

60. Rojas-Labanda et al. (2015), 'Automatic penalty continuation in structural topology optimization'

42. Brackett et al. (2011), 'Topology Optimization for Additive Manufacturing'

61. Zhou et al. (2002), 'Progress in Topology Optimization with Manufacturing Constraints'

62. Liu et al. (2018), 'Current and future trends in topology optimization for additive manufacturing'

63. Aage et al. (2017), 'Giga-voxel computational morphogenesis for structural design'

64. Salazar de Troya et al. (2018), 'Adaptive mesh refinement in stress-constrained topology optimization'

65. Zhang et al. (2020), 'Adaptive mesh refinement for topology optimization with discrete geometric components'

66. Sigmund et al. (2016), 'On the (non-)optimality of Michell structures'

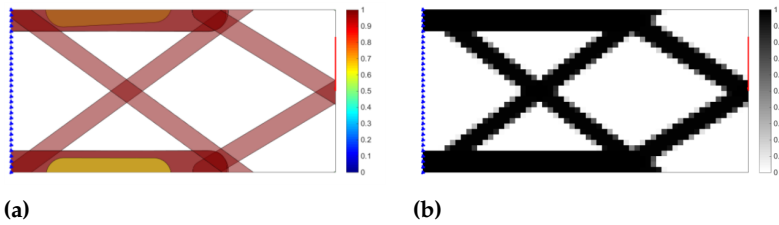


Figure 1.5.: Component (a) and density (b) plot of a short cantilever beam optimized using the component-based topology optimization method GGP [72].

known as feature-mapping topology optimization (also called topology optimization with explicitly defined components).

1.2.2. FEATURE-MAPPING TOPOLOGY OPTIMIZATION

Topology optimization methods using explicitly defined components have been developed to permit an easier interpretation of the solution, finding the optimal shape, size, and connectivity of components projected over a finite element continuum mesh (see Fig. 1.5). Two main feature-mapping methods applied to topology optimization have been developed [67], the Moving Morphable Components (MMC) approach [68, 69] and the Geometry Projection (GP) approach [70, 71], later combined in a unique methodology called Generalized Geometry Projection (GGP) [72]. Recently, the GP approach has been used to optimize light lattice structures, proving the effectiveness of the method to provide easy-to-interpret solutions [73]. Nevertheless, the optimization is still based on a density field projected on a continuum mesh, that needs to be refined to correctly discretize low-volume fraction structures. Additionally, truss structure design naturally depends on constraints on maximum allowable stress and buckling which are all known for being difficult to implement on topology optimization using the Nested Analysis and Design (NAND) formulation. This is principally due to the singular optima (or topologies) phenomenon [74, 75] and the pseudo-modes of buckling of low-density elements [76].

- 67. Wein et al. (2020), 'A review on feature-mapping methods for structural optimization'
- 68. Guo et al. (2014), 'Doing Topology Optimization Explicitly and Geometrically—A New Moving Morphable Components Based Framework'
- 69. Zhang et al. (2017), 'A new three-dimensional topology optimization method based on moving morphable components (MMCs)'
- 70. Norato et al. (2015), 'A geometry projection method for continuum-based topology optimization with discrete elements'
- 71. Zhang et al. (2016), 'A geometry projection method for the topology optimization of plate structures'
- 72. Coniglio et al. (2020), 'Generalized Geometry Projection'
- 73. Kazemi et al. (2020), 'Multi-material topology optimization of lattice structures using geometry projection'
- 74. Cheng et al. (1997), ' ε -relaxed approach in structural topology optimization'
- 75. Rozvany (2001), 'On design-dependent constraints and singular topologies'
- 76. Gao et al. (2015), 'Topology optimization of continuum structures under buckling constraints'
- 31. Dorn et al. (1964), 'Automatic design of optimal structures'
- 33. Hemp (1973), 'Optimum Structures'

1.2.3. TRUSS TOPOLOGY OPTIMIZATION (TTO)

Truss Topology Optimization (TTO) focuses on optimizing the topology of the truss structure itself, instead of operating on a continuous mesh. It involves selecting the cross-sectional areas and the connectivity of a discrete and dense mesh called ground structure, aiming to minimize weight while satisfying structural constraints. The process is graphically presented in Fig. 1.6.

In the early works, the TTO problem was formulated in terms of member forces [31, 33] with plastic material modelization, ignoring the kinematic compatibility to obtain a LP problem. Formulated using the SAND approach, the equations of structural mechanics of the problem are imposed as constraints of the optimization and, contrary to NAND approaches, are not explicitly solved. Formulated that way, it is trivial to add maximum stress constraints compared to an equivalent

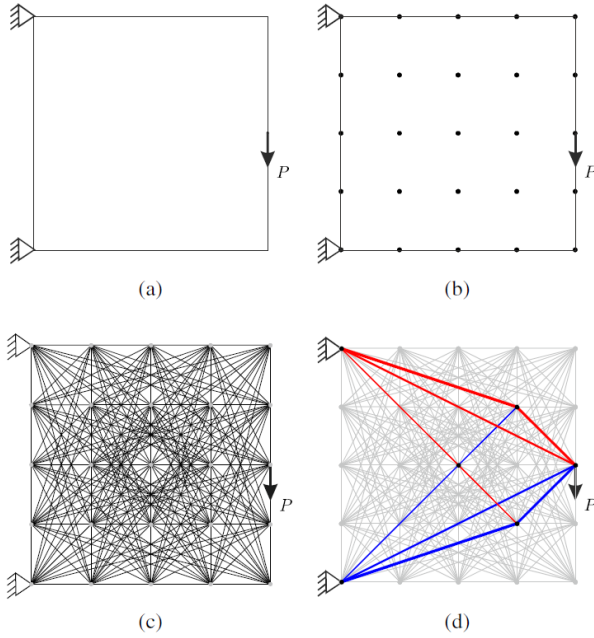


Figure 1.6.: The TTO algorithm can be divided into 4 steps: (a) specification of the design space, loads, and boundary conditions; (b) discretization of the design space; (c) the ground structure is generated depending on the desired connectivity level; (d) resolution of the optimization problem and plot of the solution [77].

NAND formulation. However, the SAND formulation with plastic material modelization only correctly predicts the mechanical behavior of statically determinate structures or mechanisms [78, 79]. Moreover, adding local buckling constraints to the optimization formulation is fundamental, as ultralight truss structures are often dominated by this mode of failure [66]. Multiple works in the field of truss structure optimization have focused on addressing these two crucial challenges [80–82].

CLASSICAL MICHELL STRUCTURES The characteristics of this class of truss structures are described by some simple criteria that date to the end of the 19th and the beginning of the 20th century. When a structure is statically determinate — i.e. the structure is not a mechanism, and it is not over-constrained by the supports — the Maxwell theorem [83] states that:

$$\sum_{\forall i | q_i > 0} \ell_i q_i + \sum_{\forall i | q_i < 0} \ell_i q_i = \text{const.} \quad (1.6)$$

where ℓ_i and q_i represent the length and the axial force of the i -th member, respectively. The constant value at the right of Equation 1.6 depends on the nature of the boundary conditions and the material used. The Maxwell theorem dictates that any increment in compression forces must be counterbalanced by an equivalent increase in tension forces when the structure remains topologically unchanged. So for statically determinate structures the structure layout is not influenced by the ratio between σ_c and σ_t , Young's modulus E of the material, nor the force magnitude.

Starting from Maxwell's findings, Michell theorized two further criteria for optimal truss structures [84] valid when the maximum

78. Kirsch (1989), 'Optimal topologies of truss structures'

79. Rozvany et al. (1995), 'Layout Optimization of Structures'

66. Sigmund et al. (2016), 'On the (non-)optimality of Michell structures'

80. Kirsch (1980), 'Optimal design of trusses by approximate compatibility'

81. Cheng (1995), 'Some aspects of truss topology optimization'

82. Achtziger (1999), 'Local stability of trusses in the context of topology optimization Part I'

83. Maxwell (1870), 'I.—On Reciprocal Figures, Frames, and Diagrams of Forces'

84. Michell (1904), 'The limits of economy of material in frame-structures'

33. Hemp (1973), 'Optimum Structures'

allowable stress is equal in tension and compression ($\sigma_t = \sigma_c$) and when the supports of the structure are statically determinate. The first one states that all the members of an optimal structure should present internal stress equal in magnitude to the maximum allowable value of the material – i.e. the structure is *fully stressed*. The second criterion asserts that the strain of all the members of the structure should be equal and there should be no other point having a strain higher than this value. As formulated, these two criteria are known as the Michell criteria. The second criterion was later generalized by Hemp [33] as:

$$-\frac{1}{\sigma_c} \leq \varepsilon \leq \frac{1}{\sigma_t}. \quad (1.7)$$

Compared to the second Michell criterion, Equation 1.7 permits the correct identification of the minimum volume structure even when different strength values for compression and tension and different support types are taken. These criteria are known as the Michell-Hemp criteria.

31. Dorn et al. (1964), 'Automatic design of optimal structures'

32. Chan (1964), 'Optimum structural design and linear programming'

33. Hemp (1973), 'Optimum Structures'

The first use of the ground structure in structural optimization is by Dorn et al. [31]

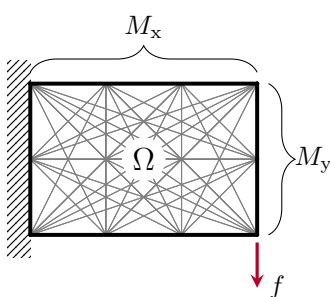


Figure 1.7.: The domain Ω is discretized using a set of straight members connecting a set of nodes. This framework is known as the ground structure.

PLASTIC MATERIAL FORMULATION The rigid-plastic formulation characterizes the material as entirely rigid up to the point of reaching the yield stress, denoted as σ_y , and subsequently assumes a constant stress level of σ_y once that threshold is exceeded. This formulation is a clear consequence of the application of the Michell-Hemp criteria and has thus been used in the very first work of TTO [31–33].

THE GROUND STRUCTURE APPROACH The ground structure is a framework composed of various structural members that connect specified points or nodes in two- or three-dimensional space (see Fig. 1.7). These members can take the form of beams, columns, wires, or bar elements, depending on the specific structural requirements, but the most used is historically the bar element. Since the nodes within the ground structure are considered as pin-joints, all straight members exclusively face either tension or compression loads.

Depending on how the connectivity of the grid of nodes is, we can experience very different ground structures. In a fully connected ground structure, every node within the system is linked to every other node, resulting in a dense and redundant structural configuration. The number of bars N_{el} of a fully connected ground structure can be determined using the following formula:

$$N_{el} = \frac{M \cdot (M - 1)}{2}, \quad (1.8)$$

where M represents the number of nodes of the structure.

In classic works, the ground structure is used as the start of the optimization, where the optimized structure is obtained as a subset of

the initial ground structure, but multiple alternative approaches have been proposed since then, e.g. starting from a very coarse ground structure that is enriched during the analysis [85], or giving the nodes of a coarse ground structure the possibility to move, during [86–88], or after the optimization, simultaneously reducing the number of active members of the solution [89, 90]. Recently, a hybrid method based on the projection of explicitly defined components on a discrete ground structure has been proposed, easing the interpretation of the stiffening pattern of the optimized truss [91].

OPTIMIZATION FORMULATION The volume minimization formulation with maximum stress constraints is stated in terms of members' cross-sectional areas α and member forces q as follows:

$$\begin{aligned} \min_{\alpha, q} \quad & V = \ell^T \alpha \quad (\text{Volume minimization}) \\ \text{s.t.} \quad & Bq = f \quad (g_{\text{eq}}) \\ & -\sigma_c \alpha \leq q \leq \sigma_t \alpha \quad (g_{\text{st,c}}, g_{\text{st,t}}) \\ & \alpha \geq 0, \end{aligned} \quad (\mathbb{P}_0)$$

where B is a $N_{\text{dof}} \times N_{\text{el}}$ matrix containing the direction cosines of the i -th member with respect to the i -th degree of freedom to calculate the nodal force equilibrium constraints g_{eq} , and where N_{dof} is the number of Degrees Of Freedom (DOFs), equal to $2M$ or $3M$ for a two- or a three-dimensional load case, respectively. $q = [q_1, q_2, \dots, q_{N_{\text{el}}}]^T$ is the vector containing the internal member forces, with a positive sign when in tension, caused by the external load $f = [f_1, f_2, \dots, f_{N_{\text{dof}}}]^T$. The state variable $\alpha = [\alpha_1, \alpha_2, \dots, \alpha_{N_{\text{el}}}]^T$ represents the cross-sectional area of the N_{el} members of the structure. σ_c and σ_t are the compressive and tensile maximum allowable stresses of the material, respectively, used in the stress constraints $g_{\text{st,c}}$ and $g_{\text{st,t}}$. This formulation takes into account only the linear behavior of the structure and is equivalent to the original and well-studied member force formulation [1, 31].

The resolution of Problem \mathbb{P}_0 frequently produces complex structures made up of a multitude of small members that tend to the shapes of Michell structures (see Fig 1.8) [84]. While it is known that these structures are nearly optimal, one would want to limit the complexity of the resulting structure. Substituting ℓ with $\tilde{\ell} = [\ell_1 + s, \ell_2 + s, \dots, \ell_{N_{\text{el}}} + s]^T$ in the objective function of \mathbb{P}_0 , one would penalize the appearance of small members [92]. $\tilde{\ell}$ is called augmented member length and s the joint cost. This approach mimics the mesh-independency regularization filter of topology optimization, avoiding the inevitable apparition of structures with tiny features when a fine mesh is adopted.

- 85. Gilbert et al. (2003), 'Layout optimization of large-scale pin-jointed frames'
- 86. Pedersen (1973), 'Optimal Joint Positions for Space Trusses'
- 87. Achtziger (2007), 'On simultaneous optimization of truss geometry and topology'
- 88. Descamps et al. (2013), 'A lower-bound formulation for the geometry and topology optimization of truss structures under multiple loading'
- 89. He et al. (2015), 'Rationalization of trusses generated via layout optimization'
- 90. Lu et al. (2023), 'Reducing the number of different members in truss layout optimization'
- 91. Savine et al. (2021), 'A component-based method for the optimization of stiffener layout on large cylindrical rib-stiffened shell structures'

- 1. Bendsøe et al. (2004), 'Topology Optimization'
- 31. Dorn et al. (1964), 'Automatic design of optimal structures'
- 84. Michell (1904), 'The limits of economy of material in frame-structures'
- 92. Parkes (1975), 'Joints in optimum frameworks'

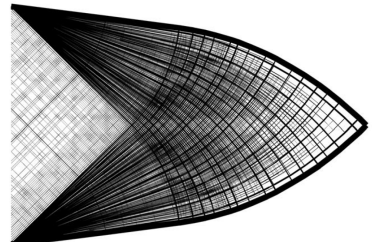


Figure 1.8.: The optimal structures found by layout optimization tend at Michell-like structures, made up of a very large number of infinitesimal struts [85].

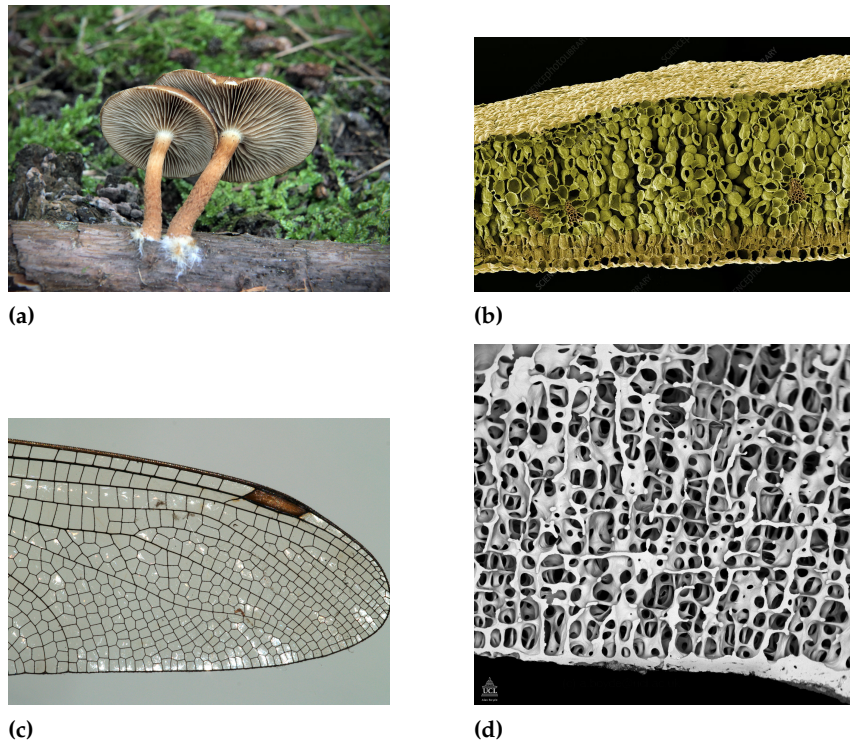


Figure 1.9.: The natural evolution process frequently generates lattice materials and modular structures; (a) The spore-bearing gills of a *Hypholoma fasciculare* [97] (b) SEM image of a leaf microstructure [98] (c) cellular stucture of the wing of a dragonfly [99] (d) internal structure of a human bone [100].

1.3. MODULAR STRUCTURES AND LATTICE MATERIALS

93. Schaedler et al. (2016), 'Architected Cellular Materials'

Historically, material properties were modified by manipulating chemical composition, microstructure, and production processes [93]. Another possible way to enhance material properties involves tailoring the spatial arrangement of solids and voids within the material. Referred to as architected materials, this concept has gained significant traction in research, particularly with recent advancements in additive manufacturing. These materials, often observed in natural structures like bone microstructures or birds' beaks (refer to Fig. 1.9 for additional examples), have garnered interest due to the recognition that optimal structures exhibit stiffness across multiple scales [94, 95]. Additionally, Fleck noted [96] that one reason for structural hierarchy in engineering is to augment buckling strength. Local buckling strength scales with the strut length l following l^{-2} , indicating that finer length scales contribute to higher buckling strength.

94. Kohn et al. (1986), 'Optimal design and relaxation of variational problems'

95. Allaire et al. (1999), 'On optimal microstructures for a plane shape optimization problem'

96. Fleck et al. (2010), 'Microarchitected materials'

101. Ashby (1999), 'Materials selection in mechanical design'

2: The HS bounds are the tightest bounds possible from the range of composite moduli for a two-phase isotropic mixture. In lattices, usually, the second material is void.

If we observe the Ashby material chart [101] shown in Fig. 1.10, where the material yield strength is plotted against density, it becomes evident that numerous empty spaces exist. Besides some unattainable areas delineated by the HS bounds², these empty spaces can be filled by architected structures, extending the property space of actual materials.

A highly interesting class of architected materials and structures is represented by lattices, alternatively referred to in the literature

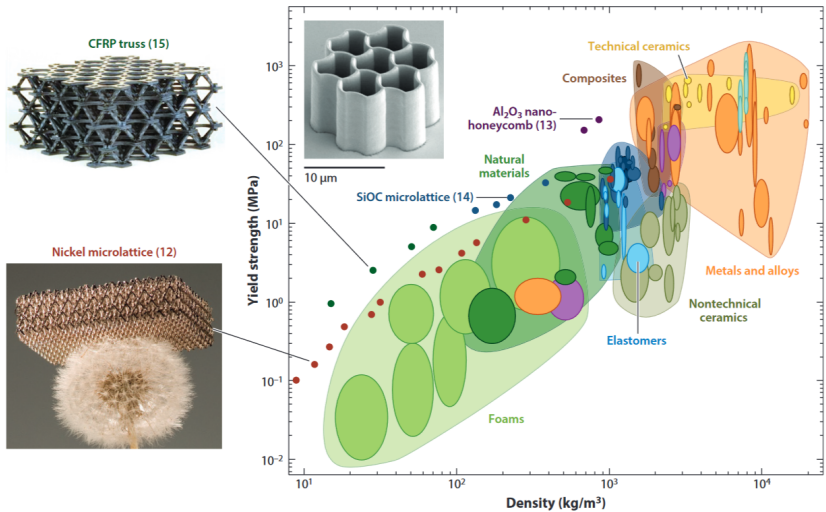


Figure 1.10.: Density versus yield strength Ashby chart. Exploiting the architecture of the material as a variable to design new metamaterials, empty spaces of the graph can be filled (see dots) [93].

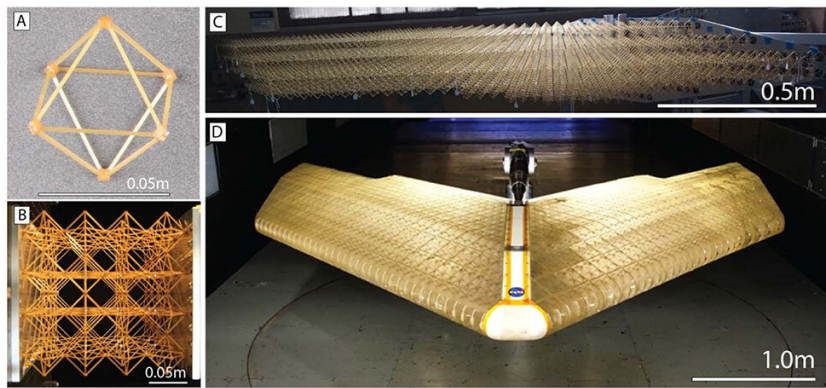


Figure 1.11.: The different length scales present in a modular structure [107]. The size of the RVE is comparable with the dimensions of the wing, especially in the thickness. We therefore talk about modular structure and not lattice material.

as cellular architected or modular materials and structures. The defining feature of lattices is to exhibit a repetitive Representative Volume Element (RVE) (also commonly called module or cell) that is replicated throughout space. This characteristic allows for the establishment of a systematic and reproducible unit that captures the essential structural and material properties of the lattice. The study of the repetitive nature of the RVE permits a comprehensive understanding of the lattice's behavior, enabling researchers to analyze and predict its mechanical, thermal, and other pertinent properties with a high degree of accuracy [102]. It is possible to differentiate between a lattice material and a lattice structure based on the size of the RVE with respect to the considered structure. In a lattice structure, there is no clear physical scale separation between the RVE and the macrostructure, indicating that the lattice's characteristics are manifested at both the micro and macro scales (see Fig. 1.11). However, defining a specific threshold to distinctly categorize the two is challenging, as the transition from lattice material to lattice structure can be gradual and context-dependent [103–106].

Lattice structures and materials exhibit a wide range of promising applications. They showcase notable energy-absorbing properties, particularly when designed as bending-dominated structures [108–

102. Bensoussan et al. (1978), 'Asymptotic analysis for periodic structures'

103. Dai et al. (2008), 'Size effects of basic cell in static analysis of sandwich beams'

104. Kalamkarov et al. (2009), 'Asymptotic Homogenization of Composite Materials and Structures'

105. Coelho et al. (2016), 'Scale-size effects analysis of optimal periodic material microstructures designed by the inverse homogenization method'

106. Zhang et al. (2018), 'Multiscale concurrent topology optimization for cellular structures with multiple microstructures based on ordered SIMP interpolation'

- 108. Evans et al. (2010), 'Concepts for Enhanced Energy Absorption Using Hollow Micro-Lattices'
- 109. Schaedler et al. (2014), 'Designing Metallic Microlattices for Energy Absorber Applications'
- 110. Ozdemir et al. (2016), 'Energy absorption in lattice structures in dynamics'
- 107. Cramer et al. (2019), 'Elastic shape morphing of ultralight structures by programmable assembly'
- 111. Opgenoord et al. (2018), 'Aeroelastic Tailoring using Additively Manufactured Lattice Structures'
- 112. Hutmacher (2000), 'Scaffolds in tissue engineering bone and cartilage'
- 113. Mota et al. (2015), 'Additive manufacturing techniques for the production of tissue engineering constructs'
- 114. Nikolova et al. (2019), 'Recent advances in biomaterials for 3D scaffolds'
- 115. Lu et al. (1998), 'Heat transfer in open-cell metal foams'
- 116. Wadley et al. (2007), 'Thermal Applications of Cellular Lattice Structures'



Figure 1.12.: Vickers Wellingtons, bombers utilized during World War II, remained operational despite sustaining extensive damage, thanks to their lattice fuselage. When one of the ribs was damaged, the load was redistributed to the others, allowing the structure to remain functional [117].

[110]. This quality positions lattice structures as potential candidates for a novel design scheme in aerodynamics, thanks to their remarkable aeroelastic properties [107, 111]. Additionally, lattices have proven to be compelling choices for constructing biomedical scaffolds [112–114]. Furthermore, lattice materials demonstrate excellent heat exchanger properties, attributed to their high surface-to-volume ratio and the turbulent mixing flow they induce when a fluid passes through [115, 116].

Lattices show additional captivating properties that demonstrate their versatility. Firstly, modular structures can be purposefully designed for reversible assembly, introducing the concept of rapid assembly and easily repairable structures. Various approaches, such as utilizing fasteners [107, 118, 119], or incorporating snap-fit joints [120], have been proposed to realize this idea. Furthermore, lattice structures inherently exhibit damage tolerance [121, 122]. In a skin-lattice design, the skin is non-load-bearing, ensuring that skin damage does not lead to progressive structural failure. Additionally, in cases of rib damage, the affected rib can be isolated from the load without compromising the integrity of the entire structure (refer to Fig. 1.12). Lastly, lattice structures pave the way for extensive utilization of robotics in both the manufacturing [123] and assembly phases [124–127].

Lattices can be categorized as open- or closed-wall structures based on the topology of the repeating RVE. Despite closed-wall lattices potentially resulting in stiffer structures, the preference for open-cell configurations is well-articulated by Sigmund *et al.* [66]. They emphasize that the outcome of minimum compliance-type continuum topology optimization studies should inherently be of sheet type unless explicit constraints favoring Michell-like structures are specified. These constraints include considerations of structural and microstructural stability, where the load required to initiate buckling in a slender strut of an open-cell lattice is significantly higher than that of a comparable closed-cell lattice [128]. Consequently, open-cell structures are less prone to buckling. Additionally, the porosity of open-wall cells allows for the passage of flow, making them suitable for applications such as heat exchangers or promoting bone regrowth in biomedical scaffolds. From a manufacturing perspective, open-cell designs are preferable, as very thin walls are challenging to manufacture. The transparency inherent in open-cell structures is advantageous for tasks such as repair and health monitoring. Finally, an open-cell design is considered elegant and aesthetic, as it embodies Michell-like structures, which are described as "inarguably beautiful" and "look elegant and efficient" by Sigmund *et al.* [66].

Lattice structures are further categorized into stretching- and bending-dominated based on the RVE topology. A stretching-dominated structure is characterized as a lattice in which its constitutive struts exclusively experience tension and compression loads. In such a structure,

the nodal stiffness does not contribute to the overall structural stiffness, and the truss undergoes collapse primarily through the stretching of its struts. Desphande *et al.* [128] noted that freezing the joints of a stretching-dominated truss has minimal impact on its macroscopic stiffness or strength. Despite the bending of the struts, the frame remains stretching-dominated, and the collapse load is predominantly determined by the axial strength of the struts. Consequently, if an open-cell structure is stretching-dominated, it can effectively be treated as a connected set of pin-jointed struts.

The relative density of the lattice is defined as:

$$\bar{\rho} = \frac{\rho_l}{\rho} \quad (1.9)$$

where ρ_l and ρ represent the density of the lattice and the dense material, respectively [129]. A stretching-dominated structure exhibits approximately 10 times greater stiffness and 3 times greater strength than a bending-dominated structure at $\bar{\rho} = 0.1$, as illustrated in Figure 1.13 [128]. Nevertheless, when subjected to compression, stretching-dominated structures display a softening post-yield response attributed to the buckling of struts, rendering them less suitable for energy absorption tasks. In contrast, bending-dominated lattices showcase a more favorable energy-absorbing behavior, characterized by a plateau-like response.

1.3.1. MODULAR STRUCTURES AND LATTICE MATERIALS OPTIMIZATION

The initial density-based topology optimization method, as seen in Bendsøe and Kikuchi's foundational work [5], employed numerical homogenization to model a meta-material consisting of infinitesimally small square cells with square holes. Notably, this marked the advent of multi-scale optimization, driven by the observation that optimal stiffness for a structure encompasses various scales [94, 95].

In the 1990s, the focus shifted from homogenization algorithms to mono-scale algorithms, where the optimization involved a homogeneous distribution of an isotropic material [35, 130]. This shift was primarily caused by the manufacturing challenges associated with producing multi-scale meta-materials. Subsequently, these approaches evolved into what is now known as density-based topology optimization. Mono-scale methods, where the design domain discretization results in structures at a single scale, can achieve theoretical stiffness-optimal structures spanning multiple scales with fine mesh discretization and careful continuation techniques, provided there is no regularization for mesh independence. Bendsøe and Kikuchi's original work and homogenization-based algorithms have gained recently more interest due to the advances in additive manufacturing technologies. Contemporary studies are combining asymptotic

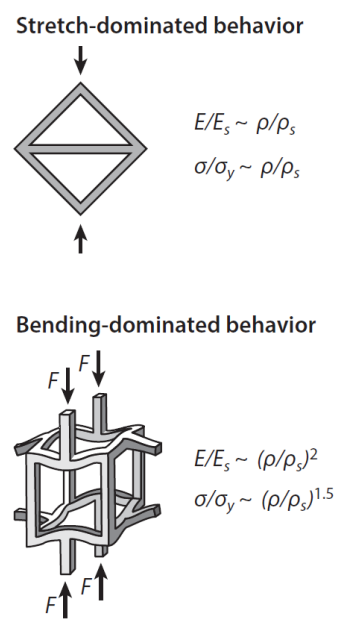


Figure 1.13.: A stretch-dominated and a bending-dominated RVE. Bending-dominated structures act as a mechanism if the joints cannot withstand moments. The scaling laws are different for the two structure families [93].

107. Cramer et al. (2019), 'Elastic shape morphing of ultralight structures by programmable assembly'

118. Cheung et al. (2013), 'Reversibly Assembled Cellular Composite Materials'

119. Jenett et al. (2017), 'Digital Morphing Wing: Active Wing Shaping Concept Using Composite Lattice-Based Cellular Structures'

120. Dong et al. (2015), 'Mechanical response of Ti-6Al-4V octet-truss lattice structures'

121. Stolpe (2019), 'Fail-safe truss topology optimization'

122. Wu et al. (2021), 'Topology optimization of multi-scale structures'

123. Hunt et al. (2019), 'WrapToR composite truss structures'

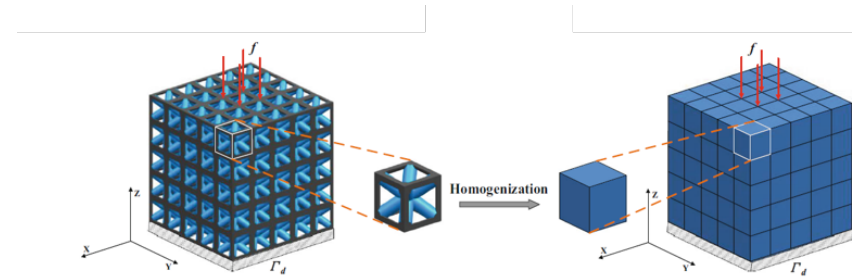


Figure 1.14: Graphical representation of the asymptotic homogenization method used to retrieve the equivalent mechanical properties of a periodic cell [134].

- 124. Gershenfeld et al. (2015), 'Macro-fabrication with Digital Materials'
- 125. Jenett et al. (2017), 'BILL-E: Robotic Platform for Locomotion and Manipulation of Lightweight Space Structures'
- 126. Costa et al. (2020), 'Algorithmic Approaches to Reconfigurable Assembly Systems'
- 127. Niehs et al. (2020), 'Recognition and Reconfiguration of Lattice-Based Cellular Structures by Simple Robots'
- 66. Sigmund et al. (2016), 'On the (non-)optimality of Michell structures'
- 128. Deshpande et al. (2001), 'Foam topology'
- 129. Ashby (2006), 'The properties of foams and lattices'
- 5. Bendsøe et al. (1988), 'Generating optimal topologies in structural design using a homogenization method'
- 94. Kohn et al. (1986), 'Optimal design and relaxation of variational problems'
- 95. Allaire et al. (1999), 'On optimal microstructures for a plane shape optimization problem'
- 35. Bendsøe (1989), 'Optimal shape design as a material distribution problem'
- 130. Zhou et al. (1991), 'The COC algorithm, Part II'
- 122. Wu et al. (2021), 'Topology optimization of multi-scale structures'
- 131. Rodrigues et al. (2002), 'Hierarchical optimization of material and structure'
- 132. Pantz et al. (2008), 'A Post-Treatment of the Homogenization Method for Shape Optimization'
- 133. Groen et al. (2018), 'Homogenization-based topology optimization for high-resolution manufacturable microstructures'

homogenization and topology optimization to optimize multi-scale structures.

Lattice structures are optimized through either a multi-scale or a full-scale approach. Multi-scale algorithms operate on structures with different physical scales between the micro- and macro-levels, assuming periodic boundary conditions for the RVE. Doing that allows for the use of a material model with micro-structure properties evaluated using asymptotic homogenization. In contrast, full-scale methods represent mono-scale approaches where optimization is achieved by directly controlling the layout locally. In these full-scale approaches, both analysis and optimization are conducted at the full resolution of the domain. For a more in-depth exploration and comparison of full-scale and multi-scale approaches, interested readers can refer to the comprehensive review by Wu *et al.* [122].

1.3.2. MULTI-SCALE STRUCTURES OPTIMIZATION

Multi-scale topology optimization approaches aim to speed up computations for optimizing structures at full resolution. Optimal structures span multiple scales, and using a finer mesh allows for detailed geometric improvements, potentially enhancing optimized structures. However, higher-resolution mono-scale approaches come with increased computational costs. To tackle this, multi-scale approaches like the hierarchical method by Rodrigues *et al.* [131] and de-homogenization techniques [132, 133] have been introduced.

The hierarchical optimization framework consists of a master problem addressing the global spatial distribution of material and an inner problem tackling the optimal choice of material at the local level. This approach shifts the focus from a specific composite's material distribution problem to a more comprehensive challenge involving both topology and material optimal design. The idea is to use the homogenized micro-scale cell as the base material of the macro-scale topology optimization. Fig. 1.14 gives a graphical representation of how asymptotic homogenization works. The equivalent elastic tensor \mathbf{C}^H is calculated using the following formula [135]:

$$\mathbf{C}^H = \frac{1}{|\Omega_m|} \int_{\Omega_m} (\varepsilon_m^0 - \varepsilon_m) \mathbf{C} (\varepsilon_m^0 - \varepsilon_m) d\Omega_m \quad (1.10)$$

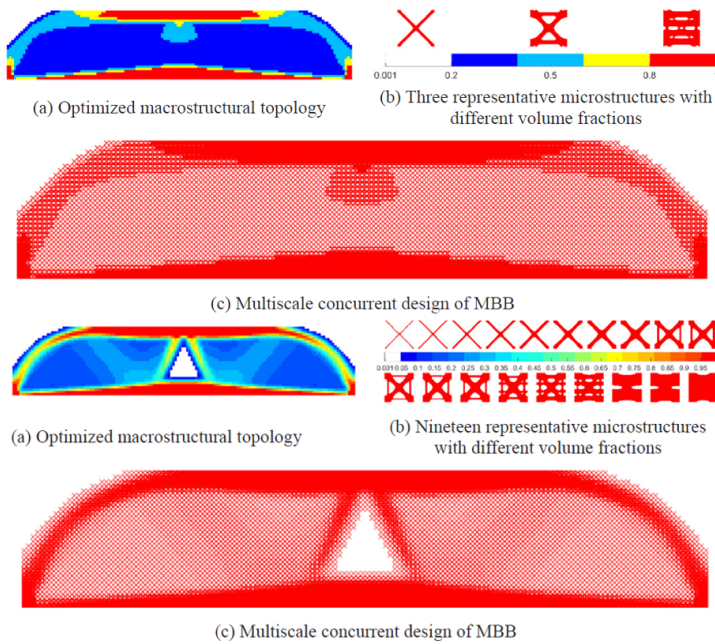


Figure 1.15.: In the study of Zhang *et al.* [106] the same test case is optimized using a different number of microstructures. Here we show the multi-scale optimized structures using 3 and 19 different microstructures.

where \mathbf{C}^H is the homogenized elastic tensor, Ω_m represents the RVE volume, \mathbf{C} is the base material elastic tensor and ε_m^0 are called unit test strain and are defined as $\varepsilon^{11} = (1, 0, 0)^T$, $\varepsilon^{22} = (0, 1, 0)^T$, $\varepsilon^{12} = (0, 0, 1)^T$. An example of the results obtained using a hierarchical method is presented in Fig. 1.15.

De-homogenization is an approach where the optimization problem is initially solved solely on the macroscopic level using a homogenization method. Subsequently, an additional phase is introduced to obtain connected and physically realizable microstructures based on the obtained macroscopic result. In the macroscale optimization, multiple additional parameters are typically optimized concurrently with the density of the Representative Volume Element (RVE). These parameters may include microstructure orientation, contributing to the creation of a smooth mapping function [133, 136–138]. An alternative approach involves approximating the material behavior through a reduced database model, as demonstrated by Xia and Breitkopf [139]. In this method, microstructural computations are performed offline, only once. Precomputed databases are often employed to obtain the full design for the parametrized lattice RVE, often using a polynomial model to interpolate between the database microstructures [140, 141]. Recent approaches are now using Artificial Intelligence (AI) and deep learning to speed up the de-homogenization phase [142–145]

In conclusion, despite maintaining the separation of the two physical scales during the optimization process, it is imperative to conduct a full-scale validation for all multi-scale methods, as highlighted in various studies [122, 133, 146, 147]. Additionally, the multi-scale optimization approaches in which the microstructure is aligned to local stress fields without constraints imposed by cell geometry or

135. Guedes *et al.* (1990), 'Preprocessing and postprocessing for materials based on the homogenization method with adaptive finite element methods'

133. Groen *et al.* (2018), 'Homogenization-based topology optimization for high-resolution manufacturable microstructures'

136. Allaire *et al.* (2019), 'Topology optimization of modulated and oriented periodic microstructures by the homogenization method'

137. Geoffroy-Donders *et al.* (2020), '3-d topology optimization of modulated and oriented periodic microstructures by the homogenization method'

138. Kumar *et al.* (2020), 'A density-and-strain-based K-clustering approach to microstructural topology optimization'

139. Xia *et al.* (2015), 'Multiscale structural topology optimization with an approximate constitutive model for local material microstructure'

140. Wang *et al.* (2018), 'Concurrent topology optimization design of structures and non-uniform parameterized lattice microstructures'

141. Imediegwu *et al.* (2019), 'Multiscale structural optimization towards three-dimensional printable structures'

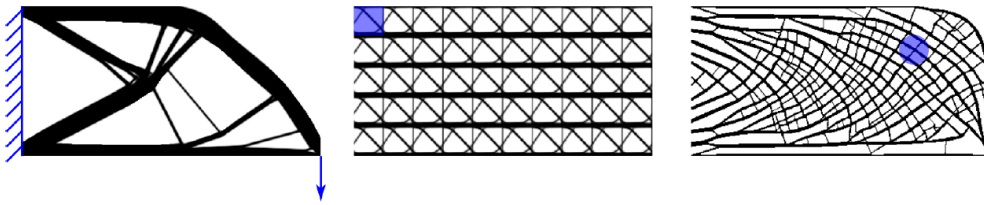


Figure 1.16.: Three structures with the same volume are optimized for compliance minimization using three different methods: on the left, a classic mono-scale topology optimization algorithm. Middle: the variable linking method is used to enforce the pattern repetition on the structure. On the right an optimized structure with local volume constraints. The algorithms used to optimize the last two structures belong to the family of *full-scale* methods. [122].

142. Kim et al. (2021), 'Machine learning-combined topology optimization for functionary graded composite structure design'

143. White et al. (2019), 'Multiscale topology optimization using neural network surrogate models'

144. Chandrasekhar et al. (2021), 'Multi-Material Topology Optimization Using Neural Networks'

145. Wang et al. (2021), 'Enhancing Data-driven Multiscale Topology Optimization with Generalized De-homogenization'

122. Wu et al. (2021), 'Topology optimization of multi-scale structures'

133. Groen et al. (2018), 'Homogenization-based topology optimization for high-resolution manufacturable microstructures'

146. Duriez et al. (2021), 'A well connected, locally-oriented and efficient multi-scale topology optimization (EMTO) strategy'

147. Sigmund (2022), 'On benchmarking and good scientific practise in topology optimization'

133. Groen et al. (2018), 'Homogenization-based topology optimization for high-resolution manufacturable microstructures'

105. Coelho et al. (2016), 'Scale-size effects analysis of optimal periodic material microstructures designed by the inverse homogenization method'

148. Cheng et al. (2019), 'Functionally graded lattice structure topology optimization for the design of additive manufactured components with stress constraints'

orientation [133], deliver good performance even for structures with less periodicity compared to a bulk distribution.

1.3.3. FULL-SCALE STRUCTURES OPTIMIZATION

Recent studies have focused on assessing homogenization predictions compared to mechanical responses, revealing up to a 20 % variation in the effective components of the stiffness tensor for a $6 \times 6 \times 6$ cube when compared to homogenized models [105, 148]. This variability is attributed to the "boundary layer phenomenon" observed in the late 70s, challenging the assumptions of periodic boundary conditions and scale separability inherent in homogenization [102, 104]. To address these limitations, a new family of methodologies, known as full-scale approaches, has emerged. Unlike homogenization-based methods, full-scale approaches, such as pattern repetition (also known as variable linking) and local volume constraints, avoid reliance on homogenization. In pattern repetition, the initial design space is partitioned into repetitive domains that are optimized and constrained to ensure their uniformity [37]. In contrast, the local volume constraints method imposes an upper limit on the solid elements' fraction in a neighborhood radius centered at each point within the design domain. The objective is to generate porous structures aligned with principal stress directions. While experiencing a modest stiffness reduction compared to mono-scale designs, these structures demonstrate heightened resilience against variations in load angle, local material failure, and buckling [149].

Variable linking approach faces a common limitation, leading to compromised structural performance due to topological periodicity [37, 150]. This limitation arises as the design converges toward solutions influenced by the region with the highest compliance, resulting in suboptimal solutions for other regions where the same module design is applied [151]. To address this, Bakker [152] identified two key approaches. The first involves extending the solution space by introducing additional module properties as design variables. For instance, allowing module rotations has proven effective, as it modifies the local material distribution and enhances structural performance [153]. Another extension involves allowing the module unit

to resize, providing flexibility in adapting to different regions within the global domain [154, 155]. These strategies offer ways to overcome the challenges associated with topological periodicity and achieve more optimal solutions for diverse regions within the structure.

- 102. Bensoussan et al. (1978), 'Asymptotic analysis for periodic structures'
- 104. Kalamkarov et al. (2009), 'Asymptotic Homogenization of Composite Materials and Structures'
- 37. Zhang et al. (2006), 'Scale-related topology optimization of cellular materials and structures'
- 149. Wu et al. (2018), 'Infill Optimization for Additive Manufacturing—Approaching Bone-Like Porous Structures'
- 37. Zhang et al. (2006), 'Scale-related topology optimization of cellular materials and structures'
- 150. Huang et al. (2008), 'Optimal design of periodic structures using evolutionary topology optimization'
- 151. Tugilimana et al. (2019), 'An integrated design methodology for modular trusses including dynamic grouping, module spatial orientation, and topology optimization'
- 152. Bakker et al. (2021), 'Simultaneous optimization of topology and layout of modular stiffeners on shells and plates'
- 153. Tugilimana et al. (2017), 'Spatial orientation and topology optimization of modular trusses'
- 154. Stromberg et al. (2011), 'Application of layout and topology optimization using pattern gradation for the conceptual design of buildings'
- 155. Wu et al. (2016), 'A System for High-Resolution Topology Optimization'

EVALUATING DISCRETIZATION APPROACHES FOR ULTRALIGHT STRUCTURE OPTIMIZATION

2

The process of topology optimization for a structure involves the selection and sizing of optimal elements within a predetermined set. As discussed in the previous chapter, in our context this set could be composed of either continuum elements (shell or volumetric) or truss-like elements. Based on the discretization choice we distinguish between density-based topology optimization and Truss Topology Optimization (TTO). This chapter aims to assess the suitability and the inherent advantages and disadvantages of both methods when optimizing ultralight structures i.e. structures that exhibit a low volume fraction, typically below 5%.

For this purpose, we initially formulate a volume minimization problem subject to maximum stress constraints for both discretizations in Section 2.1. Later, a two-dimensional test case, featuring identical dimensions, loads, and material properties is optimized using the density-based topology optimization and the TTO algorithms. The outcomes of the comparison of both optimization approaches are presented and discussed in Section 2.2.

2.1. THE FORMULATION OF A SHARED PROBLEM: VOLUME MINIMIZATION WITH STRESS CONSTRAINTS

Instead of focusing on the commonly used compliance minimization formulation in density-based topology optimization, our emphasis on the aerospace sector leans towards the volume minimization problem. Prioritizing volume minimization, directly linked to the more crucial mass minimization objective, is driven by economic, environmental, and performance considerations within the aerospace industry. This strategic approach supports industry goals of sustainability, efficiency, and technological advancement. Therefore, we have chosen to adopt the volume minimization optimization formulation for our study, and we will now implement it on both continuum and truss-like meshes.

2.1.1. DENSITY-BASED TOPOLOGY OPTIMIZATION MINIMUM VOLUME FORMULATION

This section introduces the Nested Analysis and Design (NAND) volume minimization formulation for topology optimization on continuum meshes. We will begin by explaining important notations and concepts that are essential for developing the volume minimization formulation.

2.1 THE FORMULATION OF A SHARED PROBLEM: VOLUME MINIMIZATION WITH STRESS CONSTRAINTS	23
2.2 COMPARISON BETWEEN DENSITY-BASED TOPOLOGY OPTIMIZATION AND TTO	32
2.3 CONCLUSION	43

Part of the content presented in this chapter has been published and showcased during a conference as: Stragiotti, E. et al. (2021) "Towards manufactured lattice structures: a comparison between layout and topology optimization", in *AeroBest 2021 International Conference on Multidisciplinary Design Optimization of Aerospace Systems*. Book of proceedings. Lisbon, Portugal: ECCOMAS [156].

OBJECTIVE AND CONSTRAINT FUNCTIONS The goal of the optimization is to minimize the volume fraction occupied by a structure under a specified load case. In this thesis, as we deal with two- and three-dimensional structures, we should differentiate between area and volume, but for the sake of generality, we talk about volume. The volume fraction of the structure, denoted as V_f , is expressed as the ratio between the structural volume $V = \sum_{i \in \Omega} \bar{\rho}_i v_i$ and the total volume V_0 of the domain Ω :

$$V_f = \frac{V}{V_0} = \frac{1}{V_0} \sum_{i \in \Omega} \bar{\rho}_i v_i. \quad (2.1)$$

We assume that the elementary volume v_i occupied by the i -th element is equal for all the elements, and thus Equation 2.1 is simplified as follows:

$$V_f = \frac{1}{N_e} \sum_{i \in \Omega} \bar{\rho}_i. \quad (2.2)$$

The normalized local stress constraint g_{st} is formulated as:

$$g_{st} := \frac{\sigma_{VM,i}}{\sigma_L} - 1 \leq 0, \quad \forall i \in \Omega_{mat}(\rho) \quad (2.3)$$

where $\Omega_{mat}(\rho) \subseteq \Omega$ represents the design-dependent set of elements with a non-zero density i.e., stress constraints are defined only for the active elements, $\sigma_{VM,i}$ is the equivalent Von Mises stress for the i -th element, and σ_L is the maximum allowable of the material.

157. Achtziger et al. (2008), 'Mathematical programs with vanishing constraints'

158. Cheng et al. (1992), 'Study on Topology Optimization with Stress Constraints'

The first difficulty that arises using this formulation is that the stress constraints are defined only for the elements where $\bar{\rho}_i > 0$, while $\bar{\rho}_i \in [0, 1]$. Thus, the set of constraints changes during the optimization. This class of problems is called Mathematical Programs with Vanishing Constraints (MPVCs) [157] and is known for being difficult to solve with a gradient descent optimization algorithm. The original set of constraints g_{st} is then reformulated into an equivalent design-independent set of constraints \bar{g} as follows [158]:

$$\bar{g} := \bar{\rho}_i \left(\frac{\sigma_{VM,i}}{\sigma_L} - 1 \right) \leq 0, \quad \forall i \in \Omega. \quad (2.4)$$

VON MISES STRESS EVALUATION The evaluation of the equivalent stress of a two-dimensional element follows the formulation proposed by Von Mises. Let us take a four-node quadrilateral linear element with a single integration (or Gauss) point in the center and four $2a$ equal-length sides (see Fig. 2.1). If bilinear shape functions are used to interpolate the displacement field, we can evaluate the deformations

at the integration point as:

$$\begin{pmatrix} \varepsilon_x \\ \varepsilon_y \\ \gamma_{xy} \end{pmatrix} = \mathbf{B}_s \mathbf{q}_s, \text{ with } \mathbf{B}_s = \frac{1}{4a} \begin{pmatrix} -1 & 1 & 1 & -1 & 0 & 0 & 0 & 0 \\ 0 & 0 & 0 & 0 & -1 & -1 & 1 & 1 \\ -1 & -1 & 1 & 1 & -1 & 1 & 1 & -1 \end{pmatrix}, \quad (2.5)$$

where $\mathbf{q}_s = (u_1, u_2, u_3, u_4, v_1, v_2, v_3, v_4)^T$ represents the vector of the displacement degrees of freedom of the element.

The stress tensor is evaluated using the elasticity Hooke's law in 2D as follows:

$$\begin{pmatrix} \sigma_x \\ \sigma_y \\ \tau_{xy} \end{pmatrix} = \mathbf{C}_e \begin{pmatrix} \varepsilon_x \\ \varepsilon_y \\ \gamma_{xy} \end{pmatrix} \quad \text{with} \quad \mathbf{C}_e = \frac{E}{1-\nu^2} \begin{pmatrix} 1 & \nu & 0 \\ \nu & 1 & 0 \\ 0 & 0 & G \end{pmatrix}. \quad (2.6)$$

The equivalent Von Mises stress of the element can then be written as:

$$\langle \sigma_{VM} \rangle = \sqrt{\sigma_x^2 + \sigma_y^2 - \sigma_x \sigma_y + 3\tau_{xy}} \quad (2.7)$$

$$= \sqrt{\begin{pmatrix} \sigma_x & \sigma_y & \tau_{xy} \end{pmatrix} \begin{pmatrix} 1 & -1/2 & 0 \\ -1/2 & 1 & 0 \\ 0 & 0 & 3 \end{pmatrix} \begin{pmatrix} \sigma_x \\ \sigma_y \\ \tau_{xy} \end{pmatrix}} \quad (2.8)$$

$$= \sqrt{\mathbf{q}_s^T \mathbf{B}_s^T \mathbf{C}_e^T \mathbf{D}_{VM} \mathbf{C}_e \mathbf{B}_s \mathbf{q}_s}, \text{ with } \mathbf{D}_{VM} = \begin{pmatrix} 1 & -1/2 & 0 \\ -1/2 & 1 & 0 \\ 0 & 0 & 3 \end{pmatrix} \quad (2.9)$$

$$\langle \sigma_{VM} \rangle = \sqrt{\mathbf{q}_s^T \mathbf{S} \mathbf{q}_s}, \quad \text{with } \mathbf{S} = \mathbf{B}_s^T \mathbf{C}_e^T \mathbf{D}_{VM} \mathbf{C}_e \mathbf{B}_s. \quad (2.10)$$

in which we used the notation introduced by Verbart [159] $\langle \dots \rangle$ to represent macroscopic (or homogenized) variables.

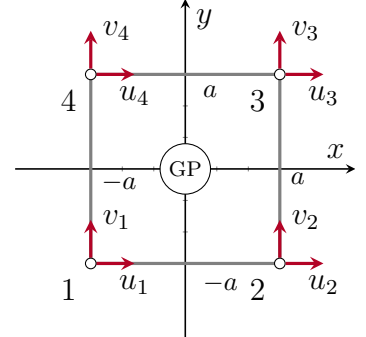


Figure 2.1.: A four-node quadrilateral element. GP is the Gaussian integration point for which the equivalent stress is evaluated.

[159]. Verbart et al. (2017), 'A unified aggregation and relaxation approach for stress-constrained topology optimization'

MICROSCOPIC AND MACROSCOPIC STRESS In stress-constrained topology optimization, the element stress is usually evaluated using the microscopic stress formulation, assuming that there is no direct correlation between stress and density [160]. Indeed, the use of the macroscopic stress in volume minimization optimization problems creates an all-void design [161]. The properties that the microscopic stress should present are:

- (i) The stress criterion should be mathematically as simple as possible, as the relationship between Young's modulus and density. This permits a simple numerical implementation.
- (ii) To mimic the real physical behavior, the microscopic stress should be inversely proportional to density.

[160]. Duysinx et al. (1998), 'Topology optimization of continuum structures with local stress constraints'

[161]. Le et al. (2010), 'Stress-based topology optimization for continua'

^{159.} Verbart et al. (2017), 'A unified aggregation and relaxation approach for stress-constrained topology optimization'

Equation 1.2 reads as follows:

$$E_i(\bar{\rho}_i) = E_{\min} + \bar{\rho}_i^p (E_0 - E_{\min})$$

where the parameter p is called SIMP penalization parameter, and it is used to reduce the quantity of intermediate densities, pushing the result to a black-and-white result.

^{159.} Verbart et al. (2017), 'A unified aggregation and relaxation approach for stress-constrained topology optimization'

^{161.} Le et al. (2010), 'Stress-based topology optimization for continua'
^{162.} Holmberg et al. (2013), 'Stress constrained topology optimization'
^{163.} Silva et al. (2019), 'Stress-constrained topology optimization considering uniform manufacturing uncertainties'

^{75.} Rozvany (2001), 'On design-dependent constraints and singular topologies'

^{164.} Stolpe (2003), 'On Models and Methods for Global Optimization of Structural Topology'

^{165.} Sved et al. (1968), 'Structural optimization under multiple loading'

^{74.} Cheng et al. (1997), ' ε -relaxed approach in structural topology optimization'

- (iii) The microscopic stress should converge to a non-zero value at zero density. This requisite is deduced from investigations into the asymptotic stress behavior in thin layers [159].

The relation between stress and displacement is written as:

$$\langle \sigma_{VM} \rangle = C_e(\langle E \rangle) \langle \varepsilon \rangle, \quad (2.11)$$

where the variables between angular brackets $\langle \dots \rangle$ represent macroscopic variables.

Combining (i) and (ii) with Equations 1.2, and 2.11, the microscopic stress can be written as:

$$\sigma_{VM} = \frac{\langle \sigma_{VM} \rangle}{\rho_e^q} = \rho_e^{p-q} C_e(E_0) \langle \varepsilon \rangle, \quad (2.12)$$

where the exponent q is a number greater than 1.

One possible choice that satisfy all the requirements is $q = p$ [159, 161–163]. Thus, the microscopic stress is defined as:

$$\sigma_{VM} = C_e(E_0) \langle \varepsilon \rangle. \quad (2.13)$$

The significance of microscopic stress becomes evident when considering an element with intermediate density, that is physically realized by a porous microstructure. The microscopic stress presented in Equation 2.13 measures the stress in the material of the microstructure. It is grounded in the assumption that the macroscopic deformations of the homogenized element generate within the microstructure of the element a stress state that remains unaffected by the density of the element itself.

CONSTRAINTS AGGREGATION AND RELAXATION When optimizing a structure with stress constraints using a NAND formulation, two primary challenges commonly arise:

- (i) Is it known in the literature [75, 164] that stress-based topology optimization suffers from the *singular minima* (or *singularity*) problem: firstly observed on truss structure optimization [165], these *minima* are almost inaccessible to a standard gradient-based optimizer, often preventing it to reach the global optimum of the optimization [75]. This is because achieving the optimal solution to a problem using continuous design variables may necessitate passing through a state where the optimization constraints are violated, i.e. the *minimum* is on a lower dimension compared to the design space. This problem is often solved using a technique called *constraints relaxation* [74].
- (ii) The stress is a local measure, and thus a large set of constraints is generated when a reasonably fine mesh is used (one element,

one constraint). This problem is often solved using a technique called *constraints aggregation* or *global constraints* [166].

Following the work developed by Verbart *et al.* [159], the lower bound Kreisselmeier-Steinhauser (KS) function [167] is used to approximate the local relaxed stress constraint maximum. The authors showed that employing lower-bound KS aggregation functions to approximate the maximum operator in stress-constrained topology optimization ensures the relaxation and aggregation of the constraints simultaneously. The KS aggregated stress constraint function is defined as follows:

$$G_{\text{KS}}^{\text{L}} = \frac{1}{P} \ln \left(\frac{1}{N_e} \sum_{i \in \Omega} e^{P \bar{g}_i} \right). \quad (2.14)$$

Its main advantage over other different formulations is that it uses a single hyperparameter P to control the aggregation and the relaxation of the constraints simultaneously.

[166]. Silva et al. (2021), 'Local versus global stress constraint strategies in topology optimization'

[159]. Verbart et al. (2017), 'A unified aggregation and relaxation approach for stress-constrained topology optimization'

[167]. Kreisselmeier et al. (1979), 'Systematic Control Design by Optimizing a Vector Performance Index'

We remember that the stress constraints are defined as follows:

$$\bar{g} := \bar{\rho}_i \left(\frac{\sigma_{\text{VM},i}}{\sigma_{\text{L}}} - 1 \right) \leq 0.$$

MINIMUM VOLUME FORMULATION The NAND minimum volume formulation for continuous discretization is written combining Equations 2.2, and 2.14 as:

$$\begin{aligned} \min_{\rho} \quad & V = \frac{1}{N_e} \sum_{i \in \Omega} \bar{\rho}_i, && \text{(Volume minimization)} \\ \text{s.t.} \quad & G_{\text{KS}}^{\text{L}} = \frac{1}{P} \ln \left(\frac{1}{N_e} \sum_{i \in \Omega} e^{P \bar{g}_i} \right) \leq 0 && \text{(Stress constraints)} \quad (\mathbb{T}_1) \\ & \mathbf{K}\mathbf{u} = \mathbf{F} && \text{(FEM equation)} \\ & 0 \leq \rho_i \leq 1, \end{aligned}$$

The optimization is carried out using a gradient descent optimization algorithm for which the sensitivities are given in analytical form. Using analytic gradients is in general more efficient than finite differences as it avoids the need for multiple function evaluations, making the optimization process faster and more precise.

SENSITIVITY ANALYSIS OF THE OBJECTIVE FUNCTION Deriving Equation 2.2 with respect to $\bar{\rho}$ we obtain:

$$\frac{\partial V}{\partial \bar{\rho}_i} = \frac{1}{N_e}. \quad (2.15)$$

The sensitivity of the objective function can then be evaluated using Equation 2.15 as follows:

$$\frac{dV}{d\rho_i} = \sum_{j \in \mathbb{N}_{i,R}} \frac{\partial V}{\partial \bar{\rho}_j} \frac{\partial \bar{\rho}_j}{\partial \bar{\rho}_i} \frac{\partial \bar{\rho}_i}{\partial \rho_i}. \quad (2.16)$$

Equation 1.4 reads:

$$\tilde{\rho}_i = \frac{\sum_{j \in \mathbb{N}_{i,R}} w(d_j) v_j \rho_j}{\sum_{j \in \mathbb{N}_{i,R}} w(d_j) v_j}.$$

Equation 1.5 reads:

$$\bar{\tilde{\rho}}_j = \frac{\tanh(\beta\eta) + \tanh(\beta(\tilde{\rho}_j - \eta))}{\tanh(\beta\eta) + \tanh(\beta(1 - \eta))}.$$

in which the derivative of the filtered density $\tilde{\rho}$ with respect to the design variable ρ is written deriving Equation 1.4:

$$\frac{\partial \tilde{\rho}_i}{\partial \rho_j} = \frac{w(d_j) v_j}{\sum_{j \in \mathbb{N}_{i,R}} w(d_j) v_j}. \quad (2.17)$$

The sensitivity of the physical densities $\bar{\tilde{\rho}}$ with respect to the filtered $\tilde{\rho}$ can be written deriving Equation 1.5 as:

$$\frac{\partial \bar{\tilde{\rho}}_j}{\partial \tilde{\rho}_j} = \beta \frac{1 - \tanh^2(\beta(\tilde{\rho}_j - \eta))}{\tanh(\beta\eta) + \tanh(\beta(1 - \eta))}. \quad (2.18)$$

Using the chain rule it is possible to write:

$$\frac{\partial h}{\partial \rho_i} = \sum_{j \in \mathbb{N}_{i,R}} \frac{\partial h}{\partial \bar{\tilde{\rho}}_j} \frac{\partial \bar{\tilde{\rho}}_j}{\partial \tilde{\rho}_j} \frac{\partial \tilde{\rho}_j}{\partial \rho_i}, \quad (2.19)$$

where h represents a generic function.

SENSITIVITY ANALYSIS OF THE CONSTRAINT FUNCTION The sensitivity of the aggregated constraint function G_{KS}^L with respect to the design variable ρ is evaluated using:

$$\frac{dG_{KS}^L}{d\rho_i} = \sum_{j \in \mathbb{N}_{i,R}} \frac{\partial G_{KS}^L}{\partial \bar{\tilde{\rho}}_j} \frac{\partial \bar{\tilde{\rho}}_j}{\partial \tilde{\rho}_j} \frac{\partial \tilde{\rho}_j}{\partial \rho_i}. \quad (2.20)$$

we remember that

$$K(\bar{\tilde{\rho}})\mathbf{u} = f$$

As the constraint function $G_{KS}^L = G(\bar{\tilde{\rho}}, \mathbf{u}(\bar{\tilde{\rho}}))$ is explicitly and implicitly (via the relationship with \mathbf{u}) depending on $\bar{\tilde{\rho}}$, the first-order derivative is evaluated using the total derivative formula:

$$\frac{dG}{d\bar{\tilde{\rho}}_j} = \frac{\partial G}{\partial \bar{\tilde{\rho}}_j} + \frac{\partial G}{\partial \mathbf{u}} \frac{\partial \mathbf{u}}{\partial \bar{\tilde{\rho}}_j}. \quad (2.21)$$

As function G_{KS}^L depends on \mathbf{u} via the stresses σ_i , it is possible to write:

$$\frac{\partial G}{\partial \mathbf{u}} = \sum_{i \in \Omega} \left(\frac{\partial G}{\partial \sigma_i} \frac{\partial \sigma_i}{\partial \mathbf{u}} \right). \quad (2.22)$$

Combining Eq. 2.21 with Eq. 2.22, we obtain:

$$\frac{dG}{d\bar{\tilde{\rho}}_j} = \underbrace{\frac{\partial G}{\partial \bar{\tilde{\rho}}_j}}_A + \sum_{i \in \Omega} \left(\underbrace{\frac{\partial G}{\partial \sigma_i}}_B \underbrace{\frac{\partial \sigma_i}{\partial \mathbf{u}}}_C \right) \underbrace{\frac{\partial \mathbf{u}}{\partial \bar{\tilde{\rho}}_j}}_D. \quad (2.23)$$

We compute the four factors separately:

A – The first term represents the explicit relationship of G to the physical densities and its calculation is straightforward:

$$\frac{\partial G}{\partial \bar{\rho}_j} = \frac{1}{P} \frac{\left(\frac{\sigma_{VM,j}}{\sigma_L} - 1 \right) \frac{1}{N_e} P e^{P \bar{g}_j}}{\frac{1}{N_e} \sum_k e^{P \bar{g}_k}} = \left(\frac{\sigma_{VM,j}}{\sigma_L} - 1 \right) \frac{e^{P \bar{g}_j}}{\sum_k e^{P \bar{g}_k}}. \quad (2.24)$$

B – The second term can be calculated using the chain rule:

$$\frac{\partial G}{\partial \sigma_i} = \frac{\partial G}{\partial \bar{g}_i} \frac{\partial \bar{g}_i}{\partial \sigma_i} = \frac{1}{P} \frac{\frac{1}{N_e} P e^{P \bar{g}_i} \bar{\rho}_i}{\frac{1}{N_e} \sum_k e^{P \bar{g}_k} \sigma_L} = \frac{\bar{\rho}_i}{\sigma_L} \frac{e^{P \bar{g}_i}}{\sum_k e^{P \bar{g}_k}}. \quad (2.25)$$

C – We reformulate Equation 2.10 to be written in global coordinates instead of local:

$$\sigma_i^2 = q_s^T S q_s = u^T S_g u, \quad (2.26)$$

Equation 2.10 reads:

$$\langle \sigma_{VM} \rangle = \sqrt{q_s^T S q_s}.$$

where S_g represents the matrix S of Equation 2.10 written on global coordinates¹. We can now differentiate Equation 2.26 with respect of the displacement field in global coordinates u to obtain:

$$\frac{\partial \sigma_i}{\partial u} = \frac{S_g u}{\sigma_i}. \quad (2.27)$$

Equations 2.25, and 2.27 are now combined to obtain the result of the product of the \mathbf{B} and \mathbf{C} terms. As a result, the derivatives of G with respect to u , are written as:

$$\frac{\partial G}{\partial u} = \frac{\bar{\rho}_j}{\sigma_L \sigma_j} e^{P \bar{g}_i} |S_j|_g u. \quad (2.28)$$

1: The matrix S_g can be calculated using the very same assembling approach used for the stiffness matrix K starting from the elemental stiffness matrix K_e . As the global stiffness matrix K , S_g is symmetric and sparse.

D – To calculate the last term, we take the static equilibrium equation $Ku = f$ and differentiate it with respect to the physical densities $\bar{\rho}_j$, obtaining:

$$\frac{\partial K}{\partial \bar{\rho}_j} u + K \frac{\partial u}{\partial \bar{\rho}_j} = 0 \iff \frac{\partial u}{\partial \bar{\rho}_j} = -K^{-1} \frac{\partial K}{\partial \bar{\rho}_j} u, \quad (2.29)$$

where

$$\frac{\partial K}{\partial \bar{\rho}_j} = (E_0 - E_{min}) p \bar{\rho}_j^{p-1} K_{e,j}. \quad (2.30)$$

Equation 2.30 represent the well-known first-derivative term of the global stiffness matrix K with respect to the physical densities $\bar{\rho}_j$ when using Solid Isotropic Material with Penalization Method (SIMP) material scheme [1]. We obtain the last term:

$$\frac{\partial u}{\partial \bar{\rho}_j} = -K^{-1} \left((E_0 - E_{min}) p \bar{\rho}_j^{p-1} K_{e,j} \right) u. \quad (2.31)$$

1. Bendsøe et al. (2004), 'Topology Optimization'

Combining Eq. 2.23, Eq. 2.24, Eq. 2.28, and Eq. 2.31, we finally obtain:

$$\frac{\partial G_{KS}^L}{\partial \bar{\rho}_j} = \left(\frac{\sigma_{VM,j}}{\sigma_L} - 1 \right) \frac{e^{P\bar{g}_j}}{\sum_k e^{P\bar{g}_k}} - K^{-1} \frac{\partial G}{\partial u} \left(\frac{\partial K}{\partial \bar{\rho}_j} \right) u. \quad (2.32)$$

2: More information about the adjoint method used to analytically calculate the first-order derivatives can be found on the Martins *et al.* book [2].

To avoid the explicit calculation of K^{-1} we use the *adjoint method*². Here is the linear system that, once solved, permits to calculate ψ :

$$K\psi = \frac{\partial G}{\partial u} \iff \psi = K^{-1} \frac{\partial G}{\partial u}. \quad (2.33)$$

This formula is called *adjoint equation*. This equation is solved for ψ and the result used to evaluate:

$$\frac{\partial G_{KS}^L}{\partial \bar{\rho}_j} = \left(\frac{\sigma_{VM,j}}{\sigma_L} - 1 \right) \frac{e^{P\bar{g}_j}}{\sum_k e^{P\bar{g}_k}} - \psi \left(\frac{\partial K}{\partial \bar{\rho}_j} \right) u. \quad (2.34)$$

Solving linear system 2.33 instead of directly calculating the inverse matrix of K is more efficient from a performance perspective. The cost of solving a system using the Cholesky decomposition is $\mathcal{O}(N^3/3)$, while a matrix inversion is $\mathcal{O}(N^3)$.

where N represents the size of the square matrix describing the linear system. Equation 2.34 represents the first-order derivative equation used to evaluate the sensitivity of the constraint function G_{KS}^L with respect to the physical densities $\bar{\rho}$. The value of ψ is calculated every iteration solving the linear system 2.33.

2.1.2. TRUSS TOPOLOGY OPTIMIZATION (TTO) MINIMUM VOLUME FORMULATION

We are now shifting our focus from continuous structures to discrete truss systems, describing the Truss Topology Optimization (TTO) (also known in early literature as layout optimization), a structure optimization method that focuses on discrete structures. In his most used formulation, TTO aims at reducing structural volume while meeting stress criteria using a Simultaneous Analysis and Design (SAND) approach. The problem is already well-posed for the comparison with continuous discretization.

OBJECTIVE AND CONSTRAINT FUNCTIONS The goal of the optimization is to minimize the volume occupied by a structure under a specified load case. For a truss structure, we can write:

$$V = \ell^T a \quad (2.35)$$

in which $\ell = [\ell_1, \ell_2, \dots, \ell_{Nel}]^T$ is the length vector of the member of the ground structure. The volume fraction is evaluated as the ratio $V_f = \frac{V}{V_0}$, where V_0 represents the total volume of the design domain Ω .

As the volume minimization problem is stated using the SAND approach, both the members' cross-sectional areas a and member

forces \mathbf{q} are design variables of the problem. For that reason, the stress constraints in tension and compression ($g_{st,t}$ and $g_{st,c}$) can be trivially written as:

$$-\sigma_c \mathbf{a} \leq \mathbf{q} \leq \sigma_t \mathbf{a} \quad (2.36)$$

in which σ_c and σ_t are the compressive and tensile maximum allowable stresses of the material.

MINIMUM VOLUME FORMULATION We recall the full volume minimization formulation here, stated in terms of members' cross-sectional areas \mathbf{a} and member forces \mathbf{q} as follows:

$$\begin{aligned} \min_{\mathbf{a}, \mathbf{q}} \quad & V = \tilde{\ell}^T \mathbf{a} \quad (\text{Volume minimization}) \\ \text{s.t.} \quad & \mathbf{B}\mathbf{q} = \mathbf{f} \quad (g_{eq}) \\ & -\sigma_c \mathbf{a} \leq \mathbf{q} \leq \sigma_t \mathbf{a} \quad (g_{st,c}, g_{st,t}) \\ & \mathbf{a} \geq 0, \end{aligned} \quad (\mathbb{P}_0)$$

where $\tilde{\ell} = [\ell_1 + s, \ell_2 + s, \dots, \ell_{Nel} + s]^T$ is called augmented member length and s the joint cost, used to penalize the appearance of small members [92]. The listing and explanation of the other parameters is given in Section 1.2.3. This formulation takes into account only the linear behavior of the structure and is equivalent to the original and well-studied member force formulation [1, 31].

It is worth listing the key distinctions of the TTO formulation compared to the density-based topology optimization formulation described earlier in this chapter. Firstly, the TTO problem is formulated using the SAND approach, in which the equations of structural mechanics are treated as constraints in the optimization. Unlike NAND approaches, these equations are not explicitly solved. Consequently, concerns about the singularity of the stiffness matrix \mathbf{K} are avoided, and bars can potentially vanish from the structure during the optimization ($\mathbf{a} = 0$). Secondly, the TTO problem is expressed in terms of members' cross-sectional areas \mathbf{a} and member forces \mathbf{q} with a plastic material model, disregarding kinematic compatibility to formulate a Linear Programming (LP) problem. Due to its linearity, this optimization problem is convex, ensuring that the solutions found are global optima. Moreover, the linear nature of the formulation \mathbb{P}_0 makes it computationally efficient, even with a large number of design variables, when employing modern interior point optimizers. However, the SAND formulation with a plastic material model accurately predicts the mechanical behavior of only statically determinate structures or mechanisms [78, 79]. When dealing with more complex structures, such as those that are statically indeterminate due to symmetry or multiple load cases, explicit consideration of the linear kinematic constraints is necessary, leading to a loss of the linear property of the formulation.

92. Parkes (1975), 'Joints in optimum frameworks'

1. Bendsøe et al. (2004), 'Topology Optimization'

31. Dorn et al. (1964), 'Automatic design of optimal structures'

78. Kirsch (1989), 'Optimal topologies of truss structures'

79. Rozvany et al. (1995), 'Layout Optimization of Structures'

2.2. COMPARISON BETWEEN DENSITY-BASED TOPOLOGY OPTIMIZATION AND TTO

In the upcoming discussion, we will be comparing the optimized structures obtained using the density-based topology optimization and the TTO optimization algorithms. Our primary objective in this comparison is to choose the most appropriate method for our study by understanding the application limits inherent in these two structural discretization methods. If, indeed, we identify such limitations, the aim is to discern and define them. Such discussions have already been briefly addressed in the literature [35, 168], but treating the problem without providing numerical results as a basis for making the choice.

Since our interest is in ultralight structures, we are willing to compare the results of both optimization methods when dealing with different volume fractions on a common load case. The volume minimization formulation with stress constraints we use cannot, however, directly control the volume of the optimized structure. For that reason, we decided to adjust the material strength σ_L to influence the volume fraction of the optimized structure i.e. employing more resistant material results in a lower volume fraction and *vice versa*. For this comparative analysis, we have selected three key performance metrics: the volume fraction V_f , the structural compliance C , and the maximum material allowable – or strength σ_L . Among these, we classify stress limit as the active metric used to influence the optimization, while volume and compliance are the objective of the optimization and a passive metric, respectively. In addition to the aforementioned performance metrics, we will also track the execution time of the algorithms.

2.2.1. DEFINITION OF A TEST CASE FOR THE COMPARISON

The L-shape beam is one of the most used load case benchmarks for stress-based topology optimization [160, 161]. This choice is driven by the distinctive geometry of the problem, which generates a stress concentration at the sharp corner in the case of linear elasticity—a phenomenon approaching infinity. Consequently, optimized solutions often feature a large fillet, mitigating the intensity of the stress singularity. The geometric description of the test case is given in Fig. 2.2. The beam with dimensions $L \times L$ presents a fixed support on the nodes in the top part and a load on the right extremity.

To permit the methods' comparison, the design domain Ω is discretized using two distinct meshes: in the continuous case, we employ a mesh consisting of 600×600 quadrilateral elements, totaling 270 000 elements. For this mesh, the load is distributed over multiple elements (5% of L) to avoid local stress concentrations. Additionally, the stress constraints are not evaluated on the corresponding elements, and this

³⁵. Bendsøe (1989), 'Optimal shape design as a material distribution problem'

¹⁶⁸. Watts et al. (2019), 'Simple, accurate surrogate models of the elastic response of three-dimensional open truss micro-architectures with applications to multiscale topology design'

¹⁶⁰. Duysinx et al. (1998), 'Topology optimization of continuum structures with local stress constraints'
¹⁶¹. Le et al. (2010), 'Stress-based topology optimization for continua'

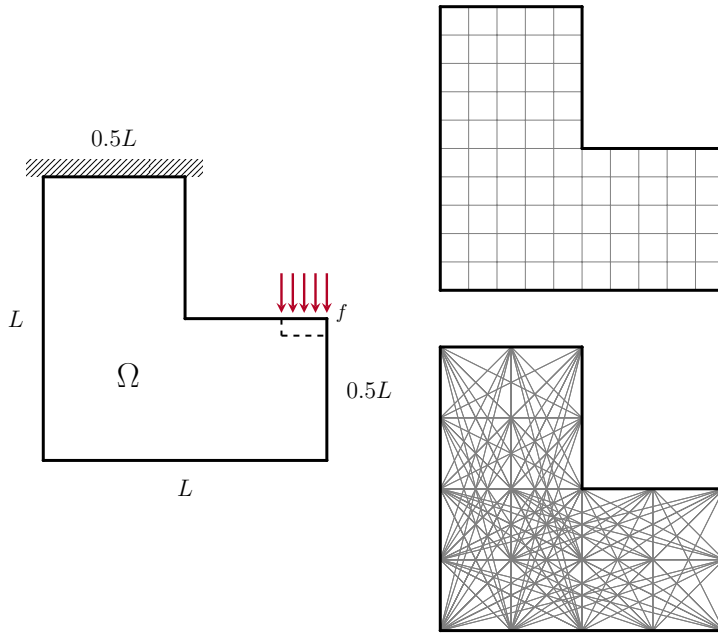


Figure 2.2.: On the left, plot of the L-shape beam test case, on the right the graphical representations of the two discretizations used, the continuous (above) composed of 600×600 quadrilateral elements, and the truss-like (below) discretized using 33×33 nodes and a fully connected ground structure. The images represent a coarser discretization for visual clarity.

zone is considered outside of the design domain Ω . Concerning the truss discretization for the TTO algorithm, we employ a mesh with 33×33 nodes and a fully connected ground structure, comprising a total of 305 728 candidates. The load is applied only on one single node.

We employ the same isotropic material and structure dimensions for the two optimizations, and the complete data is resumed in Table 2.1. The value of the maximum material allowable σ_L is used to control, although not directly, the volume fraction of the solutions. For simplicity, all numeric values are assumed normalized and dimensionless.

2.2.2. NUMERICAL APPLICATION

The density-based topology optimization and the TTO have both been implemented using Python, employing different optimization algorithms. For density-based topology optimization, the chosen optimization algorithm is the Method of Moving Asymptotes (MMA), developed by Svanberg [25]. The parameter called *movelimit*³ is set to 0.1 while the other algorithm's parameters are set to their default value. We chose to filter the density field ρ using the 2D convolution operator [55] and the projection technique based on the *tanh* function [50] precedently described. The radius of the filter is set to $R = 5$ elements. Using the projection Equation 1.5 is not volume conservative for all values of η , and to stay conservative we use a volume-increasing filter [10]. The value of $\eta = 0.4$ is then chosen. A continuation scheme for the projection parameter β is set to increase by one every 200 iterations and starting from 1, the number of maximum iterations is set to 7500, and the stopping criteria is calculated as $\|\Delta x\|_2 / \sqrt{N_e}$ [10] on the absolute difference between two successive iterations of the physical densities $\bar{\rho}$, and it is set to 10^{-4} . The aggregation parameter P

Parameter	Value
E	1
ν	0.3
L	100
σ_L	[0.20, 20]

Table 2.1.: Material data used for the optimizations. The value of the maximum material allowable σ_L is used as the parameter to generate multiple optimized topologies. The Poisson module is used only in density-based topology optimization.

25. Svanberg (1987), 'The method of moving asymptotes—a new method for structural optimization'

3: More information on the implementation of the *movelimit* parameter can be found on the paper by Verbart [159].

55. Sigmund (2007), 'Morphology-based black and white filters for topology optimization'

50. Wang et al. (2011), 'On projection methods, convergence and robust formulations in topology optimization'

Equation 1.5 reads:

$$\bar{\bar{\rho}}_j = \frac{\tanh(\beta\eta) + \tanh(\beta(\bar{\rho}_j - \eta))}{\tanh(\beta\eta) + \tanh(\beta(1 - \eta))}.$$

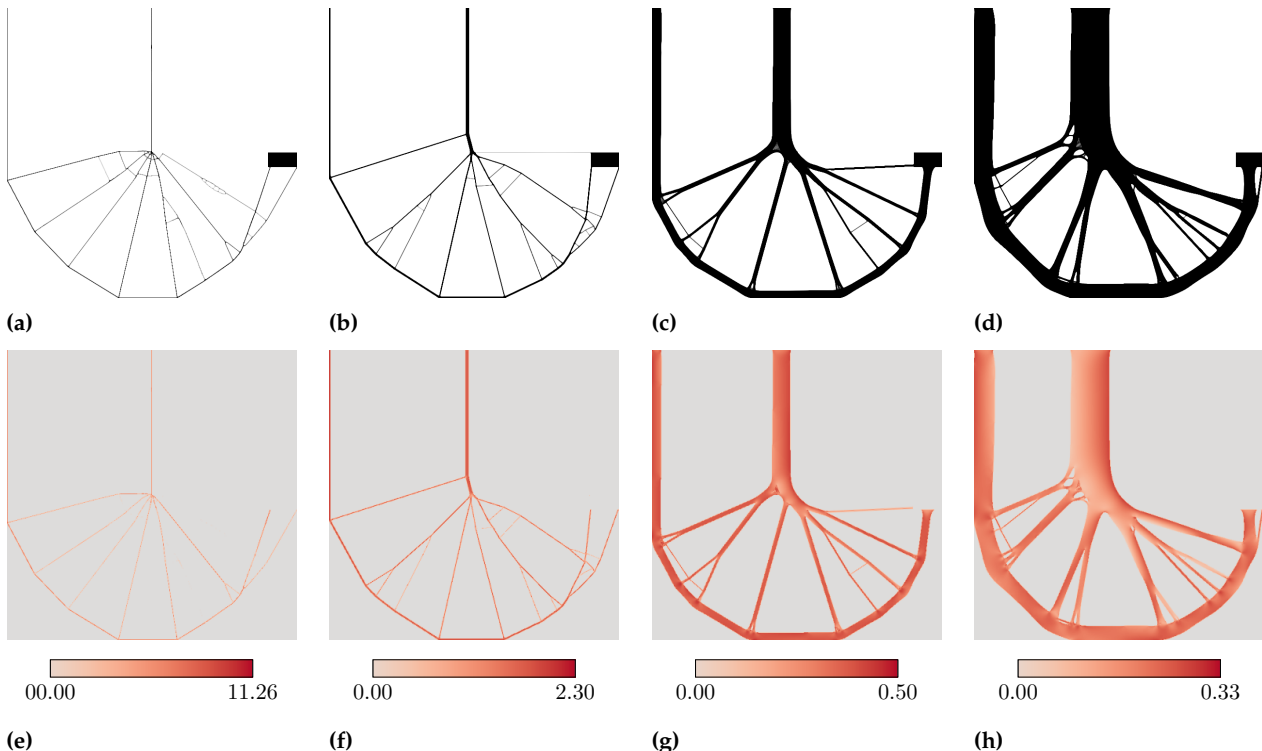


Figure 2.3.: (a-d) Topology of the optimized structures for different values of the material allowable $\sigma_L = 10.00, 2.00, 0.40$, and 0.25 , showing a volume fraction of $V_f = 1.60\%, 4.04\%, 18.03\%$ and 34.71% , respectively. **(e-h)** Von Mises stress distribution for the optimized structures.

10. Ferrari et al. (2020), 'A new generation 99 line Matlab code for compliance topology optimization and its extension to 3D'

169. Johnson (2007), 'The NLOpt nonlinear-optimization package'

170. Diamond et al. (2016), 'CVXPY: A Python-Embedded Modeling Language for Convex Optimization'

171. Domahidi et al. (2013), 'ECOS: An SOCP solver for embedded systems'

of the aggregation function G_{KS}^L is set to 32. The SIMP parameters of Equation 1.2 are set to $E_0 = 1$, and $E_{min} = 10^{-9}$. The value of the penalization parameter p is selected as $p = 3$. The optimization is carried out using the NLOpt Python optimization package [169], analytically evaluating the sensitivity using Equations 2.15, and 2.23.

The volume minimization TTO problem as formulated in \mathbb{P}_0 represents a LP problem that can be efficiently solved by contemporary optimization algorithms. In this work, we used the Python package CVXPY 1.2.2 [170] with the ECOS 2.0.7 [171] solver. The joint cost s is set to 0.001 and the stopping criterion is chosen as $\|\Delta x\|_\infty \leq 10^{-8}$. As the formulation is linear, no sensitivity calculation is carried out.

The optimizations presented in this section are performed using a single core on a cluster equipped with an Intel® Xeon® CPU E5-2650 @ 2.20 GHz and using 8 GB of RAM.

DENSITY-BASED TOPOLOGY OPTIMIZATION RESULTS We generate multiple optimized structures with different volume fractions V_f by launching the optimization code for continuous mesh with different values of the material allowable σ_L spanning from 0.2 to 20.

The results obtained for $\sigma_L = 10.00, 2.00, 0.40$ and 0.25 are shown in

Fig. 2.3. In the upper part of the figure (a-d), we see the topology of the optimized structures with an increasing volume fraction V_f . Interestingly, the topology of the solution remains almost unchanged, varying principally in the thickness of its members. We notice the classic large fillet around the corner that alleviates the local stress concentration. As the volume decreases, the optimized structure tends to a solution that resembles a truss-like structure, with a reducing fillet radius. In those cases, we know that the density-based topology optimization algorithm acts as a method for the layout of truss-like structures [5]. This effect is caused by the combination of different factors, such as the regularization filter, the mesh size, and the low volume fraction [66].

A summary of the numerical results is presented in Table 2.2. Firstly, we can observe how we successfully controlled the volume fraction V_f by modifying the material resistance σ_L , obtaining results that perfectly follow a monotonically decreasing function. Additionally, as expected, a more voluminous solution also exhibits a lower value of structural compliance. Next, we notice that the optimization processes exhibit long execution times, especially when dealing with extreme cases like low-material resistance and high-volume fractions. This effect is caused by the very fine mesh used to discretize the design domain Ω , the sensitivity calculation using the adjoint method, and the increasing difficulty of satisfying the stress constraints. Furthermore, it is observed that the maximum stress exceeds the material allowable σ_L . This is because we are employing an aggregation function for the stress constraints that estimates the maximum value of the constraint across a group of elements. However, these aggregation methods do not perfectly align with the exact maximum value, which is a recognized limitation.

On top of volume fraction, compliance, and stress, we evaluate an additional metric specific to continuous meshes called the *greyness level* or *measure of non-discreteness* [55] to evaluate the quality of the solutions. It is defined as:

$$M_{nd} = \frac{\sum_e 4\bar{\rho}_e(1 - \bar{\rho}_e)}{n} \times 100\%, \quad (2.37)$$

where results near zero mean a completely black-and-white design. Observing the M_{nd} values in Table 2.2, we notice that all the optimized structures converged to nearly black-and-white solutions, confirming the correct numerical implementation of the problem.

In the lower part of Fig. 2.3 (e-f), we plot the equivalent Von Mises stress for every element of the solution with physical density $\bar{\rho} > 0.5$. Multiple interesting observations can be made. First, we notice that the stress distribution is almost uniform in the structure, and it tends to the value of the material allowable σ_L – i.e. we approach a *fully stressed*

5. Bendsøe et al. (1988), 'Generating optimal topologies in structural design using a homogenization method'

66. Sigmund et al. (2016), 'On the (non-)optimality of Michell structures'

55. Sigmund (2007), 'Morphology-based black and white filters for topology optimization'

Table 2.2.: Numerical results of the topology optimization method of the L-shape beam load case with varying material allowable σ_L on a 600×600 elements mesh. Numbers in red highlight the results that have not converged.

σ_L	max σ_L	V_f	C	M_{nd}	It.	Time
20.00	23.51	1.18 %	6992	1.91 %	1142	8 h 11 m
10.00	11.26	1.60 %	3837	2.19 %	1147	7 h 55 m
8.00	8.78	1.74 %	2766	1.95 %	792	5 h 39 m
6.00	7.15	1.89 %	2243	1.81 %	806	5 h 35 m
5.00	5.81	2.17 %	1823	1.81 %	849	5 h 53 m
4.00	4.69	2.67 %	1424	2.02 %	894	6 h 12 m
3.00	3.47	3.00 %	1133	1.64 %	993	6 h 45 m
2.00	2.30	4.04 %	781	1.45 %	1189	8 h 20 m
1.00	1.18	7.28 %	404	1.35 %	1621	11 h 41 m
0.90	1.06	8.09 %	365	1.31 %	1656	11 h 36 m
0.80	0.96	8.82 %	332	1.21 %	1937	15 h 21 m
0.70	0.84	10.05 %	292	1.09 %	1827	13 h 21 m
0.60	0.73	11.80 %	250	1.19 %	1955	14 h 21 m
0.50	0.61	14.18 %	213	1.06 %	2032	15 h 39 m
0.40	0.50	18.03 %	170	1.08 %	2259	17 h 6 m
0.35	0.44	21.12 %	148	1.15 %	2421	19 h 29 m
0.30	0.38	26.21 %	126	1.50 %	3100	24 h 46 m
0.25	0.33	34.71 %	104	1.04 %	3484	27 h 39 m
0.20	0.27	48.08 %	77	1.26 %	7500	91 h 46 m

Michell theorized two criteria for optimal truss structures [84] valid when the maximum allowable stress is equal in tension and compression ($\sigma_t = \sigma_c$) and when the supports of the structure are statically determinate. The first one states that all the members of an optimal structure should present internal stress equal in magnitude to the maximum allowable value of the material – i.e. the structure is *fully stressed*. The second criterion asserts that the strain of all the members of the structure should be equal and there should be no other point having a strain higher than this value.

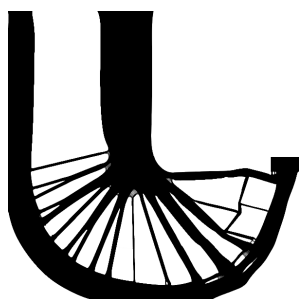


Figure 2.4.: The intermediate resulting structure for $\sigma_L = 0.2$ with $V_f = 48.08\%$ after 7500 optimization iterations.

structure. Even if the geometric support of the theory is different, it looks like the topology-optimized structures follow the Michell criteria presented in Section 1.2.3 for optimal truss structures.

As previously mentioned, our focus lies in exploring the method's limits, particularly at the volume fraction boundaries. When dealing with low-resistance materials – i.e. materials that show a low σ_L , we encounter a scenario where no solution can be attained since no distribution can fulfill the imposed constraints. Throughout our research with this specific test case and mesh size, we did not produce any solutions with a volume fraction exceeding 50%, suggesting we have encountered a limitation of the problem. With this combination of material properties, loading conditions, geometry, and mesh, it appears that there is no feasible solution for $V_f > 50\%$. We notice that the calculation time has significantly increased with the increase of V_f because the algorithm needs more iterations to converge and faces greater difficulty in satisfying the stress constraints. Fig. 2.4 shows the topology of the non-converged solution with $\sigma_L = 0.2$, $V_f = 48.08\%$ and over five days of optimization.

Conversely, when dealing with excessively strong material – i.e. materials that show a high σ_L , the optimal scenario would demand such minimal material usage that certain sections of the structure become thinner than the width of a single element. In this case, the mesh used for discretization is too coarse to accurately represent the solution, and finer meshing becomes essential to capture the details of the optimized design. Fig. 2.5 shows the limit case when $\sigma_L = 10.0$ and $V_f = 1.60\%$.

Finally, in Fig. 2.6 we show the plots summarizing our results, with

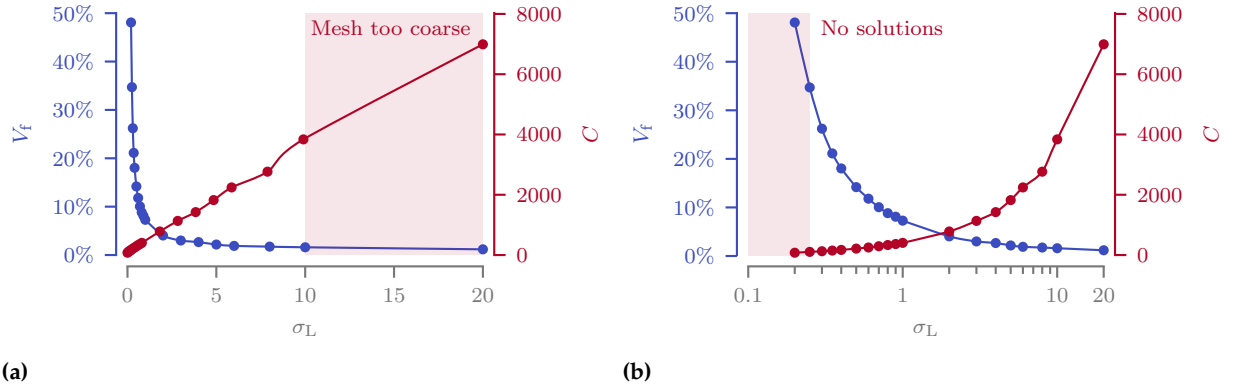


Figure 2.6.: Linear (a) and logarithmic (b) plot of the volume fraction V_f and the compliance C with respect to the maximum material allowable σ_L for the continuous mesh structures. Areas in red represent the zones outside the domains of applicability of the applied method.

the method's limits highlighted. To effectively show the different orders of magnitude present in the plot, we have used both linear and logarithmic scales simultaneously. We notice that the volume fraction V_f follows a hyperbolic relationship, while compliance C exhibits a linear correlation with respect to the material allowable σ_L .

TTO OPTIMIZATION RESULTS In this section, we present the optimized structures of the TTO formulation with different values of the material allowable σ_L spanning from 0.2 to 20. Due to the inherent linearity of Formulation \mathbb{P}_0 , the solutions exhibit several intriguing characteristics. Notably, in cases such as the tested L-shaped test case where the structures are not overconstrained and are not subject to asymmetric stress constraints, the formulation aligns with the Michell criteria. Consequently, the topology remains unchanged regardless of the imposed stress limit, and the stress distribution results in a fully stressed structure. Fig. 2.7 provides a visual representation of the optimized topology and the corresponding stress distribution for the different values of the material allowable σ_L . By examining the figure, it is evident that the node positions are constrained by the initial ground structure. The solution resembles half of a spoked wheel, with an irregular distribution of these spokes. One might expect a more evenly distributed arrangement of these spokes. Interestingly, no fillet is formed at the corner of the L-shaped beam. This observation is attributed to the modeling of truss nodes as frictionless joints that do not support moments. However, this aligns with our earlier findings in density-based topology optimization, where the fillet radius diminishes as the volume fraction decreases. Finally, it is crucial to note that in this simple test case with only a single load case, linear elasticity is inherently considered in the formulation. There is no need to explicitly account for it by imposing kinematic compatibility constraints, as highlighted in previous studies [1, 31, 33].

The following equation consistently holds for the optimized structures,

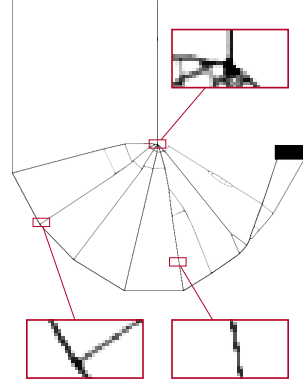


Figure 2.5.: The optimized structure for $\sigma_L = 10.0$ with $V_f = 1.60\%$. Some of the structure's features present not even a fully-dense element in their thickness.

1. Bendsøe et al. (2004), 'Topology Optimization'

31. Dorn et al. (1964), 'Automatic design of optimal structures'

33. Hemp (1973), 'Optimum Structures'

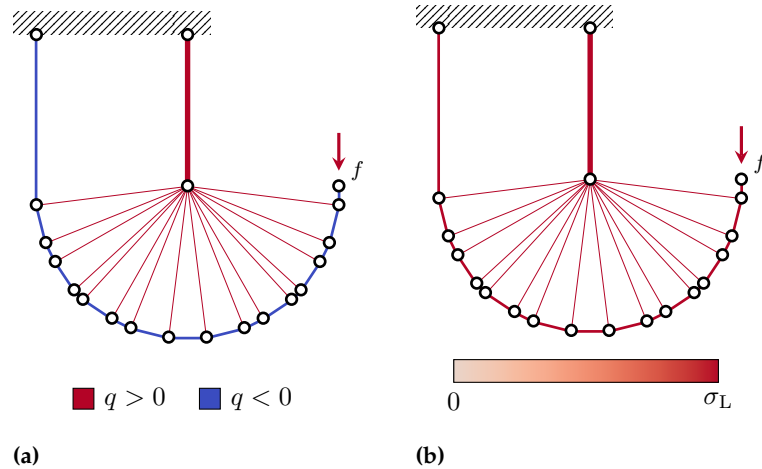


Figure 2.7.: Topology (a) and stress distribution (b) plot for the TTO optimized structure of the L-shape beam test case with varying values of the material allowable σ_L on a 33×33 nodes ground structure. The structure topology is invariant with respect to the value of σ_L .

Table 2.3.: Numerical results of the TTO method of the L-shape beam test case with varying values of the material allowable σ_L on a 33×33 nodes ground structure. Numbers in red highlight the results that lie outside the domains of applicability of the optimization method.

σ_L	V_f	C	Min λ	Time
50.0	0.12 %	23 282	111.7	1 m 6 s
20.0	0.31 %	9313	70.6	1 m 9 s
10.0	0.62 %	4656	49.9	1 m 18 s
8.0	0.78 %	3725	44.7	1 m 15 s
6.0	1.03 %	2794	38.7	1 m 10 s
5.0	1.24 %	2328	35.3	1 m 24 s
4.0	1.55 %	1863	31.6	1 m 18 s
3.0	2.07 %	1397	27.4	1 m 15 s
2.0	3.10 %	931	22.3	1 m 15 s
1.0	6.21 %	466	15.8	1 m 17 s
0.9	6.90 %	419	15.0	1 m 20 s
0.8	7.76 %	373	14.1	1 m 21 s
0.7	8.87 %	326	13.2	1 m 16 s
0.6	10.35 %	279	12.2	1 m 20 s
0.5	12.42 %	233	11.2	1 m 22 s

regardless of the value of σ_L :

$$V^* = \frac{fL}{\sigma_L} \cdot \Gamma, \quad (2.38)$$

172. Lewiński et al. (1994), 'Extended exact solutions for least-weight truss layouts—Part I'

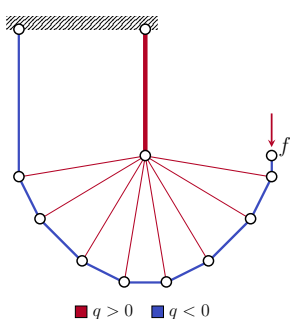


Figure 2.8.: Optimized structure obtained using a fully connected ground structure with 13×13 nodes and 7705 candidates.

where the volume multiplicative constant Γ depends on the load case and the ground structure used to discretize the design space Ω [172]. For this specific test case with the 33×33 nodes ground structure, we found $\Gamma = 4.656$. The execution time of the optimization is approximately 90 s and does not change with respect to the maximum stress σ_L . The full numerical results of the multiple optimizations can be found in Table 2.3.

It's worth noting that we have intentionally opted for a dense ground structure here to achieve an element count roughly equivalent to that of the continuous mesh case (305 728 and 270 000 for the TTO and the density-based topology optimization, respectively). We have utilized a fully connected ground structure with 33×33 nodes, but we obtained satisfactory results with just 13×13 nodes (see Fig. 2.8). In this case, we obtain a volume multiplicative constant $\Gamma = 4.705$,

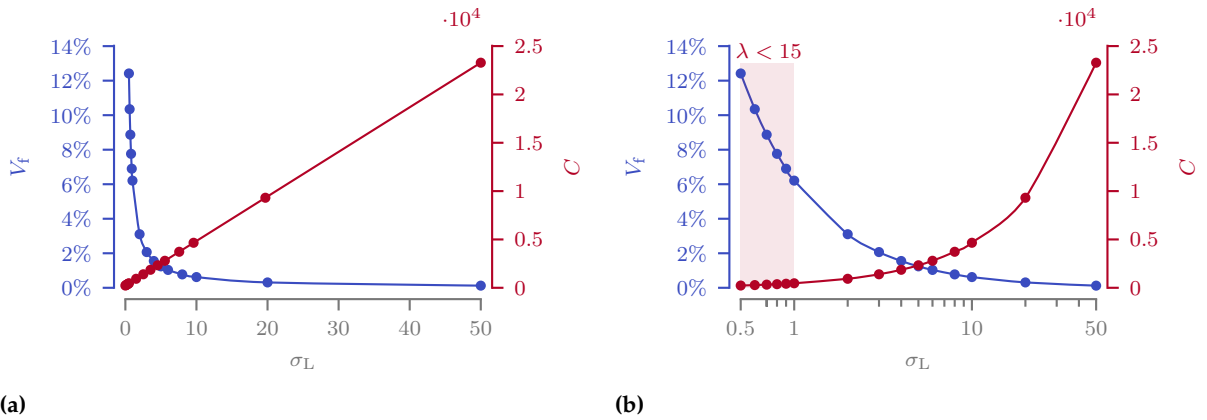


Figure 2.9.: Linear (a) and logarithmic (b) plot of the volume fraction V_f and the compliance C with respect to the value of the maximum material allowable σ_L for the TTO optimized structures. Areas in red represent the zones outside the domains of applicability of the truss discretization.

signifying a 1.05 % increase compared to the 33×33 case with $\Gamma = 4.656$. However, the element number is reduced by 97.4 % (305 728 versus 7705 candidates). The computational time for this simplified test case is below one second.

With this example, we notice that refining the continuous mesh and refining the ground structure are not equivalent operations. In one case, it allows for representing finer details, while in the other, it permits new shapes for the structure. The choice of the ground structure dictates the final form; it is more restrictive than merely allowing finer details. If bars are missing initially, they will not be added later on.

In assessing solution quality, we employ a distinct metric known as the slenderness ratio, denoted as λ , which represents the ratio between the length and the radius of gyration of the bars of the ground structure. In our specific case, we have established a minimum slenderness ratio of 15. For a bar with a circular cross-sectional area, this corresponds to a radius of R_λ for a bar length of $7.5 R_\lambda$. We highlighted in red the optimized structures that do not respect the minimum slenderness ratio in Table 2.3.

Lastly, Fig. 2.9 provides a visual summary of our findings, emphasizing in red the solutions that do not respect the minimum slenderness ratio $\lambda < 15$. To effectively show the different orders of magnitude present in the plot and how already done for the continuous mesh case, we have used both linear and logarithmic scales simultaneously. In this case, the compliance exhibits a perfectly linear relationship with respect to σ_L , while the volume follows a hyperbolic law in accordance with Equation 2.38.

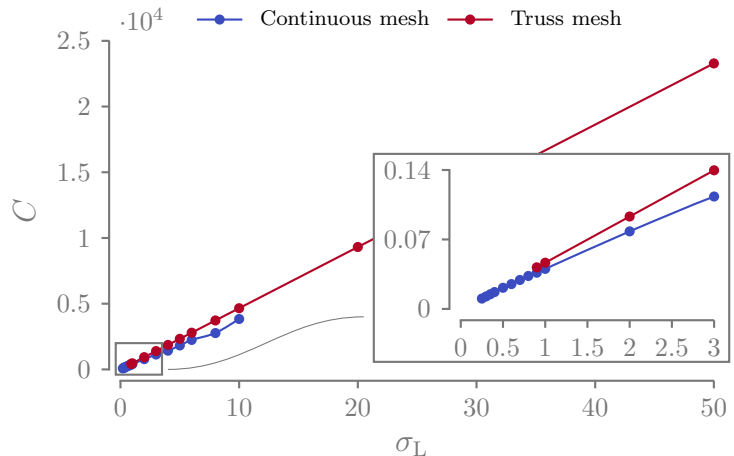


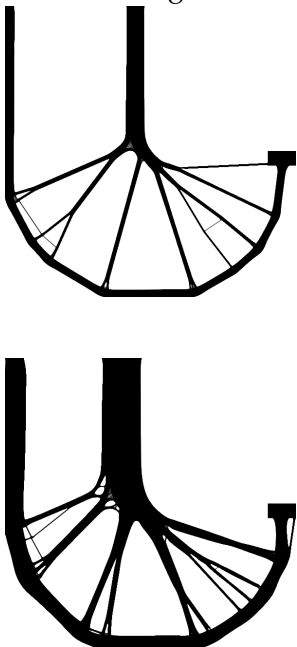
Figure 2.10.: Compliance C versus maximum material allowable σ_L plot for the density-based topology optimization and the TTO algorithms.

2.2.3. DISCUSSION

Up until now, we have discussed the results of the density-based topology optimization and the TTO algorithms separately. Here, we provide a comparative analysis by presenting a series of graphs showcasing the key performance indicators considered for both formulations: the maximum material allowable stress σ_L , the compliance C , the volume fraction V_f , and the computational time t . It is important to note that the data presented in these graphs excludes the values that fall outside the methods' limits, highlighted for the two different algorithms in the previous subsections.

Fig. 2.10 depicts the compliance C versus maximum material allowable σ_L graph for the L-shaped beam test case. It is evident that the truss discretization of TTO consistently exhibits lower compliance values for every considered material allowable and maintains a perfectly linear relationship, in contrast to the continuous discretization approach. We speculate that the difference may be attributed to the more complex formulation (non-linearity, use of the filter, and projection), potentially causing the continuous approach to converge to a local minimum. It is worth noting that the differences between the two methods reduce for small σ_L values.

Recall of Fig. 2.3c and d:



In Fig. 2.11 we plot the different volume fractions obtained for a given material allowable (the axis in the graph are swapped as for us the most important figure of merit is the volume fraction). The density-based topology optimization yields structures that are more massive for a given material resistance. This outcome can be attributed not only to the aforementioned non-linearity in the formulation but also to another intriguing phenomenon. When dealing with high volume fractions (see e.g. Fig. 2.3c and d), we observe that the material that composes the “beams” of the structure is distributed across multiple elements, appearing somewhat “smeared”. In contrast, the truss representation concentrates all the structural mass along the line extending from one node to another, putting the material exactly

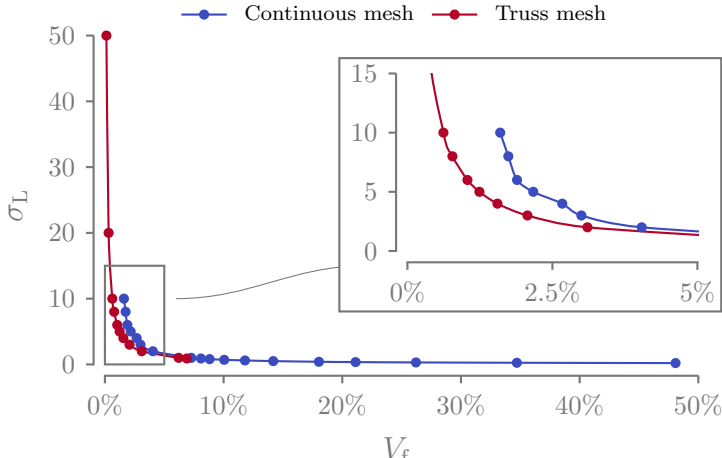


Figure 2.11: Maximum material allowable σ_L versus volume fraction V_f plot for the density-based topology optimization and the TTO algorithms.

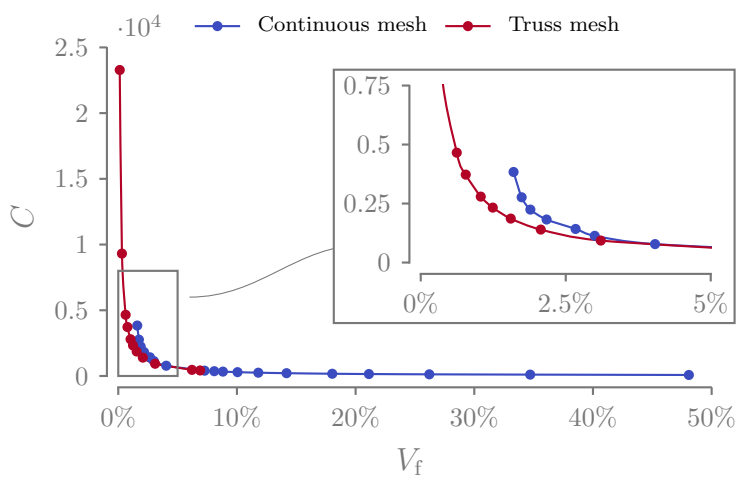


Figure 2.12: Compliance C versus volume fraction V_f plot for the density-based topology optimization and the TTO algorithms.

where needed and being, thus, numerically more efficient. This fact happens because the truss representation is an idealization, and it emphasizes the importance of ensuring that the chosen discretization remains within its applicable domain.

We can also observe that the truss representation serves as the lower limit of the topology optimization. We speculate that improving the convergence of the density-based topology optimization could potentially lead to results approaching those provided by the TTO algorithm. Interestingly, both discretizations follow a similar trend for high-volume fractions, despite the significant disparity in their physical description models. The very same trends can be observed watching the volume-compliance graph of Fig. 2.12.

Finally, in Fig. 2.13 we turn our attention to the computational time comparison between the two optimization methods. It is noteworthy that a consistent three-order of magnitude difference is observed between the two methods (days vs. minutes) for every value of V_f . Additionally, it's worth recalling that for this specific test case, employing an extremely fine ground structure is not always a necessity, as we were able to obtain similar results (slightly more than 1 % volume

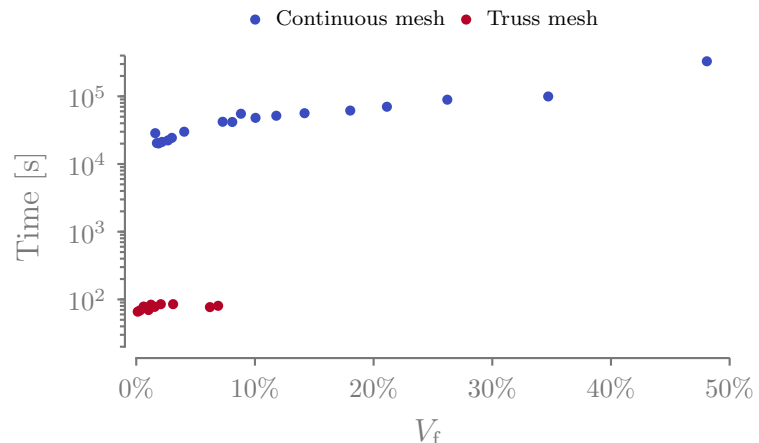


Figure 2.13.: Computational time t versus volume fraction V_f plot for the density-based topology optimization and the TTO algorithms.

difference) with coarser ground structures (97 % fewer bars). This fact implies that the calculation time difference between density-based topology optimization and TTO could potentially be even bigger.

The notable difference in computation time for stress-based density-based topology optimization (which is not self-adjoint, in contrast to compliance minimization) points to the potential for exploring SAND approaches for density-based topology optimization. It's worth mentioning that SAND approaches typically lead to a substantial increase in the number of design variables⁴, but could be beneficial when advanced mechanical constraints are used. In TTO problems, this is less of a concern due to the use of the ground structure approach, which results in numerous cross-sectional area design variables and fewer displacement-related ones. This, however, does not hold when dealing with a continuous mesh. While preliminary studies in this direction have been conducted [173], they lie beyond the scope of this thesis and will not be further investigated.

To sum up, the advantages of the TTO optimization algorithm become evident when considering the limitations of continuous discretization for optimizing ultralight structures. The first key drawback of density-based topology optimization is its increasing need for more elements to correctly discretize low-volume fraction structures, substantially augmenting computational time. Additionally, density-based topology optimization faces several numerical challenges, such as the need for constraint aggregation and relaxation. The optimization formulation proposed in this chapter addresses these problems but introduces another drawback: stress limit in optimized structures often exceed the specified allowable limit. To address this challenge, multiple approaches have been proposed within the aggregation framework to accurately account for the true constraint value, like using a set of active stress constraints [174], several aggregation clusters [175] or rectifier functions [176]. However, all of these strategies come at the cost of increased computation time. Furthermore, stress constraints in continuous discretization are often defined for equivalent von

4: In the SAND approach the displacements \mathbf{u} are no more evaluated using the linear Finite Element Method (FEM) equation $\mathbf{K}\mathbf{u} = \mathbf{f}$, but used as design variables of the optimization.

173. Munro et al. (2017), 'Local stress-constrained and slope-constrained SAND topology optimisation'

174. Bruggi et al. (2012), 'Topology optimization for minimum weight with compliance and stress constraints'

175. París et al. (2010), 'Block aggregation of stress constraints in topology optimization of structures'

176. Norato et al. (2022), 'A maximum-rectifier-function approach to stress-constrained topology optimization'

Mises stress, making it more challenging to distinguish between asymmetric bounds for tension and compression. New failure criteria should then be implemented. Finally, the optimization of ultralight structures naturally tends to result in truss-like topologies regardless of the chosen optimization formulation. These structures are naturally subject to local buckling as a mode of failure [66], a phenomenon that is difficult to describe when using continuous elements.

While truss discretization offers advantages in terms of computational efficiency, it does come with certain limitations. In the minimum volume formulation, the problem is linear and cost-effective to solve. However, the linearity is lost when additional constraints, such as local buckling, are introduced. Moreover, as the FEM equation $\mathbf{K}\mathbf{u} = \mathbf{f}$ is never explicitly solved during the optimization, the SAND formulation does not inherently account for the kinematic compatibility of the displacements and the forces of the problem. This limitation restricts its applicability to relatively simple problems, such as those presented in this chapter, where kinematic compatibility was inherently satisfied. Issues can arise, however, when dealing with complex scenarios involving multiple loads or constraints that may lead to statically indeterminate structures. These limitations are well-known in the literature of TTO and should be taken into account during the optimization if we decide to pursue the development of the optimization algorithm using the TTO framework.

2.3. CONCLUSION

Since the first developments of the topology optimization method, it has been recognized that "For moderately low volume fractions the lay-out of truss-like structures is predicted, but for very low volume fractions it is recommended that the traditional layout theory be employed..." [35]. However, the performance gap has never been quantified, nor has the domain of applicability been assessed. Additionally, it's important to note that these assumptions were primarily based on compliance formulations and not on volume minimization formulations, which are more pertinent to the aeronautical context.

In this chapter, we assessed the suitability of employing the TTO algorithm for the optimization of ultralight structures by quantifying the disparities between density-based topology optimization and TTO under the volume minimization under strength constraints formulation. We introduced a standardized two-dimensional test case, the L-shaped beam, commonly utilized in stress-based optimization scenarios. Multiple optimization runs are conducted for both discretization methods, employing various materials, and the results are subsequently compared, with a primary focus on volume fraction, compliance, stress, and computational time in the optimized structures.

⁶⁶. Sigmund et al. (2016), 'On the (non-)optimality of Michell structures'

³⁵. Bendsøe (1989), 'Optimal shape design as a material distribution problem'

The sensitivity calculation is easier, as the different design variables are not explicitly dependent on each other.

Considering the limitations encountered with the continuous approach, particularly at very low volume fractions, we opted to pursue our optimization algorithm development using the Truss Topology Optimization (TTO) framework. The use of a ground structure to discretize the design space is more coherent with the type of structures we are working on, and the use of the SAND approach permits us to drastically reduce the computational time and take into account additional constraints more easily. We also identified certain limitations inherent to truss discretizations, namely the need to take into account the kinematic compatibility of the structure and the local buckling failure mode, which will be addressed in the following chapter.

ENRICHING THE CLASSIC TTO FORMULATION WITH ADVANCED MECHANICAL CONSTRAINTS

3

Chapter 2 highlighted some inherent limitations of the truss modeling and the conventional optimization formulation of Truss Topology Optimization (TTO). These limitations include the minimum slenderness problem and the absence of local buckling and kinematic compatibility constraints. The primary objective of this chapter is to propose a comprehensive formulation capable of addressing these shortcomings. As we will observe, the resulting formulation, if solved in its original form, tends to yield solutions characterized by numerous active and intersecting bars. To mitigate this, we propose a two-step optimization algorithm that offers a means to reduce the solution complexity. Additionally, we introduce a heuristic designed to reduce the influence of the starting point within this two-step optimization algorithm.

In Section 3.1, we detail and model the various mechanical constraints applied in the context of TTO. Subsequently, in Section 3.2, a comprehensive formulation is presented along with an accompanying optimization algorithm. Through the utilization of this optimization algorithm, we are able to maintain control over the complexity of the design. Finally, in Section 3.3, we put the proposed formulation to the test, applying it to various 2D and 3D test cases sourced from the literature, as well as novel cases. The objective is to assess its capabilities and numerical performance.

3.1. ADVANCED MECHANICAL CONSTRAINTS

This section aims to introduce additional mechanical constraints that will be utilized in this study, to reduce the need for post-processing at the end of the optimization process, just before the manufacturing phase begins. We begin by addressing the issue of minimum slenderness, a side constraint that is imposed on the cross-sectional area of the active members to guarantee that the solution adheres to the truss modeling. Subsequently, we address the local buckling constraints, a critical failure mode observed in ultra-light truss structures. Particular attention is devoted to examining the stability of nodes within what are known as compressive chains. The combination of local buckling and nodal stability, a phenomenon known in the literature as topological buckling, is discussed. Furthermore, as we want our formulation to be as versatile as possible, we explore the extension of these constraints to accommodate multi-load cases. A challenge arises from the fact that the resulting structures are frequently statically indeterminate. To address this, we introduce an additional mechanical constraint

3.1 ADVANCED MECHANICAL CONSTRAINTS	45
3.2 OPTIMIZATION FORMULATION AND SOLVING STRATEGY	50
3.3 NUMERICAL APPLICATION	56
3.4 CONCLUSION	70

Part of the content presented in this chapter has been published [finish](#).

Table 3.1.: Non-exhaustive list of the existing research in Truss Topology Optimization (TTO) with their corresponding scientific contributions.

Authors	Stress	Local Buckling	Topological buckling	Kinematic compatibility	Multi-load cases	Minimum slenderness
Dorn et al. (1964) [31]	x	-	-	-	-	-
Hemp (1973) [33]	x	-	-	-	x	-
Reinschmidt et al. (1974) [177]	x	x	-	~	-	-
Kirsch (1980) [80]	x	-	-	x	-	-
Oberndorfer et al. (1996) [178]	x	x	-	-	-	-
Silva Smith (1997) [179]	x	x	~	-	x	-
Achtziger (1999a, 1999b) [82, 180]	x	x	x	-	x	-
Stolpe (2004) [19]	x	x	-	x	x	-
Pritchard et al. (2005) [181]	x	-	-	-	x	-
Tyas et al. (2006) [182]	x	x	x	-	x	-
Descamps et al. (2014) [183]	x	x	x	-	x	-
Schwarz et al. (2018) [184]	x	x	-	-	-	-
Cai et al. (2022) [185]	x	x	x	-	-	-
Present work	x	x	x	x	x	x

known as "kinematic compatibility" to ensure that the predicted force field aligns with the displacements of the structure.

In Table 3.1, we provide an overview of historical and contemporary research in the field of TTO, along with their respective scientific contributions. This serves to highlight the necessity for a more comprehensive formulation that incorporates these mechanical constraints, reducing the gap between the optimized design and the actual manufactured structure.

3.1.1. MINIMUM SLENDERNESS CONSTRAINTS

As previously discussed in Section 2.2.2, the TTO method shows numerous limitations due to its reliance on the truss model. Therefore, the resulting structures may not be acceptable if the model falls outside the bounds of this idealization. To better study this limit, as outlined in Section 2.2.2, we introduced a metric called bar slenderness, which is defined as follows:

$$\lambda = \frac{\ell}{R_g}, \quad (3.1)$$

where R_g represents the gyration radius of the cross-sectional area, defined as $R_g = \sqrt{I/a_i}$. The primary objective of this section is to introduce an upper limit constraint on the cross-sectional area design variable. This constraint prevents a bar from exceeding the bounds of its idealized model, thereby enhancing the optimization process's robustness.

Remembering that for a circular cross-section $I = \pi r_i^4/4$, we can write

$$R_{g,i} = \frac{r_i}{2}. \quad (3.2)$$

The minimum slenderness limit constraints g_{slend} are then stated as:

$$g_{\text{slend}} := a_i \leq \frac{4\pi\ell_i^2}{\lambda_{\max}}, \quad \forall i \in [1, \dots, N_{\text{el}}] \quad (3.3)$$

for a fixed λ_{\max} . In this thesis we set $\lambda_{\max} = 15$.

3.1.2. LOCAL AND TOPOLOGICAL BUCKLING CONSTRAINTS

Adding local buckling constraints to the optimization formulation is fundamental, as ultralight truss structures are often dominated by this mode of failure [66]. By imposing local buckling constraints over a TTO problem (where the lower bound for the members' cross-sectional areas is 0), the optimization domain becomes disjointed [81]. The solution is to be searched inside a degenerate space of the design space of the optimization, known in the literature as singular optimum [186]. Stolpe [187] showed how using the Simultaneous Analysis and Design (SAND) formulation with local buckling and kinematic compatibility constraints, it is possible to find well-optimized structures without the use of relaxation techniques. The authors, however, point out how the solution is still very sensitive to the initialization point of the Non-Linear Programming (NLP) formulation. The local buckling constraints g_{buck} are stated using Euler's critical load formula as:

$$g_{\text{buck}} := q_i + \frac{s_i a_i^2}{\ell_i^2} \geq 0 \quad \forall i \in [1, \dots, N_{\text{el}}], \quad (3.4)$$

where s_i is a parameter dependent on the member material and section topology as follows:

$$s_i = \pi^2 E \beta_i. \quad (3.5)$$

$\beta_i = I_i/a_i^2$ is a positive constant dependent on the moment of inertia and the section of the i -th bar, and E is Young's modulus of the material. Assuming that the shape of the cross-section is identical over the whole structure and is independent of a , it follows that $\beta_i = \beta$ and $s_i = s$, $\forall i \in [1, \dots, N_{\text{el}}]$.

Direct application of the local buckling constraint g_{buck} in the optimization formulation tends to create "chains" of unstable compressive members [6, 188, 189]. This problem is known in the literature as topological buckling [82], as the definition of the compressive chains is a function of the topology of the structure, and is one of the elements of the nodal stability of the structure. Additional forms of structure instability, such as global buckling [190–193] or the use of lateral perturbing forces to obtain nodal stability [182, 194] have been studied in the literature. However, since they are beyond the scope of this work, they will not be discussed further.

To illustrate the topological buckling phenomenon, we consider the

- 66. Sigmund et al. (2016), 'On the (non-)optimality of Michell structures'
- 81. Cheng (1995), 'Some aspects of truss topology optimization'
- 186. Guo et al. (2001), 'A new approach for the solution of singular optima in truss topology optimization with stress and local buckling constraints'
- 187. Stolpe et al. (2003), 'A note on stress-constrained truss topology optimization'
- 6. Bendsøe (1995), 'Optimization of Structural Topology, Shape, and Material'
- 188. Zhou (1996), 'Difficulties in truss topology optimization with stress and local buckling constraints'
- 189. Rozvany (1996), 'Difficulties in truss topology optimization with stress, local buckling and system stability constraints'
- 82. Achtziger (1999), 'Local stability of trusses in the context of topology optimization Part I'
- 190. Ben-Tal et al. (2000), 'Optimal Design of Trusses Under a Nonconvex Global Buckling Constraint'
- 191. Kočvara (2002), 'On the modelling and solving of the truss design problem with global stability constraints'
- 192. Neves et al. (1995), 'Generalized topology design of structures with a buckling load criterion'
- 193. Ferrari et al. (2021), 'Topology optimization with linearized buckling criteria in 250 lines of Matlab'
- 182. Tyas et al. (2006), 'Practical plastic layout optimization of trusses incorporating stability considerations'
- 194. Mela (2014), 'Resolving issues with member buckling in truss topology optimization using a mixed variable approach'

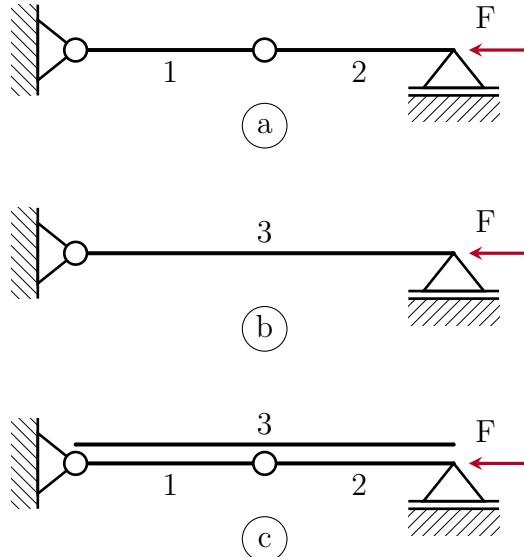


Figure 3.1. The three ground structures loaded in compression are used to highlight the topological buckling problem in TTO. (a) Two-bar ground structure loaded in compression; (b) single bar ground structure; (c) overlap of the *a* and *b* ground structures.

case shown in Fig. 3.1a. It consists of a ground structure with $M = 3$ nodes and $N_{\text{el}} = 2$ bars with length $\ell_1 = \ell_2 = \ell$, and a compressive load of magnitude F applied at the right-hand side node. For this trivial structure, we can state that $q_1 = q_2 = F$ and thus $a_1 = a_2 = a$. We suppose here that the allowables of the material are such that the local buckling (and not the stress) is the most limiting failure criterion for the bars. Assuming that the shape of the section is equal, the local buckling constraints are written as:

$$q_i \geq -\frac{sa^2}{\ell^2}, \quad i \in [1, 2]. \quad (3.6)$$

However, the structure is unstable because the vertical force equilibrium equation evaluated on the central hinge is satisfied only in an ideal case where no structural imperfections are taken into account.

If the hinge between bars 1 and 2 is deleted, we obtain the structure pictured in Fig. 3.1b with $\ell_3 = 2\ell$. The local buckling constraints for bar 3 are thus:

$$q_3 \geq -\frac{sa_3^2}{(2\ell)^2}. \quad (3.7)$$

Combining Equations 3.6, 3.7 and observing that $q_1 = q_2 = q_3 = F$, it is now trivial to demonstrate that $a_3 = 2a$. Constraint 3.7 leads, then, to more voluminous structures compared to constraint 3.6. For that reason, even if we consider the ground structure given in Fig. 3.1c composed by the superposition of the ground structures given in Fig. 3.1a and Fig. 3.1b, the optimization with a uniform initialization tends to converge to the solution $a^* = [a, a, 0]$, unstable but lighter than the physical solution $a_p^* = [0, 0, 2a]$.

The easiest way to get rid of the instability of the compressive chains is to post-process the optimized structure and remove the unstable

hinges between the compressive bars. Doing that, the local buckling constraints are not satisfied anymore as the effective buckling length has increased. It is, then, necessary to calculate the section of the new compressive bars to comply with the newly introduced buckling constraints. As extensively shown by Achtziger [180], this post-processing phase leads to structures that are less optimal compared to the ones we could obtain if we take into account the topological buckling in the optimization in the first place.

For that reason, Achtziger proposes an update strategy to modify the length used to evaluate the critical buckling force of 3.4 as follows:

$$\ell_i^*(\boldsymbol{a}) := \begin{cases} \ell_i & \text{if } i \notin \mathcal{C}_{l,r}(\boldsymbol{a}) \\ \sum \ell_r \mid r \in \mathcal{C}_{l,r}(\boldsymbol{a}) & \text{otherwise,} \end{cases} \quad (3.8)$$

where r represents the r -th bar of the l -th compression chain of the structure. The topology-dependent set $\mathcal{C}_{l,r}(\boldsymbol{a})$ is defined as the set of r member indexes of the l -th buckling chain. As internal forces on buckling chains are constant, only the buckling length of the first member of the chain ($\ell_i^*(\boldsymbol{a})$ with $i \in \mathcal{C}_{l,1}(\boldsymbol{a})$) is modified. Additionally, we add the following side constraints on the other members of the l -th chain to ensure feasibility:

$$a_r \geq a_{r=1} \quad r \in \mathcal{C}_{l,r}(\boldsymbol{a}), \quad \forall r \neq 1. \quad (3.9)$$

3.1.3. KINEMATIC COMPATIBILITY CONSTRAINTS

To optimize test cases that result in statically indeterminate structures, such as structures loaded with multiple load cases or imposed symmetries, we add an additional mechanical constraint called kinematic compatibility [78, 79]. Compatibility can be imposed as a nonlinear constraint in the optimization formulation [80], or can be taken into account by prestressing the initial structure [195].

The kinematic compatibility constraints restrict the displacement field $\boldsymbol{U} = [U_1, \dots, U_{N_{\text{dof}}}]^T$ in such a way that strains ε_i and internal stresses σ_i comply with Hooke's law $\sigma_i = E_i \varepsilon_i$ with $i \in [1, \dots, N_{\text{el}}]$. Recalling that in a truss the relationship between nodal displacements and member deformations is $\boldsymbol{b}_i^T \boldsymbol{U} = \ell_i \varepsilon_i$ with \boldsymbol{b} as the i -th column of the \boldsymbol{B} matrix, we can formulate the kinematic compatibility constraints $\boldsymbol{g}_{\text{comp}}$ as:

$$\boldsymbol{g}_{\text{comp}} := q_i - \frac{a_i E_i}{\ell_i} \boldsymbol{b}_i^T \boldsymbol{U} = 0 \quad \forall i \in [1, \dots, N_{\text{el}}]. \quad (3.10)$$

Kinematic compatibility constraints are non-linear as the design variable \boldsymbol{q} is dependent on \boldsymbol{a} and \boldsymbol{U} .

¹⁸⁰. Achtziger (1999), 'Local stability of trusses in the context of topology optimization Part II'

⁷⁸. Kirsch (1989), 'Optimal topologies of truss structures'

⁷⁹. Rozvany et al. (1995), 'Layout Optimization of Structures'

⁸⁰. Kirsch (1980), 'Optimal design of trusses by approximate compatibility'

¹⁹⁵. Kirsch (1989), 'Effect of Compatibility and Prestressing on Optimized Trusses'

3.2. OPTIMIZATION FORMULATION AND SOLVING STRATEGY

In this section, we propose an innovative TTO formulation developed specifically to minimize the mass of 3D ultralight truss structures, taking into account maximum stress, topological buckling, kinematic compatibility, and minimum slenderness constraints. Combining Formulation \mathbb{P}_0 with Equations 3.4, 3.3, 3.8, 3.9, and 3.10, Formulation \mathbb{P}_1 is stated in terms of members' cross-sectional area \mathbf{a} , member forces \mathbf{q} and nodal displacements \mathbf{U} as follows:

$$\begin{aligned} \min_{\mathbf{a}, \mathbf{q}^0, \dots, \mathbf{q}^{N_p}, \mathbf{U}^0, \dots, \mathbf{U}^{N_p}} \quad & V = \ell^T \mathbf{a} \\ \text{s.t.} \quad & \mathbf{B}\mathbf{q}^p = \mathbf{f}^p \quad \forall p \in [0, \dots, N_p] \\ & \mathbf{q}^p = \frac{\mathbf{a}\mathbf{E}}{\ell} \mathbf{b}^T \mathbf{U}^p \quad \forall p \in [0, \dots, N_p] \\ & \mathbf{q}^p \geq -\frac{s\mathbf{a}^2}{\ell^{*2}} \quad \forall p \in [0, \dots, N_p] \\ & -\sigma_c \mathbf{a} \leq \mathbf{q}^p \leq \sigma_t \mathbf{a} \quad \forall p \in [0, \dots, N_p] \\ & a_r \geq a_{r=1} \quad r \in \mathcal{C}_{l,r}(\mathbf{a}) \\ & 0 \leq \mathbf{a} \leq \frac{4\pi\ell^2}{\lambda_{\max}}. \end{aligned} \quad (\mathbb{P}_1)$$

The formulation has been extended to multiple load cases given by N_p external loads vector $\mathbf{f}^0, \dots, \mathbf{f}^{N_p}$ and the resulting internal forces $\mathbf{q} = [\mathbf{q}^0, \dots, \mathbf{q}^{N_p}]$ and displacements $\mathbf{U} = [\mathbf{U}^0, \dots, \mathbf{U}^{N_p}]$. This proposed formulation expands the multiple load cases formulation of Achitziger [82] with kinematic compatibility constraints, permitting the correct evaluation of the mechanical state of statically indeterminate structures.

82. Achitziger (1999), 'Local stability of trusses in the context of topology optimization Part I'

34. Sankaranarayanan et al. (1994), 'Truss topology optimization with simultaneous analysis and design'

The formulation follows the SAND approach [34], where, in addition to the members' cross-sectional area \mathbf{a} , the member forces \mathbf{q} and the structure displacements \mathbf{U} are used as state variables. One of the advantages of SAND approach is that the state variables are independent of each other and, thus, the sensitivity calculation of the constraints functions is usually simpler and leads to sparse partial derivatives. Additionally, compared to Nested Analysis and Design (NAND) formulations, the problem stays well-posed even if the cross-sectional area goes to 0. As the linear system $\mathbf{K}\mathbf{U} = \mathbf{f}$ is never explicitly solved during the optimization, it is not necessary to impose a lower bound on the members' cross-sectional area \mathbf{a} to avoid a singular stiffness matrix. The last important advantage is that thanks to \mathbf{U} being design variables, it is trivial to add bound constraints on the nodal displacements of the structure if needed.

3.2.1. OPTIMIZATION STRATEGY

Formulation \mathbb{P}_1 presents multiple constraints and design variables for every physical bar of the ground structure. The quantity of constraints creates a highly multimodal problem and it proved to be hard for the optimizer to bring to zero the value of the cross-sectional areas. If a NLP optimizer is directly used on Formulation \mathbb{P}_1 , the resulting structure will be composed of a multitude of intersecting bars. The optimizer is, thus, working like it is performing sizing optimization instead of topology optimization—i.e. in the final design all the members of the ground structure are active.

Inspired by the early works by Reinschmidt [177], we propose a novel two-step optimization strategy in which a first optimization solving a relaxed formulation is used to find a good starting point for the second optimization, solving the full Formulation \mathbb{P}_1 . Doing that way, the first optimization explores extensively the relaxed and more regular design space and finds simpler structures, while the second optimization refines the solution imposing additional mechanical constraints. The complete solving strategy is graphically presented in Fig. 3.2.

¹⁷⁷ Reinschmidt et al. (1974), 'Applications of linear programming in structural layout and optimization'

In the first step, Problem \mathbb{P}_1 is relaxed: kinematic compatibility constraints are omitted. We call this relaxed Problem \mathbb{P}_2 . Problem \mathbb{P}_2 is solved using a Sequential Linear Programming (SLP) method by iteratively linearizing the local buckling constraints. A heuristic strategy called Reinitialization is iteratively used to reduce the influence of the starting point a_0 . The resulting structure described by the design variables vector \tilde{x}^* is then post-processed, removing the members whose optimized area is below a fixed cross-sectional area threshold value. The structures generated by solving the relaxed Problem \mathbb{P}_2 proved to be simpler i.e. fewer active members compared to directly solving \mathbb{P}_1 with a NLP optimizer. If the solution is not statically indeterminate the optimization is completed as the kinematic compatibility constraints 3.10 are automatically satisfied and, thus, used to evaluate the optimal displacements.

Otherwise, a second step is needed. Firstly, the ground structure of the problem is simplified, removing all the members that do not appear in the solution of the relaxed Problem \mathbb{P}_2 i.e. avoiding the reintroduction of members discarded by the SLP step. Then, the kinematic compatibility and the exact local buckling constraints are restored, and Problem \mathbb{P}_1 is solved in its original form on the simplified ground structure using a NLP optimizer. The initial values for the cross-sectional areas are the solution \tilde{x}^* of Problem \mathbb{P}_2 .

3.2.2. FIRST STEP: SLP OPTIMIZATION

The first step of the proposed optimization strategy is here described in detail. The relaxed Problem \mathbb{P}_2 obtained by omitting 3.10 and the

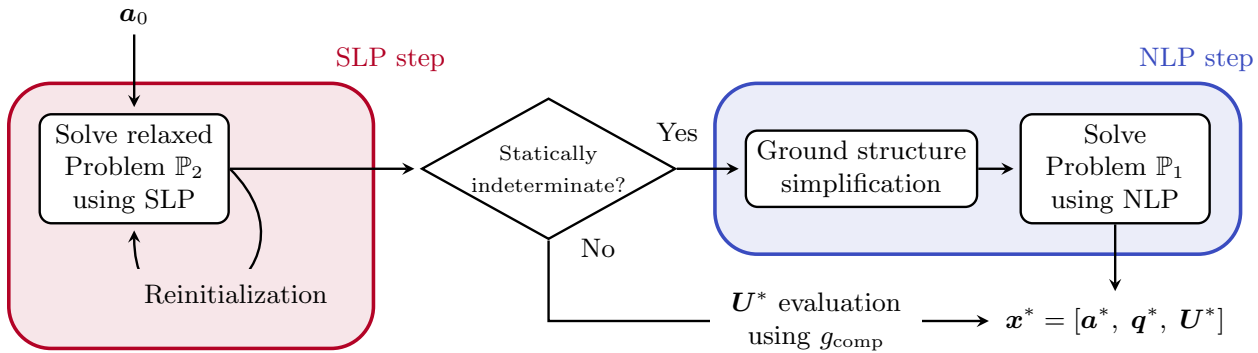


Figure 3.2.: Flowchart of the two-step optimization strategy used to solve Problem \mathbb{P}_1 .

displacements \mathbf{U} in Formulation \mathbb{P}_1 is stated as:

$$\begin{aligned}
 & \min_{\mathbf{a}, \mathbf{q}^0, \dots, \mathbf{q}^p} \quad V = \ell^T \mathbf{a} \\
 \text{s.t.} \quad & \mathbf{B} \mathbf{q}^p = \mathbf{f}^p \quad \forall p \in [0, \dots, N_p] \\
 & \mathbf{q}^p \geq -\frac{s \mathbf{a}^2}{\ell^{*2}} \quad \forall p \in [0, \dots, N_p] \\
 & -\sigma_c \mathbf{a} \leq \mathbf{q}^p \leq \sigma_t \mathbf{a} \quad \forall p \in [0, \dots, N_p] \\
 & \mathbf{a}_r \geq \mathbf{a}_{r=1} \quad r \in \mathcal{C}_{l,r}(\mathbf{a}) \\
 & 0 \leq \mathbf{a} \leq \frac{4\pi\ell^2}{\lambda_{\max}}
 \end{aligned} \tag{\mathbb{P}_2}$$

[184] Schwarz et al. (2018), 'Efficient size and shape optimization of truss structures subject to stress and local buckling constraints using sequential linear programming'

Since the objective function and all of its constraints are linear, except for the buckling constraint, this problem is solved by iteratively linearizing the non-linear buckling constraints and using a SLP algorithm. Following the work of [184], the Euler's critical load is iteratively updated using a first-order Taylor expansion for every i member with cross-sectional area a_i^k at the iteration k in the neighborhood of the point P_k (see Fig. 3.3):

$$\tilde{q}_{i,k}^{\text{cr}} = q_{i,k}^{\text{cr}}(a_i^k) + (a_i^{k+1} - a_i^k) \left. \frac{\partial q_{i,k}^{\text{cr}}(a_i^k)}{\partial a} \right|_{a=a_i^k} \tag{3.11}$$

where a_i^{k+1} represent the design variable of the SLP at the current iteration and $q_{i,k}^{\text{cr}}(a_i^k) = -s(a_i^k)^2/\ell_i^{*2}$ represents the Euler's critical load with cross-sectional area a_i^k and modified buckling length ℓ_i^* .

The linearized local buckling constraints \tilde{g}_{buck} are then stated as:

$$q_i \geq \tilde{q}_{i,k}^{\text{cr}}, \text{ with } \tilde{q}_{i,k}^{\text{cr}} = -\frac{s a_i^k (2a_i^{k+1} - a_i^k)}{\ell_i^{*2}} \quad \forall i \in [1, \dots, N_{\text{el}}], \quad (\tilde{g}_{\text{buck}})$$

where superscript \sim indicates linearized functions and variables.

We can now state the relaxed linearized sub-problem $\tilde{\mathbb{P}}_2$ obtained

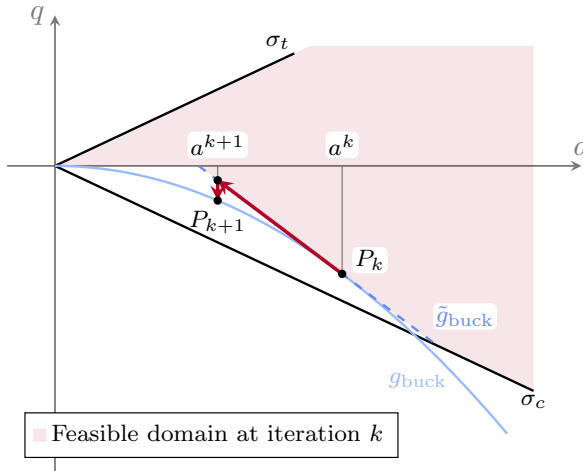


Figure 3.3.: Linearization of the local buckling constraints for a single bar.

substituting 3.4 with \tilde{g}_{buck} in Formulation \mathbb{P}_2 :

$$\begin{aligned}
 \min_{\boldsymbol{a}, q^0, \dots, q^P} \quad & V = \boldsymbol{\ell}^T \boldsymbol{a} \\
 \text{s.t.} \quad & \boldsymbol{B} \boldsymbol{q}^p = \boldsymbol{f}^p \quad \forall p \in [0, \dots, N_p] \\
 & \boldsymbol{q}^p \geq -\frac{s \boldsymbol{a}^k (2\boldsymbol{a}^{k+1} - \boldsymbol{a}^k)}{\ell^{*2}} \quad \forall p \in [0, \dots, N_p] \\
 & -\sigma_c \boldsymbol{a} \leq \boldsymbol{q}^p \leq \sigma_t \boldsymbol{a} \quad \forall p \in [0, \dots, N_p] \\
 & \boldsymbol{a}_r \geq \boldsymbol{a}_{r=1} \quad r \in \mathcal{C}_{l,r}(\boldsymbol{a}) \\
 & 0 \leq \boldsymbol{a} \leq \frac{4\pi\ell^2}{\lambda_{\max}}.
 \end{aligned} \tag{\tilde{\mathbb{P}}_2}$$

Since the objective function and all of its constraints are linear, we can approximate the solution of \mathbb{P}_2 by iteratively solving the subproblem $\tilde{\mathbb{P}}_2$. At every iteration k , the vector of cross-sectional areas \boldsymbol{a}^k is used to evaluate the linearization point P_k and calculate the set of linearized buckling constraints \tilde{g}_{buck} (see Fig. 3.3). The sub-problem $\tilde{\mathbb{P}}_2$ is, then, solved using a Linear Programming (LP) solver, and the updated vector of cross-sectional areas \boldsymbol{a}^{k+1} is used to evaluate the set of linearized buckling constraints of the $k + 1$ iteration. These steps are repeated until convergence i.e. when $\|\Delta \boldsymbol{x}\|_\infty \leq \text{tol}_{slp}$, where $\Delta \boldsymbol{x}$ represents the difference of the design variable vector \boldsymbol{x} between two successive iterations.

3.2.3. HANDLING LOCAL MINIMA: REINITIALIZATION STRATEGY

If at the end of iteration $k - 1$ the cross-sectional area of bar i , a_i^k , becomes very small, the gradient of the corresponding local buckling constraint at iteration k will tend towards 0 and the feasible domain will shrink (see Fig. 3.4). Any bar with near-zero sections will remain as such in future iterations since there is no incentive for the SLP optimizer to increase its value. This is one of the possible reasons why the SLP optimizer gets stuck in local minima.

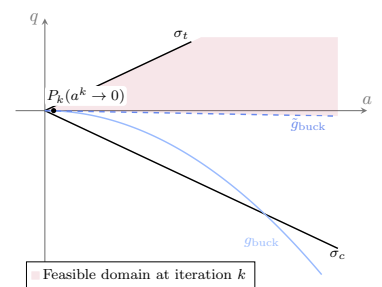


Figure 3.4.: The linearized buckling constraints (blue dashed line) limit the design space of successive iterations when evaluated on compressive bars with very small areas. Additionally, the gradient of the linearized buckling constraint tends to 0.

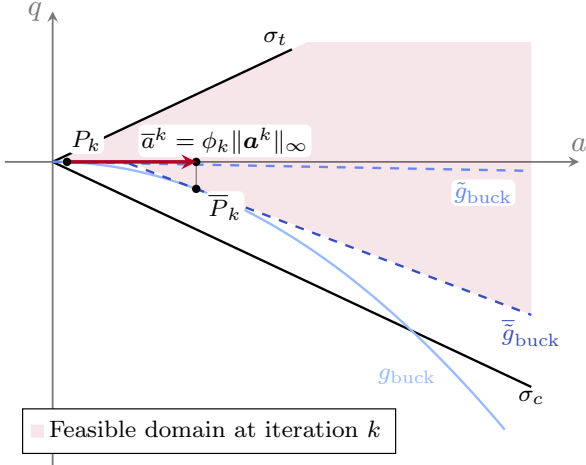


Figure 3.5.: The reinitialization strategy modifies the linearization point of the members with a small area to promote their reintroduction in the optimization problem.

Subsequently, we propose a heuristic strategy to reinitialize the small cross-sectional area values a^k used to evaluate the linearized local buckling constraints \tilde{g}_{buck} at iteration k . The strategy is called multiple times during the optimization when the solver converges to a minimum, i.e. when $\|\Delta x\|_\infty \leq \text{tol}_{slp}$. It affects only the cross-sectional areas that are smaller than a fraction value τ of the maximum value at iteration k , $\|a^k\|_\infty$. The updated cross-sectional area \bar{a}^k used to evaluate the linearization point \bar{P}_k is updated as follows:

$$\bar{a}_i^k := \begin{cases} \phi_n \|a^k\|_\infty & \text{if } a_i^k \leq \tau \|a^k\|_\infty \\ a_i^k & \text{otherwise.} \end{cases} \quad (3.12)$$

The effects of this approach are shown in Fig. 3.5, where it is clear that updating the constraint \tilde{g}_{buck} with \bar{g}_{buck} reduces the gap between the original and the linearized design space and permits the exploration of new solutions. Additionally, the gradient of the constraint is restored to a non-zero value.

The ϕ_n parameter is used in Equation 3.12 to influence how much the reinitialization heuristic modifies the original formulation. Subsequently, to reach convergence, we propose a continuation scheme on ϕ_n to reduce its impact on the optimization following an exponential decay law:

$$\phi_n = \phi_{n-1}^\beta \quad \forall n \in [1, \dots, n_{\max}], \quad (3.13)$$

where n_{\max} represent the maximum number of reinitialization calls and the β parameter control the steepness of the exponential progression. In that way, as the number of calls to the reinitialization strategy increases, its influence on the original formulation decreases.

The complete SLP strategy with reinitialization used to solve Problem \mathbb{P}_2 is presented in Fig. 3.6, where the SLP optimized design variable vector is noted as $\tilde{x}^* = [\tilde{a}^*, \tilde{q}^*]$.

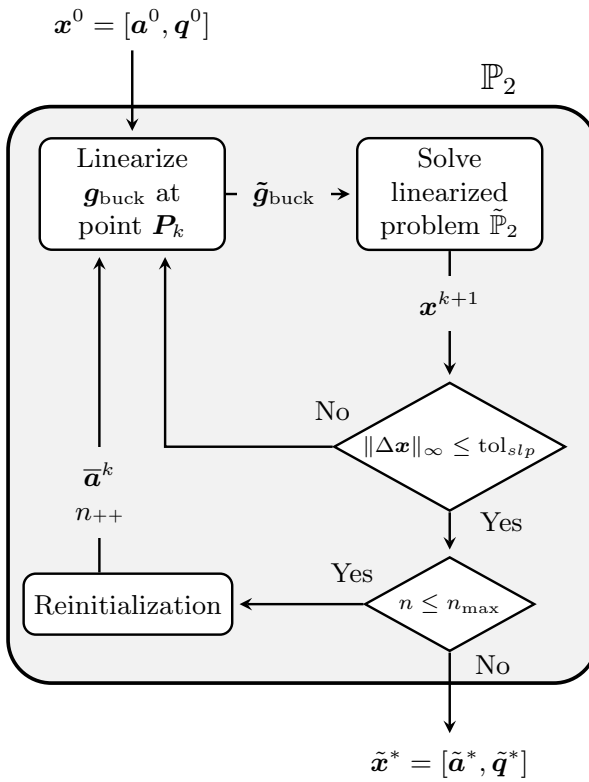


Figure 3.6.: Flowchart of the SLP strategy with reinitialization used to solve Problem \mathbb{P}_2 .

3.2.4. SECOND STEP: NLP OPTIMIZATION

If only one load case and no particular symmetries are imposed on the initial ground structure, the SLP solution \tilde{x}^* is not statically indeterminate [78, 79]. In that case, it is trivial to evaluate the displacements using 3.10 and the optimization is complete. However, if this is not the case, the stability of the structure is to be tested.

- 78. Kirsch (1989), 'Optimal topologies of truss structures'
- 79. Rozvany et al. (1995), 'Layout Optimization of Structures'

The stability of the SLP-optimized structure is assessed by evaluating the Degree of Static Indeterminacy (DSI) of the truss using Maxwell's criterion:

$$DSI = N_{el} - N_{DOF} - r \quad (3.14)$$

with r the number of fixed Degrees Of Freedom (DOFs) of the test case. If $DSI \leq 0$, the number of equilibrium equations is less than or equal to the number of the internal forces and Equation 3.10 suffices to evaluate the correct displacements of the truss. If, however, $DSI > 0$, the truss is potentially statically indeterminate and additional nonlinear constraints must be added to ensure the structure's kinematic compatibility. The optimization is then performed again. We call this second step the NLP step (see Fig. 3.2).

To mitigate the risk of becoming trapped in local minima, the NLP optimizer is employed on a reduced design space. The solution \tilde{x}^* of the SLP serves the purpose of simplifying the initial ground structure, thereby eliminating elements from the NLP optimization that fall

below the specified threshold value a_{thr} :

$$a_i < a_{\text{thr}} \quad \forall i, \text{ with } a_{\text{thr}} = \chi \max(\tilde{\mathbf{a}}^*), \quad (3.15)$$

with the parameter χ called the cross-sectional area threshold value.

A linear Finite Element Analysis (FEA) based on the direct stiffness method is performed to provide a correct estimate of forces and displacements caused by the external forces on the solution of Problem \mathbb{P}_2 for the initial point of the optimization. The initial displacement vector \mathbf{U}^0 is calculated as the unique solution to:

$$\mathbf{f} = \mathbf{B}^T \mathbf{q} = \mathbf{B}^T \mathbf{D} \mathbf{e} = \mathbf{B}^T \mathbf{D} \mathbf{B} \mathbf{U}^0 = \mathbf{K} \mathbf{U}^0. \quad (3.16)$$

where \mathbf{K} is the stiffness matrix of the truss, defined as $\mathbf{K} = \mathbf{B}^T \mathbf{D} \mathbf{B}$, with $\mathbf{D} = \text{diag}(E(\tilde{\mathbf{a}}^* + \delta \mathbf{e})/\ell)$, $\mathbf{e} = [1, \dots, 1]^T$, and $\delta = 10^{-12}$. This last term is added as the structures coming from the SLP step could result in a mechanism with respect to load cases different from the one used for the optimization [31]. Then the initial member forces vector \mathbf{q}^0 is evaluated using 3.10. $\tilde{\mathbf{a}}^*$, \mathbf{q}^0 and \mathbf{U}^0 are used as the starting point of the full NLP formulation where the kinematic compatibility and the exact local buckling formulation are restored. The NLP solver finally outputs the optimized structure variables $\mathbf{x}^* = [\mathbf{a}^*, \mathbf{q}^*, \mathbf{U}^*]$.

³¹Dorn et al. (1964), 'Automatic design of optimal structures'

3.3. NUMERICAL APPLICATION

In this section, the proposed method is benchmarked against multiple classical and innovative test cases. Firstly, we show how the proposed two-step solution strategy with reinitialization reduces the influence of the starting point on the optimization result compared to the direct NLP optimization of Problem \mathbb{P}_1 . Additionally, as the response surface of the SLP of the proposed method is more regular than the original NLP, the two-step solution strategy generates simple structures i.e. with a low number of active bars, as it is efficient at driving the cross-sectional areas to zero. To show that, we implement and optimize the ten-bar truss and the 2D cantilever beam, two of the most common benchmarks in TTO with buckling constraints. Secondly, to show the ability of the proposed method to work on structures with multiple load cases we implemented a modified ten-bar truss test case where several load cases are applied to the same ground structure. Finally, to assess the computational efficiency and validate the proposed strategy, we optimize a three-dimensional supported beam test case.

The test cases are optimized using different resolution strategies. The proposed method is compared against the direct NLP optimization of Problem \mathbb{P}_1 , denoted in our analysis as NLP. The proposed two-step resolution strategy is implemented with three different maximum numbers of reinitialization calls n_{max} : no reinitialization (2S-0R) with

Parameter	Value	Description
tol_{slp}	10^{-6}	Stopping criterion SLP
tol_{nlp}	10^{-4}	Stopping criterion NLP
$\text{max}_{\text{it,SLP}}$	400	Maximum iterations of the SLP algorithm
$\text{max}_{\text{it,NLP}}$	5000	Maximum iterations of the NLP algorithm
χ	10^{-6}	Threshold for the ground structure reduction
τ	0.05	Threshold for the reinitialization
ϕ_0	0.8	Initial reinitialization magnitude parameter
β	2	Index of the exponential decay law

Table 3.2.: Values and description of the parameters used for the SLP and NLP optimizations.

$n_{\text{max}} = 0$, one call of reinitialization (2S-1R) with $n_{\text{max}} = 1$, and finally five calls of reinitialization (2S-5R) with $n_{\text{max}} = 5$. The reinitialization magnitude parameter ϕ is set up using Equation 3.13 and the parameters listed in Table 3.2, leading to $\phi = 0.8000$ for the 2S-1R algorithm and to $\phi = [0.8000, 0.6400, 0.4096, 0.1677, 0.0281]$ for the five reinitialization calls of 2S-5R.

The optimizations are performed using the Python package CVXPY 1.2.2 [170] with the ECOS 2.0.7 [171] solver to solve the relaxed LP Problem $\tilde{\mathbb{P}}_2$. The NLP Problem \mathbb{P}_1 is solved using cyipopt [196], a Python wrapper for IPOPT 3.14.11 [29], a large-scale nonlinear optimization package using PARDISO 6.0 [197] as linear solver. The Jacobian and the Hessian of the Lagrangian of the NLP step are calculated at every optimization iteration to allow faster convergence. As every state variable of the optimization is independent of the others, these responses are derived analytically and will not be detailed there. The stopping criteria used for the SLP and NLP optimizations are $\|\Delta x\|_\infty \leq \text{tol}_{\text{slp}}$, and $\|\Delta_{\text{NLP}}\|_\infty \leq \text{tol}_{\text{nlp}}$, with $\text{tol}_{\text{slp}} = 10^{-6}$ and $\text{tol}_{\text{nlp}} = 10^{-4}$ respectively. Δ_{NLP} represents the scaled NLP error, a more comprehensive value used by IPOPT to take into account the optimality of the solution and the constraints violation. The objective function is scaled so that the initial volume is 1000, the areas are in the interval $[0, 1000]$, the initial forces in $[0, 1000]$, and the displacement in $[0, 1000]$ for the SLP and the NLP. The full list of parameters used to set up the variable scaling, the SLP optimization, the reinitialization, and the NLP optimization is listed in Table 3.2. Several additional parameters are used in the NLP step for cyipopt and IPOPT:

- ▶ `mu_strategy` is set to `adaptive`
- ▶ `grad_f_constant` is set to `yes`
- ▶ `hessian_constant` is set to `yes`
- ▶ `alpha_for_y` is set to `min-dual-infeas`
- ▶ `linear_solver` is set to `pardiso`
- ▶ `expect_infeasible_problem` is set to `yes`
- ▶ `bound_push` is set to `1e-12`
- ▶ `constr_viol_tol` is set to `1e-6`
- ▶ `nlp_scaling_method` is set to `user-scaling`.

The optimizations presented in this section are performed on a note-

170. Diamond et al. (2016), 'CVXPY: A Python-Embedded Modeling Language for Convex Optimization'

171. Domahidi et al. (2013), 'ECOS: An SOCP solver for embedded systems'

196. Moore et al. (2018), 'cyipopt: Cython interface for the interior point optimizer IPOPT'

29. Wächter et al. (2006), 'On the implementation of an interior-point filter line-search algorithm for large-scale nonlinear programming'

197. Alappat et al. (2020), 'A Recursive Algebraic Coloring Technique for Hardware-efficient Symmetric Sparse Matrix-vector Multiplication'

198. Stragiotti (2023), 'Truss Topology Optimization with Topological Buckling Constraints Data Set'

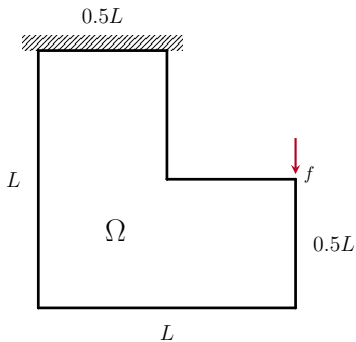


Figure 3.7.: Boundary conditions of the L-shaped beam test case.

Parameter	Value
E	1
L	100
σ_L	[0.20, 1]

Table 3.3.: Material data used for the optimizations.

book equipped with an Intel Core™ i5-9400H Processor @ 2.50 GHz (4 cores) and 16 GB of RAM. Additionally, the load cases, the starting point, and the result data of all the presented test cases are available in the reference data set [198].

3.3.1. L-SHAPED BEAM

To assess the effectiveness of the proposed minimum slenderness limit, we conducted a new round of optimization on the L-shaped beam described in Section 2.2.2 and showed in Fig. 3.7. The material and geometric data are presented in Table 3.3. In the Fig. 3.8, we present the optimized structures obtained using this modified formulation and the stress limits σ_L values of 1, 0.8, 0.3, and 0.2. The first two values have already been used and the results have been presented in Table 2.3. They highlighted the limits of Formulation \mathbb{P}_0 when imposing a specified slenderness limit ($\lambda < 15$). The last two values are introduced here to test how the 3.3 constraints affect the truss topology for extreme cases.

A major focus is put on the shorter bar of the optimized structures to observe how the solution evolved. We observe a redistribution of the same load across multiple smaller bars. More bars became active because there is an upper limit on the cross-sectional area (and thus the force) they can withstand. The four structures present $N_{el,sl} = 34, 38, 56$, and 79 active bars, respectively.

In Table 3.4 we compared the new designs limited in minimum slenderness (noted in the table with the 'sl' subscript) to the ones presented in Section 2.2.2 and found that the new designs meet the bar model's slenderness requirements correctly. The number of active bars increases along with the calculation time, but the volume remains nearly the same, indicating there are many solutions with similar volumes. Adding this upper bound constraint, we have extended the domain of application of the TTO. However, we must be careful because very high volumes of fraction solutions can lead to too many bar intersections, resulting in structures with no physical meaning.

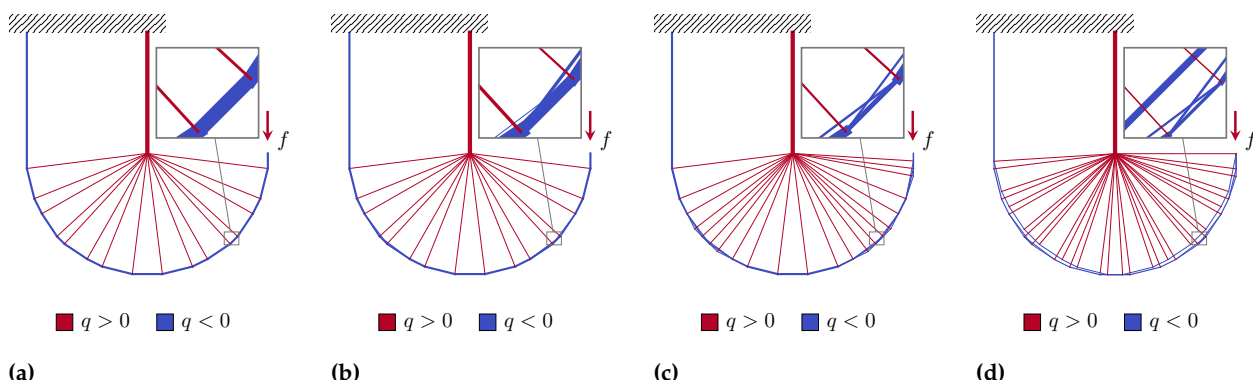


Figure 3.8.: Topology of the optimized truss structures for different material admissibles $\sigma_L = 1.0, 0.8, 0.3$ and 0.2 with a minimum slenderness limit $\lambda < 15$.

Table 3.4.: Numerical comparison of the effect of the minimum slenderness constraint on the optimization of the 2D L-shaped beam.

σ_L	V_f	Min λ	$V_{f,sl}$	Min λ_{sl}	$V_{f,sl}/V_f$	$N_{el,sl}/N_{el}$	t_{sl}/t
1.0	6.21 %	15.8	6.21 %	15.8	1.0000	1.00	1.02
0.9	6.90 %	15.0	6.90 %	15.0	1.0000	1.00	1.03
0.8	7.76 %	14.1	7.76 %	15.0	1.0001	1.12	2.27
0.7	8.87 %	13.2	8.87 %	15.0	1.0001	1.12	2.21
0.6	10.35 %	12.2	10.35 %	15.0	1.0002	1.12	1.12
0.5	12.42 %	11.2	12.42 %	15.0	1.0003	1.12	1.07
0.4	–	–	15.53 %	15.0	–	–	–
0.3	–	–	20.71 %	15.0	–	–	–
0.2	–	–	31.06 %	15.0	–	–	–

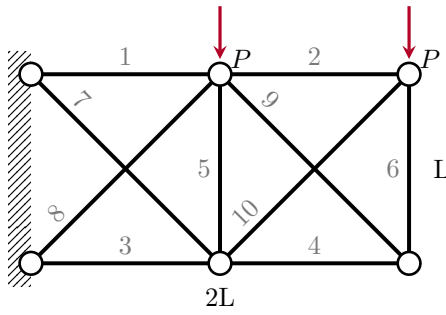


Figure 3.9.: The ten-bar truss ground structure and load case.

3.3.2. TEN-BAR TRUSS

The ten-bar truss is a test case subjected to maximum stress and local buckling constraints proposed by [186] and is shown in Fig. 3.9. It is a small test case with 32 design variables (10 cross-sectional area, 10 internal force, and 12 displacement variables) and 42 constraints (12 force equilibrium, 20 maximum stress, 10 local buckling, and 10 kinematic compatibility constraints) when solved using Formulation \mathbb{P}_1 . The geometry and material data are given in Table 3.5. For simplicity, all numeric values are assumed normalized and dimensionless. We compare the results obtained by our method with those obtained by direct NLP resolution and with the results published by [186] and [187].

The robustness of the optimization algorithms to local minima is evaluated by running 50 optimizations from different initialization points a^0 randomly chosen in the interval $[0, 100]$. The first initialization point, denoted a_s^0 , is specifically chosen to match the one used by [187] ($a_{s,2}^0 = a_{s,8}^0 = a_{s,10}^0 = 0$ and $a_{s,i}^0 = 50$ elsewhere). This is the starting point from which the authors conclude that the problem is initialization-dependent.

In Fig. 3.10 we show the scatter plot of the optimization of the ten-bar truss for the four considered resolution algorithms, where for every initialization point (X-axis) we show the final volume of the structure. The NLP algorithm converges to different solutions with varying volume values, confirming an abundance of local minima

Parameter	Value
L	360
E	1.0×10^4
s	$\pi E/4$
σ_c, σ_t	± 20
P	100

Table 3.5.: Material data used for the ten-bar truss optimization.

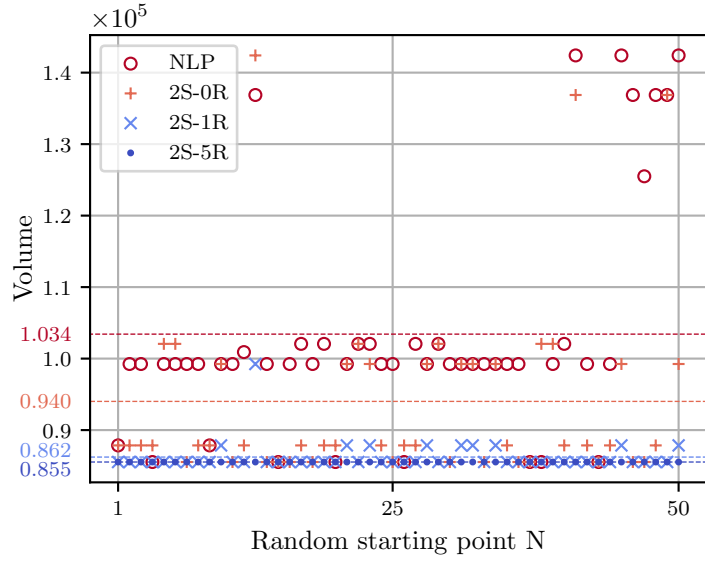


Figure 3.10.: Scatter plot of the four benchmarked optimization algorithms on the ten-bar truss. The 2S-5R shows a 100 % convergence rate to the lightest structure found. The dashed lines represent the mean of the distributions.

Table 3.6.: Numerical comparison of the four optimization algorithms on the ten-bar truss for 50 different initial points. The 2S-5R algorithm shows a 100 % convergence rate to the lightest structure found. The iteration count and time are from the first initialization point a_s^0 .

Algorithm	$\bar{V} \pm SD$	Conv.	It.	t [s]
NLP	$(1.03 \pm 0.15) \times 10^5$	14 %	22	0.25
2S-0R	$(9.40 \pm 1.22) \times 10^4$	20 %	4	0.06
2S-1R	$(8.62 \pm 0.21) \times 10^4$	80 %	17	0.24
2S-5R	$(8.55 \pm 0.00) \times 10^4$	100 %	73	1.18
[186]	8.78×10^4	-	-	-
[187]	8.55×10^4	-	-	-

even for such a small test case with 10 bars. The optimized results are dispersed, and the best design found ($V = 85534$) is only attained 7 times over the 50 optimization runs (14 %). To properly compare the different algorithms, we use two different figures of merit: the mean \bar{V} and the standard deviation SD of the distribution of the volume of the optimized designs and the ratio of solutions converged to the best result to the total number of initialization points. The numerical results are listed in Table 3.6. The proposed two-step optimization strategy (2S-0R) already reduces \bar{V} by approximately 9 % compared to NLP, but it is only when we introduce the reinitialization strategy that major improvements are observed, especially when multiple calls of the heuristic are done. The five-calls reinitialization optimization strategy (2S-5R) is not influenced by the initialization point ($SD = 0$), with all solutions successfully converging to the lightest structure.

Let us consider only the first initialization point a_s^0 . In Fig. 3.11 we show the convergence history and the design of the structure throughout the iterations for that specific case. We notice how the initialization point a_s^0 (represented in Fig. 3.11a) corresponds to the topology of the local minimum found by [186]. As extensively shown in Section 3.2.3, if the cross-sectional area of one member is almost or exactly zero the gradient of the local buckling constraint tends to zero and the bar is not considered in the optimization anymore. For that reason, the

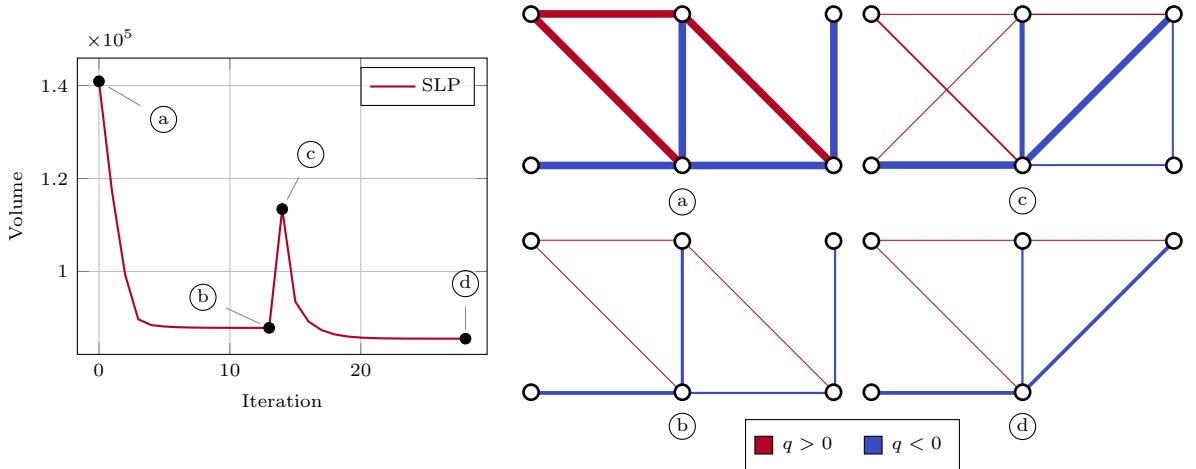


Figure 3.11.: Volume convergence history for the proposed two-step resolution strategy with one step of reinitialization (2S-1R) for the initialization point a_s^0 . The reinitialization strategy permits to jump from the local minimum (b), with $V = 87857$, to the lighter structure (d), with $V = 85534$. Only the SLP step is plotted because the solution is statically determinate and kinematic compatibility constraints are already satisfied. In red the members loaded in tension, in blue the members loaded in compression.

optimizer is not able to restore the bars initialized at 0 and promptly converges to a solution that presents the very same topology (see Fig. 3.11b, $V = 87857$). This structure would be the optimization result if no additional steps are done. With a single call of the reinitialization heuristic, the topology is modified as shown in Fig. 3.11c, in which bars 2 and 10 are reintroduced in the set of active members. From this iteration, the optimizer finally converges to the lighter structure shown in Fig. 3.11d with $V = 85534$, showing the interest of the reinitialization strategy. We notice how only the SLP step of the proposed two-step strategy is shown here as the optimized structure is statically determinate ($DSI=0$ and stiffness matrix K non-singular) and the kinematic compatibility is already satisfied by the optimized design.

It should be mentioned that the proposed heuristic comes with an increase in computational cost. While for the first initialization point, the 2S-0R algorithm converges in only 4 iterations, the single-step 2S-1R and the five-step 2S-5R algorithms converge after 17 and 73 iterations, respectively. The optimization time is slightly more than one second (see the last column of Table 3.6). However, this increase in calculation time is justified by the fact that a single initialization point should suffice to reach an acceptable solution, instead of using a multistart approach.

It is advisable to select the highest number of reinitialization calls (parameter n_{\max} of Equation 3.13) that is compatible with the user's computational budget. Our research findings suggest that once the parameter ϕ_k (which determines the strength of the heuristic perturbation) drops below 0.01, the reinitialization has no more influence on the result of the linearized problem. Therefore, with the proposed

parameterization of the continuation scheme, pursuing more than five reinitialization calls does not yield additional benefits in the studied test cases.

3.3.3. 2D CANTILEVER BEAM

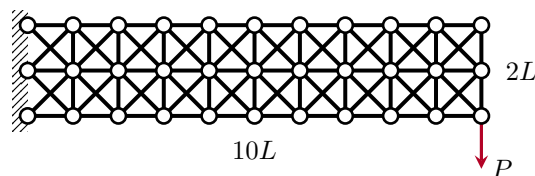
The second example we consider is a 2D cantilever beam charged on one extremity as shown in Fig. 3.12. This test case was proposed by Achtziger [180] with the geometry and dimensionless material data given in Table 3.7. The number of the candidate bars of the initial ground structure is $N_{\text{el}} = 90$. The complexity of this problem resides in the fact that the geometry and material data are chosen in such a way that the solution with or without local buckling constraints coincides if topological buckling is not considered. The optimized structure shows in this case a volume of $V = 70.00$. However, as this structure presents multiple bars in compressive chains, we need to merge them into single bars, recalculate their length, and evaluate their sections to comply with local buckling constraints. By doing so, we would obtain $V = 99.99$, an increase of more than 40 % with respect to the optimized structure just found. This load case is built to show the importance of topological buckling and suggests that a lighter solution is to be found between these two bounds.

The 2D cantilever is optimized starting from 100 random points $\mathbf{a}^0 \in [0, 100]$ and the same four algorithms presented in the previous section. At the end of the optimization, the resulting structures are checked for compressive chains and, if present, they are merged into single bars. The final volume does not change as the effective buckling length ℓ^* is iteratively updated using Equation 3.8 during the optimization. The numerical results are presented in Table 3.8.

Table 3.7.: Material data used for the 2D cantilever beam optimization.

180. Achtziger (1999), ‘Local stability of trusses in the context of topology optimization Part II’

Figure 3.12.: The 2D cantilever beam load case with a first-order connectivity ground structure. The total number of candidate members is $N_{\text{el}} = 90$.



Algorithm	V_{\min}	$\bar{V} \pm \text{SD}$	N_{\min}	$\bar{N}_{\text{el}} \pm \text{SD}$
NLP	80.67	81.34 ± 2.98	58	66.57 ± 1.13
2S-0R	79.88	92.80 ± 7.45	10	25.61 ± 7.94
2S-1R	77.78	88.42 ± 6.29	10	27.86 ± 6.56
2S-5R	77.78	86.72 ± 6.05	10	28.60 ± 6.44
[180]	85.58	-	18	-

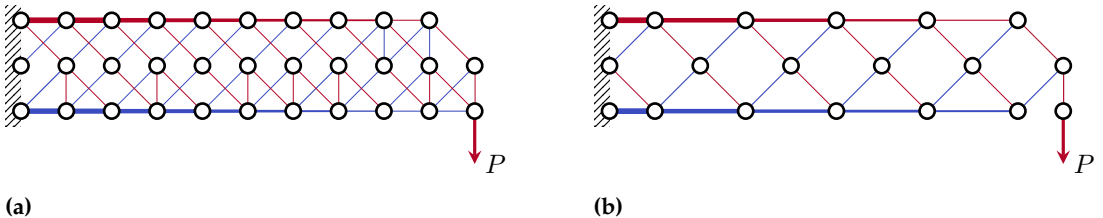


Figure 3.13.: (a) NLP optimized design of the 2D cantilever beam with a volume of $V = 80.67$ and high number of active and crossing bars $N_{\text{el}} = 66$; (b) 2S-5R solution $V = 77.78$ with $N_{\text{el}} = 31$. In red the members loaded in tension, in blue the members loaded in compression.

The NLP algorithm shows a good consistency with a mean volume $\bar{V} = 81.34$ and a low dispersion of the results ($\text{SD} = 2.98$), repeatedly converging to a specific solution with $V = 80.85$. However, despite the apparent good numerical performance, the solutions always present a high number of active bars, with an average \bar{N}_{el} of over 66 bars. As discussed in Section 3.2, the NLP algorithm encounters difficulties in driving the cross-sectional areas to 0. Fig. 3.13a shows the lightest design found using NLP, with $V = 80.67$ and $N_{\text{el}} = 66$.

The proposed two-step formulation without reinitialization 2S-0R drastically reduces the complexity of the structure, with an average number of active bars \bar{N}_{el} of around 27, and an absolute minimum of $N_{\min} = 10$. However, this simplification of the design comes at the expense of an increased average volume and dispersion ($\bar{V} = 92.80$ and $\text{SD} = 7.45$). This detrimental effect is efficiently counterbalanced with the proposed reinitialization strategy, which reduces the average volume to $\bar{V} = 86.72$ and $\text{SD} = 6.05$ for 2S-5R. To sum up, the NLP remains stuck in a low-volume local optimum whose volume varies little and that shows a very high number of active bars. With the two-stage strategy, the number of bars of the optimized structures is 58 % lower, resulting in a lighter design in 30 % of cases, and with the best design found that is 3.5 % lighter.

Fig. 3.14 shows how the results of the proposed algorithm are more scattered and do not converge to a single minimum as precedently seen on the ten-bar truss example of Section 3.3.2. A possible explanation for this difference in performance might be the discrete nature of the optimization when topological buckling constraints are taken into account. In some rare cases, we observed that calling the reinitialization makes the optimization converge to a more voluminous design compared to the one we had just before—i.e. the optimizer

Table 3.8.: Numerical comparison of the 2D cantilever beam of the four algorithms for 100 random initial points. The 2S-5R algorithm shows a good balance between the volume, complexity, and dispersion of the solutions.

(x_a, y_a)	(x_b, y_b)	ℓ	q	a	V
(0 0)	(1 0)	1.00–5.00	5.00	5.00	
(1 0)	(0 1)	1.41	0.71	0.71	1.00
(1 0)	(2 1)	1.41–0.71	1.02	1.45	
(3 0)	(2 1)	1.41	0.71	0.71	1.00
(3 0)	(4 1)	1.41–0.71	1.02	1.45	
(5 0)	(4 1)	1.41	0.71	0.71	1.00
(5 0)	(6 1)	1.41–0.71	1.02	1.45	
(7 0)	(6 1)	1.41	0.71	0.71	1.00
(7 0)	(8 1)	1.41–0.71	1.02	1.45	
(9 0)	(8 1)	1.41	0.71	0.71	1.00
(9 0)	(10 1)	1.41–0.71	1.02	1.45	
(10 0)	(10 1)	1.00	1.00	1.00	1.00
(0 1)	(1 2)	1.41–0.71	1.02	1.45	
(2 1)	(1 2)	1.41	0.71	0.71	1.00
(2 1)	(3 2)	1.41–0.71	1.02	1.45	
(4 1)	(3 2)	1.41	0.71	0.71	1.00
(4 1)	(5 2)	1.41–0.71	1.02	1.45	
(6 1)	(5 2)	1.41	0.71	0.71	1.00
(6 1)	(7 2)	1.41–0.71	1.02	1.45	
(8 1)	(7 2)	1.41	0.71	0.71	1.00
(8 1)	(9 2)	1.41–0.71	1.02	1.45	
(10 1)	(9 2)	1.41	0.71	0.71	1.00
(0 2)	(1 2)	1.00	5.00	5.00	5.00
(1 0)	(3 0)	2.00–4.00	4.00	8.00	
(3 0)	(5 0)	2.00–3.00	3.00	6.00	
(5 0)	(7 0)	2.00–2.00	2.43	4.87	
(7 0)	(9 0)	2.00–1.00	1.72	3.44	
(1 2)	(3 2)	2.00	4.00	4.00	8.00
(3 2)	(5 2)	2.00	3.00	3.00	6.00
(5 2)	(7 2)	2.00	2.00	2.00	4.00
(7 2)	(9 2)	2.00	1.00	1.00	2.00
				V_{tot}	77.78 ^a

^aThe total volume value is lower than the sum of the member volumes due to the 2 decimal places round-off.

Table 3.9.: Optimal values of the member forces, areas, and volumes of the 2D cantilever beam.

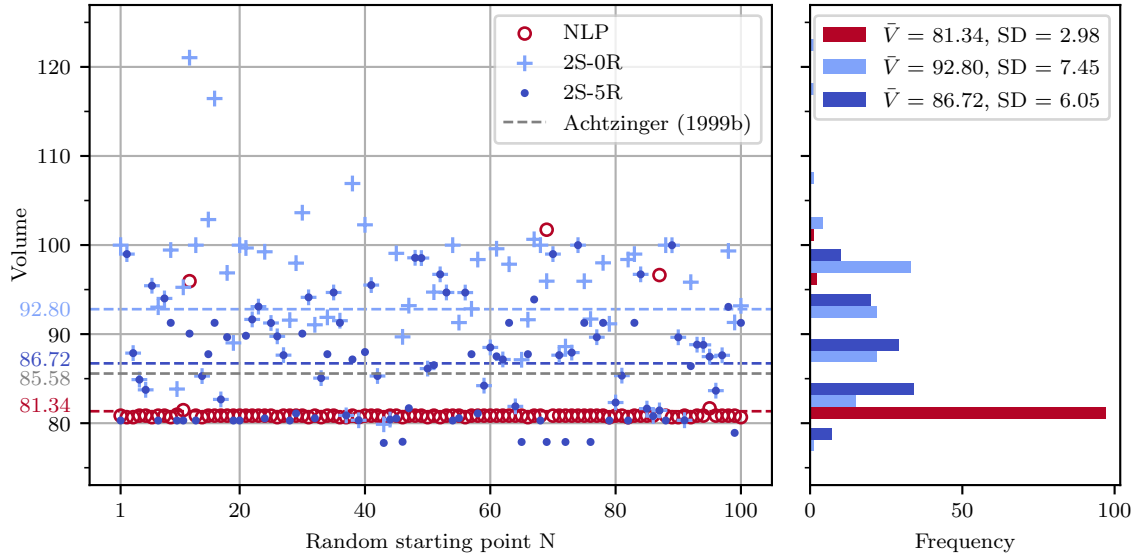


Figure 3.14.: Left: scatter plot of three of the four benchmarked optimization algorithms on the 2D cantilever beam compared to the solution by Achtziger [180]. The dashed lines represent the mean of distributions. Right: histogram of the distribution of the results of the optimization algorithms.

at the end of the optimization converges to a worse local minimum compared to the ones found just before calling the reinitialization. In these cases, the results presented are the best ones encountered over the optimization steps and not the final ones.

The lightest solution found by 2S-5R with a volume of $V = 77.78$ and with $N_{el} = 31$ is presented in Fig. 3.13b. Some of the active members of the optimized design are not present in the original ground structure but are the result of the bar merging process. The optimized design shows a 9 % lower volume with respect to the solution found by Achtziger [180] with $V = 85.57^1$. The detailed value of the design variables of the solution can be found in Table 3.9 and in the referenced data set [198]. Approximately 45 % of the solutions of the 2S-5R algorithm are less voluminous than the one found by Achtziger.

180. Achtziger (1999), 'Local stability of trusses in the context of topology optimization Part II'

1: Even if Achtziger [180] reports an optimized volume of $V = 79.57$, we use here the value corrected by Tyas [182] of $V = 85.57$.

198. Stragiotti (2023), 'Truss Topology Optimization with Topological Buckling Constraints Data Set'

We are aware of the less voluminous solution ($V = 73.44$) found by [182]. The main reason for the difference is that Tyas's method allows the inclusion of bracing-only members that are not required for primary load-carrying purposes to reduce the effective buckling lengths ℓ of internal members. The incorporation of these members is regulated by introducing perturbative forces applied to the structure as additional load cases at unstable nodes. In the specific example of Tyas' structure, the resulting structure is statically admissible, and this ensures that kinematic compatibility is satisfied. However, as demonstrated later in this Chapter, this may not always be the case. Tyas' formulation, in this context, serves only as a lower-bound formulation for minimizing the structure's volume.

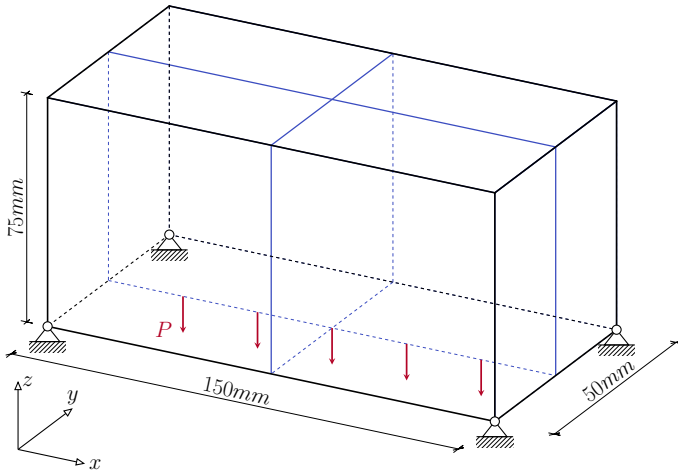


Figure 3.15.: The simply supported 3D beam example with the load case and boundary conditions. In blue we plot the symmetry planes.

3.3.4. SIMPLY SUPPORTED 3D BEAM

In this subsection, we focus on optimizing a simply supported three-dimensional beam. The supports are positioned at all four lower extremities of the design volume, the structure is subjected to five equispaced nodal loads, with each load magnitude set to $P = 100 \text{ N}$, applied on the XZ symmetry plane of the structure, as depicted in Fig. 3.15. The volume of the design space is $150 \text{ mm} \times 50 \text{ mm} \times 75 \text{ mm}$. These specific dimensions have been selected to accommodate the printing volume of the Creality Halot One, which is an Stereolithography (SLA) 3D printer with maximal printing dimensions of $127 \text{ mm} \times 80 \text{ mm} \times 160 \text{ mm}$. The material properties used for the optimization are given in Table 3.10 and mimic a tough SLA resin². The test case exhibits symmetry concerning the XZ and YZ planes (see blue lines of Fig. 3.15), enabling us to mesh and optimize just one-quarter of the structure. This specific portion is meshed using a fully connected ground structure with dimensions of $4 \times 2 \times 4$ nodes, resulting in a total of 496 elements (or 1984 for the entire structure). For this case, we employ the 2S-5R solving algorithm.

2: The material data has been sourced from 3ds.com/make/solutions/blog/sla-3d-printing-materials-compared and hubs.com/knowledge-base/sla-3d-printing-materials-compared.

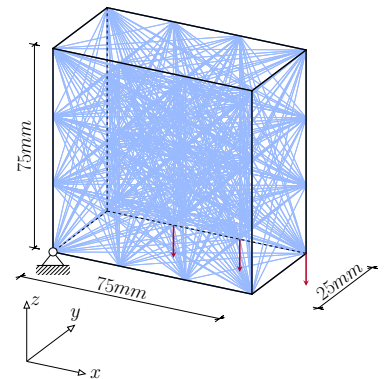


Figure 3.16.: Ground structure composed of $N_{\text{el}} = 496$ elements of the symmetric portion used to optimize the simply supported 3D beam.

Table 3.11 and Fig. 3.17 show the numerical results and topology of the optimized structure, respectively. The entire structure features 20 active bars, approximately 1 percent of the original ground structure. In Fig. 3.18, we visualize the stress and buckling constraints applied to the optimized structure. Every compression-loaded bar of the optimized structure activates the buckling constraint, underscoring the critical importance of accounting for this mode of structural failure in a truss. The final structure weights 11.294 g and achieves a volume fraction of 1.761 %. The optimization process is completed within 4 seconds, with only the SLP solved, as the resultant structure is statically determinate and kinematic constraints are inherently satisfied.

Parameter	Value
E	2.7 GPa
ν	0.3
σ_c, σ_t	$\pm 55 \text{ MPa}$
ρ	1.14 g cm^{-3}
P	100 N

Table 3.10.: Material data used for the simply supported 3D beam optimization.

Table 3.11.: Numerical results of the optimization of the simply supported 3D beam.

Quantity	Value
N_{el}	1984
N_{opt}	20
V	9.907 cm^3
$V\%$	1.761 %
Mass	11.294 g
a_{max}	37.61 mm^2
C	3.71 J
t	4 s

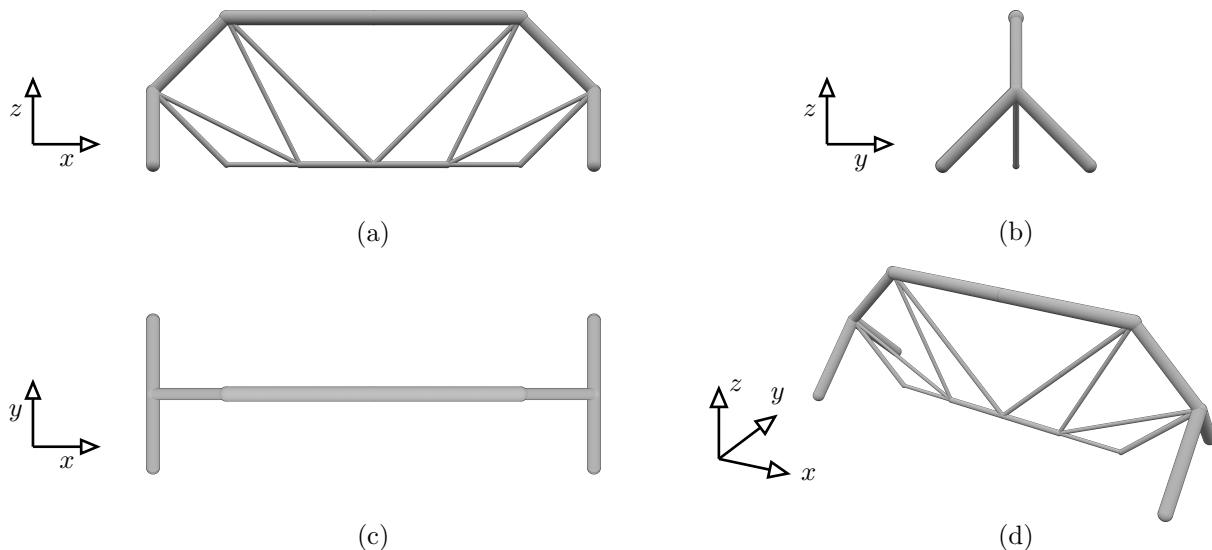


Figure 3.17.: Orthographic views of the topology of the optimized simply supported 3D beam. (a) XZ plane (b) YZ plane (c) XY plane (d) auxiliary perspective view.

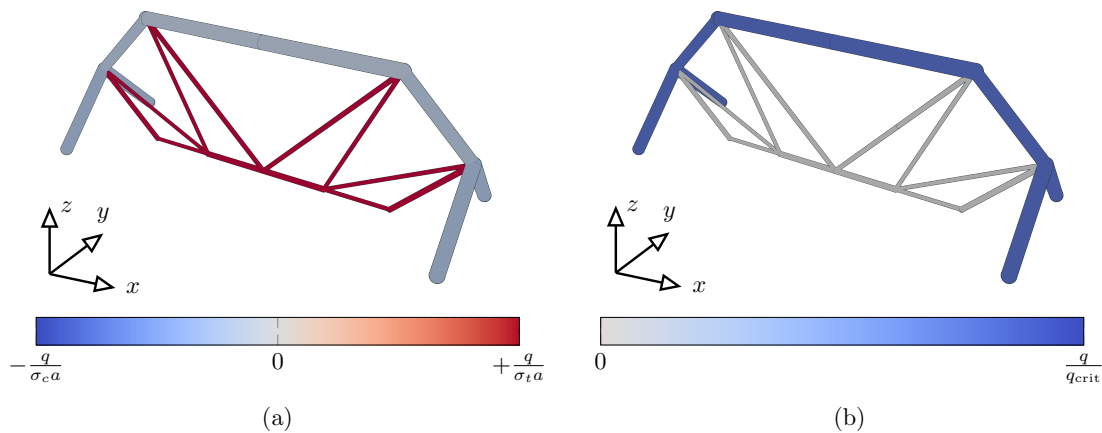


Figure 3.18.: Maximum stress constraint value (a) and buckling constraint value (b) plotted on the optimized topology of the simply supported 3D beam.

3.3.5. TEN-BAR TRUSS WITH MULTIPLE LOAD CASES

We introduce here a more complex example to validate the proposed algorithm on a multiple load cases structure with maximum stress and topological buckling constraints. The test case is obtained by slightly modifying the ten-bar truss presented in Section 3.3.2. The ground structure and the material data are the same, and two load cases P_1 and P_2 are applied at the structure's free extremity symmetrically with respect to the horizontal axis. A graphical presentation of the load case is shown in Fig. 3.19. The loads' magnitude is set to $P_1 = P_2 = 100$ and the other parameters are listed in Table 3.12.

First, we optimize the structure using the same four algorithms and the starting point presented in Section 3.3.2. Differently from the structures optimized earlier in Sections 3.3.2 and 3.3.3, the solutions of the SLP step are statically indeterminate, as they show a $DSI > 0$ and a non-singular \mathbf{K} stiffness matrix. For that reason, the structures undergo the second optimization step in which the kinematic compatibility and the exact buckling constraints are restored (NLP step, see Formulation \mathbb{P}_1). The numerical findings of the four algorithms are presented in Table 3.13.

In agreement with previous results, the proposed 2S-5R strategy reduces simultaneously the volume and the dispersion of the solutions. Interestingly, the mean value \bar{V} of the 2S-0R algorithm is 1.3 % lower with respect to 2S-5R, a fact never observed before. This is due to the 2S-0R algorithm occasionally converging to a heavier solution in the SLP phase that results in a lighter solution once optimized by the NLP, suggesting that the lightest SLP configuration does not always correspond to the lightest NLP design. However, as the difference between the two solutions is low (3.9 %), the 2S-5R algorithm is still preferred thanks to its higher solution consistency (the dispersion σ of 2S-5R is 71 % lower than the dispersion σ of 2S-0R).

We now analyze the lightest solution with a final volume of $V = 134279.32$. The optimized design obtained is symmetric. This is consistent with Conjecture 4 made by Rozvany [199], according to which if the boundary conditions and the ground structure are symmetric, and two alternate load conditions are mirror images of each other with respect to the symmetry axis, then at least one globally optimal topology is symmetric. This conjecture has been confirmed in [200] in the case of symmetric convex optimization problems. It is interesting

Parameter	Value
L	360
E	1.0×10^4
s	$\pi E / 4$
σ_c, σ_t	± 20

Table 3.12.: Material data used for the ten-bar truss optimization.

[199]. Rozvany (2011), 'On symmetry and non-uniqueness in exact topology optimization'

[200]. Guo et al. (2014), 'A confirmation of a conjecture on the existence of symmetric optimal solution under multiple loads'

Algorithm	$\bar{V} \pm SD$
NLP	$1.45 \times 10^5 \pm 1.44 \times 10^4$
2S-0R	$1.33 \times 10^5 \pm 9.56 \times 10^3$
2S-1R	$1.35 \times 10^5 \pm 2.73 \times 10^3$
2S-5R	$1.35 \times 10^5 \pm 2.73 \times 10^3$

Table 3.13.: Numerical comparison of the four optimization algorithms on the ten-bar truss for 50 different initial points.

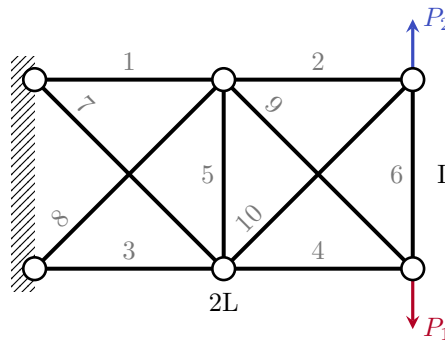


Figure 3.19.: Ground structure of the ten-bar truss with two applied load cases P_1 and P_2 .

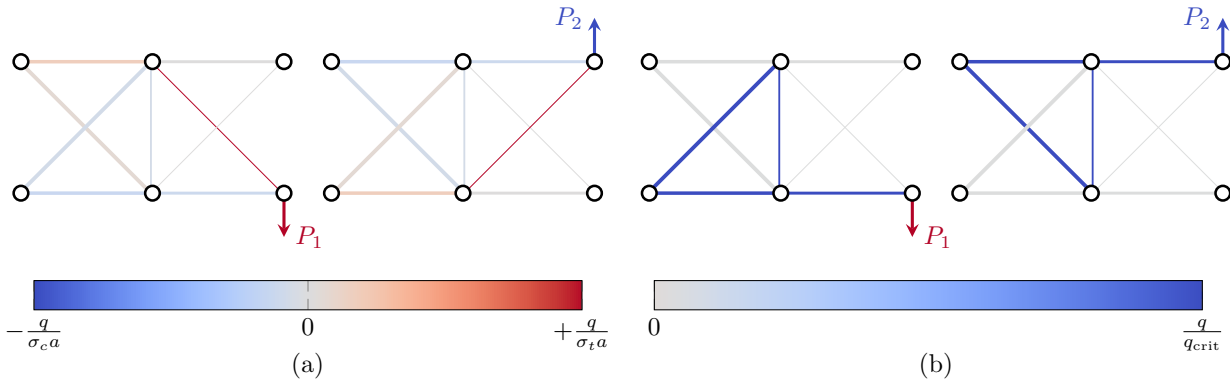


Figure 3.20.: Maximum stress constraint value (left) and buckling constraint value (right) plotted on the optimized design of the multiple load cases ten-bar truss.

to note that the Conjecture still holds for this specific example even if problem \mathbb{P}_1 is non-linear and non-convex. In Table 3.14 we list the cross-sectional area of the members for the two steps of the proposed solving optimization strategy. The NLP optimized structure presents a volume $V = 134279.32$, a 35.15 % increase compared to the predicted volume of the SLP step of $V = 99084.93$. Incorporating kinematic constraints to achieve a solution that adheres to elasticity requirements significantly impacts the volume of the optimized solution. The design for the two different load cases P_1 and P_2 is shown in Fig. 3.20, where a side-by-side plot of the maximum stress and buckling constraints is presented. In this example, the bars are constrained by either the buckling or the stress of one of the two load cases. The detailed value of the design variables of the solution is given in Table 3.15, while the iteration history curves of the optimization can be found in Fig. 3.21.

In Fig. 3.21 we provide the iteration history of the objective function and the constraint violation for the SLP and the NLP steps. The graphs on the left depict the evolution of volume during optimization in both the SLP and NLP steps. Looking at the SLP step (red plot), we can see that the SLP reduces the volume and exhibits occasional "spikes," which correspond to the reinitialization heuristic calls. The gradual diminishment of these spikes throughout the optimization is due to the incorporation of the continuation scheme on the parameter ϕ_k of Equation 3.13. Turning our attention to the NLP step, we observe that

Bar	SLP step \mathbb{P}_2	NLP step \mathbb{P}_1	Difference
a_1	57.296	47.987	-16.24 %
a_2	40.408	40.621	+0.05 %
a_3	57.296	47.987	-16.24 %
a_4	40.408	40.621	+0.05 %
a_5	40.193	25.547	-36.43 %
a_6	0.052	0.000	—
a_7	6.997	53.115	+659.11 %
a_8	6.997	53.115	+659.11 %
a_9	6.997	7.071	+0.01 %
a_{10}	6.997	7.071	+0.01 %
V	99084.93	134279.32	+35.51 %

Table 3.14.: Comparison of the results of the SLP step and NLP step for the multiple load cases ten-bar truss.

$(x_a \ y_a)$	$(x_b \ y_b)$	ℓ	q_1	q_2	\mathbf{a}	\mathbf{V}
(0 360)	(360 360)	360.0	160.5	-139.6	48.0	17 275.4
(360 360)	(720 360)	360.0	0.0	-100.0	40.6	14 623.8
(0 0)	(360 0)	360.0	-139.6	160.5	48.0	17 275.4
(360 0)	(720 0)	360.0	-100.0	0.0	40.6	14 623.8
(360 0)	(360 360)	360.0	-39.6	-39.6	25.6	9197.0
(360 0)	(0 360)	509.1	55.9	-85.5	53.1	27 042.0
(0 0)	(360 360)	509.1	-85.5	55.9	53.1	27 042.0
(720 0)	(360 360)	509.1	141.4	0.0	7.1	3600.0
(360 0)	(720 360)	509.1	0.0	141.4	7.1	3600.0
V_{tot}						134279.32 ^a

^aThe total volume value is lower than the sum of the member volumes due to the one decimal places round-off.

Table 3.15.: Optimal values of the member forces, areas, and volumes of the members of the ten-bar truss with multiple load cases.

initially the volume is increased and then it descends again, stabilizing at a value that is higher than the one of the NLP starting point. To elucidate this behavior, we refer to the graphs on the right, which present the history of constraint violations in the NLP step. Notably, the starting point of the NLP step always respects equilibrium g_{eq} and kinematic compatibility g_{comp} , as displacements and forces are evaluated using Equation 3.16. However, stress $g_{\text{st,c}}$ and $g_{\text{st,t}}$ and buckling constraints g_{buck} are not initially respected, because the force field provided by the SLP does not account for the kinematic compatibility constraint. The NLP optimizer then tries to reduce violations of buckling and stress while temporarily increasing its volume (a phase referred to as the "restoration phase" in the IPOPT algorithm). Ultimately, the optimizer converges to a volume that is slightly higher than what was predicted by the SLP. This aligns with the concept that, by disregarding kinematic compatibility in the SLP step, we have a lower-bound formulation for the volume.

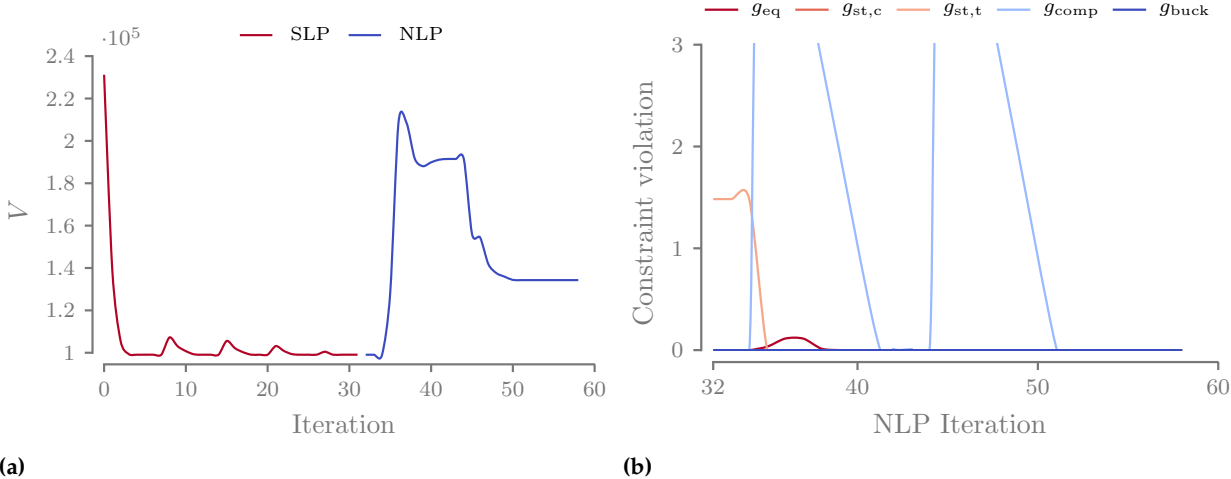


Figure 3.21.: Iteration history of the ten-bar truss with multiple load cases example solved with the 2S-5R algorithm; (a) objective function history for the SLP and NLP step (b) constraint violation for the NLP step.

3.4. CONCLUSION

In this chapter, we presented a structural optimization formulation that minimizes the mass of two- and three-dimensional truss structures subject to multiple load cases, maximum stress, topological buckling, and minimum slenderness constraints. The optimization is solved using an efficient two-step method and shows a reduced influence on the starting point thanks to the proposed reinitialization heuristic. Several numeric examples are presented using the proposed optimization algorithm. Optimized structures display designs with fewer active members compared to traditional optimization methods, leading to lower overall manufacturing complexity. Additionally, thanks to the computational efficiency of the proposed optimization strategy, we show how advanced mechanical constraints such as maximum stress, topological buckling, and kinematic compatibility constraints can be applied and solved on structures with thousands of candidates on a notebook computer.

However, some research questions still remain open. The manufacturing complexity is discussed here only as an outcome of the optimization strategy, but a direct way to impose manufacturing constraints (maximum numbers of bars converging to a single node, minimum section, imposed periodicity of the structure) during the optimization would be beneficial. For that reason, in the next chapters, we study the mechanical behavior of modular structures, exploring the trade-off between mechanical performance and manufacturing complexity.

OPTIMIZING MODULAR STRUCTURES

Introduction TODO EVALUATE DENSITIES

In Section 4.1, we provide a detailed explanation of the modifications needed to apply modular constraints to the Truss Topology Optimization (TTO). Specifically, we focus on how to model the problem when multiple modules are used and how topological buckling constraints are implemented in modular structures. Finally, in Section 4.2, we evaluate the proposed formulation through various 2D and 3D test cases, aiming to gain a better understanding of modular structures.

4.1. FORMULATION OF A MODULAR STRUCTURE OPTIMIZATION ALGORITHM

Assembled modular ultralight structures present an opportunity to greatly improve the performance and cost efficiency of modern aerostructures [107]. The repetitive nature brings various interesting features among which reduced tooling, fast assembly, and short repair time. Additionally, as the mechanical performance of the structure is greatly influenced by the topology and the materials of the repetitive pattern, modular structures are naturally prone to optimization.

In the field of structure optimization, periodic materials are often modeled through asymptotic homogenization [202]. The heterogeneous module topology (also called Representative Volume Element (RVE)) is treated as homogeneous material with associated mechanical properties i.e. equivalent elastic tensor, shear modulus, etc. The homogenization approach is valid only if the RVE contains enough information about the heterogeneous material and if the structure presents significant periodicity [104, 203].

Nevertheless, our work pertains to structures that frequently exhibit one or more dimensions significantly smaller than the remaining dimensions, such as the thickness of a wingbox or a sandwich panel. In the context of designing modular structures (and not materials), no scale separation is assumed between the repetitive pattern and the structure itself. Consequently, the assumptions of asymptotic homogenization are not always verified. To address this, full-scale approaches [122] have been developed.

4.1.1. VARIABLE LINKING

The variable linking approach [37] is a full-scale optimization technique that involves first dividing a structure into several subdomains, which are connected in the optimization process – i.e. subdomains

4.1 FORMULATION OF A MODULAR STRUCTURE OPTIMIZATION ALGORITHM	71
4.2 NUMERICAL APPLICATION	76
4.3 CONCLUSION	94

Part of the content presented in this chapter has been published and showcased during a conference as: Stragiotti, E. et al. (2022) "Enhanced truss topology optimization (TTO) applied to a cellular wing box", in *ASMO-UK 12, an ISSMO Conference on Engineering Design Optimization*. Book of proceedings. Leeds, United Kingdom [201].

¹⁰⁷ Cramer et al. (2019), 'Elastic shape morphing of ultralight structures by programmable assembly'

²⁰² Zhou et al. (2008), 'Design of graded two-phase microstructures for tailored elasticity gradients'

¹⁰⁴ Kalamkarov et al. (2009), 'Asymptotic Homogenization of Composite Materials and Structures'
²⁰³ Li et al. (2020), 'Anisotropic design and optimization of conformal gradient lattice structures'

¹²² Wu et al. (2021), 'Topology optimization of multi-scale structures'

³⁷ Zhang et al. (2006), 'Scale-related topology optimization of cellular materials and structures'

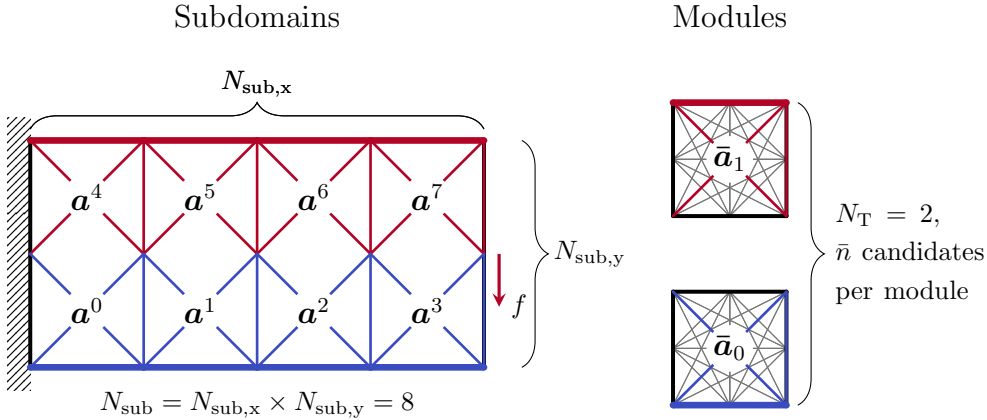


Figure 4.1: Notations used for the definition of the variable linking approach used to apply the modularity constraints.

that belong to the same module all share the same cross-sectional areas. The primary goal is to make the manufacturing phase simpler and more efficient, allowing to assemble of big structures starting from smaller repetitive modules. With this approach, the optimization perspective shifts. The optimizer design space using the variable linking approach is restricted to the optimization of the topology of the modules, using the whole structure just to evaluate and impose the necessary mechanical constraints.

We use Fig. 4.1 to illustrate the notation employed in this thesis for modular structures. On the left-hand side of the image, we have the whole test case that we aim to optimize, which is divided into \$N_{\text{sub}}\$ subdomains. Each of these subdomains is bound to exhibit the topology of one of the \$N_T\$ module topologies presented on the right side of the image. It is assumed for simplicity that each module has the same external shape and an identical ground structure used for discretizing the module volume. Within this framework, \$\bar{n}\$ represents the number of candidate bars in one module, and if we assume a fully connected mesh, we can define \$\bar{n} = \bar{m} \cdot (\bar{m} - 1)/2\$, where \$\bar{m}\$ stands for the number of nodes in the module. Consequently, for the overall structure, we can write the relationship \$N_{\text{el}} = N_{\text{sub}} \bar{n}\$.

The vector that holds all the cross-sectional areas of the modules is represented by \$\bar{a}\$, and it belongs to the set of positive real numbers \$\mathbb{R}_+^{N_T \cdot \bar{n}}\$. This vector is essentially a grouping of individual cross-sectional areas \$\bar{a}_t\$ for each of the \$N_T\$ modules. In mathematical terms, \$\bar{a}\$ is defined as follows:

$$\bar{a} := \{\bar{a}_t \in \mathbb{R}_+^{\bar{n}} \mid \forall t \in [1, \dots, N_T]\} \quad (4.1)$$

The topology of the entire structure a , which originates from the submodules' topology \$\bar{a}\$, is the assembly of the individual cross-sectional areas of every one of the \$N_{\text{sub}}\$ subdomains and is defined as follows:

$$a := \{a^j \mid \forall j \in [1, \dots, N_{\text{sub}}]\} \quad (4.2)$$

and is evaluated using:

$$\mathbf{a} = \sum_{t=1}^{N_T} \mathbf{h}_t \otimes \bar{\mathbf{a}}_t = \sum_{t=1}^{N_T} \begin{bmatrix} h_{1,t} & \bar{\mathbf{a}}_t \\ \vdots & \\ h_{N_{\text{sub}},t} & \bar{\mathbf{a}}_t \end{bmatrix} \quad (4.3)$$

where the \otimes operator represents the Kronecker product and \mathbf{h}_t is the t -th column of the module mapping matrix $\mathbf{H} = [\mathbf{h}_0, \dots, \mathbf{h}_{N_T}] \in \mathbb{B}^{N_{\text{sub}}, N_T}$, where $\mathbb{B} = \{0, 1\}$ is the Boolean domain. $h_{j,t}$ is the element at the j -th row and t -th column of the matrix \mathbf{H} . The module mapping matrix \mathbf{H} indexes are defined as follows:

$$h_{j,t} = \begin{cases} 1 & \text{if the } j\text{-th subdomain presents the topology of the } t\text{-th module,} \\ 0 & \text{otherwise.} \end{cases} \quad (4.5)$$

Lastly, we introduce some notation to denote specific bars within the modules and subdomains. We represent the cross-sectional area of the i -th bar of the t -th module as $\bar{\mathbf{a}}_{t,i}$, while the cross-sectional area of the i -th bar of the j -th subdomain as a_i^j .

4.1.2. TOPOLOGICAL BUCKLING OF MODULAR STRUCTURES

Addressing topological buckling in modular structures is a more complex task compared to monolithic structures. This complexity arises from the fact that we must not only consider bars within a single module's design space but also those connecting different modules. Since the nature of this problem heavily relies on how the modules are arranged within the structure, we have opted for a simplification. We focus only on the assessment of nodal instability within each module, modifying the length ℓ^* used to evaluate the critical buckling force of 3.4 and Equation 3.8 only of compressive chains of bars that fall inside a module. Additionally, Equation 3.9 is modified as follows:

$$\bar{\mathbf{a}}_{t,r} \geq \bar{\mathbf{a}}_{t,r=1} \quad r \in \mathcal{C}_{l,r}(\bar{\mathbf{a}}_t) \quad \forall t \in [1, \dots, N_T]. \quad (4.6)$$

We have made this choice knowing that the high connectivity of modular structures tends to reduce the occurrence of nodal instability within the structure. Any potential nodal instability in compressive chains at the structure level is addressed in a subsequent post-processing phase.

4.1.3. OPTIMIZATION FORMULATION

The monolithic formulation \mathbb{P}_1 is updated using Equations 4.3, and 4.6 to obtain the modular optimization formulation $\mathbb{M}_{1,\text{VL}}$ that use the variable linking approach. Formulation $\mathbb{M}_{1,\text{VL}}$ is stated in terms of modular cross-sectional areas $\bar{\mathbf{a}}$, member forces \mathbf{q} and nodal

In the case of the structure shown in Fig. 4.1 we have:

$$\mathbf{H} = \begin{bmatrix} t=0 & t=1 \\ \begin{array}{cc|c} 1 & 0 & j=0 \\ 1 & 0 & j=1 \\ 1 & 0 & j=2 \\ 1 & 0 & j=3 \\ 0 & 1 & j=4 \\ 0 & 1 & j=5 \\ 0 & 1 & j=6 \\ 0 & 1 & j=7 \end{array} \end{bmatrix} \quad (4.4)$$

as the lower submodules (numbered from 0 to 3) exhibit the topology of module $t = 0$, while the upper submodules (numbered 4 to 7) the topology of module $t = 1$.

Equation 3.8:

$$\ell_i^*(\mathbf{a}) := \begin{cases} \ell_i & \text{if } i \notin \mathcal{C}_{l,r}(\mathbf{a}) \\ \sum \ell_r \mid r \in \mathcal{C}_{l,r}(\mathbf{a}) & \text{otherwise.} \end{cases}$$

Equation 3.9:

$$a_r \geq a_{r=1}, \quad r \in \mathcal{C}_{l,r}(\mathbf{a}), \quad \forall r \neq 1.$$

displacements \mathbf{U} as follows:

$$\begin{aligned}
 \min_{\bar{\mathbf{a}}, \mathbf{q}, \mathbf{U}} \quad & V = \boldsymbol{\ell}^T \mathbf{a} \\
 \text{s.t.} \quad & \mathbf{a} = \sum_{t=1}^{N_T} \mathbf{h}_t \otimes \bar{\mathbf{a}}_t \\
 & \mathbf{B}\mathbf{q} = \mathbf{f} \\
 & \mathbf{q} = \frac{\mathbf{a}^E}{\boldsymbol{\ell}} \mathbf{b}^T \mathbf{U} \\
 & \mathbf{q} \geq -\frac{s\mathbf{a}^2}{\boldsymbol{\ell}^{*2}} \\
 & -\sigma_c \mathbf{a} \leq \mathbf{q} \leq \sigma_t \mathbf{a} \\
 & \bar{\mathbf{a}}_{t,r} \geq \bar{\mathbf{a}}_{t,r=1} \quad r \in \mathcal{C}_{l,r}(\bar{\mathbf{a}}_t), \forall t \\
 & 0 \leq \bar{\mathbf{a}} \leq \frac{4\pi\bar{\boldsymbol{\ell}}^2}{\lambda_{\max}}
 \end{aligned} \tag{\mathbb{M}_{1,VL}}$$

where $\bar{\boldsymbol{\ell}}$ represents the vector of the lengths of the bars within the modules.

The total number of design variables in the formulation is expressed as $N_T \bar{n} + N_{\text{sub}} \bar{n} + 2M$ or $N_T \bar{n} + N_{\text{sub}} \bar{n} + 3M$, depending on whether the test case is two or three-dimensional. The number of constraints is, however, equal to the monolithic optimization. This fact arises due to the localized nature of stress, buckling, and compatibility constraints, which are all referenced not only to individual modules but to the entire structure.

The formulation is solved by reusing the proposed two-step optimization algorithm, incorporating the reinitialization heuristic to mitigate dependence on the optimization starting point, as detailed in Section 3.2.1. We state here the formulation $\mathbb{M}_{2,VL}$ with relaxed compatibility constraints that are solved as the first step of the optimization.

$$\begin{aligned}
 \min_{\bar{\mathbf{a}}, \mathbf{q}, \mathbf{U}} \quad & V = \boldsymbol{\ell}^T \mathbf{a} \\
 \text{s.t.} \quad & \mathbf{a} = \sum_{t=1}^{N_T} \mathbf{h}_t \otimes \bar{\mathbf{a}}_t \\
 & \mathbf{B}\mathbf{q} = \mathbf{f} \\
 & \mathbf{q} \geq -\frac{s\mathbf{a}^2}{\boldsymbol{\ell}^{*2}} \\
 & -\sigma_c \mathbf{a} \leq \mathbf{q} \leq \sigma_t \mathbf{a} \\
 & \bar{\mathbf{a}}_{t,r} \geq \bar{\mathbf{a}}_{t,r=1} \quad r \in \mathcal{C}_{l,r}(\bar{\mathbf{a}}_t), \forall t \\
 & 0 \leq \bar{\mathbf{a}} \leq \frac{4\pi\bar{\boldsymbol{\ell}}^2}{\lambda_{\max}}
 \end{aligned} \tag{\mathbb{M}_{2,VL}}$$

We can solve Formulation $\mathbb{M}_{2,VL}$ by breaking it down into simpler

linearized problems using a Sequential Linear Programming (SLP) algorithm. This is possible because the Kronecker product is a linear operator, and the buckling constraints can be linearized, as previously demonstrated in Section 3.2.1.

4.1.4. SENSITIVITY ANALYSIS

During each iteration of the optimization process, the current state of the structure is determined by the values assigned to the design variables. In structure optimization, the evolution of the structure's design is guided by assessing the sensitivities of both the objective function and constraints with respect to the design variables. In the specific context of modular structure optimization, the module (and not the structure divided into the subdomains) is identified as the design domain, and for that reason necessitating the derivation of corresponding modular sensitivities.

The approach involves initially computing gradients for all candidates for the full monolithic structure, without considering the modularity. Subsequently, the contributions of each i -th bar belonging to a specific module topology t are summed together. Mathematically, this can be expressed as follows:

$$\frac{\partial(\cdot)_i}{\partial \bar{a}_{t,i}} = \sum_{j=0}^{N_{\text{sub}}} h_t^T \frac{\partial(\cdot)_i}{\partial a_i^j} \quad (4.7)$$

where (\cdot) is a generic function for which the sensitivity is calculated. This process is graphically represented in Fig. 4.2.

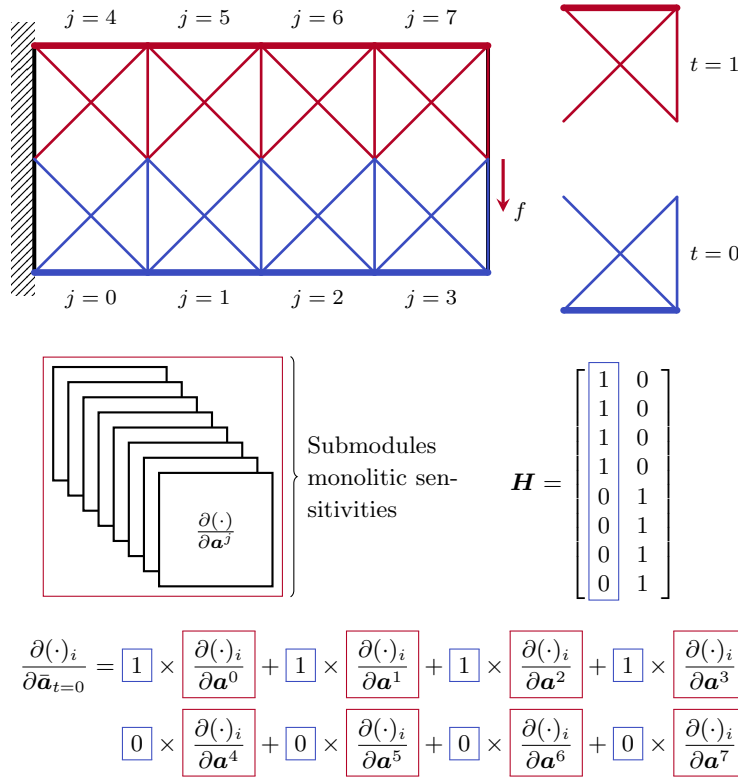


Figure 4.2.: Notations used for the evaluation of the sensitivities for the modular structure optimization based on the variable linking scheme.

4.2. NUMERICAL APPLICATION

Parameter	Value
ϕ_0	0.8
β	2

Table 4.1.: Reminder of the parameters used to set the reinitialization parameters for the modular optimization. The full list of values and tolerances used for the setup of the optimization algorithm can be found in Table 3.2.

170. Diamond et al. (2016), 'CVXPY: A Python-Embedded Modeling Language for Convex Optimization'

171. Domahidi et al. (2013), 'ECOS: An SOCP solver for embedded systems'

196. Moore et al. (2018), 'cyipopt: Cython interface for the interior point optimizer IPOPT'

29. Wächter et al. (2006), 'On the implementation of an interior-point filter line-search algorithm for large-scale nonlinear programming'

In this section, we formulate multiple test cases used to explore the limits and the characteristics of modular structures and the proposed modular structure optimization formulation $M_{1,VL}$.

The test cases are optimized using the two-step resolution strategy implemented with five calls of reinitialization (2S-5R) with $n_{\max} = 5$. The reinitialization magnitude parameter ϕ is set up using the same parameters listed in Table 4.1, that leads to $\phi = [0.8000, 0.6400, 0.4096, 0.1677, 0.0281]$.

The optimizations are performed using the Python package CVXPY 1.2.2 [170] with the ECOS 2.0.7 [171] solver to solve the relaxed Linear Programming (LP) Problem $M_{2,VL}$. The Non-Linear Programming (NLP) Problem $M_{1,VL}$ is solved using cyipopt [196], a Python wrapper for IPOPT 3.14.11 [29], a large-scale nonlinear optimization package using PARDISO 6.0 [197] as linear solver.

4.2.1. ON THE EQUIVALENCE OF MULTI-LOAD CASES AND MODULAR STRUCTURES

The first test case we deal with is a two-dimensional bridge structure segment composed of two subdomains ($n_{\text{sub}} = 2$) with symmetric boundary conditions, as illustrated in Fig. 4.3a. In this test case, two

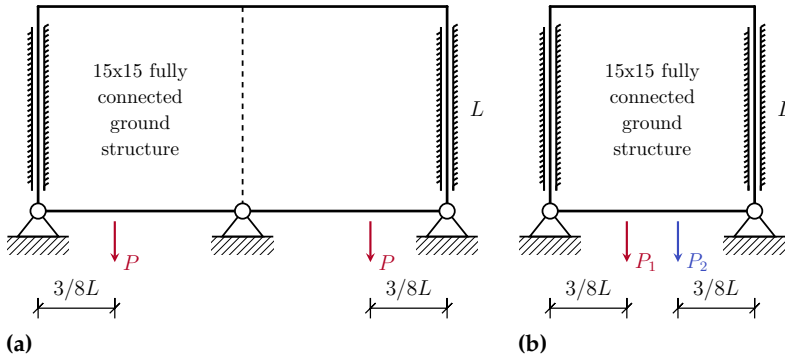


Figure 4.3.: Boundary conditions of the multi-subdomains (a) and the multi-load cases (b) test cases.

Table 4.3.

Quantity	Multi-subdomain	Multi-loads
N_{sub}	2	1
$N_{\text{opt}} (N_{\text{el}})$	62 (50400)	31 (25200)
V	182.692	91.346

vertical loads of magnitude $P=1$ are applied to the lower side of the design space. The material and geometrical details are given in Table 4.2 and are normalized and adimensional for simplicity. Each subdomain of the structure is discretized using a 15×15 fully connected ground structure, with a number of candidates $\bar{n} = 25200$ per subdomain. It is important to note that, for this example, buckling constraints have been deactivated.

Additionally, a similar structure is optimized, comprising only a single subdomain, subjected to two distinct load cases, denoted as P_1 and P_2 . These loads are positioned at precisely the same distance from the support as the structure with multiple subdomains, as illustrated in Fig. 4.3b. The subdomain is discretized using the same 15×15 fully connected ground structure.

The optimization is carried out for both structures, utilizing the material data specified in Table 4.2. The joint cost is set at $s = 0.05$ for the multi-subdomain structure and $s = 0.1$ for the multi-load case structure. the graphical representation of the optimized structures is given in Fig. 4.4. Remarkably, the resulting subdomain topologies are identical, with the volume of the multi-subdomain structure V_1 being precisely twice the volume of the multi-load cases structure V_2 .

This straightforward example highlights an interesting aspect of modular structure optimization that aligns with common sense. When a loaded structure is divided into multiple subdomains, each subdomain, when isolated and subjected to appropriate boundary conditions defined by the reaction forces of adjacent bars and supports, experiences multiple loading conditions. By imposing modularity constraints on all these subdomains, the optimization process seeks the optimal structure that simultaneously meets the mechanical needs of all these diverse load cases. Hence, there exists an equivalence between optimizing a multi-subdomain structure with modular constraints

197. Alappat et al. (2020), 'A Recursive Algebraic Coloring Technique for Hardware-efficient Symmetric Sparse Matrix-vector Multiplication'

Parameter	Value
L	100
E	1
σ_c, σ_t	± 1
P	1

Table 4.2.: Material data used for the modular bridge section 2D structure.

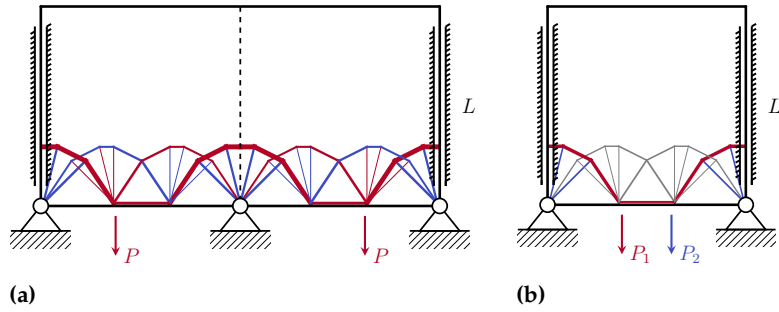


Figure 4.4: Optimized structures of the multi-subdomains (a) and the multi-load cases (b) test cases. The resulting module topology is equal for the two cases. In red the bars are in a tensile state, and in blue the bars are in a compressive state.

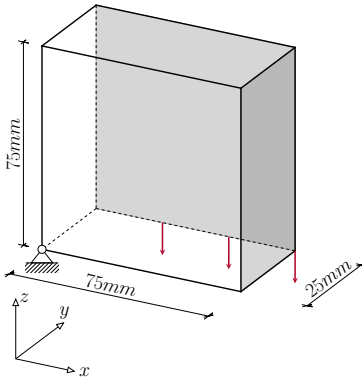


Figure 4.5: Symmetric boundary conditions of the simply supported 3D beam. In gray are the symmetry planes of the test case.

Parameter	Value
E	2.7 GPa
ν	0.3
σ_c, σ_t	± 55 MPa
ρ	1.14 g cm^{-3}
P	100 N

Table 4.4: Material data used for the simply supported 3D beam optimization.

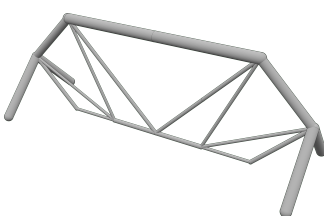


Figure 4.6: Perspective view of the monolithic simply supported 3D beam optimized structure with $V = 9.907 \text{ cm}^3$

⁸⁴ Michell (1904), 'The limits of economy of material in frame-structures'

and performing a multi-load case optimization solely on the module. Moreover, these examples confirm the necessity of adding kinematic compatibility constraints when addressing modularity constraints.

4.2.2. PARAMETRIC STUDY ON THE NUMBER OF SUBDOMAINS AND THE COMPLEXITY OF THE MODULE

Here, we perform a parametric study on the modular parameters that we use to optimize the simply supported 3D truss, which was previously analyzed as a monolithic structure in Section 3.3.4. In this study, we focus on a single module $N_T = 1$, excluding for the moment an examination of the impact of multiple module topologies on the optimized structure. Additionally, we restrict our investigation to a cubic cell shape. A summary of the loading case, as well as the geometric and material properties of the test case, is presented in Table 4.4 and depicted in Fig. 4.5.

We introduce two new metrics used to enhance our understanding of how modular structures are subjected to loading. The first metric, named the structural efficiency index and denoted as φ , enables a rapid assessment of how close the structure is to the optimal fully stressed state as described by Michell [84]. Since we are accounting for not only tensile and compressive stress but also local buckling, we define a bar as fully stressed when it activates one or more of the three mechanical failure constraints. It is defined by the equation:

$$\varphi = \frac{N_{\text{opt},f} \times 100}{N_{\text{opt}}}. \quad (4.8)$$

Here, $N_{\text{opt},f}$ represents the number of bars that activate either the tensile stress, compressive stress, or buckling constraints and is expressed as:

$$N_{\text{opt},f} = \text{card}(\{i \mid c_{f,i} > 0.95\}), \quad (4.9)$$

where $c_f = \max(-q/\sigma_c a, q/\sigma_t a, q/q_{\text{crit}})$ represent the normalized mechanical failure criterion and $\text{card}(\{\cdot\})$ represent the cardinality of the set $\{\cdot\}$.

The second metric, denoted as ψ , is defined as the mean value of the normalized mechanical failure criterion c_f , weighted by the volumes

of individual bars v :

$$\psi = \frac{1}{V} \left(\sum_{i=0}^{N_{\text{opt}}} v_i c_{f,i} \right) \quad (4.10)$$

This parameter ranges between 0 and 1, with higher values indicating that, on average, bars are closer to the upper limit of one of the mechanical failure constraints. Notably, greater importance is attributed to more voluminous bars.

INFLUENCE OF THE NUMBER OF THE SUBDOMAINS We begin by examining the impact of the number (and consequently, the scale, interchangeably used here) of subdomains N_{sub} in the structure. The structure is partitioned into varying numbers of cubic and equal-sized subdomains while keeping the test case and material constant. Specifically, the entire structure is subdivided into $6 \times 2 \times 3$, $12 \times 4 \times 6$, $18 \times 6 \times 9$, and $30 \times 10 \times 15$ submodules along the X , Y , and Z axes, and each subdomain is discretized by a $2 \times 2 \times 2$ fully connected ground structure with $n_{\text{bar}} = 28$. The same analysis is also conducted on a $3 \times 3 \times 3$ fully connected ground structure with $n_{\text{bar}} = 351$ to ensure that trends remain consistent across varying cell complexities.

The parametric findings on the impact of the number of subdomains in the structure are summarized in Table 4.5. The table presents numerical results alongside graphical representations of the optimized structures' modules for varying sizes of the repeating module. The first key observation is the significant influence of the module scale on the optimized volume. This relationship is evident in Fig. 4.7, where the volume exhibits an almost linear correlation with the number of submodules, a trend that persists even for the higher complexity $3 \times 3 \times 3$ modules. Regarding computational time, a similar relationship is noted. Despite the number of design variables remaining constant, the increase is attributed to the growing number of mechanical constraints. It is important to highlight that in modular optimization, mechanical constraints are evaluated for every member of the structure, not just within the module. Finally, the number of active bars in the optimized module shows little dependence on the module scale.

A graphical representation of the 3D structures is provided in Fig. 4.9, showing isometric views as well as views on the XZ planes for the case with a module featuring a $2 \times 2 \times 2$ ground structure. It is interesting to observe how, with increasing physical dimensions of the module, the optimizer naturally converges toward solutions that prioritize long tensile members and short compressive members to satisfy local buckling constraints. However, as the module size decreases (as seen in the $30 \times 10 \times 15$ results), and consequently, the buckling effective length of the members diminishes the optimized design transitions to a configuration where both tensile and compressive members are

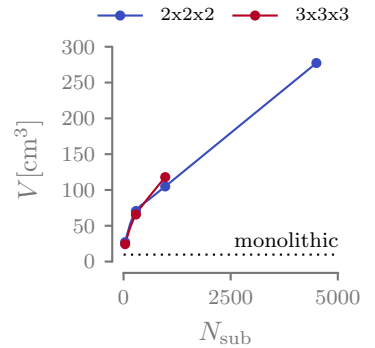


Figure 4.7.: Influence of the number of subdomains on the volume of the optimized modular structure.

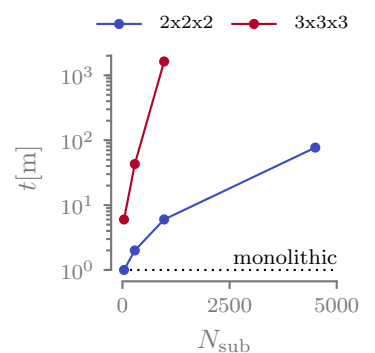


Figure 4.8.: Influence of the number of subdomains on the computational time of the optimization.

Table 4.5.: Numeric results of the parametric study on the influence of the number of subdomains on the optimized structures.

Quantity	7x3x4	2x2x2				3x3x3		
	1x1x1	6x2x3	12x4x6	18x6x9	30x10x15 ^a	6x2x3	12x4x6	18x6x9
—	—							
$\bar{n}_{\text{opt}} (\bar{n})$	1984	9 (28)	9 (28)	8 (28)	8 (28)	19 (351)	15 (351)	16 (351)
N_{sub}	1	36	288	972	4500	36	288	972
$N_{\text{opt}} (N_{\text{el}})$	20 (1984)	(1008)	(8064)	(27216)	(126000)	(12636)	(101088)	(341172)
$V [\text{cm}^3]$	9.907	27.074	70.559	104.891	277.238	24.323	65.723	117.904
$V [\%]$	1.761	4.812	12.544	18.648	49.288	4.324	11.684	20.960
$\bar{\rho} [\text{kg/m}^3]$	80.31	219.48	571.99	850.31	2247.47	197.17	529.55	955.80
$C [\text{J}]$	3.71	4.22	3.35	3.19	1.12	3.63	1.84	2.02
$a_{\max} [\text{mm}^2]$	37.61	9.40	5.45	5.45	3.55	5.33	2.60	3.14
φ	100.00 %	14.81 %	1.85 %	0.67 %	0.12 %	20.51 %	1.46 %	0.62 %
ψ	1.000	0.446	0.178	0.105	0.030	0.327	0.127	0.096
t	4 s	6 s	48 s	5 m 6 s	1 h 17 m	5 m 42 s	42 m 50 s	27 h 17 m

^aIn this test case the minimum slenderness limit is relaxed to $\lambda_{\max} = 10$ instead of 15.

66. Sigmund et al. (2016), 'On the (non-)optimality of Michell structures'

present. This observation aligns with the findings of Sigmund on Michell-like structures [66].

In an attempt to understand why the volume is significantly influenced by the number of submodules, we visualize the trends of the parameters φ and ψ in Fig. 4.10. As depicted, every bar in the monolithic structure activates either the buckling or the stress constraint, resulting in $\varphi = 100\%$ and $\psi = 1$. However, this is not true for any of the modular structures, as seen in the case of 12x4x6-3x3x3, where numerous bars remain inactive and are represented in gray.

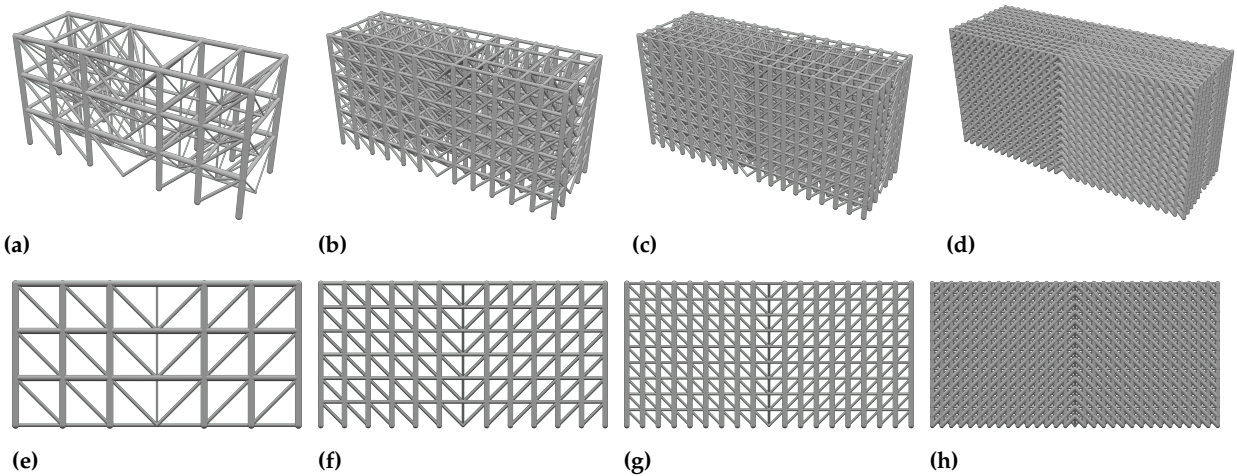


Figure 4.9.: Rendering of the optimized structures with $6 \times 2 \times 3$ (a-e), $12 \times 4 \times 6$ (b-f), $18 \times 6 \times 9$ (c-g), and $30 \times 10 \times 15$ (d-h) subdomains. The module presents a $2 \times 2 \times 2$ complexity.

This phenomenon becomes more apparent in Fig. 4.11, where the stress and buckling constraints are plotted to the optimized structures of both the monolithic and the $12 \times 4 \times 6$ - $3 \times 3 \times 3$ cases. In this illustration, it is evident that in the $12 \times 4 \times 6$ - $3 \times 3 \times 3$ case, many bars remain inactive (gray). Examining Fig. 4.11c and d, we notice that the stress and buckling constraints activate only in one submodule but influence the entire structure to display these constraints. As a result, the modular structure is highly redundant and fail-safe, but this comes at the cost of increased total volume.

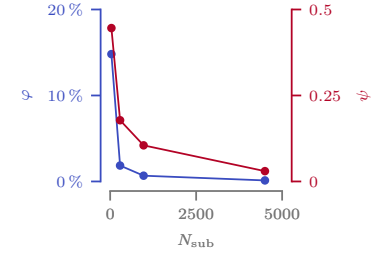


Figure 4.10.: Influence of the number of subdomains on the loading metrics φ and ψ of the optimized structures.

INFLUENCE OF THE COMPLEXITY OF THE MODULE We now shift our focus to another parameter of modular structures: the module complexity, defined as the number of candidate members \bar{n} inside a module. To understand how this parameter influences the optimized structures, we set up an analysis similar to the one previously conducted for the module scale. Utilizing the same test case, we divide the structure into $6 \times 2 \times 3$ submodules along the X, Y, and Z axes, respectively. We discretize each module using a $2 \times 2 \times 2$, a $3 \times 3 \times 3$, a $4 \times 4 \times 4$, and a $5 \times 5 \times 5$ fully connected ground structure ($\bar{n} = 28$, $\bar{n} = 351$, $\bar{n} = 2016$, $\bar{n} = 7750$, respectively). The same analysis is conducted on a $12 \times 4 \times 6$ structure to validate the test on a different modular structure.

The results of the parametric study are presented in a tabular format in Table 4.6, along with the rendering of the module. Once again, we have plotted the most interesting aspects separately. The first aspect we examine is how the volume of the optimized structure is influenced by the module complexity \bar{n} . In Fig. 4.13, we observe that an increase in \bar{n} generally has a beneficial effect on volume. However, this effect becomes less pronounced as complexity increases, and in this particular test case, the volume reduction stagnates after the

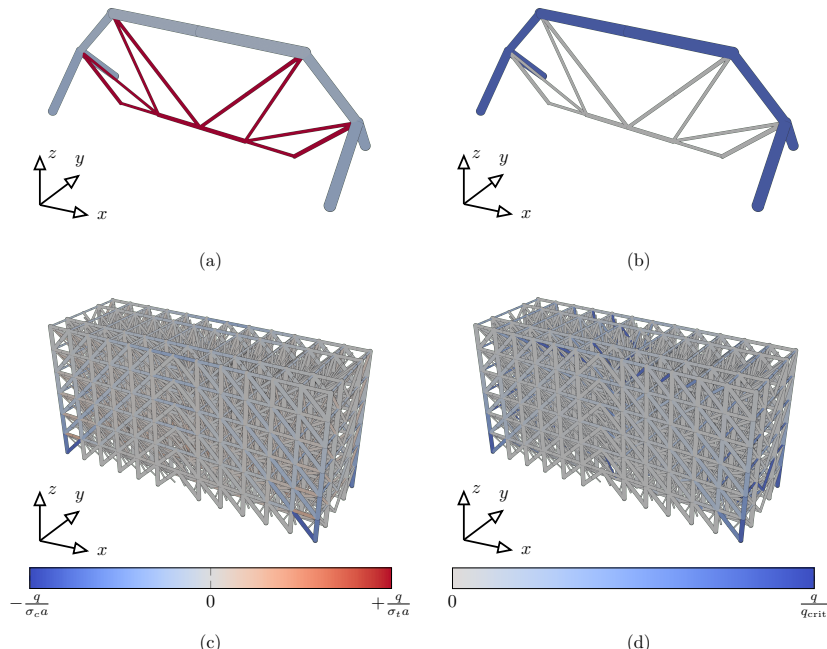


Figure 4.11.: Stress (a-c) and local buckling (b-d) failure criteria plotted on the monolithic and the 12x4x6-3x3x3 cases.

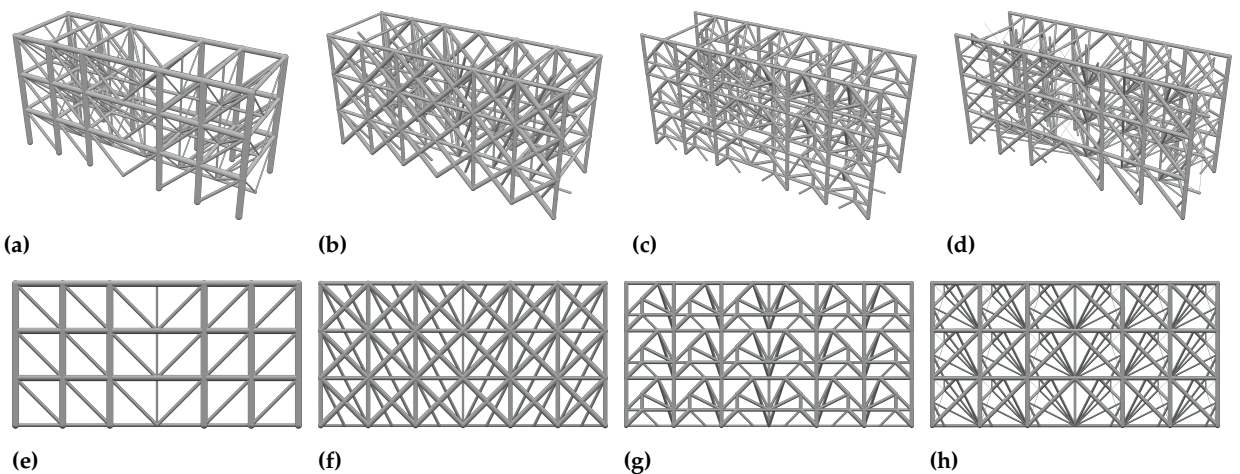
module complexity reaches 4x4x4.

Regarding computational time (see Fig. 4.14), we notice a relationship similar to the one already observed for the submodule scale. The computational time goes up as the module complexity increases. This is understandable because, unlike the case with the number of subdomains, in this scenario, the number of design variables increases along with the number of candidates and, consequently, the constraints.

The 3D renderings of the optimized structures for the 6x2x3 submodules case are presented in Fig. 4.12, allowing the reader to observe the evolution of the module's topology toward greater complexity (from $\bar{n}_{\text{opt}} = 9$ to $\bar{n}_{\text{opt}} = 88$ for the 2x2x2 and 5x5x5 cases, respectively). While in low complexity, the optimizer prioritizes tensile elements, in more complex cases, we observe the apparition of shorter elements less influenced by local buckling.

Table 4.6.: Numeric results of the parametric study on the influence of the module complexity on the optimized structures.

Quantity	6x2x3				12x4x6		
	2x2x2	3x3x3	4x4x4	5x5x5	2x2x2	3x3x3	4x4x4
$\bar{n}_{\text{opt}} (\bar{n})$	9 (28)	19 (351)	88 (2016)	88 (7750)	9 (28)	15 (351)	22 (2016)
N_{sub}	36	36	36	36	288	288	288
$N_{\text{opt}} (N_{\text{el}})$	324 (1008)	468 (12636)	792 (72576)	792 (279000)	2592 (8064)	4320 (101088)	6336 (580608)
$V [\text{cm}^3]$	27.074	24.323	17.098	17.083	70.559	65.723	60.368
$V [\%]$	4.812	4.324	3.040	3.036	12.544	11.684	10.732
$\bar{\rho} [\text{kg/m}^3]$	219.48	197.18	138.60	138.49	571.99	532.79	489.38
$C [\text{J}]$	4.22	3.63	4.49	3.91	3.35	1.84	2.43
$a_{\max} [\text{mm}^2]$	9.40	5.33	3.39	3.77	5.45	2.60	2.97
φ	14.81 %	20.51 %	12.12 %	20.20 %	1.85 %	1.46 %	1.32 %
ψ	0.446	0.327	0.414	0.419	0.178	0.127	0.136
t	6 s	5 m 42 s	14 m 20 s	3 h 17 m	48 s	42 m 50 s	32 h 4 m

**Figure 4.12.:** Rendering of the optimized structures with 2x2x2 (a-e), 3x3x3 (b-f), 4x4x4 (c-g), and 5x5x5 (d-h) module complexity. The number of subdomains is 6x2x3.

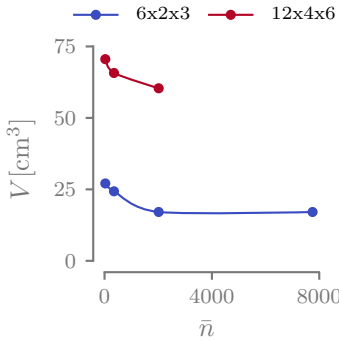


Figure 4.13.: Influence of the module complexity on the volume of the optimized modular structure.

It is interesting to note that the number of active bars in the optimized structure is quite dependent on the complexity of the module. However, in this specific case, we see that it saturates at $\bar{n} = 88$ in the $6 \times 2 \times 3$ case, suggesting that we have reached the convergence of the discretization.

Finally, in Fig. 4.15, we present the numerical values of φ and ψ . Unlike our earlier observations, the trends of these parameters are not monotonic and do not follow an explicit trend. While these indices aid in understanding how much a truss is loaded, they don't necessarily provide clear hints on optimality. A structure loaded to the maximum of the material contributes to achieving a lighter design but is not sufficient, as this example demonstrates.

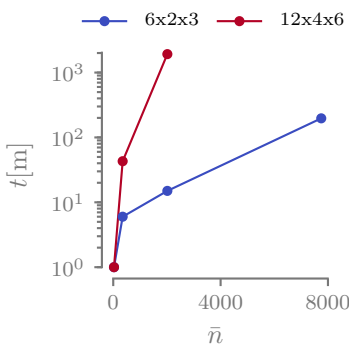


Figure 4.14.: Influence of the module complexity on the computational time of the optimization.

DESIGN OF EXPERIMENTS With the data gathered thus far, we aim to construct the Design of experiments (DOE) for optimized modular structures. The objective is to monitor how the outcomes vary by introducing a change in the preconditions, represented by one or more independent variables. In our case, the chosen independent variables are the number of subdomains N_{sub} (x_1) and module complexity \bar{n} (x_2), while the observed responses are the total structural volume V and the computational time t . For simplicity, we continue to limit ourselves to cubic cells.

We have chosen to use a quadratic model with interaction (the term $x_1 x_2$) in an attempt to capture a potential interference between x_1 and x_2 , represented as follows:

$$a x_1^2 + b x_2^2 + c x_1 x_2 + d x_1 + e x_2 + f \quad (4.11)$$

The coefficients are determined by solving a least squares system using the data presented earlier in this section.

We present the outcomes of the DOE in Fig. 4.16 for the structure volume V . In the upper part of the image, we display the surface response along with a scatter plot of the optimized structures (a), and additionally, the isovalue lines plot (b). It is noticeable that the volume V is strongly influenced by the number of subdomains N_{sub} , as indicated by the horizontal orientation of the isovalue lines. This suggests that the steepest gradient of the function is in the vertical direction. Less voluminous modular structures tend to be structures with fewer subdomains characterized by high complexity \bar{n} . However, when examining subfigures (c) and (d), representing the surface response for computational time t , it is evident that high module complexity \bar{n} is associated with an elevated computational time.

The coefficients of the quadratic model are given in Table 4.7 and Table 4.8 for the volume and computational time, respectively. We see that for the volume the coefficient that defines the most the behavior

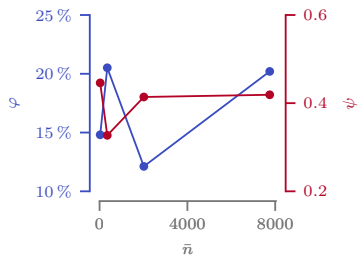


Figure 4.15.: Influence of the module complexity on the loading metrics φ and ψ of the optimized structures.

of the response surface is e , the coefficient that relates to the linear term for the number of subdomains. The interaction between the two independent variables – the coefficient c – is low, showing that the two variables do not add up when modified together. This is not true for the computation time, where the interaction coefficient is relevant, together with the two linear terms. Once again, the quadratic coefficients a and b are less important, suggesting in general a linear response.

The coefficients of the quadratic model are presented in Table 4.7 and Table 4.8 for the volume and computational time, respectively. Notably, for the volume V , the coefficient that predominantly influences the behavior of the response surface is e , which corresponds to the linear term for the number of subdomains N_{sub} . The interaction coefficient between the two independent variables, denoted as c , is low, indicating that the two variables do not significantly contribute when modified together. This is in contrast to computational time, where the interaction coefficient is relevant, along with the two linear terms. In the two cases, the quadratic coefficients a and b are relatively less important, suggesting a generally linear response.

Finally, we present the main effects plot for the volume and module complexity in Fig. 4.17. The concept is to plot, for each factor or interaction, the effect (summed with the overall mean) as a function of the level. The advantage of this representation is to offer an immediate visualization of the various effects.

DISCUSSION ON THE DOE We can utilize this DOE as a tool to give general recommendations. While the specific numeric values and their magnitudes just found are tailored to the presented example, we assume that the observed trends are generally correct and applicable to modular structures as a whole. Therefore, we can conclude that in scenarios where minimizing mass is the primary objective, aiming for the fewest possible number of subdomains is preferred. However, additional constraints must be considered. For example, having fewer subdomains implies an increase in the physical size of individual submodules. Yet, there is often a manufacturing maximum size that restricts this increase. Consequently, the recommendation is to achieve the largest possible subdomains that can be produced within the limitations of the chosen manufacturing technology.

Although higher complexity significantly impacts computational time, its influence on optimization outcomes is not substantial. Therefore, opting for a medium complexity, such as 3x3x3 nodes in the module (or 4x4 in 2D), strikes a balance between computational cost and optimization effectiveness.

Coeff.	Value
a	9.00×10^{-8}
b	-1.02×10^{-5}
c	-1.77×10^{-6}
d	-2.64×10^{-3}
e	1.01×10^{-1}
f	2.88×10^1

Table 4.7.: Coefficients of the quadratic function used to model how the volume V varies with the number of subdomains N_{sub} and the module complexity \bar{n} .

Coeff.	Value
a	1.55×10^{-3}
b	-2.87×10^{-4}
c	2.90×10^{-1}
d	-2.08×10^1
e	-5.54
f	0.00

Table 4.8.: Coefficients of the quadratic function used to model how the computational time t varies with the number of subdomains N_{sub} and the module complexity \bar{n} .

4.2.3. COMPARISON WITH THE OPTIMIZED OCTET-TRUSS

[204.](#) Deshpande et al. (2001), 'Effective properties of the octet-truss lattice material'

The proposed modular TTO algorithm is benchmarked against one of the most popular cell topologies found in the literature: the octet-truss (see Fig. 4.18). The octet-truss is a cell known for its highly effective mechanical properties, achieving about half the theoretical values of the upper Hashin-Shtrikman bounds [204] for isotropic materials.

To conduct the benchmark, the simply supported 3D beam is divided into $6 \times 2 \times 3$ and $12 \times 4 \times 6$ cubic subdomains, which are then populated with the octet-truss topology. The cross-sectional areas of the cell members are all equal, and the numerical value is determined by performing a parametric optimization. The octet-truss structure is constrained by stress, local buckling, and kinematic compatibility constraints for every member of the structure. The optimization is performed using Altair OptiStruct.

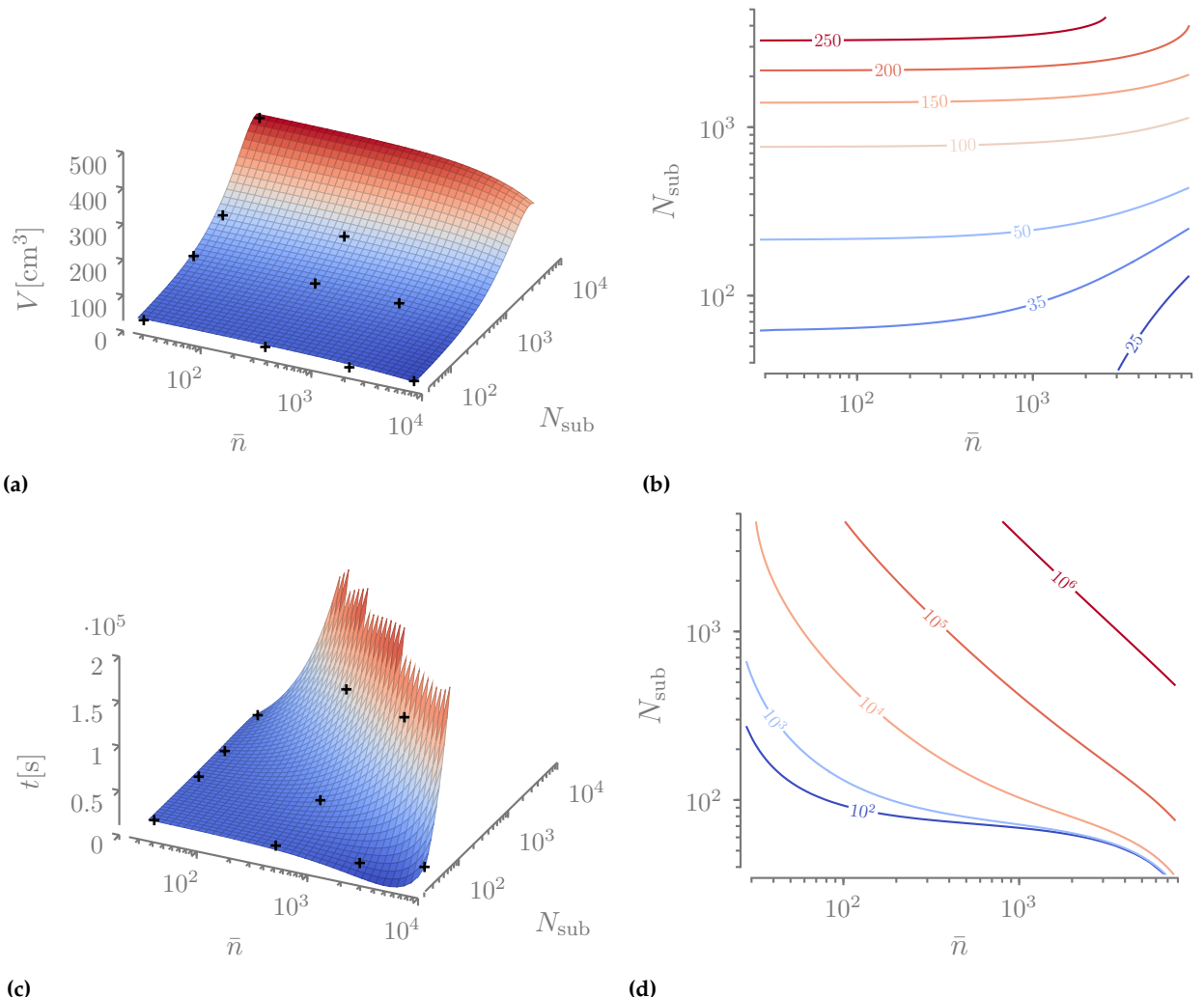


Figure 4.16.: Design of experiments (DOE) response curves and isocurves plot for the volume (a-b) and computational time (c-d).

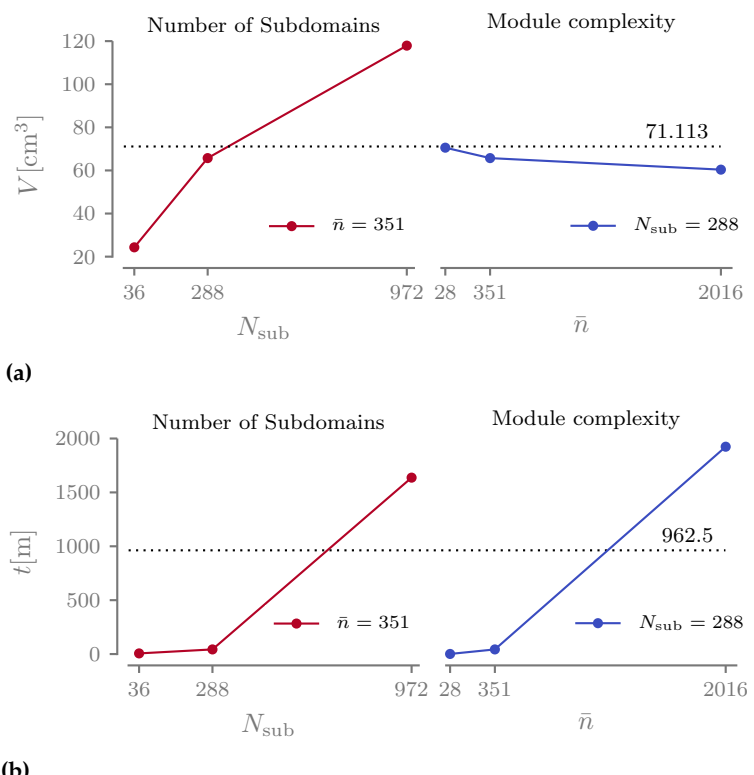


Figure 4.17.: Main effects plot of volume (a) and computational time (b).

Fig. 4.19 displays the 3D rendering of the two optimized octet-truss structures (left part of the image) compared to the modular TTO structures (right part of the image). It is noticeable how the TTO algorithm guides the topology of the module toward higher efficiency, creating vertical columns loaded in compression that support thin wires loaded in tension. On the other hand, the octet-truss topology is fixed and exhibits quasi-isotropic mechanical behavior. The octet-truss is a module with good homogenized elastic properties in all directions, thanks to its numerous planes of symmetry. It is, thus, less suitable for structural applications where all the subdomains experience similar loading conditions. In such cases, the module will be equally stiff and strong in every direction, not aligned with the principal stress directions.

We notice that in the octet-truss structure, there are no members orientated exactly along the z axis, while in the TTO optimized cell, they are the most massive. This tells us that this is the most efficient direction to put the material to get a strong cell. On top of that, the upper and lower faces of the cell present a cross design (see Fig. 4.18) that works well for torque but not for tension and compression loading. A new study exploring what happens if we rotate the cell could be interesting.

The numerical results are presented in Table 4.9 and confirm our observations. The volume of the octet-truss structures is approximately three times and twice the volume of the modular TTO optimized structures for the $6 \times 2 \times 3$ and the $12 \times 4 \times 6$ test cases, respectively. This significant gap between the two types of structures is also evident when examining the values of φ and ψ . These values drop to very low levels because the cross-sectional value of the entire structure is determined by the value at which a bar on the structure becomes critical. For these structures, only four bars are critical (due to symmetry). Better results could have been obtained by providing more design freedom to the optimization of the octet-truss, using multiple cross-sectional design variables, but this approach has not been taken here. It is important to note that the comparison presented here does

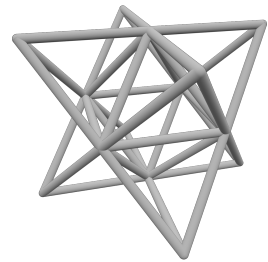


Figure 4.18.: Rendering of a single octet-truss module.

Quantity	$6 \times 2 \times 3$		$12 \times 4 \times 6$	
	Octet	$3 \times 3 \times 3$	Octet	$3 \times 3 \times 3$
N_{sub}	36	36	288	288
$N_{\text{opt}} (N_{\text{el}})$	1008	468 (12636)	7488	4320 (101088)
$V [\text{cm}^3]$	65.752	24.323	121.038	65.723
$V [\%]$	11.692	4.324	21.524	11.684
$\bar{\rho} [\text{kg/m}^3]$	533.03	197.18	981.21	532.79
$C [\text{J}]$	1.67	3.63	1.12	1.84
$a_{\max} [\text{mm}^2]$	3.69	5.33	1.83	2.60
φ	0.39 %	20.51 %	0.05 %	1.46 %
ψ	0.075	0.327	0.026	0.127

Table 4.9.: Numerical results of the comparison between octet-truss and TTO structures.

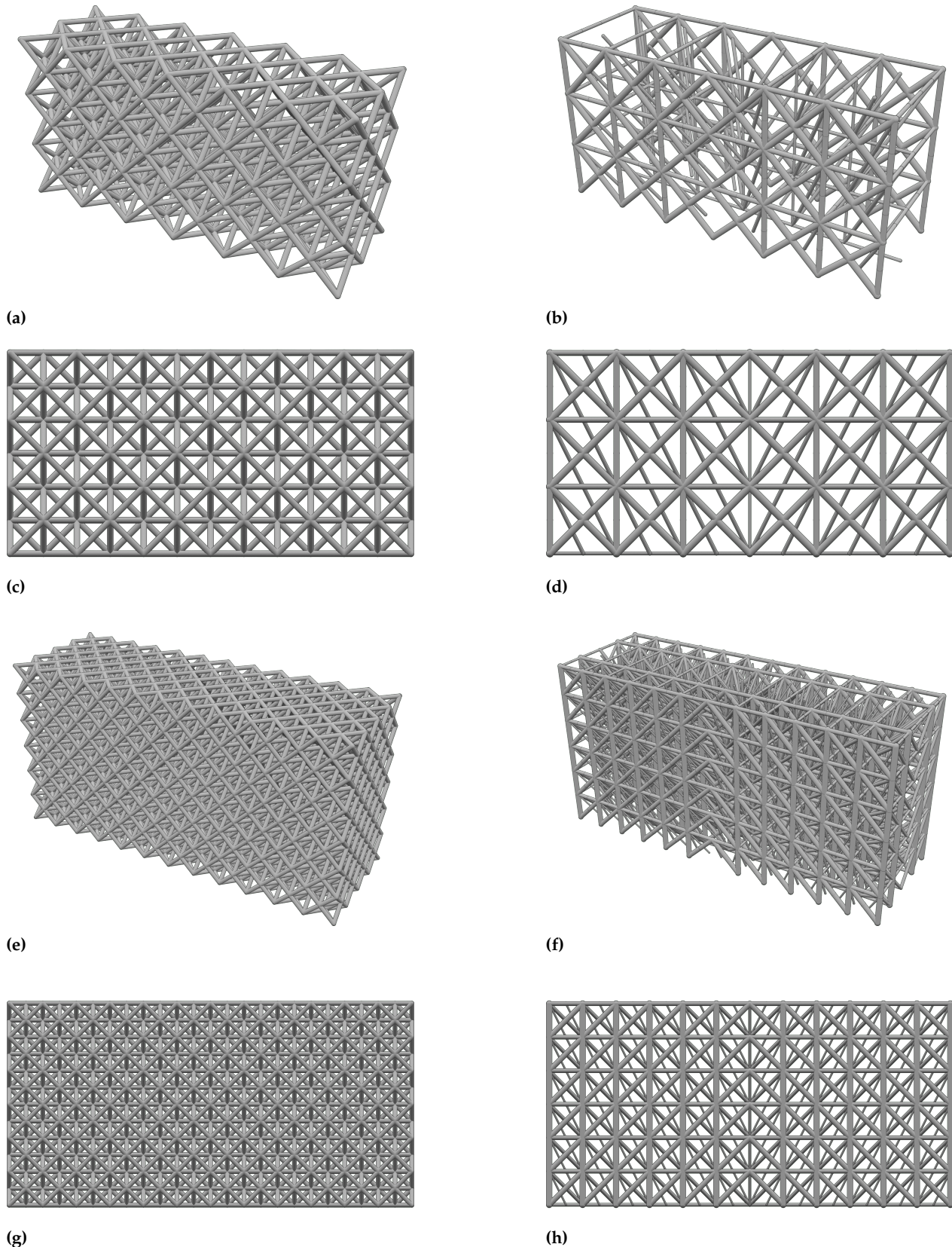


Figure 4.19.: Comparison of the octet-truss structures (a-c-e-g) and the TTO structures (b-d-f-h) for two different numbers of submodules, 6x2x3 and 12x4x6.

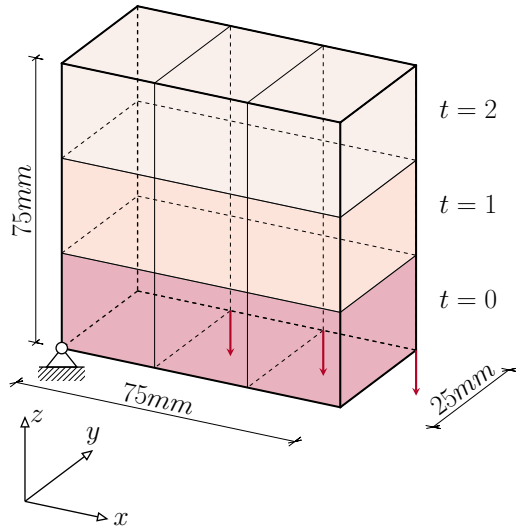


Figure 4.20.: Graphical representation of the given module layout for the simply supported 3D beam.

not account for the weight of fasteners and joints necessary to link the cells together.

4.2.4. USING MULTIPLE MODULE TOPOLOGIES

We have explored two extremes so far – the fully modular and the monolithic structures. Now, we aim to investigate the scenarios in between. Up to this point, our study on modular structures has been limited to a single topology of the module, i.e., $N_T = 1$. This is because, when dealing with multiple module topologies, another crucial question arises: how to optimize the module layout? How should the modules be arranged in the structure to minimize the overall volume of the part? This critical question will be discussed in-depth later in the thesis. For now, as we begin to consider multiple module topologies, we make a significant simplification by determining the layout based solely on good engineering common sense, without an additional optimization process.

Let us reconsider the simply supported 3D beam divided into a grid of $6 \times 2 \times 3$ subdomains. This time, we optimize the structure using three different modules $N_T = 3$. The modules are discretized using an equal fully connected ground structure with $3 \times 3 \times 3$ nodes. The module mapping matrix of the structure is provided as an input for the optimization¹ and it represents the module layout shown in Fig. 4.20.

The optimized structure features an interesting design made by two elongated spars that support multiple tensile members responsible for carrying the given loads. The spars exhibit a design that favors long tensile members, interconnected by compressive bars. The resulting optimized structure is illustrated in Figure 4.21.

We now examine the modules of the optimized structure. Firstly, we observe that the optimizer sets all the cross-sectional areas of module $t = 2$ to zero, judging it as unimportant for the mass optimization of the

1: The module mapping matrix is

$$H = \begin{bmatrix} 1 & 0 & 0 \\ 1 & 0 & 0 \\ 1 & 0 & 0 \\ 0 & 0 & 0 \\ 0 & 1 & 0 \\ 0 & 1 & 0 \\ 0 & 1 & 0 \\ 0 & 0 & 1 \\ 0 & 0 & 1 \\ 0 & 0 & 1 \end{bmatrix}$$

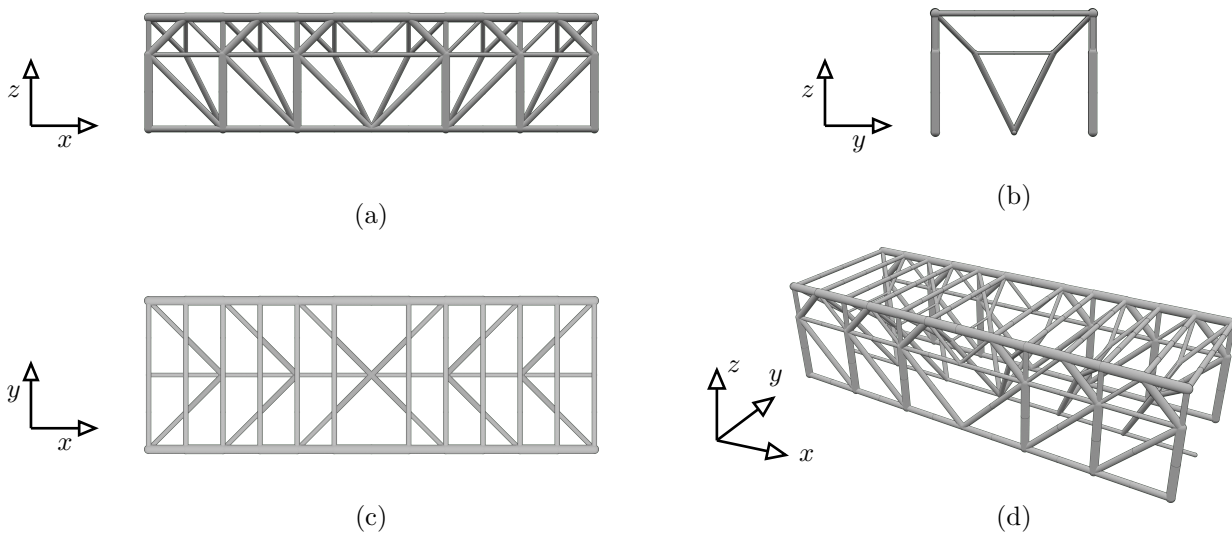


Figure 4.21.: Orthographic views of the topology of the optimized modular simply supported 3D beam. (a) XZ plane (b) YZ plane (c) XY plane (d) auxiliary perspective view.

structure. This highlights the importance of considering the possibility of an empty topology when optimizing the module layout in the structure. Secondly, we note instances where the module is composed of bars that are disconnected e.g. in $t = 0$, potentially necessitating additional post-processing for obtaining a manufacturable design.

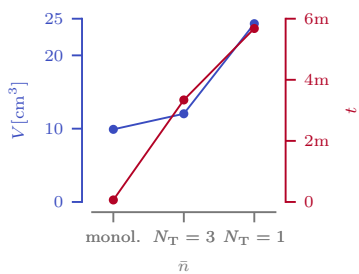


Figure 4.22.: Comparison of the volume and computational time of the structure with multiple modules with the monolithic and the fully modular structures.

The optimized structure with $N_T = 3$ is now compared to the reference monolithic structure and the $6 \times 2 \times 3 - 3 \times 3 \times 3$ structure with $N_T = 3$ to assess the difference in mechanical performance due to the increased number of modules. The results are presented in Table 4.10. Interestingly, the computational time of the $N_T = 1$ solution is lower ($t = 3\text{ m }22\text{ s}$) compared to the $N_T = 3$ structure ($t = 5\text{ m }42\text{ s}$). This comes as a surprise, considering that the $N_T = 1$ optimization problem involves more design variables (as three times the number of cross-sectional areas are optimized). However, it turns out that having more design freedom makes the optimization process easier, as the constraints are more straightforward to satisfy. The trends of the volume and computational time are illustrated graphically in Fig. 4.22.

The volume reduction is attributed to a more efficient utilization of the subdomains' topology, which now varies with the subdomain position. This can be observed by examining the more efficient use of material, with a greater number of bars reaching the mechanical failure limit ($\varphi = 61.90\%$ for $N_t = 3$ compared to $\varphi = 61.90\%$ for $N_t = 1$) and, in general, a more uniform structure loading ($\psi = 0.716$ vs. $\psi = 0.327$). The stress and buckling failure criteria are shown in Fig. 4.23 for further insight.

This study suggests that employing more modules for optimization

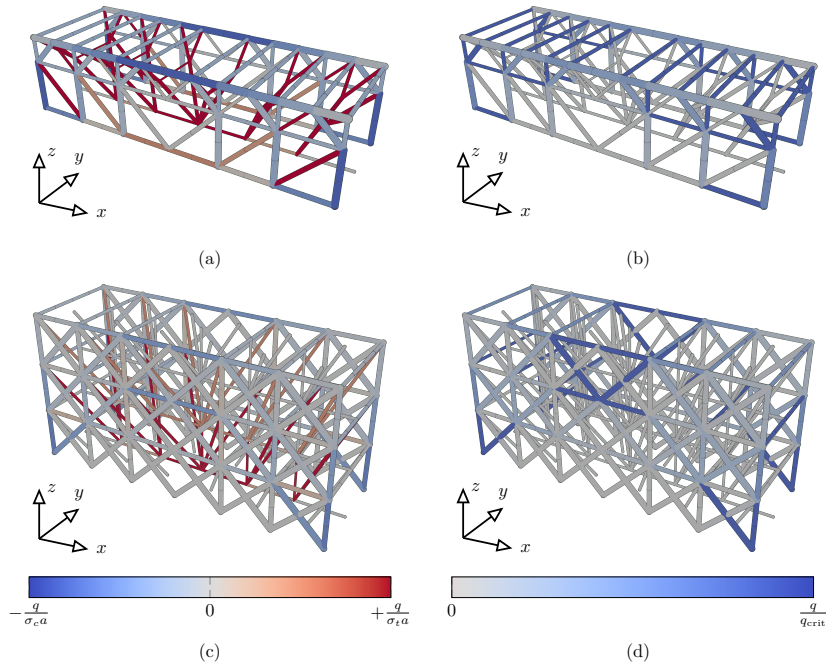


Figure 4.23.: Stress (a-c) and local buckling (b-d) failure criteria plotted on the multiple and single module modular structures.

allows the achievement of less voluminous structures, potentially approaching the performance of monolithic structures. However, this introduces a compromise between volume (and consequently mass) and the ease of manufacturing, a topic we will delve into further in the upcoming chapter.

Table 4.10.: Numerical results of the comparison between the structure with multiple modules with the monolithic and the fully-modular structures.

Quantity	7x3x4	6x2x3-3x3x3- $N_T = 3$			6x2x3 3x3x3 $N_T = 1$
	-	$t = 0$	$t = 1$	$t = 2$	$t = 0$
	-			-	
$\bar{n}_{\text{opt}} (\bar{n})$	1984	10 (351)	18 (351)	- (351)	19 (351)
N_{sub}	1		36		36
$N_{\text{opt}} (N_{\text{el}})$	20 (1984)		336 (12636)		468 (12636)
$V [\text{cm}^3]$	9.907		12.032		24.323
$V [\%]$	1.761		2.139		4.324
$\bar{\rho} [\text{kg/m}^3]$	80.31		97.54		197.18
$C [\text{J}]$	3.71		6.14		3.63
$a_{\max} [\text{mm}^2]$	37.61		7.13		5.33
φ	100.00 %		61.90 %		20.51 %
ψ	1.000		0.716		0.327
t	4 s		3 m 22 s		5 m 42 s

4.3. CONCLUSION

In this chapter, we introduced a modular structure optimization algorithm based on the Truss Topology Optimization (TTO) and variable linking. Initially, we investigated the impact of modularity constraints on the topological buckling phenomenon and sensitivity analysis. Subsequently, we adapted the two-step optimization algorithm with reinitialization presented in Chapter 3 to solve the proposed modular formulation.

The modular TTO algorithm is then tested on multiple two- and three-dimensional test cases. Initially, we observe an equivalence between modular structures and structures loaded with multiple load cases. The utilization of a repeating module throughout the structure significantly impacts the volume, as the module needs to perform well under various loading conditions concurrently. Subsequently, we conducted an extensive parametric analysis of the number of subdomains and module complexity. Based on the results of the Design of experiments (DOE), we provide recommendations: fewer subdomains are generally preferable, with the module as large as manufacturably possible. Module complexity plays a role in volume minimization but has a relatively low impact. Finally, the modular TTO structures are benchmarked against one of the most commonly used module topologies in the literature: the octet-truss lattice.

At the end of the chapter, we conducted a final optimization using multiple module topologies. The incorporation of multiple modules, some of which may have an entirely empty topology, emerged as a crucial factor that contributes to the reduction of modular structure volume. This approach allows modular structures to approach the

volume of monolithic structures while offering additional ease of manufacturing. However, the utilization of multiple modules raises a new question: how are the modules arranged within the different subdomains of the structure?

Chapter 4 introduced the foundational concepts of modular structures and formulated an optimization algorithm designed to optimize structures exhibiting the repetition of a single module topology. Additionally, it conducted a design of experiments to gain insights into the general mechanical behavior of modular structures. We observed that, especially in terms of volume, such structures are significantly penalized when compared to monolithic structures. Towards the end of the chapter, we identified two concepts that could potentially bridge this gap and enhance the performance of modular structures: the incorporation of multiple module topologies and the presence of empty subdomains in the structure where not structurally necessary. In this chapter we formulate an optimization algorithm that incorporates these two improvements.

The chapter is outlined as follows: In Section 5.1, we present an innovative optimization algorithm for modular structures, which concurrently optimizes both the layout and topology of the modules. The initial layout for the optimization is determined by identifying similarly behaving subdomains through a k-means clustering technique. Section 5.2 tests the proposed formulation on multiple two- and three-dimensional cases, considering both normalized and real engineering dimensions and material data.

5.1. OPTIMIZE THE MODULES' LAYOUT USING A MODIFIED DMO ALGORITHM

The objective of this chapter is to address the concurrent optimization of both the layout and topology of multiple modules within a modular structure. The key scientific challenge lies in the discrete nature of the layout optimization problem i.e. find the optimal distribution of the different modules within the subdomains of the structure, an inherently discrete problem. Given our intent to employ a gradient descent algorithm [16], it is imperative to design a methodology for converting the discrete nature of the problem into a continuous one, permitting the application of gradient-based optimization techniques.

5.1 OPTIMIZE THE MODULES' LAYOUT USING A MODIFIED DMO ALGORITHM	97
5.2 NUMERICAL APPLICATION	104
5.3 CONCLUSION	116

16. Sigmund (2011), 'On the usefulness of non-gradient approaches in topology optimization'

5.1.1. DEFINITION OF THE SUBDOMAINS CROSS-SECTIONAL AREAS

In this study, our strategy for addressing the discrete layout problem of modules as a continuous one involves defining the variables of the subdomains (i.e., the structure's variables) as a weighted sum of the module variables. This approach draws inspiration from the seminal work of Stegmann and Lund in the Discrete Material Optimization

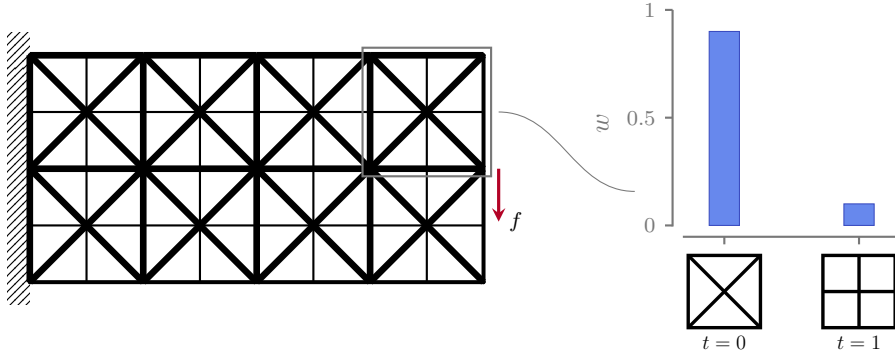


Figure 5.1.: A modular cantilever beam with $N_{\text{sub}} = 8$. The subdomains' topology is defined as the weighted sum of two modules' topologies.

205. Stegmann et al. (2005), 'Discrete material optimization of general composite shell structures'

(DMO) algorithm [205], where an optimizer selects from a set of fixed tensors the optimal homogenized stiffness tensor for each subdomain to minimize the compliance of a given structure. In the scenario of discretizing a ground structure into N_{sub} subdomains and utilizing N_T distinct modules, the cross-sectional areas of subdomain j are expressed as:

$$\bar{a}^j = \sum_{t=1}^{N_T} w_t^j \bar{a}_t \quad (5.1)$$

where \bar{a}_t represent the vector of cross-sectional areas of the t module and w^j is the vector of weight relatives to the j subdomain, defined as $w^j \in \mathbb{R}^t \mid w_j^t \in [0, 1]$.

An example of a cantilever beam with $N_{\text{sub}} = 8$ and $N_T = 2$ is illustrated in Fig. 5.1, in which we visually show the impact of modifying the weight values w on the structure topology.

5.1.2. VARIABLES PENALIZATION SCHEMES

206. Stolpe et al. (2001), 'An alternative interpolation scheme for minimum compliance topology optimization'

The inherent limitation of the proposed approach is that, when the optimizer converges to a solution, the weights of all subdomains must converge to either zero or one, with the additional constraint that only one weight per subdomain can be equal to one. This condition is necessary to avoid intermediate weights, which would imply a combination of multiple modules' topologies lacking mechanical significance and proving impractical for manufacturing. To address this issue, we implement an interpolation scheme that penalizes intermediate weights. Specifically, we opt for the Rational Approximation of Material Properties (RAMP) method [206] instead of the more commonly used Solid Isotropic Material with Penalization Method (SIMP) interpolation scheme. This choice is motivated by RAMP's advantageous property of ensuring that the derivative is never infinite nor zero when the weights approaches a value of zero.

We define the design variable $\alpha \in \mathbb{R}^{j,t}$ as the modules' layout variable, responsible for the module selection within the subdomain j . Its

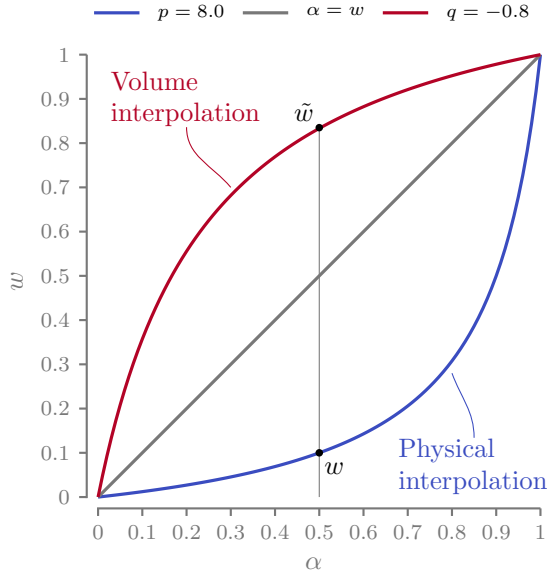


Figure 5.2.: A dual-phase RAMP interpolation scheme is used to penalize the intermediate weights and promote 0-1 designs.

relationship with the weight w is the following:

$$w_t^j = \frac{\alpha_t^j}{1 + p(1 - \alpha_t^j)} \quad (5.2)$$

where $p \in \mathbb{R}^+$ denotes a parameter governing the steepness of the RAMP interpolation. Drawing inspiration from the works of Hvejsel *et al.* [207], we introduce a multi-phase variant of the RAMP interpolation, in which we concurrently penalize mechanical properties while artificially increasing the volume of modules with intermediate densities. To achieve this, we introduce an additional RAMP parameter, q , always negative ($q \in \mathbb{R}^-$), utilized to assess the augmented weights associated with the volume evaluation V . We can then write:

$$V = \sum_{j=1}^{N_{\text{sub}}} \bar{\ell}^T \tilde{a}^j, \quad (5.3)$$

where the vector \tilde{a}^j , representing the increases cross-sectional areas of the j -th subdomain is defined as:

$$\tilde{a}^j = \sum_{t=1}^{N_T} \tilde{w}_t^j \bar{a}_t, \quad (5.4)$$

and where \tilde{w} is:

$$\tilde{w}_t^j = \frac{\alpha_t^j}{1 + q(1 - \alpha_t^j)}. \quad (5.5)$$

So for every design variable α , we associate two different weights w and \tilde{w} that are used to evaluate the mechanical properties and the structure volume, respectively (see Fig. 5.2).

207. Hvejsel et al. (2011), 'Material interpolation schemes for unified topology and multi-material optimization'

5.1.3. THE OPTIMIZATION FORMULATION AND RESOLUTION ALGORITHM

The objective function of the optimization process is the volume minimization of the modular structure. The members of the structure are subject to multiple mechanical constraints, namely stress, topological buckling, minimum slenderness, and compatibility constraints. Formulation \mathbb{M}_1 is stated in terms of modules' cross-sectional area \bar{a} , module selection variables α , member forces q , and nodal displacements U as follows:

$$\begin{aligned}
 \min_{\bar{a}, \alpha, q, U} \quad & V = \sum_{j=1}^{N_{\text{sub}}} \bar{\ell}^T \tilde{a}^j \quad (\text{Volume minimization}) \\
 \text{s.t.} \quad & \mathbf{B}q = f \quad (\text{Force equilibrium}) \\
 & q = \frac{aE}{\ell} b^T U \quad (\text{Compatibility constraints}) \\
 & q \geq -\frac{sa^2}{\ell^2} \quad (\text{Euler buckling constraints}) \quad (\mathbb{M}_1) \\
 & -\sigma_C a \leq q \leq \sigma_T a \quad (\text{Stress constraints}) \\
 & \bar{a}_{t,r} \geq \bar{a}_{t,r=1} \quad r \in \mathcal{C}_{l,r}(\bar{a}_t), \forall t \\
 & 0 \leq \bar{a} \leq \frac{4\pi\bar{\ell}^2}{\lambda_{\max}} \quad (\text{Slenderness limit}) \\
 & \sum_{t=1}^{N_T} \alpha_t^j \leq 1, \forall j \quad (\text{One selected module max.})
 \end{aligned}$$

This formulation builds on the classic DMO approach, adding multiple mechanical constraints and while operating on a ground structure. Additionally, we are not only selecting the best module for every subdomain by changing the value of α as classic DMO does, but we are also optimizing the modules' topology simultaneously. This simultaneous optimization presents a more challenging task. The advantages of this formulation lie in dealing with a discrete problem using continuous design variables and a gradient-based optimizer. However, it comes with the drawback of increasing the problem size, as we are adding numerous additional design variables α that scale with the number of subdomains and the number of modules i.e. a vector of size $\alpha^j \in \mathbb{R}^t$ is defined for every one of the j subdomains.

The design variables α are constrained by a set of constraints that limit the maximum sum of α of a submodule j to be less than or equal to one. It is crucial to note that we treat this constraint as a disequality constraint rather than an equality. This allows the optimizer to set all α to zero, permitting the removal of the subdomain from the structure. The constraint g_{sum} is expressed as follows:

$$g_{\text{sum}} := \sum_{t=1}^{N_T} \alpha_t^j \leq 1, \forall j \quad (5.6)$$

Problem \mathbb{M}_1 is tackled using a modified version of the proposed two-step solving algorithm. In this approach, we initially solve a relaxed problem denoted as \mathbb{M}_2 , where kinematic compatibility constraints are omitted. This relaxed problem is inherently nonlinear due to the introduction of the α design variables. For this iteration, we have chosen to solve it in this form without linearizing the buckling constraints.

The relaxed formulation \mathbb{M}_2 , expressed in terms of modules' cross-sectional area \bar{a} , module selection variables α , and member forces q , is the following:

$$\begin{aligned}
 \min_{\bar{a}, \alpha, q} \quad & V = \sum_{j=1}^{N_{\text{sub}}} \bar{\ell}^T \bar{a}^j \quad (\text{Volume minimization}) \\
 \text{s.t.} \quad & \mathbf{B}q = f \quad (\text{Force equilibrium}) \\
 & q \geq -\frac{s a^2}{\ell^2} \quad (\text{Euler buckling constraints}) \\
 & -\sigma_C a \leq q \leq \sigma_T a \quad (\text{Stress constraints}) \tag{\mathbb{M}_2} \\
 & 0 \leq \bar{a} \leq \frac{4\pi\bar{\ell}^2}{\lambda_{\max}} \quad (\text{Slenderness limit}) \\
 & \sum_{t=1}^{N_T} \alpha_t^j \leq 1, \forall j \quad (\text{One selected module max.})
 \end{aligned}$$

Problem \mathbb{M}_2 is solved using a non-linear gradient-based optimizer that iteratively exploits first and second-order derivatives to achieve convergence. The computation of the Jacobian and Hessian matrices for this problem is not trivial, and the details are elaborated in Appendix A.

Once problem \mathbb{M}_2 is solved, we prepare for the second step, in which the structure's layout is fixed (we remove α from the second optimization), and the kinematic compatibility constraints are reintroduced. We use the optimized module layout α^* to establish the fixed module layout on the structure and evaluate the mapping matrix H used in the variable linking approach of problem $\mathbb{M}_{1,\text{VL}}$. The indices of the mapping matrix H are determined as follows:

$$h_{j,t} = \begin{cases} 1 & \text{if } \alpha_{j,t}^* = \max(\alpha_j^*) \text{ and } \alpha_{j,t}^* > 0.01 \\ 0 & \text{otherwise.} \end{cases} \quad (5.7)$$

Subsequently, the compatibility constraints are reintroduced, and a Finite Element Analysis (FEA) is conducted to evaluate the displacements \mathbf{U} used in the starting point of the following optimization step. To mitigate the risk of becoming trapped in local minima, the second step is solved on a reduced design space. The solution \bar{a}^* of the first optimization is used to simplifying the initial ground structure, thereby eliminating elements from the optimization that fall below

the specified threshold value a_{thr} :

$$\bar{a}_i < a_{\text{thr}} \quad \forall i, \text{ with } a_{\text{thr}} = \chi \max(\bar{a}^*), \quad (5.8)$$

with the parameter χ is the cross-sectional area threshold value.

Formulation $M_{1,\text{VL}}$, defined in Chapter 4 permits to optimize modular structures with fixed module layout using the variable linking approach. It is stated in terms of modular cross-sectional areas \bar{a} , member forces q and nodal displacements U as follows:

$$\begin{aligned} \min_{\bar{a}, q, U} \quad & V = \ell^T a \\ \text{s.t.} \quad & a = \sum_{t=1}^{N_T} h_t \otimes \bar{a}_t \\ & Bq = f \\ & q = \frac{aE}{\ell} b^T U \\ & q \geq -\frac{s a^2}{\ell^{*2}} \\ & -\sigma_c a \leq q \leq \sigma_t a \\ & \bar{a}_{t,r} \geq \bar{a}_{t,r=1} \\ & 0 \leq \bar{a} \leq \frac{4\pi\bar{\ell}^2}{\lambda_{\max}}, \end{aligned}$$

152. Bakker et al. (2021), 'Simultaneous optimization of topology and layout of modular stiffeners on shells and plates'

Now, with all the components in place, we can set up the variable linking formulation $M_{1,\text{VL}}$, as defined in Chapter 4. This formulation is employed to optimize modular structures with a fixed modules' layout and provide the final optimized design.

5.1.4. OPTIMIZATION INITIALIZATION: A CLUSTERING ALGORITHM TO IDENTIFY SIMILARLY BEHAVING SUBDOMAINS

Solving the first step of the proposed optimization formulation, we not only adjust the design variables responsible for the modules' layout (α) but also optimize the modules' topology (\bar{a}). However, a significant challenge arises in this problem due to the strong interdependence between them i.e. the topology of the module is optimized in function of the layout and *vice versa*. It becomes particularly challenging for a gradient-based optimizer to determine the appropriate direction to follow e.g. to reduce the value of the cross-sectional area of a member, the optimizer could play with α , \bar{a} or potentially both at the same time. This is especially true when starting from a completely uniform initial point (as observed in the work of [152]). To mitigate this challenge, we provide a slightly influenced starting point for the optimization process. We influence the module topology design variable at iteration zero α_{init} as follows:

$$\alpha_{t,\text{init}}^j = \begin{cases} \frac{1}{N_T} \cdot 1.1 & \text{if the } j\text{-th subdomain has the } t\text{-th module selected,} \\ \frac{N_T-1.1}{N_T(N_T-1)} & \text{otherwise.} \end{cases} \quad (5.9)$$

The idea behind how to select the best module for a subdomain is to identify subdomains that show similar mechanical behavior, grouping them based on their stress state. This grouping is assessed using a k-means clustering technique with the number of clusters equal to the number of module topologies N_T . Given a set of observations $(x_1, x_2, \dots, x_{N_{\text{sub}}})$, where each observation is a \bar{n} -dimensional real vector, k-means clustering aims to partition the N_{sub} observations into N_T sets. In our context, each observation is the vector containing the Finite Element Analysis (FEA) calculated stress distribution on the initial ground structure with a uniform cross-sectional area.

Additionally, besides the \bar{n} stress values, we introduce the stress state S for the j -th submodule as:

$$S^j = \sum_{i=0}^{\bar{n}} |\sigma_i^j| \quad (5.10)$$

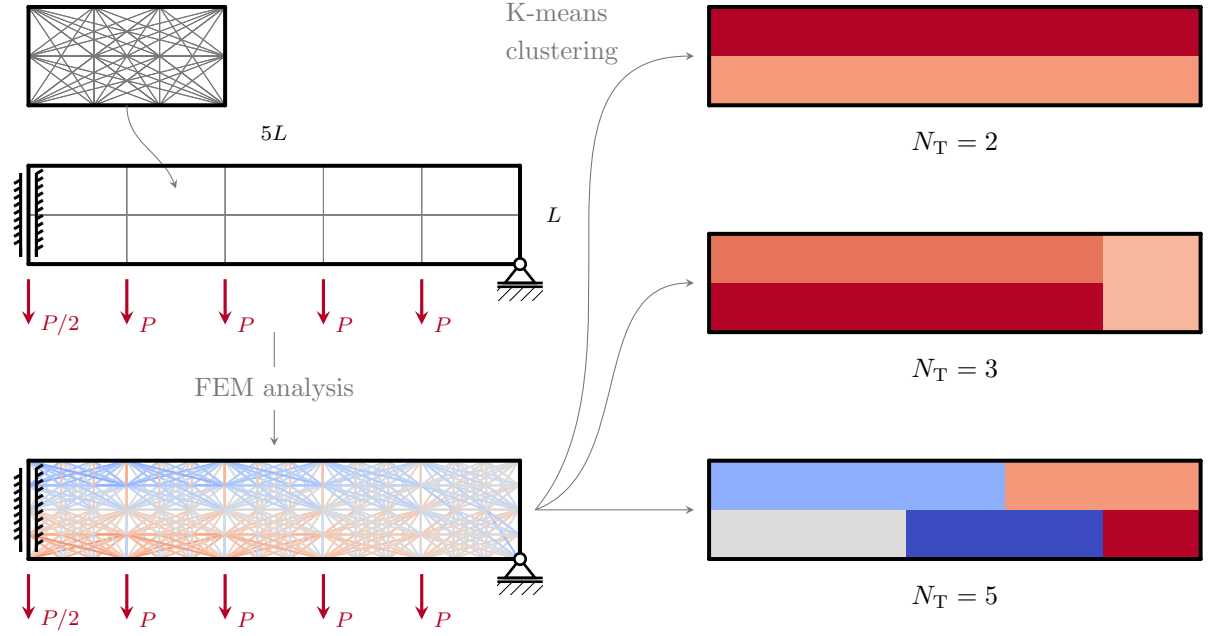


Figure 5.3.: The stress values of the initial ground structure evaluated using a Finite Element Method (FEM) analysis are used to identify similar behaving subdomains. The sets are calculated using the k-means clustering technique with N_T number of clusters.

This addition promotes the clustering not only of submodules loaded in similar ways but also based on similar magnitudes, thereby accounting for variations in voluminous and less voluminous modules.

The full clustering process is depicted in Fig. 5.3, showcasing how the grouping is conducted from the same starting point (FEA-calculated stress distribution on the uniform initial ground structure) but with different numbers of clusters ($N_T = 2, 3$, and 5). Finally, Fig. 5.4 illustrates the initial starting point of the optimization, with a uniform initialization of \bar{a} and the biased weight distribution based on the k-means clustering.

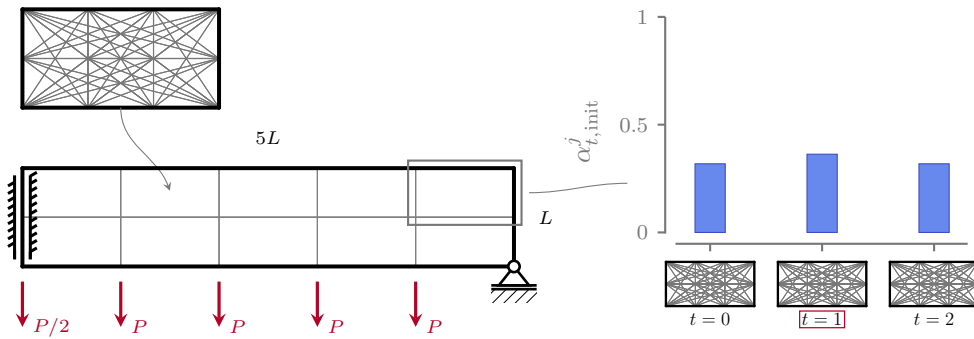


Figure 5.4.: The proposed starting point for the first-step of the optimization: a fully-connected ground structure with uniform cross-sectional areas and a biased α_{init} distribution, as suggested by the k-means clustering.

5.2. NUMERICAL APPLICATION

The proposed algorithm to optimize layout and topology of modular structures is tested in this section against multiple two- and three-dimensional test cases. All examples presented are solved using a modified version of the proposed two-step formulation. In the first step, a relaxed formulation (without compatibility constraints) is solved to determine the optimized modules' layout and topology. Subsequently, the layout of the modules is fixed, and the optimization problem is solved again to ensure compliance with the compatibility constraints. Both formulations are solved using the nonlinear interior point solver IPOPT.

A continuation scheme is established on the penalization parameter q of the RAMP interpolation scheme, utilized for evaluating the subdomains' volume. The parameter at the beginning of the optimization is set to zero and is then reduced to -0.4 and -0.8 each time the optimizer both satisfy the following criteria: the relative volume difference of two successive iterations $(V_i - V_{i-1})/V_i$ is less than 1×10^{-4} and the optimizer is not in a restoration phase. This continuation scheme is implemented only on the q parameter responsible for the volume evaluation. This because, as IPOPT is an interior point algorithm, and increasing the p parameter would place the optimizer well outside the feasible region each time it is increased, resulting in a suboptimal situation. The parameter χ , referred to as the cross-sectional area threshold value, is set to 1×10^{-4} .

The cross-sectional area threshold value χ is used to threshold the bars of the original ground structure to reduce the number of candidates of the second step of the optimization. The candidates bars are the ones that satisfy the following inequality:

$$\bar{a}_i < a_{\text{thr}} \quad \forall i, \text{ with } a_{\text{thr}} = \chi \max(\bar{a}^*)$$

The stopping criterion employed for the first step optimizations is $\|\Delta_{\text{NLP}}\|_\infty \leq \text{tol}_{nlp}$, where $\text{tol}_{nlp} = 10^{-8}$. Here, Δ_{NLP} represents the scaled Non-Linear Programming (NLP) error, a comprehensive value used by IPOPT to consider both the optimality of the solution and constraint violations. The objective function is scaled such that the initial volume is 1000, the areas fall within the interval [0, 100], the initial forces range within [0, 100], and the α design variables lie within [0, 1]. Several additional parameters are utilized in the first optimization step for CyIpopt and IPOPT:

- ▶ `mu_strategy` is set to `adaptive`
- ▶ `num_linear_variables` is set to `N`, where N is the number of bars as the force is linear in this problem
- ▶ `grad_f_constant` is set to `yes`
- ▶ `bound_push` is set to `1e-12`
- ▶ `constr_viol_tol` is set to `1e-6`
- ▶ `nlp_scaling_method` is set to `user-scaling`.

For the settings of the second step optimizer the reader can refer to Chapter 4.

5.2.1. LAYOUT OPTIMIZATION OF FIXED TOPOLOGY MODULES

The proposed optimization formulation is highly versatile, allowing the solution of various optimization problems. We begin by optimizing the most straightforward modular structure problem. The objective is to optimize the distribution i.e. the layout, of a single ($N_T = 1$) fixed-topology module within a specified domain. The optimization process involves deciding whether each subdomain should be populated or not. For this scenario, we consider a single fixed module topology, setting $\bar{a}_i = 0.6$ for all i . The only degree of freedom granted to the optimizer is, thus, the value of the weight w , controlled by the design variable α .

The structure subject to optimization is a two-dimensional cantilever beam with dimensions 200×100 , subjected to a center load of magnitude $P = 1$ and directed downward. The optimization domain is divided into 24×12 subdomains along the X and Y axes, respectively. Each subdomain is populated with a simple fully connected 2×2 nodes ground structure comprising 6 candidate bars, as illustrated in Fig. 5.5. The units of the test case are normalized, and a list of the geometry and material parameters is provided in Table 5.1. In these examples, buckling and compatibility constraints are not taken into account for simplicity and to preserve the solution symmetry.

Before showcasing and discussing the optimization results, we present two extreme cases that help us better understand and contextualize the optimization outcomes. First, we establish a monolithic optimization with no modular constraints, setting a maximum cross-sectional area $a_{\max} = 0.6$. The optimization is conducted on the same ground structure illustrated in Fig. 5.5. This result should represent a lower bound of the optimization, indicating the minimum value towards which modular optimization should tend; the closer to this value, the better. The resulting topology exhibits a volume $V = 832.848$ and a structure resembling those obtained in classic topology optimization. Secondly, we present a fully modular structure, where all subdomains adopt the topology of the fixed topology module with all cross-sectional areas set to 0.6. In this case, the structure demonstrates a volume $V = 9832.935$ and serves as the upper bound for the

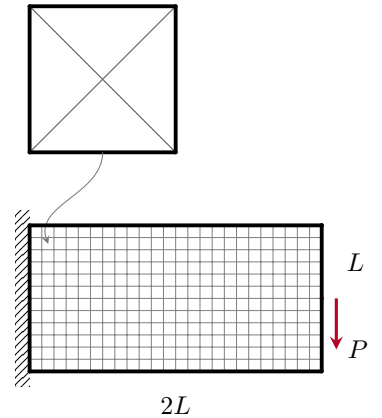


Figure 5.5.: Boundary conditions of the 2D cantilever beam divided in 24×12 subdomains. In the upper part of the image the ground structure of the module composed of $\bar{n} = 6$ elements.

Parameter	Value
L	100
σ_c, σ_t	± 1
P	1
a_{\max}	0.6

Table 5.1.: Material data used for the 2D cantilever beam.

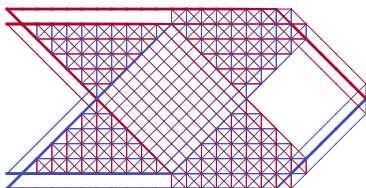


Figure 5.6.: Monolithic optimized structure for the cantilever beam 2D test case with a maximum cross-sectional area $a_{\max} = 0.6$. This solution represents the lower bound solution for this test case with a volume $V = 832.848$.

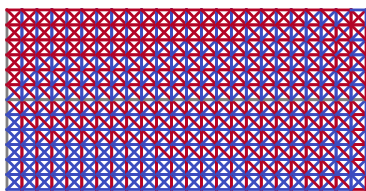


Figure 5.7.: Fully-modular structure in which every subdomain is populated with the given module. The structural volume is $V = 9832.935$.

optimization. The topology of this fully modular structure is depicted in Fig. 5.7.

Now that we have established a reference for better understanding the optimization results, we proceed with the optimization of the layout of the fixed-topology module. For the first example, we decided not to penalize intermediate weights, setting $p = q = 0$, and consequently $w = \alpha$. The optimized structure topology is illustrated in Fig. 5.8a and Fig. 5.8b, where we also depict the weight distribution of the solution. At this stage, the optimized structure exhibits a volume $V = 1567.216$, a value not significantly distant from the monolithic reference ($V = 832.848$). However, this solution is non-physical as many subdomains display intermediate weights (see the weight distribution in Fig. 5.8c), requiring a thresholding operation on the value of w . The thresholding value is set to 0.01, such that any j subdomain with a weight w less than this value is considered empty. The result of the thresholding is presented in Fig. 5.8d, where we observe that all weights are now set either to 1 or 0. The resulting structure has a volume $V = 8808.671$, indicating a noticeable volume increase due to the high number of intermediate weights in the solution shown in Fig. 5.8b and very similar to the upper bound structure for the considered problem shown in Fig. 5.7.

To address this issue, we implement a multi-phase RAMP interpolation where we simultaneously penalize mechanical properties (using the parameter p) and artificially increase the volume (using the parameter q) of modules with intermediate weights. In this optimization, we set $p = 8$ and $q_{\min} = -0.8$, and a continuation scheme is employed on the q parameter to gradually decrease it to the minimum value, as explained in Section 5.2. The optimized structure topology with penalized intermediate weights is depicted in Fig. 5.8e and Fig. 5.8f, with a resulting volume $V = 1961.175$, representing a 25 % increase compared to the unpenalized structure. However, it is evident that this solution presents fewer subdomains with intermediate weights, as reflected in the thresholding phase shown in Fig. 5.8h, where the volume is now $V = 3414.214$, more than 60 % less than the unpenalized structure. These behaviours are similar to what we already experienced with classic topology optimization [51, 66].

Now that we have assessed the need for a penalization scheme, we test the proposed optimization formulation with some test cases using multiple fixed modules. As the topology of the module (\bar{a}) is not modified, no perturbation is made to the initial starting point, and α_{init} at iteration 0 is set to $\alpha_{t,\text{init}}^j = 0.5, \forall j, t$.

The first test we conducted was to optimize the layout of two different modules ($N_T = 2$) that present the same module topology connectivity but different cross-sectional areas. We used two 2-nodes fully connected modules with uniform cross-sectional areas set to 0.6 and

51. Bendsøe et al. (1999), 'Material interpolation schemes in topology optimization'

66. Sigmund et al. (2016), 'On the (non-)optimality of Michell structures'

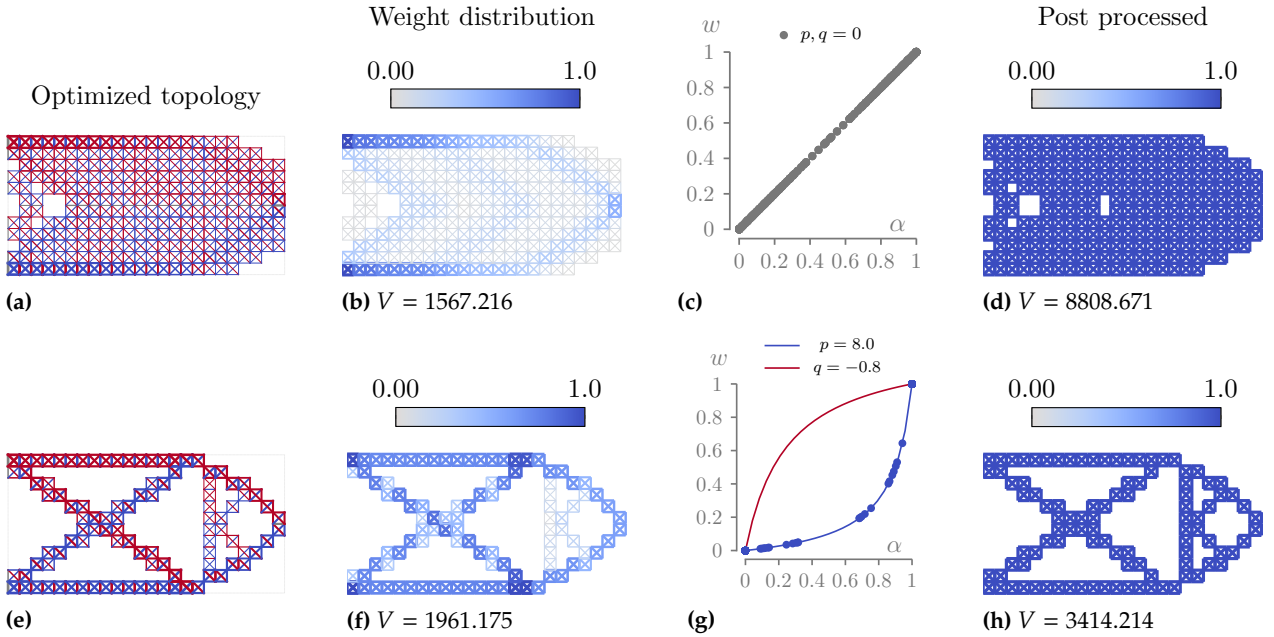


Figure 5.8.: Optimization of the fixed module topology 2D cantilever beam. (a-d) shows the solution without penalizing intermediate weights with a final volume $V = 8808.671$; (e-h) shows the solution in which the RAMP interpolation helps reducing intermediate weights. The final structural volume is $V = 3414.214$.

0.2 to simulate high and low density modules for high and low-stress parts of the structure. The results are presented in Fig. 5.9a and b, and the optimized structure has a volume $V = 2987.437$. This represents a 12 % improvement over the single fixed topology.

Similar results are presented in Fig. 5.9c and d, in which we optimize the module layout of two modules that present different mirrored topologies (see Fig. 5.9d). The structure optimized in this way exhibits a very different module layout and a final volume $V = 2317.462$, even better than before. These two examples confirm that giving more design freedom to the optimizer can enhance the mechanical performance of the modular structure.

5.2.2. MODULES AND LAYOUT OPTIMIZATION

We now optimize a modular structure using multiple modules that can vary their topology (the values of $\bar{\alpha}$ are no longer fixed). In the case of $N_T = 1$, the starting point for the value of α_{init} is still trivial to evaluate ($\alpha_{\text{init}}^j = 1, \forall j$), and the resulting structure, along with the optimized module topology, is shown in Fig. 5.10a and b. The modular structure exhibits a volume $V = 2107.983$, the best found until this point, confirming the interest in optimizing both the modules' topology and layout.

Moving on to the layout and topology optimization of modular structures with a number of module topologies $N_T > 1$, it becomes necessary to employ k-means clustering to determine the initial values

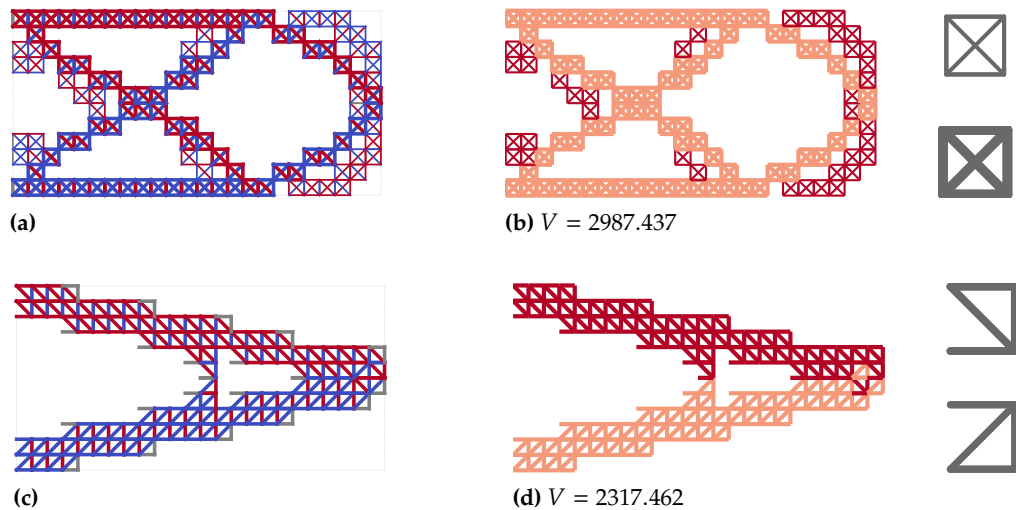


Figure 5.9.: Two different examples of the optimization of a modular 2D cantilever beam using $N_T = 2$ fixed topology modules. (a-b) show the topology and the module layout of the structure obtained using two modules with identical topology, but different cross-sectional areas, while the solution showed in (c-d) is obtained using two modules with identical cross-sectional areas, but different topology. In (a) and (c) red bars are loaded in tension, while blue bars are loaded in compression.

Figure 5.10.: Optimized topology of the modular structure (a) and the module (b) for the 2D cantilever beam optimized using a single module ($N_T = 1$). Red bars are loaded in tension, while blue bars are loaded in compression.

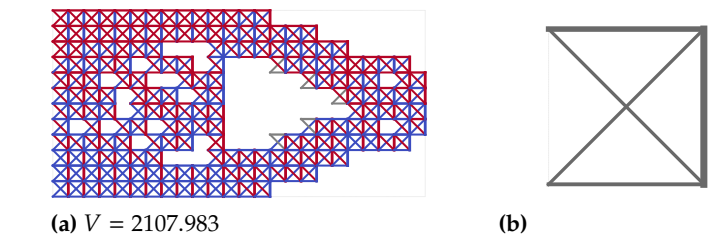
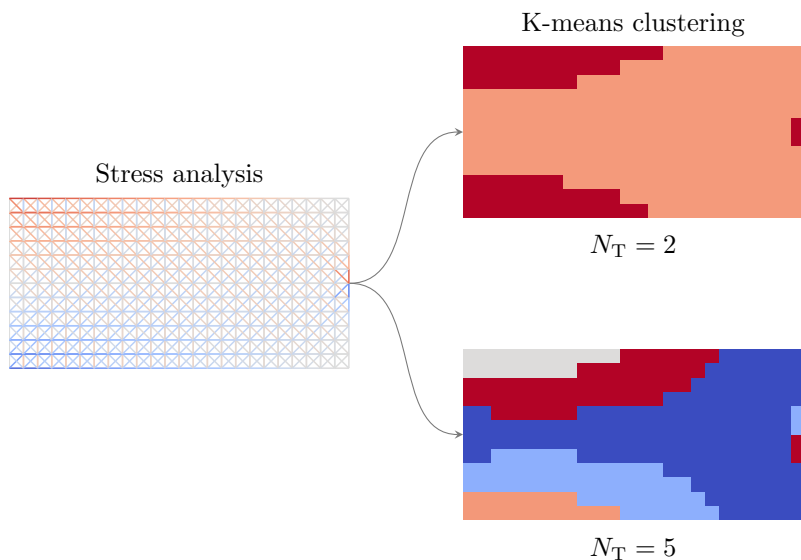


Figure 5.11.: Similarly stressed sub-modules are identified using the k-means clustering algorithm to suggest a starting point for the first step of the proposed optimization algorithm. In the figure we show the resulting distribution for $N_T = 2$ and $N_T = 5$ obtained from the FEA stress.



N_T	1	2	3	4	5
N_{sub}	288	288	288	288	288
$N_{\text{sub}, e}$	107	45	72	43	50
V	2107.983	1722.606	1730.047	1589.899	1416.048
a_{\max}	0.37	0.35	0.48	0.54	0.53
φ	17.16 %	17.86 %	14.20 %	17.95 %	16.65 %
ψ	0.52	0.59	0.57	0.61	0.67
t	35 s	18 s	14 s	17 s	26 s

for the layout module variable α_{init} . A FEM analysis is conducted on the starting ground structure with uniform cross-sectional areas, and the k-means clustering is used on the stress distribution using N_T different clusters. This process is showed for $N_T = 2$ and $N_T = 5$ in Fig. 5.11, where it is observed that, in general, the clusters tend to align with more and less stressed zones more than different type of stress solicitation i.e. direction of principal stress, more compressive or tensile loads. This fact is particularly evident in the $N_T = 2$ example. It is only when the number of clusters reaches $N_T = 5$ that a distinction between tension and compression becomes apparent, resulting in a solution that is no more symmetrical with respect to the neutral axis of the beam.

Starting from the advised starting point from the k-means clustering, the optimizations are performed for N_T from 2 to 5, and their results are summarized in Table 5.2. Here are the main takeaways: looking at the evolution of the volume of the optimized structures with the different numbers of modules N_T , we notice how they behave as expected, as a monotonically decreasing function. This behavior could be explained by the general specialization of the modules that can shape their topology for more specific load cases and be less general-purpose, increasing the structure efficiency and reducing the redundancies. Indeed, we can observe that the value of the average bar load φ is increasing with the number of module topologies. these two effects are illustrated in Fig. 5.12. Additionally, it is interesting how, with an increase in the number of module topologies, the number of empty subdomains $N_{\text{sub}, e}$ drops from 107 and stabilizes at around 50. This suggests that for this specific test case, employing more module topologies results in fewer empty subdomains, indicating that it is better to have many light modules rather than few strong and heavy ones. Concerning the calculation time, we observe no real correlation with the number of modules. We speculate that even if the number of design variables increases with the number of modules N_T , the problem is often easier to solve, and fewer iterations are necessary to attain convergence. The topology of the modular structure with $N_T = 2$ and $N_T = 5$ is shown together with their optimized modules in Fig. 5.13. Finally, it is interesting to notice how the optimized structures exhibit similar module layouts concerning the number of module topologies.

Table 5.2.: Numeric results of the parametric study on the influence of the number of modules on the optimized 2D cantilever beam.

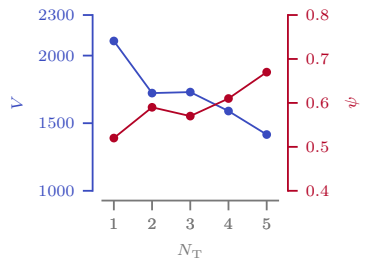


Figure 5.12.: Influence of the number of modules N_T on the volume V and the loading metric ψ of the optimized 2D cantilever beam.

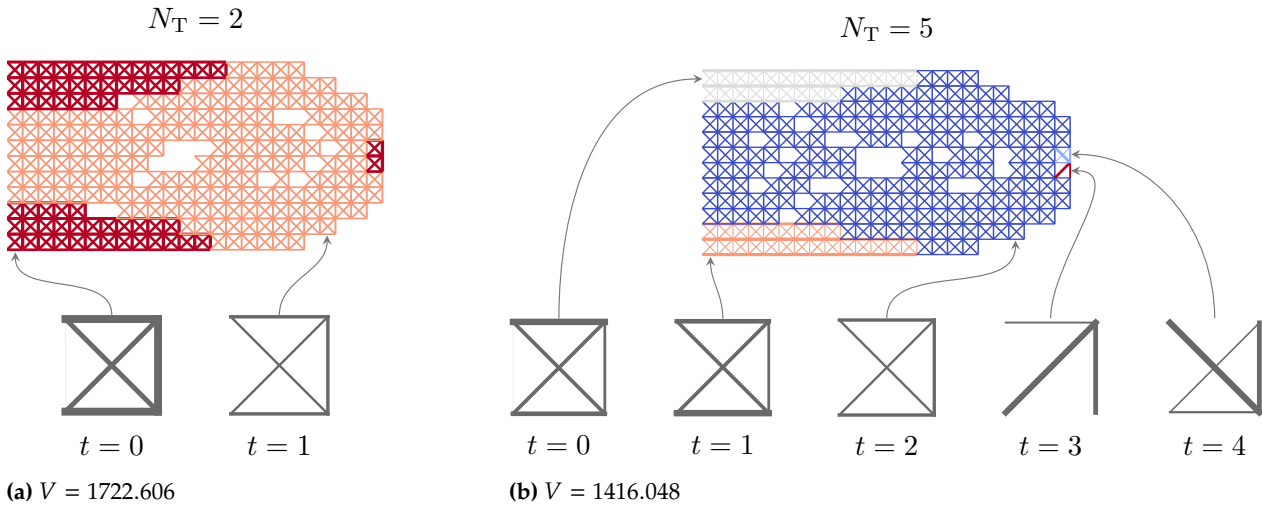


Figure 5.13.: Visual representation of the optimized modular 2D cantilever beam together with the corresponding module topologies for (a) $N_T = 2$ and (b) $N_T = 5$.

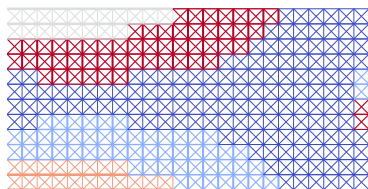


Figure 5.14.: Optimized 2D cantilever beam obtained using the variable linking formulation with fixed modules' layout and $N_T = 5$. The modules' layout is obtained using the k-means clustering technique. The final volume is $V = 1727.314$.

The last aspect we want to comment on is a comparison between the optimized structure with $N_T = 5$ presented in Fig. 5.13b and the structure we would obtain if we used the clustering algorithm-suggested module layout to set the mapping matrix H and the variable linking algorithm described in Section 4.1.3. Using this formulation, the structure's layout is fixed, and no changes or empty modules are possible. The optimized structure using this algorithm is shown in Fig. 5.14, and it has a volume $V = 1727.314$, more than 20 % greater compared to the proposed method solution. The difference can be explained by two factors: firstly, the proposed formulation allows for empty subdomains, which significantly aids in lightening the structure. Secondly, the proposed formulation uses the clustering results only as a starting point for the layout of the optimization, but the layout can then evolve to a more optimized design. This example verifies the need to consider the module layout as a variable of the optimization that should be optimized simultaneously with the modules' topology.

5.2.3. A BENCHMARK CASE STUDY: A SIMPLY SUPPORTED MODULAR BRIDGE

The proposed formulation and solution algorithm are now benchmarked against findings in the literature. To the knowledge of the authors, to this date there are no other works that optimize the layout and topology of modular structures using a gradient descent algorithm with continuous design variables. However, similar results have been achieved using Mixed-Integer Programming (MIP), Mixed-Integer Linear Programming (MILP) algorithms, or Simulated Annealing (SA) to optimize modular structures. Examples include the works of Tugilimana [151, 153], and we will now compare the results of the proposed formulation with them.

151. Tugilimana et al. (2019), 'An integrated design methodology for modular trusses including dynamic grouping, module spatial orientation, and topology optimization'
153. Tugilimana et al. (2017), 'Spatial orientation and topology optimization of modular trusses'



Figure 5.15.: Bailey bridge placed on construction site road over Orava river (Slovakia) [208].

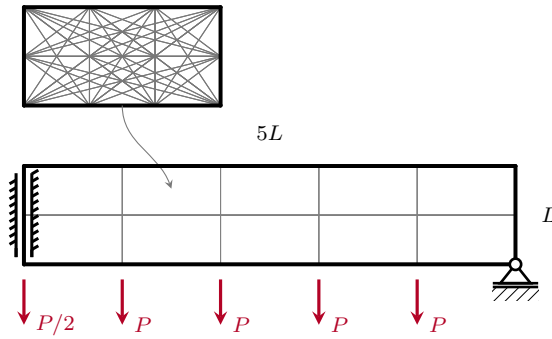


Figure 5.16.: Graphical representation of the 2D Bailey bridge test case. The structure is divided into $N_{\text{sub}} = 10$. The bridge is symmetric, and we are here optimizing only the right part of it.

The considered structure is a large modular structure based on the design of the Bailey bridge [209]. This concept has initially been studied for military purposes and later applied in civil engineering, particularly in temporary bridge structures. Its adaptability, low weight, and rapid erection, allowing almost immediate usability for traffic, make it highly versatile (see Fig. 5.15). The structure consists of 20 modules in length and 2 modules in height. Each module measures 3.050 m in length (10 ft) and 1.525 m in height (5 ft). This configuration results in a total bridge span of 30.50 m (100 ft).

The test case is based on the specifications given by Tugilimana *et al.* [151, 153] and is illustrated in Fig. 5.16, along with the geometrical and material data (normalized) utilized for the optimization (Table 5.3). The optimization is conducted only on the symmetric part of the structure. All constraints from the formulation M_1 are considered in this load case, excluding the buckling constraint, following the approach adopted by Tugilimana.

The resulting optimized structures are presented in the right part of Fig. 5.17, alongside the topology of the structures optimized by Tugilimana *et al.* [151]. Below each subfigure, the structure volume is provided, along with the value relative to the Tugilimana solution in square brackets. While the reference images (left part of the image) do not highlight the submodules with the same module topology, it can be observed that the module layout is not always the same, as seen in the cases of $N_T = 4$ or $N_T = 5$. It is noteworthy that the proposed optimization algorithm not only excels in optimizing an intrinsically discrete optimization problem using continuous design variables and a gradient-based optimizer but also improves upon the results found in the literature by up to 3 %. The structure obtained with $N_T = 10$ is exactly the same as what would be achieved by optimizing the structure without considering the modular constraints.

Up until now, we always used normalized material data and dimensions, and we never considered local buckling of the truss. For this reason, we are interested in testing what happens in this specific test case when we do consider local buckling and use a real load case with realistic dimensions and material data. We are particularly interested in seeing if these changes significantly affect the module's

[209]. Department of the Army (1986), 'Field Manual No. 5-277, Panel Bridge, Bailey Type, Washington DC.'

- [151]. Tugilimana *et al.* (2019), 'An integrated design methodology for modular trusses including dynamic grouping, module spatial orientation, and topology optimization'
[153]. Tugilimana *et al.* (2017), 'Spatial orientation and topology optimization of modular trusses'

Parameter	Value
L	3.05
σ_c, σ_t	± 1
P	1

Table 5.3.: Material data used for the 2D Bailey bridge without local buckling constraints test case to compare with the work of Tugilimana *et al.* [151].

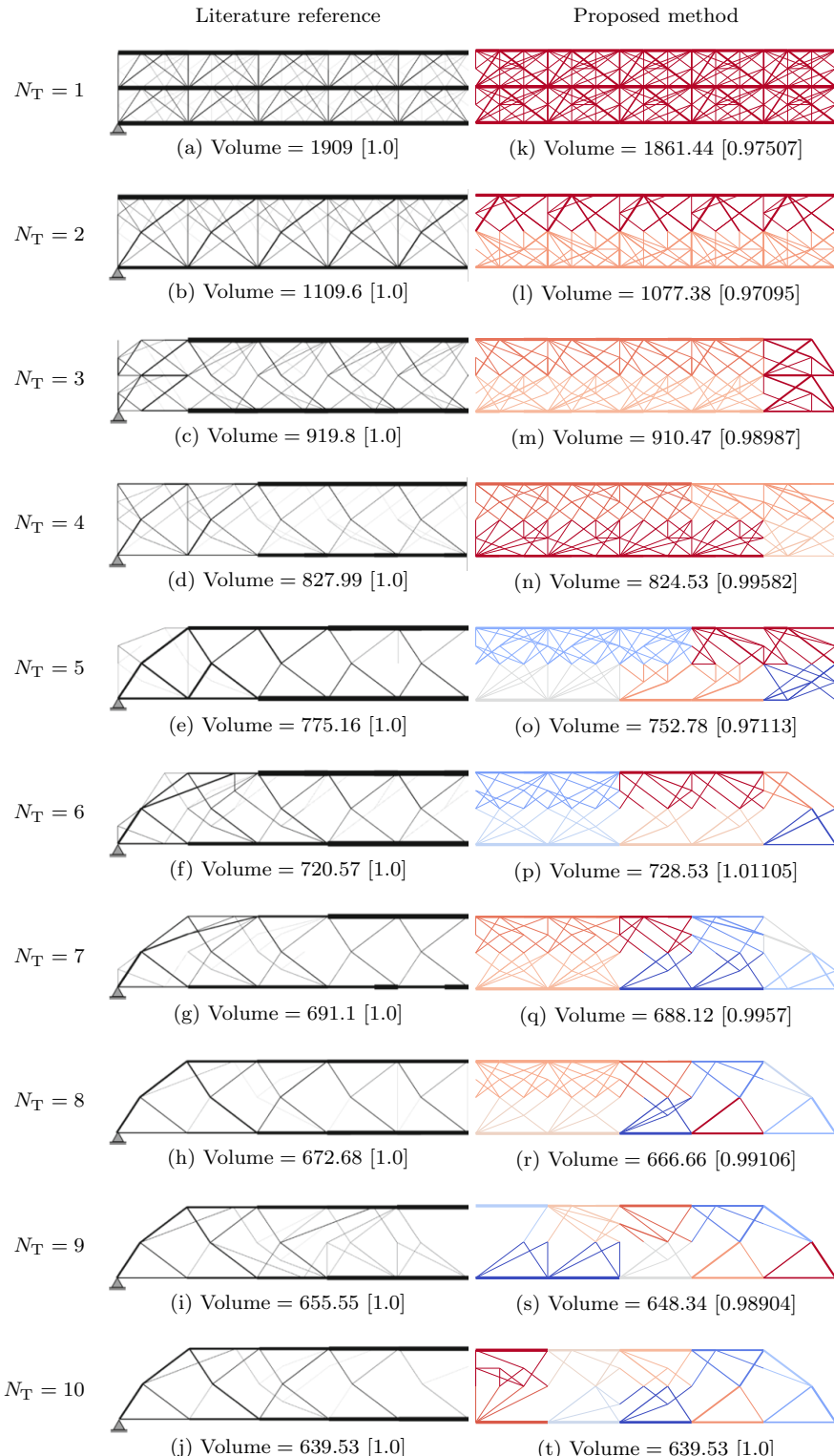


Figure 5.17.: Visual comparison of the 2D Bailey bridge test case without local buckling constraints proposed by Tugilimana *et al.* [151] obtained for different number of modules N_T . The images (a-j) represent the Tugilimana optimized structures, while the images (k-t) show the structures obtained with the proposed optimization method.

topology and layout in the structure. The material data used for the optimization is presented in Table 5.4 and represents a generic aluminum. The cross-sections are assumed to be circular for the local buckling evaluation. Topological buckling is taken into account inside the modules, as explained in Section 4.1.2.

The optimized structures for the Bailey bridge with buckling constraints are shown for different numbers of module topologies ($N_T = 1$ to 10) in Fig. 5.19. Quickly comparing them with the results without buckling, we notice that for this test case, the layout of the modules remains unchanged. The topology, however, is very different, with generally slightly fewer active bars. The volume can not be directly compared, so we normalize them with respect to the maximum volume ($N_T = 1$) and plot them in Fig. 5.18. We notice that adding multiple module topologies is beneficial in the same exact way with or without buckling constraints. We can also comment that the biggest reduction in volume from the inclusion of additional modules comes especially at the beginning, e.g., going from $N_T = 1$ to $N_T = 2$ or from $N_T = 2$ to $N_T = 3$, while the difference at higher numbers is marginal as the succession approaches a plateau.

Willing to explore how different parameters can influence the resulting volume, topology, and layout, we optimize the same test case with a different number of subdomains and modules. We use the same test case, with the only difference being that we are now using a 3x2 nodes fully connected ground structure for faster calculation times.

The results of the optimizations with different numbers of subdomains and modules are shown, together with the value of the structural volume in Fig. 5.20. Looking at the the image from left to right, we observe that the trend of volume reduction with the increase in the number of module topologies we have already acknowledged previously is still valid. It is, however, more interesting to see what happens going from top to bottom, i.e. what happens when we change the number of subdomains N_{sub} without changing the number of module topologies N_T . As expected and already observed using the variable linking algorithm (see, for example, Fig. 4.7 in Chapter 4), the volumes increase with the number of subdomains. However, in Fig. 5.21, in this case, we observe a steep increase in the structural volume and then a plateau, different from before. We speculate that this beneficial behavior comes mainly for two reasons: first, the optimization algorithm allows subdomains to show a completely empty topology. We observe that when we have not many subdomains, the structure is always fully filled, with no empty subdomains. But with the increasing number of subdomains, we notice more and more empty subdomains, helping to keep the structure light. Second, by increasing the number of subdomains, the average length of the subdomains' bars decreases. This phenomenon allows the change in the failure mode, moving from buckling to stress. For example,

Parameter	Value
L	3.05 m
E	69 GPa
σ_c, σ_t	± 270 MPa
P	1 MN

Table 5.4.: Material data used for the 2D Bailey bridge with local buckling constraints test case.

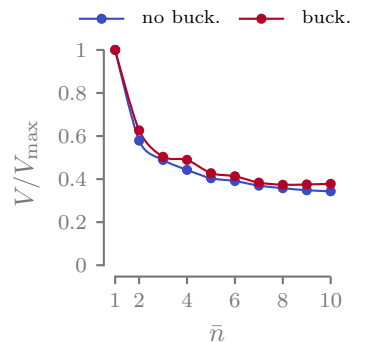


Figure 5.18.: Normalized volume values plotted against the number of modules N_T . The buckling constraints do not change the trend of the beneficial effect of using multiple N_T on the structure.

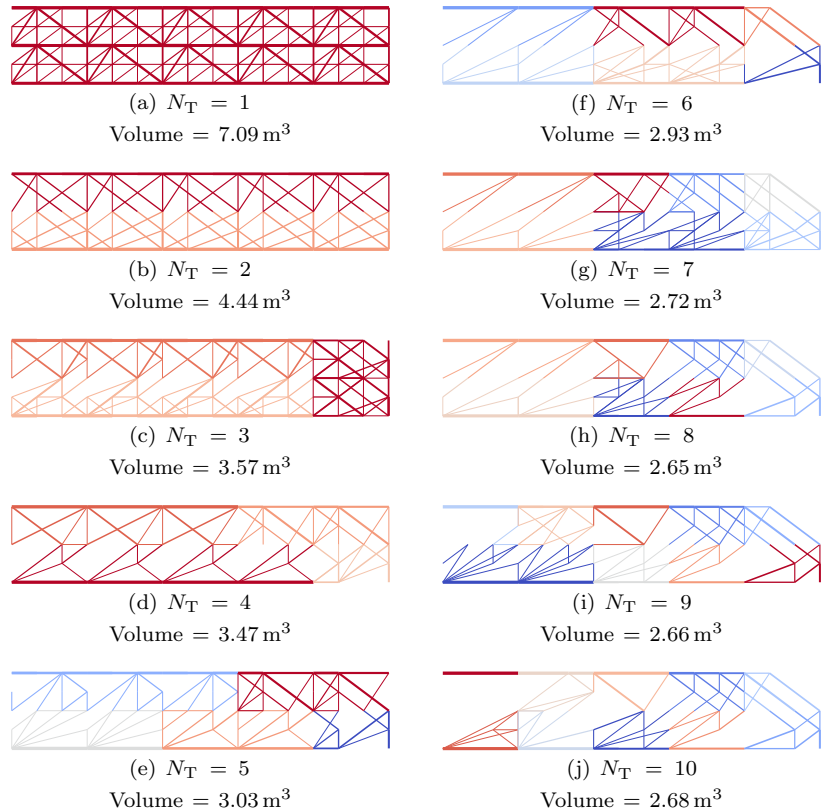


Figure 5.19.: Visual representation of the optimized structures obtained for different values of N_T for the 2D Bailey bridge test case with local buckling constraints.

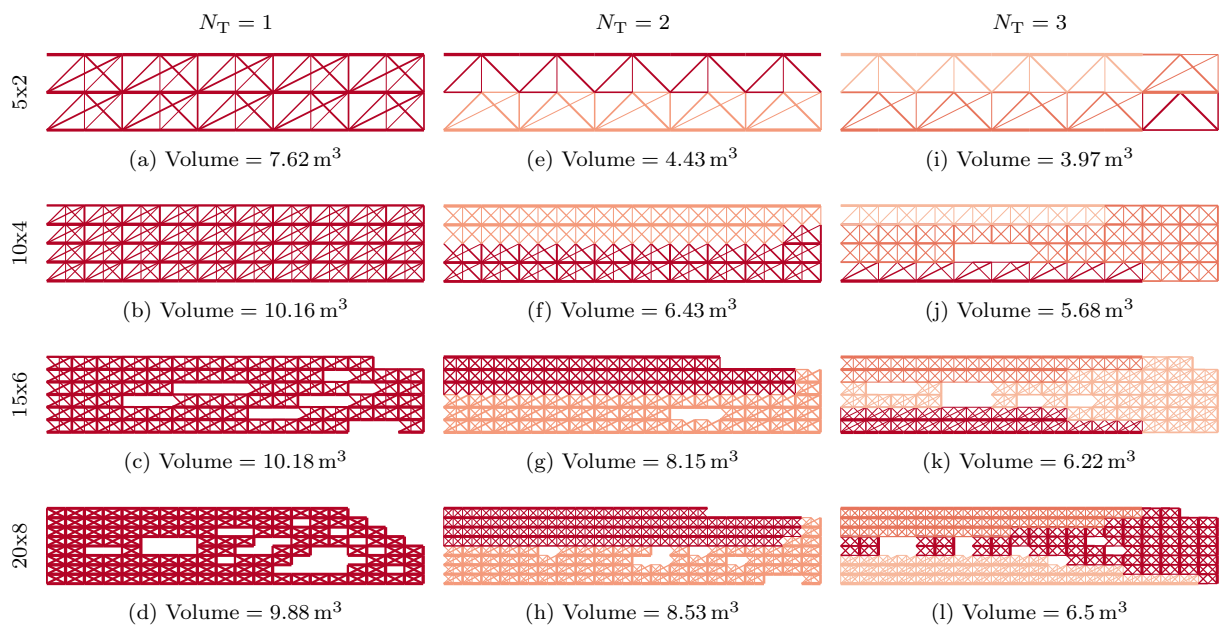


Figure 5.20.: Study of the influence of the parameters N_{sub} and N_T on the volume and the topology of the 2D Bailey bridge test case.

we observe that in Fig. 5.20d, where the failure mode is completely changed to stress, and the module presents a symmetric topology, with equal stress distribution in compression and tension. This is a very effective use of the material, and consequently, the volume decreases.

Lastly, we observe that the modules' layout is almost invariant with the increasing number of subdomains. This fact is somewhat similar to what we observe in classic topology optimization when we increase the mesh fineness with a distance-based filter. In these cases the topology remains unchanged with mesh refinement.

5.2.4. SIMPLY SUPPORTED 3D BEAM

The last test we conduct is on the simply supported 3D beam, a load case introduced in Chapter 3 and already used throughout this thesis. We recall the test case and the material and geometric data used for the optimization process in Fig. 5.22 and Table 5.5. As already done, we optimize here only one-fourth of the entire structure thanks to its symmetry planes. We conduct the optimization using $6 \times 2 \times 3$ subdomains on the X, Y, and Z axes, respectively, and every module is discretized using a $3 \times 3 \times 3$ fully connected ground structure with a total number of candidates $\bar{n} = 351$ per module. The optimization is conducted using three different numbers of modules, $N_T = 1, 2, 3$.

The resulting optimized structures are presented in Fig. 5.23, and the associated numerical results are presented in Table 5.6. The first observation is that in this specific test case, the optimizer converges to solutions in which the sum of alpha for every subdomain is equal to one. While previously, we have seen that the formulation arrived at creating empty subdomains where the sum of alpha is zero (see Fig. 5.13 or Fig. 5.20), here the optimizer failed in doing so. The empty subdomains for $N_T = 2$ and $N_T = 3$ correspond to cases where the cross-sectional areas of one module are set to zero, and the optimizer puts the value of the corresponding alpha to one. In this way, the solution is still optimized correctly, but using one module topology en plus. For example, looking at Fig. 5.23b and e, the solution for $N_T = 2$ shows that the optimized structure exhibits only one module topology, the other being empty.

We speculate that this problem arises from the optimizer's settings used to normalize the design variables and constraints for the optimization. For instance, even after scaling the layout design variable α and its corresponding constraints with multiple values, we consistently obtained the same results. This issue suggests that while the starting point perturbation certainly aids in achieving a well-optimized structure, additional work is needed to develop a new resolution strategy. One possible approach could be to separate the topology and layout variables and iteratively solve the two problems independently, one iteration at a time.

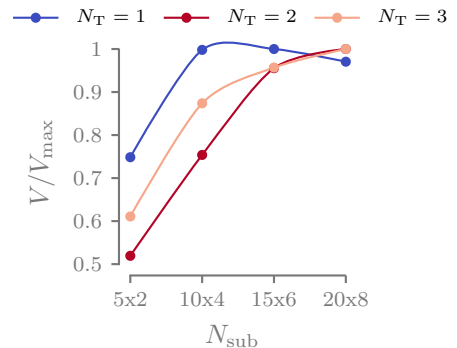


Figure 5.21.: Normalized volume values plotted against the number of subdomains N_{sub} for different values of N_T .

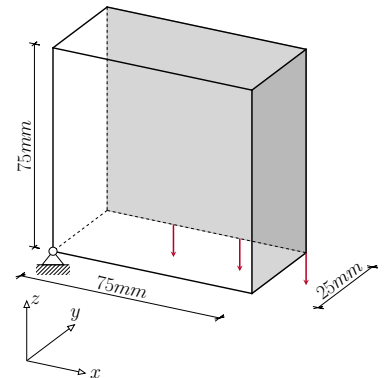


Figure 5.22.: Symmetric boundary conditions of the simply supported 3D beam. In gray are the symmetry planes of the test case.

Parameter	Value
E	2.7 GPa
σ_c, σ_t	± 55 MPa
ρ	1.14 g cm^{-3}
P	100 N

Table 5.5.: Material data used for the simply supported 3D beam optimization.

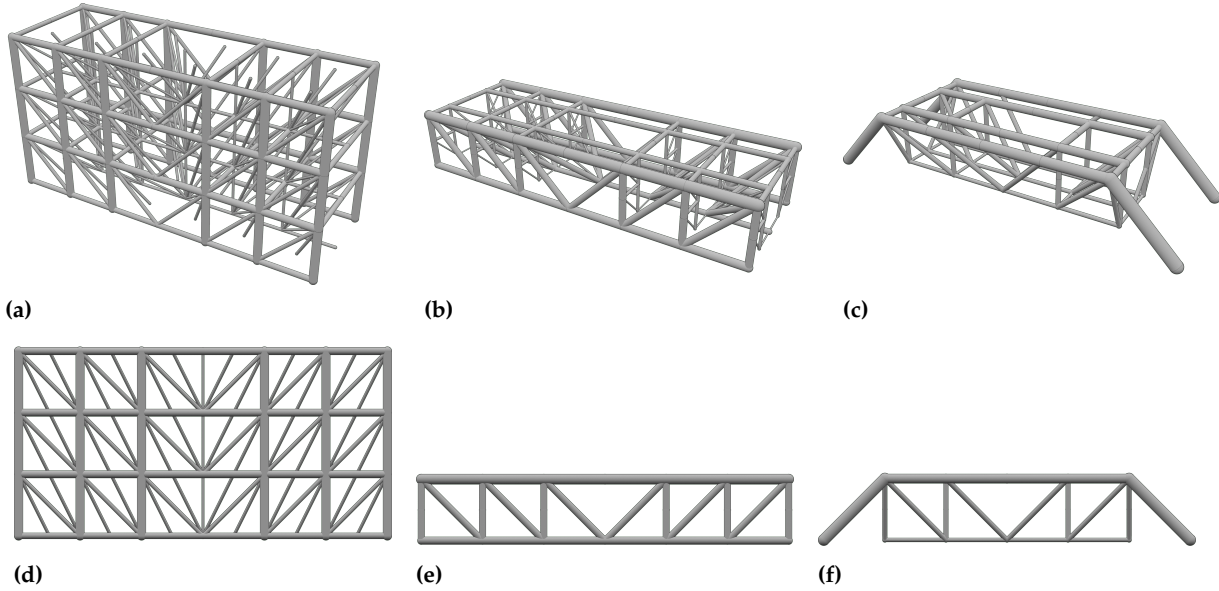


Figure 5.23.: Rendering of the optimized structures with $N_T = 1$ (a,d), $N_T = 2$ (b,e), and $N_T = 3$ (c,f).

Table 5.6.: Numeric results of the parametric study on the influence of the number of modules N_T on the simply supported 3D beam.

N_T	-	1	2	3
N_{sub}	1	36	36	36
$N_{\text{opt}} (N_{\text{el}})$	20 (1984)	360 (12636)	204 (12636)	104 (12636)
$V [\text{cm}^3]$	9.907	27.958	15.548	10.178
$V [\%]$	1.761	4.970	2.764	1.809
$\bar{\rho} [\text{kg/m}^3]$	80.31	226.65	126.05	82.51
$C [\text{J}]$	3.71	5.20	6.21	4.141
$a_{\max} [\text{mm}^2]$	37.61	9.40	12.81	15.81
φ	100.00 %	21.11 %	39.21 %	80.77 %
ψ	1.00	0.47	0.66	0.87
t	4 s	1 m 18 s	42 s	10 m 22 s

Despite encountering this issue, a careful examination of the volume V and mean densities $\bar{\rho}$ in Table 5.6 reveals that the modular structures with $N_T = 2$ and $N_T = 3$ achieve remarkably similar values to the monolithic reference ($N_{\text{sub}} = 1$) depicted in Fig. 5.24. This outcome is particularly significant as it attains the objective of achieving a lightweight structure, almost comparable to the monolithic one, while preserving modularity, highlighting the potential for a lighter structure with manufacturing advantages due to its modular nature.

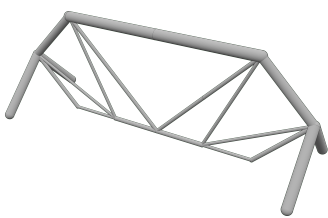


Figure 5.24.: Perspective view of the monolithic simply supported 3D beam optimized structure with $V = 9.907 \text{ cm}^3$.

In this chapter, we introduced an innovative optimization formulation designed to optimize the structural volume of modular structures. The solving algorithm leverages the physical information of the model, exploiting analytical derivatives and employing a gradient descent

5.3. CONCLUSION

optimization approach. Categorical variables, used to determine module layout, are modeled using a weighted sum of continuous weights that align with the continuous design variables of the optimization scheme. A double penalization scheme is proposed to mitigate the occurrence of non-physical intermediate weights.

The proposed formulation is tested across a variety of two- and three-dimensional test cases sourced from the literature. These tests confirm that the utilization of this optimization formulation enables modular structures to achieve volumes very close to those obtained from monolithic optimization, maintaining modularity and offering a favorable tradeoff between optimality and manufacturing complexity. However, the focus has been on simple test cases lacking engineering relevance so far. In the next chapter, we address this limitation by applying the presented optimization formulations in the aerospace context.

BIBLIOGRAPHY

- [1] Bendsøe, Martin P. and Sigmund, Ole, 'Topology Optimization'. Berlin, Heidelberg: Springer Berlin Heidelberg, 2004.
ISBN: [978-3-642-07698-5](#) [978-3-662-05086-6](#)
cited on pages 1, 6, 9, 13, 29, 31, 37
- [2] Martins, J.R.R.A. and Ning, A., 'Engineering Design Optimization'. Cambridge University Press, 2021.
ISBN: [978-1-108-83341-7](#)
cited on pages 2, 6, 30, 145
- [3] Prager, W. and Taylor, J. E., 'Problems of Optimal Structural Design', *Journal of Applied Mechanics* 35.1 (Mar. 1968), pp. 102–106.
DOI: [10.1115/1.3601120](#)
cited on page 3
- [4] Prager, William, 'Optimality Criteria in Structural Design', *Proceedings of the National Academy of Sciences of the United States of America* 61.3 (1968), Publisher: National Academy of Sciences, pp. 794–796.
cited on page 3
- [5] Bendsøe, Martin Philip and Kikuchi, Noboru, 'Generating optimal topologies in structural design using a homogenization method', *Computer Methods in Applied Mechanics and Engineering* 71.2 (Nov. 1988), pp. 197–224.
DOI: [10.1016/0045-7825\(88\)90086-2](#)
cited on pages 3, 6, 17, 18, 35
- [6] Bendsøe, Martin P., 'Optimization of Structural Topology, Shape, and Material'. Berlin, Heidelberg: Springer Berlin Heidelberg, 1995.
ISBN: [978-3-662-03117-9](#) [978-3-662-03115-5](#)
cited on pages 3, 47
- [7] Sigmund, O., 'A 99 line topology optimization code written in Matlab', *Structural and Multidisciplinary Optimization* 21.2 (Apr. 2001), pp. 120–127.
DOI: [10.1007/s001580050176](#)
cited on page 3
- [8] Allaire, Grégoire, Belhachmi, Zakaria, and Jouve, François, 'The homogenization method for topology and shape optimization. Single and multiple loads case', *Revue Européenne des Éléments Finis* 5.5-6 (Jan. 1996), pp. 649–672.
DOI: [10.1080/12506559.1996.10511241](#)
cited on page 3
- [9] Li, Weichen, Suryanarayana, Phanish, and Paulino, Glaucio H., 'Accelerated fixed-point formulation of topology optimization: Application to compliance minimization problems', *Mechanics Research Communications* 103 (Jan. 2020), p. 103469.
DOI: [10.1016/j.mechrescom.2019.103469](#)
cited on page 3
- [10] Ferrari, Federico and Sigmund, Ole, 'A new generation 99 line Matlab code for compliance topology optimization and its extension to 3D', *Structural and Multidisciplinary Optimization* 62.4 (Oct. 2020), pp. 2211–2228.
cited on pages 3, 33, 34

- cited on page 3
- [11] Anderson, Donald G., 'Iterative Procedures for Nonlinear Integral Equations', *Journal of the ACM* 12.4 (Oct. 1965), pp. 547–560.
 DOI: [10.1145/321296.321305](https://doi.org/10.1145/321296.321305)
- cited on page 4
- [12] Conn, Andrew R., Scheinberg, Katya, and Vicente, Luis N., 'Introduction to Derivative-Free Optimization'. Society for Industrial and Applied Mathematics, Jan. 2009.
 ISBN: [978-0-89871-668-9](https://doi.org/978-0-89871-668-9) [978-0-89871-876-8](https://doi.org/978-0-89871-876-8)
- cited on page 4
- [13] Audet, Charles and Hare, Warren, 'Derivative-Free and Black-box Optimization', Springer Series in Operations Research and Financial Engineering. Cham: Springer International Publishing, 2017.
 ISBN: [978-3-319-68912-8](https://doi.org/978-3-319-68912-8) [978-3-319-68913-5](https://doi.org/978-3-319-68913-5)
- cited on page 4
- [14] Simon, Dan, 'Evolutionary optimization algorithms: biologically-inspired and population-based approaches to computer intelligence', 1. ed. Hoboken, NJ: Wiley, 2013.
 ISBN: [978-1-118-65950-2](https://doi.org/978-1-118-65950-2) [978-0-470-93741-9](https://doi.org/978-0-470-93741-9)
- cited on page 4
- [15] Balamurugan, R., Ramakrishnan, C. V., and Swaminathan, N., 'A two phase approach based on skeleton convergence and geometric variables for topology optimization using genetic algorithm', *Structural and Multidisciplinary Optimization* 43.3 (Mar. 2011), pp. 381–404.
 DOI: [10.1007/s00158-010-0560-4](https://doi.org/10.1007/s00158-010-0560-4)
- cited on pages 4, 97
- [16] Sigmund, Ole, 'On the usefulness of non-gradient approaches in topology optimization', *Structural and Multidisciplinary Optimization* 43.5 (May 2011), pp. 589–596.
 DOI: [10.1007/s00158-011-0638-7](https://doi.org/10.1007/s00158-011-0638-7)
- cited on page 4
- [17] Luh, Guan-Chun and Lin, Chun-Yi, 'Structural topology optimization using ant colony optimization algorithm', *Applied Soft Computing* 9.4 (Sept. 2009), pp. 1343–1353.
 DOI: [10.1016/j.asoc.2009.06.001](https://doi.org/10.1016/j.asoc.2009.06.001)
- cited on page 4
- [18] Luh, Guan-Chun, Lin, Chun-Yi, and Lin, Yu-Shu, 'A binary particle swarm optimization for continuum structural topology optimization', *Applied Soft Computing*, The Impact of Soft Computing for the Progress of Artificial Intelligence 11.2 (Mar. 2011), pp. 2833–2844.
 DOI: [10.1016/j.asoc.2010.11.013](https://doi.org/10.1016/j.asoc.2010.11.013)
- cited on pages 4, 46
- [19] Stolpe, M., 'Global optimization of minimum weight truss topology problems with stress, displacement, and local buckling constraints using branch-and-bound', *International Journal for Numerical Methods in Engineering* 61.8 (2004), pp. 1270–1309.
 DOI: <https://doi.org/10.1002/nme.1112>

- [20] Mattheck, C. and Burkhardt, S., 'A new method of structural shape optimization based on biological growth', *International Journal of Fatigue* 12.3 (May 1990), pp. 185–190.
DOI: [10.1016/0142-1123\(90\)90094-U](https://doi.org/10.1016/0142-1123(90)90094-U)
- [21] Xie, Y. M. and Steven, G. P., 'A simple evolutionary procedure for structural optimization', *Computers & Structures* 49.5 (Dec. 1993), pp. 885–896.
DOI: [10.1016/0045-7949\(93\)90035-C](https://doi.org/10.1016/0045-7949(93)90035-C)
- [22] Manickarajah, D, Xie, Y. M, and Steven, G. P, 'An evolutionary method for optimization of plate buckling resistance', *Finite Elements in Analysis and Design* 29.3 (June 1998), pp. 205–230.
DOI: [10.1016/S0168-874X\(98\)00012-2](https://doi.org/10.1016/S0168-874X(98)00012-2)
- [23] Young, V., Querin, O. M., Steven, G. P., and Xie, Y. M., '3D and multiple load case bi-directional evolutionary structural optimization (BESO)', *Structural optimization* 18.2 (Oct. 1999), pp. 183–192.
DOI: [10.1007/BF01195993](https://doi.org/10.1007/BF01195993)
- [24] Kraft, Dieter, 'A software package for sequential quadratic programming', *Tech. Rep. DFVLR-FB 88-28, DLR German Aerospace Center — Institute for Flight Mechanics, Koln, Germany.* (1988).
- [25] Svanberg, Krister, 'The method of moving asymptotes—a new method for structural optimization', *International Journal for Numerical Methods in Engineering* 24.2 (1987), pp. 359–373.
DOI: <https://doi.org/10.1002/nme.1620240207>
- [26] Svanberg, Krister, 'A Class of Globally Convergent Optimization Methods Based on Conservative Convex Separable Approximations', *SIAM Journal on Optimization* 12.2 (Jan. 2002), Publisher: Society for Industrial and Applied Mathematics, pp. 555–573.
DOI: [10.1137/S1052623499362822](https://doi.org/10.1137/S1052623499362822)
- [27] Bruyneel, M., Duysinx, P., and Fleury, C., 'A family of MMA approximations for structural optimization', *Structural and Multidisciplinary Optimization* 24.4 (Oct. 2002), pp. 263–276.
DOI: [10.1007/s00158-002-0238-7](https://doi.org/10.1007/s00158-002-0238-7)
- [28] Fleury, Claude and Braibant, Vincent, 'Structural optimization: A new dual method using mixed variables', *International Journal for Numerical Methods in Engineering* 23.3 (1986), pp. 409–428.
DOI: [10.1002/nme.1620230307](https://doi.org/10.1002/nme.1620230307)
- [29] Wächter, Andreas and Biegler, Lorenz T., 'On the implementation of an interior-point filter line-search algorithm for large-scale nonlinear programming', *Mathematical Programming* 106.1 (Mar. 2006), pp. 25–57.
DOI: [10.1007/s10107-004-0559-y](https://doi.org/10.1007/s10107-004-0559-y)

- cited on page 5
- [30] Rojas Labanda, Susana and Stolpe, Mathias, 'Benchmarking optimization solvers for structural topology optimization', *Structural and Multidisciplinary Optimization* 52 (Sept. 2015).
DOI: [10.1007/s00158-015-1250-z](https://doi.org/10.1007/s00158-015-1250-z)
- cited on pages 5, 10, 12, 13, 31, 37, 46, 56
- cited on pages 5, 12
- cited on pages 5, 10, 12, 37, 46
- cited on pages 6, 50
- cited on pages 6, 7, 17, 18, 32, 43
- cited on page 6
- cited on pages 6, 20, 21, 71
- cited on page 6
- cited on page 6
- [31] Dorn, W. S., Gomory, Ralph E., and Greenberg, H., 'Automatic design of optimal structures', *J. Mécanique* (1964).
- [32] Chan, H. S. Y., 'Optimum structural design and linear programming', *College of Aeronautics Report Aero* 175 (1964), Publisher: College of Aeronautics Cranfield.
- [33] Hemp, W. S., 'Optimum Structures'. Clarendon Press, 1973, Google-Books-ID: cJhpAAAAMAAJ.
ISBN: [978-0-19-856110-1](https://doi.org/10.2514/3.12000)
- [34] Sankaranarayanan, S., Haftka, Raphael T., and Kapadia, Rakesh K., 'Truss topology optimization with simultaneous analysis and design', *AIAA Journal* 32.2 (Feb. 1994), pp. 420–424.
DOI: [10.2514/3.12000](https://doi.org/10.2514/3.12000)
- [35] Bendsøe, M. P., 'Optimal shape design as a material distribution problem', *Structural optimization* 1.4 (Dec. 1989), pp. 193–202.
DOI: [10.1007/BF01650949](https://doi.org/10.1007/BF01650949)
- [36] Sigmund, Ole, 'Materials with prescribed constitutive parameters: An inverse homogenization problem', *International Journal of Solids and Structures* 31.17 (Sept. 1994), pp. 2313–2329.
DOI: [10.1016/0020-7683\(94\)90154-6](https://doi.org/10.1016/0020-7683(94)90154-6)
- [37] Zhang, Weihong and Sun, Shiping, 'Scale-related topology optimization of cellular materials and structures', *International Journal for Numerical Methods in Engineering* 68.9 (2006), pp. 993–1011.
DOI: [10.1002/nme.1743](https://doi.org/10.1002/nme.1743)
- [38] Collet, Maxime, Noël, Lise, Bruggi, Matteo, and Duysinx, Pierre, 'Topology optimization for microstructural design under stress constraints', *Structural and Multidisciplinary Optimization* 58.6 (Dec. 2018), pp. 2677–2695.
DOI: [10.1007/s00158-018-2045-9](https://doi.org/10.1007/s00158-018-2045-9)
- [39] Borrvall, Thomas and Petersson, Joakim, 'Topology optimization of fluids in Stokes flow', *International Journal for Numerical Methods in Fluids* 41.1 (2003), _eprint: <https://onlinelibrary.wiley.com/doi/pdf/>
pp. 77–107.
DOI: [10.1002/fld.426](https://doi.org/10.1002/fld.426)
- [40] Bruyneel, M. and Duysinx, P., 'Note on topology optimization of continuum structures including self-weight', *Structural and Multidisciplinary Optimization* 29.4 (Apr. 2005), pp. 245–256.
DOI: [10.1007/s00158-004-0484-y](https://doi.org/10.1007/s00158-004-0484-y)

- [41] Sigmund, Ole, 'Manufacturing tolerant topology optimization', *Acta Mechanica Sinica* 25.2 (Apr. 2009), pp. 227–239.
DOI: [10.1007/s10409-009-0240-z](https://doi.org/10.1007/s10409-009-0240-z)
- [42] Brackett, D, Ashcroft, I, and Hague, R, 'Topology Optimization for Additive Manufacturing' (2011), p. 15.
DOI: [10.26153/tsw/15300](https://doi.org/10.26153/tsw/15300)
- [43] Sigmund, Ole, 'On the Design of Compliant Mechanisms Using Topology Optimization*', *Mechanics of Structures and Machines* 25.4 (Jan. 1997), Publisher: Taylor & Francis, pp. 493–524.
DOI: [10.1080/08905459708945415](https://doi.org/10.1080/08905459708945415)
- [44] Bruns, Tyler E. and Tortorelli, Daniel A., 'Topology optimization of non-linear elastic structures and compliant mechanisms', *Computer Methods in Applied Mechanics and Engineering* 190.26 (Mar. 2001), pp. 3443–3459.
DOI: [10.1016/S0045-7825\(00\)00278-4](https://doi.org/10.1016/S0045-7825(00)00278-4)
- [45] Wang, Weiming, Munro, Dirk, Wang, Charlie C. L., Keulen, Fred van, and Wu, Jun, 'Space-time topology optimization for additive manufacturing', *Structural and Multidisciplinary Optimization* 61.1 (Jan. 2020), pp. 1–18.
DOI: [10.1007/s00158-019-02420-6](https://doi.org/10.1007/s00158-019-02420-6)
- [46] Allaire, Grégoire, Jouve, François, and Toader, Anca-Maria, 'A level-set method for shape optimization', *Comptes Rendus Mathematique* 334.12 (Jan. 2002), pp. 1125–1130.
DOI: [10.1016/S1631-073X\(02\)02412-3](https://doi.org/10.1016/S1631-073X(02)02412-3)
- [47] Wang, Michael Yu, Wang, Xiaoming, and Guo, Dongming, 'A level set method for structural topology optimization', *Computer Methods in Applied Mechanics and Engineering* 192.1 (Jan. 2003), pp. 227–246.
DOI: [10.1016/S0045-7825\(02\)00559-5](https://doi.org/10.1016/S0045-7825(02)00559-5)
- [48] Allaire, Grégoire, Jouve, François, and Toader, Anca-Maria, 'Structural optimization using sensitivity analysis and a level-set method', *Journal of Computational Physics* 194.1 (Feb. 2004), pp. 363–393.
DOI: [10.1016/j.jcp.2003.09.032](https://doi.org/10.1016/j.jcp.2003.09.032)
- [49] Tortorelli, D. A. and Michaleris, P., 'Design sensitivity analysis: Overview and review', *Inverse Problems in Engineering* 1.1 (Oct. 1994), pp. 71–105.
DOI: [10.1080/174159794088027573](https://doi.org/10.1080/174159794088027573)
- [50] Wang, Fengwen, Lazarov, Boyan Stefanov, and Sigmund, Ole, 'On projection methods, convergence and robust formulations in topology optimization', *Structural and Multidisciplinary Optimization* 43.6 (June 2011), pp. 767–784.
DOI: [10.1007/s00158-010-0602-y](https://doi.org/10.1007/s00158-010-0602-y)

cited on pages 7, 8, 106

- [51] Bendsøe, M. P. and Sigmund, O., 'Material interpolation schemes in topology optimization', *Archive of Applied Mechanics* 69.9 (Nov. 1999), pp. 635–654.
 DOI: [10.1007/s004190050248](https://doi.org/10.1007/s004190050248)

cited on page 8

- [52] Hashin, Z. and Shtrikman, S., 'A variational approach to the theory of the elastic behaviour of multiphase materials', *Journal of the Mechanics and Physics of Solids* 11.2 (Mar. 1963), pp. 127–140.
 DOI: [10.1016/0022-5096\(63\)90060-7](https://doi.org/10.1016/0022-5096(63)90060-7)

cited on page 8

- [53] Díaz, A. and Sigmund, O., 'Checkerboard patterns in layout optimization', *Structural optimization* 10.1 (Aug. 1995), pp. 40–45.
 DOI: [10.1007/BF01743693](https://doi.org/10.1007/BF01743693)

cited on page 8

- [54] Sigmund, Ole, 'Design of Material Structures using Topology Optimization', PhD thesis, Technical University of Denmark, DK-2800 Lyngby, 1994.

cited on pages 8, 33, 35

- [55] Sigmund, Ole, 'Morphology-based black and white filters for topology optimization', *Structural and Multidisciplinary Optimization* 33.4 (Apr. 2007), pp. 401–424.
 DOI: [10.1007/s00158-006-0087-x](https://doi.org/10.1007/s00158-006-0087-x)

cited on page 9

- [56] Allaire, G. and Francfort, G. A., 'A Numerical Algorithm for Topology and Shape Optimization', *Topology Design of Structures*, NATO ASI Series, ed. by Bendsøe, Martin Philip and Soares, Carlos A. Mota, Dordrecht: Springer Netherlands, 1993, pp. 239–248, ISBN: 978-94-011-1804-0.
 DOI: [10.1007/978-94-011-1804-0_16](https://doi.org/10.1007/978-94-011-1804-0_16)

cited on page 9

- [57] Allaire, G. and Kohn, R. V., 'Topology Optimization and Optimal Shape Design Using Homogenization', *Topology Design of Structures*, NATO ASI Series, ed. by Bendsøe, Martin Philip and Soares, Carlos A. Mota, Dordrecht: Springer Netherlands, 1993, pp. 207–218, ISBN: 978-94-011-1804-0.
 DOI: [10.1007/978-94-011-1804-0_14](https://doi.org/10.1007/978-94-011-1804-0_14)

cited on page 9

- [58] Rozvany, G. I. N., 'A critical review of established methods of structural topology optimization', *Structural and Multidisciplinary Optimization* 37.3 (Jan. 2009), pp. 217–237.
 DOI: [10.1007/s00158-007-0217-0](https://doi.org/10.1007/s00158-007-0217-0)

cited on page 9

- [59] Petersson, Joakim and Sigmund, Ole, 'Slope constrained topology optimization', *International Journal for Numerical Methods in Engineering* 41.8 (1998), _eprint: <https://onlinelibrary.wiley.com/doi/pdf/10.100207%2819980430%2941%3A8%3C1417%3A%3AAID-NME344%3E3.0.CO%3BN>, pp. 1417–1434.
 DOI: [10.1002/\(SICI\)1097-0207\(19980430\)41:8<1417::AID-NME344>3.0.CO;2-N](https://doi.org/10.1002/(SICI)1097-0207(19980430)41:8<1417::AID-NME344>3.0.CO;2-N)

- [60] Rojas-Labanda, Susana and Stolpe, Mathias, 'Automatic penalty continuation in structural topology optimization', *Structural and Multidisciplinary Optimization* 52.6 (Dec. 2015), pp. 1205–1221.
DOI: [10.1007/s00158-015-1277-1](https://doi.org/10.1007/s00158-015-1277-1)
- [61] Zhou, Ming, Fleury, Raphael, Shyy, Yaw-Kang, Thomas, Harold, and Brennan, Jeffrey, 'Progress in Topology Optimization with Manufacturing Constraints', *9th AIAA/ISSMO Symposium on Multidisciplinary Analysis and Optimization*, Atlanta, Georgia: American Institute of Aeronautics and Astronautics, Sept. 2002, ISBN: 978-1-62410-120-5.
DOI: [10.2514/6.2002-5614](https://doi.org/10.2514/6.2002-5614)
- [62] Liu, Jikai, Gaynor, Andrew T., Chen, Shikui, Kang, Zhan, Suresh, Krishnan, Takezawa, Akihiro, Li, Lei, Kato, Junji, Tang, Jinyuan, Wang, Charlie C. L., Cheng, Lin, Liang, Xuan, and To, Albert C., 'Current and future trends in topology optimization for additive manufacturing', *Structural and Multidisciplinary Optimization* 57.6 (June 2018), Company: Springer Distributor: Springer Institution: Springer Label: Springer Number: 6 Publisher: Springer Berlin Heidelberg, pp. 2457–2483.
DOI: [10.1007/s00158-018-1994-3](https://doi.org/10.1007/s00158-018-1994-3)
- [63] Aage, Niels, Andreassen, Erik, Lazarov, Boyan S., and Sigmund, Ole, 'Giga-voxel computational morphogenesis for structural design', *Nature* 550.7674 (Oct. 2017), Number: 7674 Publisher: Nature Publishing Group, pp. 84–86.
DOI: [10.1038/nature23911](https://doi.org/10.1038/nature23911)
- [64] Salazar de Troya, Miguel A. and Tortorelli, Daniel A., 'Adaptive mesh refinement in stress-constrained topology optimization', *Structural and Multidisciplinary Optimization* 58.6 (Dec. 2018), pp. 2369–2386.
DOI: [10.1007/s00158-018-2084-2](https://doi.org/10.1007/s00158-018-2084-2)
- [65] Zhang, Shanglong, Gain, Arun L., and Norato, Julián A., 'Adaptive mesh refinement for topology optimization with discrete geometric components', *Computer Methods in Applied Mechanics and Engineering* 364 (June 2020), p. 112930.
DOI: [10.1016/j.cma.2020.112930](https://doi.org/10.1016/j.cma.2020.112930)
- [66] Sigmund, Ole, Aage, Niels, and Andreassen, Erik, 'On the (non-)optimality of Michell structures', *Structural and Multidisciplinary Optimization* 54.2 (Aug. 2016), pp. 361–373.
DOI: [10.1007/s00158-016-1420-7](https://doi.org/10.1007/s00158-016-1420-7)
- [67] Wein, Fabian, Dunning, Peter D., and Norato, Julián A., 'A review on feature-mapping methods for structural optimization', *Structural and Multidisciplinary Optimization* 62.4 (Oct. 2020), pp. 1597–1638.
DOI: [10.1007/s00158-020-02649-6](https://doi.org/10.1007/s00158-020-02649-6)

- cited on page 10
- [68] Guo, Xu, Zhang, Weisheng, and Zhong, Wenliang, 'Doing Topology Optimization Explicitly and Geometrically—A New Moving Morphable Components Based Framework', *Journal of Applied Mechanics* 81.8 (May 2014).
- DOI: [10.1115/1.4027609](https://doi.org/10.1115/1.4027609)
- cited on page 10
- [69] Zhang, Weisheng, Li, Dong, Yuan, Jie, Song, Junfu, and Guo, Xu, 'A new three-dimensional topology optimization method based on moving morphable components (MMCs)', *Computational Mechanics* 59.4 (Apr. 2017), pp. 647–665.
- DOI: [10.1007/s00466-016-1365-0](https://doi.org/10.1007/s00466-016-1365-0)
- cited on page 10
- [70] Norato, J. A., Bell, B. K., and Tortorelli, D. A., 'A geometry projection method for continuum-based topology optimization with discrete elements', *Computer Methods in Applied Mechanics and Engineering* 293 (Aug. 2015), pp. 306–327.
- DOI: [10.1016/j.cma.2015.05.005](https://doi.org/10.1016/j.cma.2015.05.005)
- cited on page 10
- [71] Zhang, Shanglong, Norato, Julián A., Gain, Arun L., and Lyu, Naesung, 'A geometry projection method for the topology optimization of plate structures', *Structural and Multidisciplinary Optimization* 54.5 (Nov. 2016), pp. 1173–1190.
- DOI: [10.1007/s00158-016-1466-6](https://doi.org/10.1007/s00158-016-1466-6)
- cited on page 10
- [72] Coniglio, Simone, Morlier, Joseph, Gogu, Christian, and Amargier, Rémi, 'Generalized Geometry Projection: A Unified Approach for Geometric Feature Based Topology Optimization', *Archives of Computational Methods in Engineering* 27.5 (Nov. 2020), pp. 1573–1610.
- DOI: [10.1007/s11831-019-09362-8](https://doi.org/10.1007/s11831-019-09362-8)
- cited on page 10
- [73] Kazemi, Hesaneh, Vaziri, Ashkan, and Norato, Julián A., 'Multi-material topology optimization of lattice structures using geometry projection', *Computer Methods in Applied Mechanics and Engineering* 363 (May 2020), p. 112895.
- DOI: [10.1016/j.cma.2020.112895](https://doi.org/10.1016/j.cma.2020.112895)
- cited on pages 10, 26
- [74] Cheng, G. D. and Guo, X., ' ε -relaxed approach in structural topology optimization', *Structural optimization* 13.4 (June 1997), pp. 258–266.
- DOI: [10.1007/BF01197454](https://doi.org/10.1007/BF01197454)
- cited on pages 10, 26
- [75] Rozvany, G.I.N., 'On design-dependent constraints and singular topologies', *Structural and Multidisciplinary Optimization* 21.2 (Apr. 2001), pp. 164–172.
- DOI: [10.1007/s001580050181](https://doi.org/10.1007/s001580050181)
- cited on page 10
- [76] Gao, Xingjun and Ma, Haitao, 'Topology optimization of continuum structures under buckling constraints', *Computers & Structures* 157 (Sept. 2015), pp. 142–152.
- DOI: [10.1016/j.compstruc.2015.05.020](https://doi.org/10.1016/j.compstruc.2015.05.020)

- [77] He, Linwei, Gilbert, Matthew, and Song, Xingyi, 'A Python script for adaptive layout optimization of trusses', *Structural and Multidisciplinary Optimization* 60.2 (Aug. 2019), pp. 835–847.
DOI: [10.1007/s00158-019-02226-6](https://doi.org/10.1007/s00158-019-02226-6)
- [78] Kirsch, Uri, 'Optimal topologies of truss structures', *Computer Methods in Applied Mechanics and Engineering* 72.1 (Jan. 1989), pp. 15–28.
DOI: [10.1016/0045-7825\(89\)90119-9](https://doi.org/10.1016/0045-7825(89)90119-9)
- [79] Rozvany, G. I. N., Bendsøe, M. P., and Kirsch, U., 'Layout Optimization of Structures', *Applied Mechanics Reviews* 48.2 (Feb. 1995), pp. 41–119.
DOI: [10.1115/1.3005097](https://doi.org/10.1115/1.3005097)
- [80] Kirsch, Uri, 'Optimal design of trusses by approximate compatibility', *Computers & Structures* 12.1 (July 1980), pp. 93–98.
DOI: [10.1016/0045-7949\(80\)90097-8](https://doi.org/10.1016/0045-7949(80)90097-8)
- [81] Cheng, G., 'Some aspects of truss topology optimization', *Structural Optimization* 10.3-4 (Dec. 1995), pp. 173–179.
DOI: [10.1007/BF01742589](https://doi.org/10.1007/BF01742589)
- [82] Achtziger, W., 'Local stability of trusses in the context of topology optimization Part I: Exact modelling', *Structural Optimization* 17.4 (Dec. 1999), pp. 235–246.
DOI: [10.1007/BF01206999](https://doi.org/10.1007/BF01206999)
- [83] Maxwell, J. Clerk, 'I.—On Reciprocal Figures, Frames, and Diagrams of Forces', *Earth and Environmental Science Transactions of The Royal Society of Edinburgh* 26.1 (1870), Publisher: Royal Society of Edinburgh Scotland Foundation, pp. 1–40.
DOI: [10.1017/S0080456800026351](https://doi.org/10.1017/S0080456800026351)
- [84] Michell, A. G. M., 'The limits of economy of material in frame-structures', *The London, Edinburgh, and Dublin Philosophical Magazine and Journal of Science* 8.47 (Nov. 1904), pp. 589–597.
DOI: [10.1080/14786440409463229](https://doi.org/10.1080/14786440409463229)
- [85] Gilbert, Matthew and Tyas, Andrew, 'Layout optimization of large-scale pin-jointed frames', *Engineering Computations* 20.8 (Dec. 2003), pp. 1044–1064.
DOI: [10.1108/02644400310503017](https://doi.org/10.1108/02644400310503017)
- [86] Pedersen, Pauli, 'Optimal Joint Positions for Space Trusses', *Journal of the Structural Division* 99.12 (Dec. 1973), Publisher: American Society of Civil Engineers, pp. 2459–2476.
DOI: [10.1061/JJSCEAG.0003669](https://doi.org/10.1061/JJSCEAG.0003669)
- [87] Achtziger, Wolfgang, 'On simultaneous optimization of truss geometry and topology', *Structural and Multidisciplinary Optimization* 33.4 (Apr. 2007), pp. 285–304.
DOI: [10.1007/s00158-006-0092-0](https://doi.org/10.1007/s00158-006-0092-0)

- cited on page 13
- [88] Descamps, Benoît and Filomeno Coelho, Rajan, 'A lower-bound formulation for the geometry and topology optimization of truss structures under multiple loading', *Structural and Multidisciplinary Optimization* 48.1 (July 2013), pp. 49–58.
DOI: [10.1007/s00158-012-0876-3](https://doi.org/10.1007/s00158-012-0876-3)
- cited on page 13
- [89] He, L. and Gilbert, M., 'Rationalization of trusses generated via layout optimization', *Structural and Multidisciplinary Optimization* 52.4 (Oct. 2015), pp. 677–694.
DOI: [10.1007/s00158-015-1260-x](https://doi.org/10.1007/s00158-015-1260-x)
- cited on page 13
- [90] Lu, Hongjia and Xie, Yi Min, 'Reducing the number of different members in truss layout optimization', *Structural and Multidisciplinary Optimization* 66.3 (Feb. 2023), p. 52.
DOI: [10.1007/s00158-023-03514-y](https://doi.org/10.1007/s00158-023-03514-y)
- cited on page 13
- [91] Savine, Florent, Irisarri, François-Xavier, Julien, Cédric, Vincenzi, Angela, and Guerin, Yannick, 'A component-based method for the optimization of stiffener layout on large cylindrical rib-stiffened shell structures', *Structural and Multidisciplinary Optimization* 64.4 (Oct. 2021), pp. 1843–1861.
DOI: [10.1007/s00158-021-02945-9](https://doi.org/10.1007/s00158-021-02945-9)
- cited on pages 13, 31
- [92] Parkes, E.W., 'Joints in optimum frameworks', *International Journal of Solids and Structures* 11.9 (Sept. 1975), pp. 1017–1022.
DOI: [10.1016/0020-7683\(75\)90044-X](https://doi.org/10.1016/0020-7683(75)90044-X)
- cited on pages 14, 15, 17
- [93] Schaedler, Tobias A. and Carter, William B., 'Architected Cellular Materials', *Annual Review of Materials Research* 46.1 (July 2016), pp. 187–210.
DOI: [10.1146/annurev-matsci-070115-031624](https://doi.org/10.1146/annurev-matsci-070115-031624)
- cited on pages 14, 17, 18
- [94] Kohn, Robert V. and Strang, Gilbert, 'Optimal design and relaxation of variational problems', *Communications on Pure and Applied Mathematics* 39.1 (1986), pp. 113–137.
DOI: [10.1002/cpa.3160390107](https://doi.org/10.1002/cpa.3160390107)
- cited on pages 14, 17, 18
- [95] Allaire, G. and Aubry, S., 'On optimal microstructures for a plane shape optimization problem', *Structural optimization* 17.2 (Apr. 1999), pp. 86–94.
DOI: [10.1007/BF01195933](https://doi.org/10.1007/BF01195933)
- cited on page 14
- [96] Fleck, N. A., Deshpande, V. S., and Ashby, M. F., 'Micro-architected materials: past, present and future', *Proceedings of the Royal Society A: Mathematical, Physical and Engineering Sciences* 466.2121 (Sept. 2010), Publisher: Royal Society, pp. 2495–2516.
DOI: [10.1098/rspa.2010.0215](https://doi.org/10.1098/rspa.2010.0215)
- cited on page 14
- [97] NZ, Bernard Spragg, 'Hypholoma fasciculare,' Apr. 2023.
URL: <https://www.flickr.com/photos/volvob12b/52833345708/>
- cited on page 14
- [98] LIBRARY, STEVE GSCHMEISSNER/SCIENCE PHOTO, 'Leaf structure, SEM'.

- URL: <https://www.sciencephoto.com/media/30288/view/leaf-structure-sem>
- [99] gripspix (mostly off, health issues), 'Wing of a dragonfly, detail', Aug. 2007.
URL: <https://www.flickr.com/photos/gripspix/1233292309/>
- [100], 'bone_03'.
URL: https://archimorph.files.wordpress.com/2010/01/bone_03.jpg
- [101] Ashby, M. F., 'Materials selection in mechanical design', 2nd ed. Oxford, OX ; Boston, MA: Butterworth-Heinemann, 1999.
ISBN: 978-0-7506-4357-3
- [102] Bensoussan, Alain, Lions, J.-L., and Papanicolaou, George, 'Asymptotic analysis for periodic structures', Studies in mathematics and its applications v. 5. Amsterdam ; New York : New York: North-Holland Pub. Co. ; sole distributors for the U.S.A. and Canada, Elsevier North-Holland, 1978.
ISBN: 978-0-444-85172-7
- [103] Dai, G. M. and Zhang, W. H., 'Size effects of basic cell in static analysis of sandwich beams', *International Journal of Solids and Structures* 45.9 (May 2008), pp. 2512–2533.
DOI: [10.1016/j.ijsolstr.2007.12.007](https://doi.org/10.1016/j.ijsolstr.2007.12.007)
- [104] Kalamkarov, Alexander L., Andrianov, Igor V., and Danielshev's'kyy, Vladyslav V., 'Asymptotic Homogenization of Composite Materials and Structures', *Applied Mechanics Reviews* 62.3 (Mar. 2009).
DOI: [10.1115/1.3090830](https://doi.org/10.1115/1.3090830)
- [105] Coelho, P. G., Amiano, L. D., Guedes, J. M., and Rodrigues, H. C., 'Scale-size effects analysis of optimal periodic material microstructures designed by the inverse homogenization method', *Computers & Structures*, CIVIL-COMP 174 (Oct. 2016), pp. 21–32.
DOI: [10.1016/j.compstruc.2015.10.001](https://doi.org/10.1016/j.compstruc.2015.10.001)
- [106] Zhang, Yan, Xiao, Mi, Li, Hao, Gao, Liang, and Chu, Sheng, 'Multiscale concurrent topology optimization for cellular structures with multiple microstructures based on ordered SIMP interpolation', *Computational Materials Science* 155 (Dec. 2018), pp. 74–91.
DOI: [10.1016/j.commatsci.2018.08.030](https://doi.org/10.1016/j.commatsci.2018.08.030)
- [107] Cramer, Nicholas B., Cellucci, Daniel W., Formoso, Olivia B., Gregg, Christine E., Jenett, Benjamin E., Kim, Joseph H., Lendraitis, Martynas, Swei, Sean S., Trinh, Greenfield T., Trinh, Khanh V., and Cheung, Kenneth C., 'Elastic shape morphing of ultralight structures by programmable assembly', *Smart Materials and Structures* 28.5 (Apr. 2019), p. 055006.
DOI: [10.1088/1361-665X/ab0ea2](https://doi.org/10.1088/1361-665X/ab0ea2)

- cited on pages 15, 16
- [108] Evans, A. G., He, M. Y., Deshpande, V. S., Hutchinson, John W., Jacobsen, A. J., and Barvosa-Carter, W., 'Concepts for Enhanced Energy Absorption Using Hollow Micro-Lattices', *International Journal of Impact Engineering* (2010).
DOI: [10.1016/j.ijimpeng.2010.03.007](https://doi.org/10.1016/j.ijimpeng.2010.03.007)
- cited on pages 15, 16
- [109] Schaedler, Tobias A., Ro, Christopher J., Sorensen, Adam E., Eckel, Zak, Yang, Sophia S., Carter, William B., and Jacobsen, Alan J., 'Designing Metallic Microlattices for Energy Absorber Applications', *Advanced Engineering Materials* 16.3 (2014), pp. 276–283.
DOI: [10.1002/adem.201300206](https://doi.org/10.1002/adem.201300206)
- cited on pages 15, 16
- [110] Ozdemir, Zuhal, Hernandez-Nava, Everth, Tyas, Andrew, Warren, James A., Fay, Stephen D., Goodall, Russell, Todd, Iain, and Askes, Harm, 'Energy absorption in lattice structures in dynamics: Experiments', *International Journal of Impact Engineering* 89 (Mar. 2016), pp. 49–61.
DOI: [10.1016/j.ijimpeng.2015.10.007](https://doi.org/10.1016/j.ijimpeng.2015.10.007)
- cited on page 16
- [111] Opgenoord, Max M. and Willcox, Karen E., 'Aeroelastic Tailoring using Additively Manufactured Lattice Structures', *2018 Multidisciplinary Analysis and Optimization Conference*, Atlanta, Georgia: American Institute of Aeronautics and Astronautics, June 2018.
DOI: [10.2514/6.2018-4055](https://doi.org/10.2514/6.2018-4055)
- cited on page 16
- [112] Hutmacher, Dietmar W., 'Scaffolds in tissue engineering bone and cartilage', *Biomaterials, Orthopaedic Polymeric Biomaterials: Applications of Biodegradables* 21.24 (Dec. 2000), pp. 2529–2543.
DOI: [10.1016/S0142-9612\(00\)00121-6](https://doi.org/10.1016/S0142-9612(00)00121-6)
- cited on page 16
- [113] Mota, Carlos, Puppi, Dario, Chiellini, Federica, and Chiellini, Emo, 'Additive manufacturing techniques for the production of tissue engineering constructs', *Journal of Tissue Engineering and Regenerative Medicine* 9.3 (Mar. 2015), pp. 174–190.
DOI: [10.1002/tterm.1635](https://doi.org/10.1002/tterm.1635)
- cited on page 16
- [114] Nikolova, Maria P. and Chavali, Murthy S., 'Recent advances in biomaterials for 3D scaffolds: A review', *Bioactive Materials* 4 (Oct. 2019), pp. 271–292.
DOI: [10.1016/j.bioactmat.2019.10.005](https://doi.org/10.1016/j.bioactmat.2019.10.005)
- cited on page 16
- [115] Lu, T. J., Stone, Howard A., and Ashby, M. F., 'Heat transfer in open-cell metal foams', *Acta Materialia* 46.10 (June 1998), Publisher: Elsevier Limited, pp. 3619–3635.
DOI: [10.1016/S1359-6454\(98\)00031-7](https://doi.org/10.1016/S1359-6454(98)00031-7)
- cited on page 16
- [116] Wadley, Haydn N. G. and Queheillalt, Douglas T., 'Thermal Applications of Cellular Lattice Structures', *Materials Science Forum* 539-543 (2007), Conference Name: THERMEC 2006, pp. 242–247.

- DOI: [10.4028/www.scientific.net/MSF.539-543.242](https://doi.org/10.4028/www.scientific.net/MSF.539-543.242)
- [117] AirShowConsultants, 'The REAL monster from Loch Ness – Vickers Wellington', June 2013. cited on page 16
URL: <https://shortfinals.org/2013/06/15/the-real-monster-from-loch-ness-vickers-wellington-r-for-robert/>
- [118] Cheung, Kenneth C. and Gershenfeld, Neil, 'Reversibly Assembled Cellular Composite Materials', *Science* 341.6151 (Sept. 2013), Publisher: American Association for the Advancement of Science Section: Report, pp. 1219–1221. cited on pages 16, 17
DOI: [10.1126/science.1240889](https://doi.org/10.1126/science.1240889)
- [119] Jenett, Benjamin, Calisch, Sam, Cellucci, Daniel, Cramer, Nick, Gershenfeld, Neil, Swei, Sean, and Cheung, Kenneth C., 'Digital Morphing Wing: Active Wing Shaping Concept Using Composite Lattice-Based Cellular Structures', *Soft Robotics* 4.1 (Mar. 2017), pp. 33–48. cited on pages 16, 17
DOI: [10.1089/soro.2016.0032](https://doi.org/10.1089/soro.2016.0032)
- [120] Dong, Liang, Deshpande, Vikram, and Wadley, Haydn, 'Mechanical response of Ti-6Al-4V octet-truss lattice structures', *International Journal of Solids and Structures* 60-61 (May 2015), pp. 107–124. cited on pages 16, 17
DOI: [10.1016/j.ijsolstr.2015.02.020](https://doi.org/10.1016/j.ijsolstr.2015.02.020)
- [121] Stolpe, Mathias, 'Fail-safe truss topology optimization', *Structural and Multidisciplinary Optimization* 60.4 (Oct. 2019), pp. 1605–1618. cited on pages 16, 17
DOI: [10.1007/s00158-019-02295-7](https://doi.org/10.1007/s00158-019-02295-7)
- [122] Wu, Jun, Sigmund, Ole, and Groen, Jeroen P., 'Topology optimization of multi-scale structures: a review', *Structural and Multidisciplinary Optimization* (Mar. 2021). cited on pages 16–20, 71
DOI: [10.1007/s00158-021-02881-8](https://doi.org/10.1007/s00158-021-02881-8)
- [123] Hunt, Christopher J., Wisnom, Michael R., and Woods, Benjamin K. S., 'WrapToR composite truss structures: Improved process and structural efficiency', *Composite Structures* 230 (Dec. 2019), p. 111467. cited on pages 16, 17
DOI: [10.1016/j.compstruct.2019.111467](https://doi.org/10.1016/j.compstruct.2019.111467)
- [124] Gershenfeld, Neil, Carney, Matthew, Jenett, Benjamin, Calisch, Sam, and Wilson, Spencer, 'Macrofabrication with Digital Materials: Robotic Assembly', *Architectural Design* 85.5 (2015), pp. 122–127. cited on pages 16, 18
DOI: [10.1002/ad.1964](https://doi.org/10.1002/ad.1964)
- [125] Jenett, Ben and Cheung, Kenneth, 'BILL-E: Robotic Platform for Locomotion and Manipulation of Lightweight Space Structures', *25th AIAA/AHS Adaptive Structures Conference*, Grapevine, Texas: American Institute of Aeronautics and Astronautics, Jan. 2017. cited on pages 16, 18

- cited on pages 16, 18
- [126] Costa, Allan, Jenett, Benjamin, Kostitsyna, Irina, Abdel-Rahman, Amira, Gershenfeld, Neil, and Cheung, Kenneth, 'Algorithmic Approaches to Reconfigurable Assembly Systems', *arXiv:2008.11925 [cs]* (Aug. 2020), arXiv: 2008.11925.
 DOI: [10.1109/AERO.2019.8741572](https://doi.org/10.1109/AERO.2019.8741572)
- cited on pages 16, 18
- [127] Niehs, Eike, Schmidt, Arne, Scheffer, Christian, Biediger, Daniel E., Yannuzzi, Michael, Jenett, Benjamin, Abdel-Rahman, Amira, Cheung, Kenneth C., Becker, Aaron T., and Fekete, Sándor P., 'Recognition and Reconfiguration of Lattice-Based Cellular Structures by Simple Robots', *2020 IEEE International Conference on Robotics and Automation (ICRA)*, ISSN: 2577-087X, May 2020, pp. 8252–8259.
 DOI: [10.1109/ICRA40945.2020.9196700](https://doi.org/10.1109/ICRA40945.2020.9196700)
- cited on pages 16–18
- [128] Deshpande, V. S., Ashby, M. F., and Fleck, N. A., 'Foam topology: bending versus stretching dominated architectures', *Acta Materialia* 49.6 (Apr. 2001), pp. 1035–1040.
 DOI: [10.1016/S1359-6454\(00\)00379-7](https://doi.org/10.1016/S1359-6454(00)00379-7)
- cited on pages 17, 18
- [129] Ashby, M.f, 'The properties of foams and lattices', *Philosophical Transactions of the Royal Society A: Mathematical, Physical and Engineering Sciences* 364.1838 (Jan. 2006), Publisher: Royal Society, pp. 15–30.
 DOI: [10.1098/rsta.2005.1678](https://doi.org/10.1098/rsta.2005.1678)
- cited on pages 17, 18
- [130] Zhou, M. and Rozvany, G. I. N., 'The COC algorithm, Part II: Topological, geometrical and generalized shape optimization', *Computer Methods in Applied Mechanics and Engineering*, Second World Congress on Computational Mechanics 89.1 (Aug. 1991), pp. 309–336.
 DOI: [10.1016/0045-7825\(91\)90046-9](https://doi.org/10.1016/0045-7825(91)90046-9)
- cited on page 18
- [131] Rodrigues, H., Guedes, J.M., and Bendsoe, M.P., 'Hierarchical optimization of material and structure', *Structural and Multidisciplinary Optimization* 24.1 (Aug. 2002), pp. 1–10.
 DOI: [10.1007/s00158-002-0209-z](https://doi.org/10.1007/s00158-002-0209-z)
- cited on page 18
- [132] Pantz, O. and Trabelsi, K., 'A Post-Treatment of the Homogenization Method for Shape Optimization', *SIAM Journal on Control and Optimization* 47.3 (Jan. 2008), Publisher: Society for Industrial and Applied Mathematics, pp. 1380–1398.
 DOI: [10.1137/070688900](https://doi.org/10.1137/070688900)
- cited on pages 18–20
- [133] Groen, Jeroen P. and Sigmund, Ole, 'Homogenization-based topology optimization for high-resolution manufacturable microstructures', *International Journal for Numerical Methods in Engineering* 113.8 (2018), _eprint: <https://onlinelibrary.wiley.com/doi/pdf/10.1002/nme.5575>

- [134] Wang, Chuang, Gu, Xiaojun, Zhu, Jihong, Zhou, Han, Li, Shaoying, and Zhang, Weihong, 'Concurrent design of hierarchical structures with three-dimensional parameterized lattice microstructures for additive manufacturing', *Structural and Multidisciplinary Optimization* 61.3 (Mar. 2020), pp. 869–894.
DOI: [10.1007/s00158-019-02408-2](https://doi.org/10.1007/s00158-019-02408-2)
- [135] Guedes, JoséMiranda and Kikuchi, Noboru, 'Preprocessing and postprocessing for materials based on the homogenization method with adaptive finite element methods', *Computer Methods in Applied Mechanics and Engineering* 83.2 (Oct. 1990), pp. 143–198.
DOI: [10.1016/0045-7825\(90\)90148-F](https://doi.org/10.1016/0045-7825(90)90148-F)
- [136] Allaire, Grégoire, Geoffroy-Donders, Perle, and Pantz, Olivier, 'Topology optimization of modulated and oriented periodic microstructures by the homogenization method', *Computers & Mathematics with Applications*, Simulation for Additive Manufacturing 78.7 (Oct. 2019), pp. 2197–2229.
DOI: [10.1016/j.camwa.2018.08.007](https://doi.org/10.1016/j.camwa.2018.08.007)
- [137] Geoffroy-Donders, Perle, Allaire, Grégoire, and Pantz, Olivier, '3-d topology optimization of modulated and oriented periodic microstructures by the homogenization method', *Journal of Computational Physics* 401 (Jan. 2020), p. 108994.
DOI: [10.1016/j.jcp.2019.108994](https://doi.org/10.1016/j.jcp.2019.108994)
- [138] Kumar, Tej and Suresh, Krishnan, 'A density-and-strain-based K-clustering approach to microstructural topology optimization', *Structural and Multidisciplinary Optimization* 61.4 (Apr. 2020), pp. 1399–1415.
DOI: [10.1007/s00158-019-02422-4](https://doi.org/10.1007/s00158-019-02422-4)
- [139] Xia, Liang and Breitkopf, Piotr, 'Multiscale structural topology optimization with an approximate constitutive model for local material microstructure', *Computer Methods in Applied Mechanics and Engineering* 286 (Apr. 2015), pp. 147–167.
DOI: [10.1016/j.cma.2014.12.018](https://doi.org/10.1016/j.cma.2014.12.018)
- [140] Wang, Chuang, Zhu, Ji Hong, Zhang, Wei Hong, Li, Shao Ying, and Kong, Jie, 'Concurrent topology optimization design of structures and non-uniform parameterized lattice microstructures', *Structural and Multidisciplinary Optimization* 58.1 (July 2018), pp. 35–50.
DOI: [10.1007/s00158-018-2009-0](https://doi.org/10.1007/s00158-018-2009-0)
- [141] Imediegwu, Chikwesiri, Murphy, Ryan, Hewson, Robert, and Santer, Mathew, 'Multiscale structural optimization towards three-dimensional printable structures', *Structural and Multidisciplinary Optimization* 60.2 (Aug. 2019), pp. 513–525.
DOI: [10.1007/s00158-019-02220-y](https://doi.org/10.1007/s00158-019-02220-y)

- cited on pages 19, 20
- [142] Kim, Cheolwoong, Lee, Jaewook, and Yoo, Jeonghoon, 'Machine learning-combined topology optimization for functionary graded composite structure design', *Computer Methods in Applied Mechanics and Engineering* 387 (Dec. 2021), p. 114158.
DOI: [10.1016/j.cma.2021.114158](https://doi.org/10.1016/j.cma.2021.114158)
- cited on pages 19, 20
- [143] White, Daniel A., Arrighi, William J., Kudo, Jun, and Watts, Seth E., 'Multiscale topology optimization using neural network surrogate models', *Computer Methods in Applied Mechanics and Engineering* 346 (Apr. 2019), pp. 1118–1135.
DOI: [10.1016/j.cma.2018.09.007](https://doi.org/10.1016/j.cma.2018.09.007)
- cited on pages 19, 20
- [144] Chandrasekhar, Aaditya and Suresh, Krishnan, 'Multi-Material Topology Optimization Using Neural Networks', *Computer-Aided Design* 136 (July 2021), p. 103017.
DOI: [10.1016/j.cad.2021.103017](https://doi.org/10.1016/j.cad.2021.103017)
- cited on pages 19, 20
- [145] Wang, Liwei, Liu, Zhao, Da, Daicong, Chan, Yu-Chin, Chen, Wei, and Zhu, Ping, 'Enhancing Data-driven Multiscale Topology Optimization with Generalized De-homogenization', Dec. 2021.
URL: <https://arxiv.org/abs/2112.02506v2>
- cited on pages 19, 20
- [146] Duriez, Edouard, Morlier, Joseph, Charlotte, Miguel, and Azzaro-Pantel, Catherine, 'A well connected, locally-oriented and efficient multi-scale topology optimization (EMTO) strategy', *Structural and Multidisciplinary Optimization* 64.6 (Dec. 2021), pp. 3705–3728.
DOI: [10.1007/s00158-021-03048-1](https://doi.org/10.1007/s00158-021-03048-1)
- cited on pages 19, 20
- [147] Sigmund, Ole, 'On benchmarking and good scientific practise in topology optimization', *Structural and Multidisciplinary Optimization* 65.11 (Oct. 2022), p. 315.
DOI: [10.1007/s00158-022-03427-2](https://doi.org/10.1007/s00158-022-03427-2)
- cited on page 20
- [148] Cheng, Lin, Bai, Jiaxi, and To, Albert C., 'Functionally graded lattice structure topology optimization for the design of additive manufactured components with stress constraints', *Computer Methods in Applied Mechanics and Engineering* 344 (Feb. 2019), pp. 334–359.
DOI: [10.1016/j.cma.2018.10.010](https://doi.org/10.1016/j.cma.2018.10.010)
- cited on pages 20, 21
- [149] Wu, Jun, Aage, Niels, Westermann, Rüdiger, and Sigmund, Ole, 'Infill Optimization for Additive Manufacturing—Approaching Bone-Like Porous Structures', *IEEE Transactions on Visualization and Computer Graphics* 24.2 (Feb. 2018), Conference Name: IEEE Transactions on Visualization and Computer Graphics, pp. 1127–1140.
DOI: [10.1109/TVCG.2017.2655523](https://doi.org/10.1109/TVCG.2017.2655523)
- cited on pages 20, 21
- [150] Huang, X. and Xie, Y. M., 'Optimal design of periodic structures using evolutionary topology optimization', *Structural and Multidisciplinary Optimization* 36.6 (Nov. 2008), pp. 597–606.

- DOI: [10.1007/s00158-007-0196-1](https://doi.org/10.1007/s00158-007-0196-1)
- [151] Tugilimana, Alexis, Coelho, Rajan Filomeno, and Thrall, Ashley P., 'An integrated design methodology for modular trusses including dynamic grouping, module spatial orientation, and topology optimization', *Structural and Multidisciplinary Optimization* 60.2 (Aug. 2019), pp. 613–638.
DOI: [10.1007/s00158-019-02230-w](https://doi.org/10.1007/s00158-019-02230-w)
- [152] Bakker, Coen, Zhang, Lidan, Higginson, Kristie, and Keulen, Fred van, 'Simultaneous optimization of topology and layout of modular stiffeners on shells and plates', *Structural and Multidisciplinary Optimization* 64.5 (Nov. 2021), pp. 3147–3161.
DOI: [10.1007/s00158-021-03081-0](https://doi.org/10.1007/s00158-021-03081-0)
- [153] Tugilimana, Alexis, Thrall, Ashley P., Descamps, Benoît, and Coelho, Rajan Filomeno, 'Spatial orientation and topology optimization of modular trusses', *Structural and Multidisciplinary Optimization* 55.2 (Feb. 2017), pp. 459–476.
DOI: [10.1007/s00158-016-1501-7](https://doi.org/10.1007/s00158-016-1501-7)
- [154] Stromberg, Lauren L., Beghini, Alessandro, Baker, William F., and Paulino, Glaucio H., 'Application of layout and topology optimization using pattern gradation for the conceptual design of buildings', *Structural and Multidisciplinary Optimization* 43.2 (Feb. 2011), pp. 165–180.
DOI: [10.1007/s00158-010-0563-1](https://doi.org/10.1007/s00158-010-0563-1)
- [155] Wu, Jun, Dick, Christian, and Westermann, Rüdiger, 'A System for High-Resolution Topology Optimization', *IEEE Transactions on Visualization and Computer Graphics* 22.3 (Mar. 2016), Conference Name: IEEE Transactions on Visualization and Computer Graphics, pp. 1195–1208.
DOI: [10.1109/TVCG.2015.2502588](https://doi.org/10.1109/TVCG.2015.2502588)
- [156] Stragiotti, Enrico, Irisarri, François-Xavier, Julien, Cédric, and Morlier, Joseph, 'Towards manufactured lattice structures: a comparison between layout and topology optimization', *AeroBest 2021 International Conference on Multidisciplinary Design Optimization of Aerospace Systems. Book of proceedings*, Lisbon, Portugal: ECCOMAS, July 2021, pp. 229–244.
- [157] Achtziger, Wolfgang and Kanzow, Christian, 'Mathematical programs with vanishing constraints: optimality conditions and constraint qualifications', *Mathematical Programming* 114.1 (July 2008), pp. 69–99.
DOI: [10.1007/s10107-006-0083-3](https://doi.org/10.1007/s10107-006-0083-3)
- [158] Cheng, Gengdong and Jiang, Zheng, 'Study on Topology Optimization with Stress Constraints', *Engineering Optimization* 20.2 (Nov. 1992), pp. 129–148.
DOI: [10.1080/03052159208941276](https://doi.org/10.1080/03052159208941276)

- cited on pages 25–27, 33
- [159] Verbart, Alexander, Langelaar, Matthijs, and Keulen, Fred van, 'A unified aggregation and relaxation approach for stress-constrained topology optimization', *Structural and Multidisciplinary Optimization* 55.2 (Feb. 2017), pp. 663–679.
 DOI: [10.1007/s00158-016-1524-0](https://doi.org/10.1007/s00158-016-1524-0)
- cited on pages 25, 32
- [160] Duysinx, P. and Bendsøe, M. P., 'Topology optimization of continuum structures with local stress constraints', *International Journal for Numerical Methods in Engineering* 43.8 (1998), pp. 1453–1478.
 DOI: [10.1002/\(SICI\)1097-0207\(19981230\)43:8<1453::AID-NME480>3.0.CO;2-2](https://doi.org/10.1002/(SICI)1097-0207(19981230)43:8<1453::AID-NME480>3.0.CO;2-2)
- cited on pages 25, 26, 32
- [161] Le, Chau, Norato, Julian, Bruns, Tyler, Ha, Christopher, and Tortorelli, Daniel, 'Stress-based topology optimization for continua', *Structural and Multidisciplinary Optimization* 41.4 (Apr. 2010), pp. 605–620.
 DOI: [10.1007/s00158-009-0440-y](https://doi.org/10.1007/s00158-009-0440-y)
- cited on page 26
- [162] Holmberg, Erik, Torstenfelt, Bo, and Klarbring, Anders, 'Stress constrained topology optimization', *Structural and Multidisciplinary Optimization* 48.1 (2013), pp. 33–47.
 DOI: [10.1007/s00158-012-0880-7](https://doi.org/10.1007/s00158-012-0880-7)
- cited on page 26
- [163] Silva, Gustavo Assis da, Beck, André Teófilo, and Sigmund, Ole, 'Stress-constrained topology optimization considering uniform manufacturing uncertainties', *Computer Methods in Applied Mechanics and Engineering* 344 (Feb. 2019), pp. 512–537.
 DOI: [10.1016/j.cma.2018.10.020](https://doi.org/10.1016/j.cma.2018.10.020)
- cited on page 26
- [164] Stolpe, Mathias, 'On Models and Methods for Global Optimization of Structural Topology', Publisher: Matematik, PhD thesis, 2003.
- cited on page 26
- [165] Sved, G. and Ginos, Z., 'Structural optimization under multiple loading', *International Journal of Mechanical Sciences* 10.10 (Oct. 1968), pp. 803–805.
 DOI: [10.1016/0020-7403\(68\)90021-0](https://doi.org/10.1016/0020-7403(68)90021-0)
- cited on page 27
- [166] Silva, Gustavo Assis da, Aage, Niels, Beck, André Teófilo, and Sigmund, Ole, 'Local versus global stress constraint strategies in topology optimization: A comparative study', *International Journal for Numerical Methods in Engineering* 122.21 (2021), pp. 6003–6036.
 DOI: [10.1002/nme.6781](https://doi.org/10.1002/nme.6781)
- cited on page 27
- [167] Kreisselmeier, G. and Steinhauser, R., 'Systematic Control Design by Optimizing a Vector Performance Index', *IFAC Proceedings Volumes*, IFAC Symposium on computer Aided Design of Control Systems, Zurich, Switzerland, 29-31 August 12.7 (Sept. 1979), pp. 113–117.
 DOI: [10.1016/S1474-6670\(17\)65584-8](https://doi.org/10.1016/S1474-6670(17)65584-8)

- [168] Watts, Seth, Arrighi, William, Kudo, Jun, Tortorelli, Daniel A., and White, Daniel A., 'Simple, accurate surrogate models of the elastic response of three-dimensional open truss micro-architectures with applications to multiscale topology design', *Structural and Multidisciplinary Optimization* 60.5 (Nov. 2019), pp. 1887–1920.
DOI: [10.1007/s00158-019-02297-5](https://doi.org/10.1007/s00158-019-02297-5)
- [169] Johnson, Steven G., 'The NLOpt nonlinear-optimization package', <https://github.com/stevengj/nlopt>, 2007.
- [170] Diamond, Steven and Boyd, Stephen, 'CVXPY: A Python-Embedded Modeling Language for Convex Optimization', 2016.
- [171] Domahidi, Alexander, Chu, Eric, and Boyd, Stephen, 'ECOS: An SOCP solver for embedded systems', *2013 European Control Conference (ECC)*, Zurich: IEEE, July 2013, pp. 3071–3076, ISBN: 978-3-033-03962-9.
DOI: [10.23919/ECC.2013.6669541](https://doi.org/10.23919/ECC.2013.6669541)
- [172] Lewiński, T., Zhou, M., and Rozvany, G. I. N., 'Extended exact solutions for least-weight truss layouts—Part I: Cantilever with a horizontal axis of symmetry', *International Journal of Mechanical Sciences* 36.5 (1994), pp. 375–398.
DOI: [10.1016/0020-7403\(94\)90043-4](https://doi.org/10.1016/0020-7403(94)90043-4)
- [173] Munro, Dirk and Groenwold, Albert, 'Local stress-constrained and slope-constrained SAND topology optimisation', *International Journal for Numerical Methods in Engineering* 110.5 (May 2017), pp. 420–439.
DOI: [10.1002/nme.5360](https://doi.org/10.1002/nme.5360)
- [174] Bruggi, Matteo and Duysinx, Pierre, 'Topology optimization for minimum weight with compliance and stress constraints', *Structural and Multidisciplinary Optimization* 46.3 (Sept. 2012), pp. 369–384.
DOI: [10.1007/s00158-012-0759-7](https://doi.org/10.1007/s00158-012-0759-7)
- [175] París, J., Navarrina, F., Colominas, I., and Casteleiro, M., 'Block aggregation of stress constraints in topology optimization of structures', *Advances in Engineering Software*, Advances in optimum engineering design 41.3 (Mar. 2010), pp. 433–441.
DOI: [10.1016/j.advengsoft.2009.03.006](https://doi.org/10.1016/j.advengsoft.2009.03.006)
- [176] Norato, Julián A., Smith, Hollis A., Deaton, Joshua D., and Kolonay, Raymond M., 'A maximum-rectifier-function approach to stress-constrained topology optimization', *Structural and Multidisciplinary Optimization* 65.10 (Sept. 2022), p. 286.
DOI: [10.1007/s00158-022-03357-z](https://doi.org/10.1007/s00158-022-03357-z)
- [177] Reinschmidt, Kenneth F. and Russell, Alan D., 'Applications of linear programming in structural layout and optimization', *Computers & Structures* 4.4 (Aug. 1974), pp. 855–869.

- cited on page 46
- DOI: [10.1016/0045-7949\(74\)90049-2](https://doi.org/10.1016/0045-7949(74)90049-2)
- [178] Oberndorfer, J. M., Achtziger, W., and Hornlein, H. R. E. M., 'Two approaches for truss topology optimization: a comparison for practical use', *Structural Optimization* 11.3-4 (June 1996), pp. 137–144.
DOI: [10.1007/BF01197027](https://doi.org/10.1007/BF01197027)
- cited on page 46
- DOI: [10.1007/BF01199235](https://doi.org/10.1007/BF01199235)
- cited on pages 46, 49, 62–64
- [179] Silva Smith, O., 'Topology optimization of trusses with local stability constraints and multiple loading conditions—a heuristic approach', *Structural Optimization* 13.2-3 (Apr. 1997), pp. 155–166.
DOI: [10.1007/BF01199235](https://doi.org/10.1007/BF01199235)
- cited on page 46
- [180] Achtziger, W., 'Local stability of trusses in the context of topology optimization Part II: A numerical approach', *Structural optimization* 17.4 (Dec. 1999), pp. 247–258.
DOI: [10.1007/BF01207000](https://doi.org/10.1007/BF01207000)
- cited on page 46
- [181] Pritchard, T., Gilbert, Matthew, and Tyas, Andrew, 'Plastic Layout Optimization of Large-Scale Frameworks Subject to Multiple Load Cases, Member Self-Weight and with Joint Length Penalties' (Jan. 2005).
- cited on pages 46, 47, 64
- [182] Tyas, A., Gilbert, M., and Pritchard, T., 'Practical plastic layout optimization of trusses incorporating stability considerations', *Computers & Structures* 84.3 (Jan. 2006), pp. 115–126.
DOI: [10.1016/j.compstruc.2005.09.032](https://doi.org/10.1016/j.compstruc.2005.09.032)
- cited on page 46
- [183] Descamps, Benoît and Filomeno Coelho, Rajan, 'The nominal force method for truss geometry and topology optimization incorporating stability considerations', *International Journal of Solids and Structures* 51.13 (June 2014), pp. 2390–2399.
DOI: [10.1016/j.ijsolstr.2014.03.003](https://doi.org/10.1016/j.ijsolstr.2014.03.003)
- cited on pages 46, 52
- [184] Schwarz, Jonas, Chen, Tian, Shea, Kristina, and Stanković, Tino, 'Efficient size and shape optimization of truss structures subject to stress and local buckling constraints using sequential linear programming', *Structural and Multidisciplinary Optimization* 58.1 (July 2018), pp. 171–184.
DOI: [10.1007/s00158-017-1885-z](https://doi.org/10.1007/s00158-017-1885-z)
- cited on page 46
- [185] Cai, Qi, Feng, Ruoqiang, and Zhang, Zhijie, 'Topology optimization of trusses incorporating practical local buckling stability considerations', *Structures* 41 (July 2022), pp. 1710–1718.
DOI: [10.1016/j.istruc.2022.05.109](https://doi.org/10.1016/j.istruc.2022.05.109)
- cited on pages 47, 59, 60
- [186] Guo, X., Cheng, G., and Yamazaki, K., 'A new approach for the solution of singular optima in truss topology optimization with stress and local buckling constraints', *Structural and Multidisciplinary Optimization* 22.5 (Dec. 2001), pp. 364–373.
DOI: [10.1007/s00158-001-0156-0](https://doi.org/10.1007/s00158-001-0156-0)

- [187] Stolpe, M. and Svanberg, K., 'A note on stress-constrained truss topology optimization', *Structural and Multidisciplinary Optimization* 25.1 (Mar. 2003), pp. 62–64.
DOI: [10.1007/s00158-002-0273-4](https://doi.org/10.1007/s00158-002-0273-4)
- [188] Zhou, M., 'Difficulties in truss topology optimization with stress and local buckling constraints', *Structural optimization* 11.2 (Apr. 1996), pp. 134–136.
DOI: [10.1007/BF01376857](https://doi.org/10.1007/BF01376857)
- [189] Rozvany, G. I. N., 'Difficulties in truss topology optimization with stress, local buckling and system stability constraints', *Structural optimization* 11.3 (June 1996), pp. 213–217.
DOI: [10.1007/BF01197036](https://doi.org/10.1007/BF01197036)
- [190] Ben-Tal, Aharon, Jarre, Florian, Kočvara, Michal, Nemirovski, Arkadi, and Zowe, Jochem, 'Optimal Design of Trusses Under a Nonconvex Global Buckling Constraint', *Optimization and Engineering* 1.2 (July 2000), pp. 189–213.
DOI: [10.1023/A:1010091831812](https://doi.org/10.1023/A:1010091831812)
- [191] Kočvara, M., 'On the modelling and solving of the truss design problem with global stability constraints', *Structural and Multidisciplinary Optimization* 23.3 (Apr. 2002), pp. 189–203.
DOI: [10.1007/s00158-002-0177-3](https://doi.org/10.1007/s00158-002-0177-3)
- [192] Neves, M. M., Rodrigues, H., and Guedes, J. M., 'Generalized topology design of structures with a buckling load criterion', *Structural optimization* 10.2 (Oct. 1995), pp. 71–78.
DOI: [10.1007/BF01743533](https://doi.org/10.1007/BF01743533)
- [193] Ferrari, Federico, Sigmund, Ole, and Guest, James K., 'Topology optimization with linearized buckling criteria in 250 lines of Matlab', *Structural and Multidisciplinary Optimization* 63.6 (June 2021), pp. 3045–3066.
DOI: [10.1007/s00158-021-02854-x](https://doi.org/10.1007/s00158-021-02854-x)
- [194] Mela, Kristo, 'Resolving issues with member buckling in truss topology optimization using a mixed variable approach', *Structural and Multidisciplinary Optimization* 50.6 (Dec. 2014), pp. 1037–1049.
DOI: [10.1007/s00158-014-1095-x](https://doi.org/10.1007/s00158-014-1095-x)
- [195] Kirsch, Uri, 'Effect of Compatibility and Prestressing on Optimized Trusses', *Journal of Structural Engineering* 115.3 (Mar. 1989), pp. 724–737.
DOI: [10.1061/\(ASCE\)0733-9445\(1989\)115:3\(724\)](https://doi.org/10.1061/(ASCE)0733-9445(1989)115:3(724))
- [196] Moore, Jason; K. and Mechmotum, 'cyipopt: Cython interface for the interior point optimizer IPOPT', 2018.
URL: <https://github.com/mechmotum/cyipopt>

- cited on pages 57, 76, 77
- [197] Alappat, Christie, Basermann, Achim, Bishop, Alan R., Fehske, Holger, Hager, Georg, Schenk, Olaf, Thies, Jonas, and Wellein, Gerhard, 'A Recursive Algebraic Coloring Technique for Hardware-efficient Symmetric Sparse Matrix-vector Multiplication', *ACM Transactions on Parallel Computing* 7.3 (2020), 19:1–19:37.
DOI: [10.1145/3399732](https://doi.org/10.1145/3399732)
- cited on pages 58, 64
- [198] Stragiotti, Enrico, 'Truss Topology Optimization with Topological Buckling Constraints Data Set', May 2023.
DOI: [10.17632/BW7XB2W6ST.1](https://doi.org/10.17632/BW7XB2W6ST.1)
, URL: <https://data.mendeley.com/datasets/bw7xb2w6st/1>
- cited on page 67
- [199] Rozvany, George I. N., 'On symmetry and non-uniqueness in exact topology optimization', *Structural and Multidisciplinary Optimization* 43.3 (Mar. 2011), pp. 297–317.
DOI: [10.1007/s00158-010-0564-0](https://doi.org/10.1007/s00158-010-0564-0)
- cited on page 67
- [200] Guo, Xu, Du, Zongliang, and Cheng, Gengdong, 'A confirmation of a conjecture on the existence of symmetric optimal solution under multiple loads', *Structural and Multidisciplinary Optimization* 50.4 (Oct. 2014), pp. 659–661.
DOI: [10.1007/s00158-014-1089-8](https://doi.org/10.1007/s00158-014-1089-8)
- cited on page 71
- [201] Stragiotti, Enrico, Irisarri, François-Xavier, Julien, Cédric, and Morlier, Joseph, 'Enhanced truss topology optimization (TTO) applied to a cellular wing box', *ASMO-UK 12 / ASMO-Europe 1 / ISSMO Conference on Engineering Design Optimization* (2022), Leeds, United Kingdom, July 2022.
- cited on page 71
- [202] Zhou, Shiwei and Li, Qing, 'Design of graded two-phase microstructures for tailored elasticity gradients', *Journal of Materials Science* 43.15 (Aug. 2008), pp. 5157–5167.
DOI: [10.1007/s10853-008-2722-y](https://doi.org/10.1007/s10853-008-2722-y)
- cited on page 71
- [203] Li, Dawei, Liao, Wenhe, Dai, Ning, and Xie, Yi Min, 'Anisotropic design and optimization of conformal gradient lattice structures', *Computer-Aided Design* 119 (Feb. 2020), p. 102787.
DOI: [10.1016/j.cad.2019.102787](https://doi.org/10.1016/j.cad.2019.102787)
- cited on page 86
- [204] Deshpande, V. S., Fleck, N. A., and Ashby, M. F., 'Effective properties of the octet-truss lattice material', *Journal of the Mechanics and Physics of Solids* 49.8 (Aug. 2001), pp. 1747–1769.
DOI: [10.1016/S0022-5096\(01\)00010-2](https://doi.org/10.1016/S0022-5096(01)00010-2)
- cited on page 98
- [205] Stegmann, J. and Lund, E., 'Discrete material optimization of general composite shell structures', *International Journal for Numerical Methods in Engineering* 62.14 (Apr. 2005), pp. 2009–2027.
DOI: [10.1002/nme.1259](https://doi.org/10.1002/nme.1259)

- [206] Stolpe, M. and Svanberg, K., 'An alternative interpolation scheme for minimum compliance topology optimization', *Structural and Multidisciplinary Optimization* 22.2 (Sept. 2001), pp. 116–124.
doi: [10.1007/s001580100129](https://doi.org/10.1007/s001580100129)
- [207] Hvejsel, Christian Frier and Lund, Erik, 'Material interpolation schemes for unified topology and multi-material optimization', *Structural and Multidisciplinary Optimization* 43.6 (June 2011), pp. 811–825.
doi: [10.1007/s00158-011-0625-z](https://doi.org/10.1007/s00158-011-0625-z)
- [208] Prokop, Jozef, Odrobiňák, Jaroslav, Farbák, Matúš, and Novotný, Vladimír, 'Load-Carrying Capacity of Bailey Bridge in Civil Applications', *Applied Sciences* 12.8 (Jan. 2022), Number: 8 Publisher: Multidisciplinary Digital Publishing Institute, p. 3788.
doi: [10.3390/app12083788](https://doi.org/10.3390/app12083788)
- [209] Department of the Army, 'Field Manual No. 5–277, Panel Bridge, Bailey Type, Washington DC.' 1986 cited on page 111

APPENDIX

SENSITIVITY ANALYSIS OF THE MODULAR STRUCTURE OPTIMIZATION ALGORITHM

A

punti e virgole equazioni In this appendix, we demonstrate how the gradient, Jacobian, and Hessian matrices of the objective function and the optimization constraints are evaluated for the layout and topology optimization formulation \mathbb{M}_2 presented in Chapter 5. This step, called sensitivity analysis, is crucial for gradient descent optimization algorithms, as it allows for faster and more accurate convergence compared to using finite differences. We remind the reader that the index i is relative to the number of bars in a module \bar{n} , the index j is relative to the number of subdomains N_{sub} in which the structure is divided, and the index t is relative to the number of different modules' topologies N_T . The indexes are summarized in Table A.1 for added clarity.

A.1. OPTIMIZATION FORMULATION, OBJECTIVE FUNCTION AND CONSTRAINTS

The relaxed formulation \mathbb{M}_2 for which we want to perform the sensitivity analysis is expressed in terms of modules' cross-sectional area \bar{a} , module selection variables α , and member forces q as:

$$\begin{aligned}
 \min_{\bar{a}, \alpha, q} \quad & V = \sum_{j=1}^{N_{\text{sub}}} \bar{\ell}^T \tilde{a}^j \quad (\text{Volume minimization}) \\
 \text{s.t.} \quad & Bq = f \quad (g_{\text{eq}}) \\
 & q \geq -\frac{s\alpha^2}{\ell^2} \quad (g_{\text{buck}}) \\
 & -\sigma_C \alpha \leq q \leq \sigma_T \alpha \quad (g_{\text{st,t}}, g_{\text{st,c}}) \\
 & 0 \leq \bar{a} \leq \frac{4\pi\bar{\ell}^2}{\lambda_{\max}} \quad (g_{\text{slend}}) \\
 & \sum_{t=1}^{N_T} \alpha_t^j \leq 1, \quad \forall j \quad (g_{\text{sum}}),
 \end{aligned} \tag{\mathbb{M}_2}$$

in which

$$V = \sum_{j=1}^{N_{\text{sub}}} \bar{\ell}^T \tilde{a}^j, \tag{A.1}$$

represents the structural volume of the modular structure and acts as the objective function to minimize for the optimization. The vector \tilde{a}^j , representing the increased cross-sectional areas of the j -th subdomain, is defined as follows:

$$\tilde{a}^j = \sum_{t=1}^{N_T} \tilde{w}_t^j \bar{a}_t, \tag{A.2}$$

More information on sensitivity analysis can be found in the book by Martins and Ning [2].

Index	Interval	Expl.
i	$[0, \bar{n}[$	# of bars in a module
j	$[0, N_{\text{sub}}[$	# of sub- domains # of
t	$[0, N_T[$	modules' topolo- gies

Table A.1.: Reminder of the indexes used for the sensitivity analysis of the layout and topology optimization of modular structures.

and where \tilde{w} is evaluated using the RAMP interpolation scheme with the q parameter as follows:

$$\tilde{w}_t^j = \frac{\alpha_t^j}{1 + q(1 - \alpha_t^j)}. \quad (\text{A.3})$$

The cross-sectional areas vector \mathbf{a}^j of subdomain j used for the constraints evaluation is expressed as:

$$\mathbf{a}^j = \sum_{t=1}^{N_T} w_t^j \bar{\mathbf{a}}_t, \quad (\text{A.4})$$

where $\bar{\mathbf{a}}_t$ represent the vector of cross-sectional areas of the t module and w^j is the vector of weight relatives to the j subdomain, defined as $w^j \in \mathbb{R}^t | w_j^t \in [0, 1]$. Its relationship with the weight w is as follows:

$$w_t^j = \frac{\alpha_t^j}{1 + p(1 - \alpha_t^j)}, \quad (\text{A.5})$$

where $p \in \mathbb{R}^+$ denotes a parameter governing the steepness of the RAMP interpolation.

A.2. COMMON DERIVATIVES

We introduce here some important derivatives that we use all along the Chapter.

$$\frac{\partial \mathbf{a}^j}{\partial \bar{\mathbf{a}}_t} = w_t^j, \quad (\text{A.6})$$

$$\frac{\partial \mathbf{a}^j}{\partial \alpha_t^j} = \frac{\partial \mathbf{a}^j}{\partial w_t^j} \frac{\partial w_t^j}{\partial \alpha_t^j}, \quad (\text{A.7})$$

where

$$\frac{\partial \mathbf{a}^j}{\partial w_t^j} = \bar{\mathbf{a}}_t, \quad (\text{A.8})$$

and

$$\frac{\partial w_t^j}{\partial \alpha_t^j} = \frac{1 + (\cdot)}{(1 + (\cdot)(1 - \alpha_t^j))^2}, \quad (\text{A.9})$$

where (\cdot) is either equal to p or q .

$$\frac{\partial^2 w_t^j}{\partial (\alpha_t^j)^2} = \frac{2(\cdot)(1 + (\cdot))}{(1 + (\cdot)(1 - \alpha_t^j))^3}. \quad (\text{A.10})$$

A.3. GRADIENT

The gradient of the objective function V is non-zero only for the design variables $\bar{\alpha}$ and α . It is evaluated for $\bar{\alpha}$ as following:

$$\frac{\partial V}{\partial \bar{\alpha}_t} = \bar{\ell}^T \sum_{j=1}^{N_{\text{sub}}} \tilde{w}_t^j, \text{ with } t \in [1, \dots, N_T]. \quad (\text{A.11})$$

The gradient with respect to α can be written as:

$$\frac{\partial V}{\partial \alpha_t^j} = \frac{\partial V}{\partial w_t^j} \frac{\partial w_t^j}{\partial \alpha_t^j}, \quad (\text{A.12})$$

where

$$\frac{\partial V}{\partial w_t^j} = \bar{\ell}^T \bar{\alpha}_t, \quad (\text{A.13})$$

and evaluated using Equation A.9 and the parameter q . As already mentioned, the gradient is zero with respect to the member forces q :

$$\frac{\partial V}{\partial q} = 0. \quad (\text{A.14})$$

A.4. JACOBIAN MATRIX

We focus now on the evaluation of the Jacobian matrix of the optimization constraints with respect to the design variables.

EQUILIBRIUM CONSTRAINTS The equilibrium constraint g_{eq} is linear on q and not dependent on $\bar{\alpha}$ and α . For that reason we can write:

$$\frac{\partial g_{\text{eq}}}{\partial \bar{\alpha}} = 0, \quad (\text{A.15})$$

$$\frac{\partial g_{\text{eq}}}{\partial \alpha} = 0, \quad (\text{A.16})$$

$$\frac{\partial g_{\text{eq}}}{\partial q} = B. \quad (\text{A.17})$$

STRESS CONSTRAINTS Knowing that:

$$\frac{\partial g_{\text{st,t}}^j}{\partial \alpha^j} = -\sigma_t, \quad (\text{A.18})$$

and

$$\frac{\partial g_{\text{st,c}}^j}{\partial \alpha^j} = \sigma_c, \quad (\text{A.19})$$

the Jacobian for the stress constraints $g_{st,t}$ and $g_{st,c}$ can be evaluated using Equation A.6 and Equation A.7 as follows:

$$\frac{\partial g_{st,*}^j}{\partial \bar{a}_t} = \frac{\partial g_{st,*}^j}{\partial \alpha^j} \frac{\partial \alpha^j}{\partial \bar{a}_t}, \quad (\text{A.20})$$

and

$$\frac{\partial g_{st,*}^j}{\partial \alpha^j} = \frac{\partial g_{st,*}^j}{\partial \alpha^j} \frac{\partial \alpha^j}{\partial \alpha^j}, \quad (\text{A.21})$$

where the asterisk * refers to either the compression and the tension constraints. The stress constraints are linear with respect to q :

$$\frac{\partial g_{st,*}}{\partial q} = \mathbf{1}, \quad (\text{A.22})$$

in which $\mathbf{1}$ represent a vector of all ones.

BUCKLING CONSTRAINTS Knowing that:

$$\frac{\partial g_{buck}^j}{\partial \alpha^j} = 2 \frac{s \alpha^j}{\ell^2}, \quad (\text{A.23})$$

the Jacobian for the buckling constraints g_{buck} with respect to \bar{a} can be evaluated using Equation A.6 as:

$$\frac{\partial g_{buck}^j}{\partial \bar{a}_t} = \frac{\partial g_{buck}^j}{\partial \alpha^j} \frac{\partial \alpha^j}{\partial \bar{a}_t}. \quad (\text{A.24})$$

Using Equation A.7 we evaluate the derivative with respect to α as:

$$\frac{\partial g_{buck}^j}{\partial \alpha^j} = \frac{\partial g_{buck}^j}{\partial \alpha^j} \frac{\partial \alpha^j}{\partial \alpha^j}. \quad (\text{A.25})$$

MAXIMUM SUM ALPHA CONSTRAINTS The constraint g_{sum} on the maximal value of α in every subdomain is linear with respect to α and it does not depend on the other design variables. For that reason we can write:

$$\frac{\partial g_{sum}}{\partial \bar{a}} = 0, \quad (\text{A.26})$$

$$\frac{\partial g_{sum}}{\partial \alpha} = \mathbf{1}, \quad (\text{A.27})$$

$$\frac{\partial g_{sum}}{\partial q} = \mathbf{0}. \quad (\text{A.28})$$

A.5. HESSIAN MATRIX

For the evaluation of the hessian matrix, we list here only the nonzero contributions, assuming that all the remaining are zero.

VOLUME The only nonzero contributions to the Hessian matrix are:

$$\frac{\partial^2 V}{\partial \bar{a}_t \partial \alpha_t^j} = \bar{\ell}^T \frac{\partial \tilde{w}_t^j}{\partial \alpha_t^j}, \quad (\text{A.29})$$

and

$$\frac{\partial^2 V}{\partial (\alpha_t^j)^2} = \bar{\ell}^T \bar{a}_t \frac{\partial^2 w_t^j}{\partial (\alpha_t^j)^2}, \quad (\text{A.30})$$

that can be evaluated using Equation A.9 and Equation A.10

EQUILIBRIUM CONSTRAINTS All terms are zero for the equilibrium constraints.

STRESS CONSTRAINTS

$$\frac{\partial^2 g_t^j}{\partial \bar{a}_t \partial \alpha_t^j} = -\sigma_t \frac{\partial w_t^j}{\partial \alpha_t^j}, \quad (\text{A.31})$$

$$\frac{\partial^2 g_t^j}{\partial (\alpha_t^j)^2} = -\sigma_t \bar{a}_t \frac{\partial^2 w_t^j}{\partial (\alpha_t^j)^2}. \quad (\text{A.32})$$

BUCKLING CONSTRAINTS To evaluate the Hessian of buckling constraints we need to define two additional indexes, l and m that are spanning from 0 to $N_T - 1$ as the index t . We can then write:

$$\frac{\partial^2 g_{\text{buck}}^j}{\partial \bar{a}_l \partial \bar{a}_m} = 2 \frac{s}{\ell^2} w_l^j w_m^j. \quad (\text{A.33})$$

The mixed term is evaluated as follow:

$$\frac{\partial^2 g_{\text{buck}}^j}{\partial \bar{a}_l \partial \alpha_m^j} = 2 \frac{s}{\ell^2} w_l^j \frac{\partial a^j}{\partial \alpha_m^j} + 2 \frac{s a^j}{\ell^2} \frac{\partial w_l^j}{\partial \alpha_m^j}, \quad (\text{A.34})$$

$$\frac{\partial^2 g_{\text{buck}}^j}{\partial \bar{a}_l \partial \alpha_m^j} = 2 \frac{s}{\ell^2} w_l^j \frac{\partial w_m^j}{\partial \alpha_m^j} \bar{a}_m + 2 \frac{s a^j}{\ell^2} \frac{\partial w_l^j}{\partial \alpha_m^j}, \quad (\text{A.35})$$

$$\frac{\partial^2 g_{\text{buck}}^j}{\partial \bar{a}_l \partial \alpha_m^j} = \begin{cases} 2 \frac{s}{\ell^2} \frac{\partial w_t^j}{\partial \alpha_t^j} (w_t^j \bar{a}_t + a^j) & \text{if } l = m = t \\ 2 \frac{s}{\ell^2} w_l^j \frac{\partial w_m^j}{\partial \alpha_m^j} \bar{a}_m & \text{otherwise.} \end{cases} \quad (\text{A.36})$$

And finally the quadratic term in α :

$$\frac{\partial^2 g_{\text{buck}}^j}{\partial \alpha_l^j \partial \alpha_m^j} = 2 \frac{s}{\ell^2} \bar{a}_l \frac{\partial a^j}{\partial \alpha_m^j} \frac{\partial w_l^j}{\partial \alpha_l^j} + 2 \frac{s a^j}{\ell^2} \bar{a}_l \frac{\partial^2 w_l^j}{\partial \alpha_l^j \partial \alpha_m^j}, \quad (\text{A.37})$$

$$\frac{\partial^2 g_{\text{buck}}^j}{\partial \alpha_l^j \partial \alpha_m^j} = \begin{cases} 2 \frac{s}{\ell^2} \bar{a}_t^2 \left(\frac{\partial w_t^j}{\partial \alpha_t^j} \right)^2 + 2 \frac{s a^j}{\ell^2} \bar{a}_t \frac{\partial^2 w_t^j}{\partial (\alpha_t^j)^2} & \text{if } l = m = t \\ 2 \frac{s}{\ell^2} \bar{a}_l \bar{a}_m \left(\frac{\partial w_m^j}{\partial \alpha_m^j} \right) \left(\frac{\partial w_l^j}{\partial \alpha_l^j} \right) & \text{otherwise.} \end{cases} \quad (\text{A.38})$$

MAXIMUM SUM ALPHA CONSTRAINTS All terms are zero for the g_{sum} constraint.